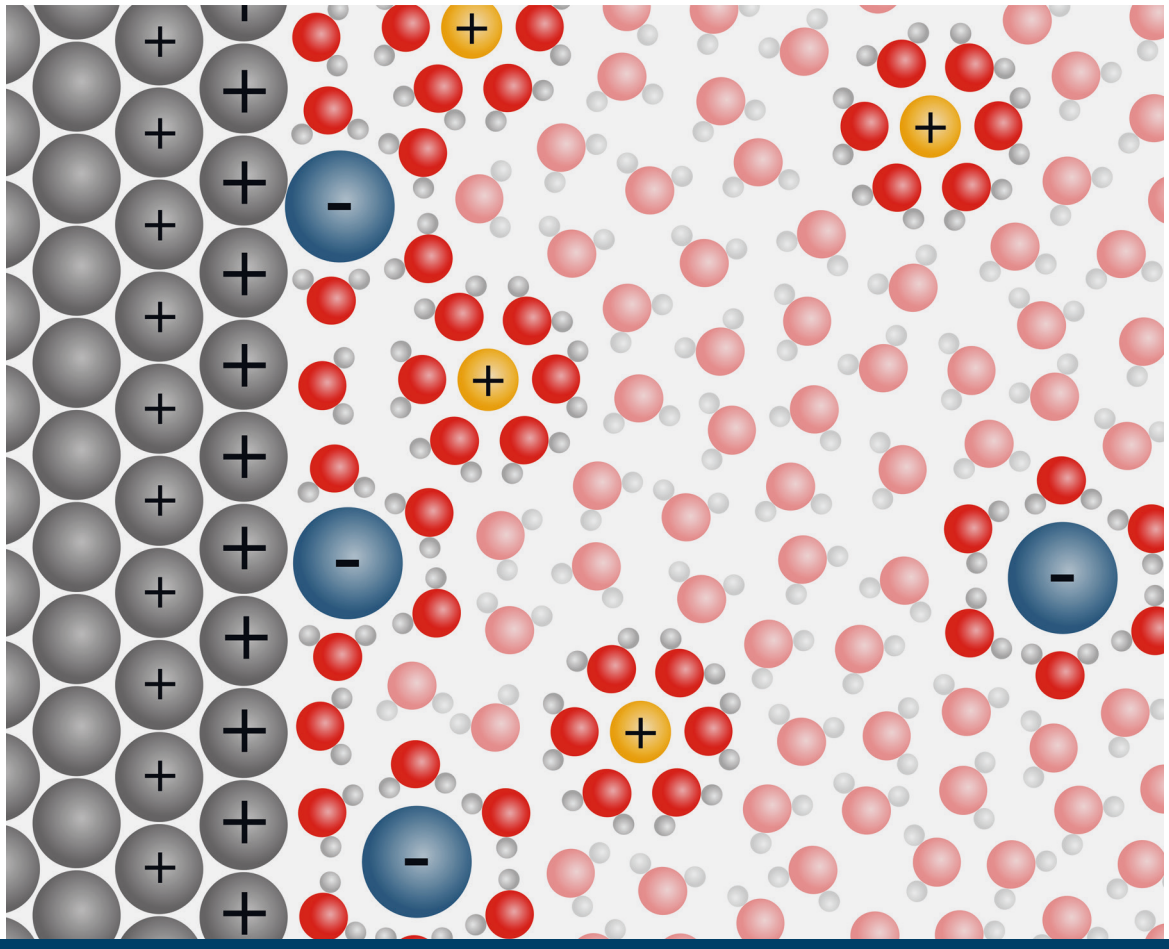

Structure and properties of electrochemical interfaces from first principles simulations

Rebekka Tesch

Energie & Umwelt / Energy & Environment
Band / Volume 629
ISBN 978-3-95806-753-0

Mitglied der Helmholtz-Gemeinschaft

JÜLICH
Forschungszentrum

Schriften des Forschungszentrums Jülich
Reihe Energie & Umwelt / Energy & Environment Band / Volume 629

Forschungszentrum Jülich GmbH
Institut für Energie- und Klimaforschung (IEK)
Theorie und computergestützte Modellierung von Materialien
in der Energietechnik (IEK-13)

Structure and properties of electrochemical interfaces from first principles simulations

Rebekka Tesch

Schriften des Forschungszentrums Jülich
Reihe Energie & Umwelt / Energy & Environment Band / Volume 629

ISSN 1866-1793 ISBN 978-3-95806-753-0

Bibliografische Information der Deutschen Nationalbibliothek.
Die Deutsche Nationalbibliothek verzeichnet diese Publikation in der
Deutschen Nationalbibliografie; detaillierte Bibliografische Daten
sind im Internet über http://dnb.d-nb.de abrufbar.

Herausgeber und Vertrieb:	Forschungszentrum Jülich GmbH Zentralbibliothek, Verlag 52425 Jülich Tel.: +49 2461 61-5368 Fax: +49 2461 61-6103 zb-publikation@fz-juelich.de www.fz-juelich.de/zb
Umschlaggestaltung:	Grafische Medien, Forschungszentrum Jülich GmbH
Druck:	Grafische Medien, Forschungszentrum Jülich GmbH
Copyright:	Forschungszentrum Jülich 2024

Schriften des Forschungszentrums Jülich
Reihe Energie & Umwelt / Energy & Environment, Band / Volume 629

D 82 (Diss. RWTH Aachen University, 2024)

ISSN 1866-1793
ISBN 978-3-95806-753-0

Vollständig frei verfügbar über das Publikationsportal des Forschungszentrums Jülich (JuSER)
unter www.fz-juelich.de/zb/openaccess.

Abstract

The transition to a sustainable energy system relies on the availability of high-performing and cost-effective energy storage and conversion devices, such as batteries, fuel cells and electrolysers. The performance of these devices is directly related to the properties of the employed electrocatalyst materials. In order to develop electrochemical devices that can respond to societal, economical and environmental needs, catalyst materials must be improved in terms of activity, long-term stability and production cost. This requires significant progress in the fundamental understanding of relevant electrochemical processes.

The majority of electrochemical processes take place at the interface between a solid electrode and a liquid electrolyte. Atomic-scale modeling is a powerful tool that can yield important information on structural, electronic and electrostatic properties of the interface. However, self-consistently modeling the two parts of the interface as well as their non-linear coupling is very challenging. Existing computational methods are limited in terms of accuracy and/or efficiency. The aim of this thesis is to address some of the limitations of existing methods and provide accurate computational methodologies for a realistic description of the local reaction conditions at the electrochemical interface and of the electrocatalytic processes.

We focus on two aspects: (1) the efficient and accurate computation of the electronic structure of materials with strongly correlated electrons, such as d- or f-electrons, and (2) the self-consistent description of phenomena at electrochemical interfaces, including the effects of electrolyte species and electrode potential. For these purposes, two methods have been studied in detail in this thesis: (1) the DFT+U approach for the description of strongly correlated electrons and (2) the recently developed effective screening medium reference interaction site method (ESM-RISM) for the description of electrochemical interfaces.

The conducted research enabled us to establish an improved DFT+U approach for the computation of the electronic structure of electrode materials. In this methodology, we derive the Hubbard U parameter from an existing first principles-based linear response method. Additionally, we use Wannier projectors instead of standard atomic orbitals projectors for more accurate counting of orbital occupations. The resulting scheme provides an improved electronic structure description of various d- and f-materials and allows, for example, for enhanced studies of catalytically active sites in oxide electrocatalysts. These results indicate that a correct electronic structure description is an important precondition for an accurate computational modeling of electrochemical interfaces.

Regarding the electrochemical interface, we extensively tested, validated and applied the ESM-RISM for metal/electrolyte interfaces. Our research showed that the ESM-RISM is a powerful method for the computation of electrochemical interfaces, when applied with care regarding the

parameterization of interactions and the description of the near-surface electrolyte structure. It is capable of delivering accurate information on various interface properties like the double layer structure, electrostatic interfacial potentials and surface charging relations. In particular, we were able to reproduce the measured non-monotonic charging relation of the partially oxidized Pt(111)/electrolyte interface.

Finally, we combined both computational approaches to study NiOOH materials as catalysts for the electrochemical oxygen evolution reaction (OER). This investigation was possible only with the non-standard DFT+U scheme, since the standard DFT+U approach incorrectly predicts a metallic state for this semiconducting material. In this respect, we discuss problems of grand canonical approaches for simulating electrified semiconductor/electrolyte interfaces. Accounting for the local reaction environment, we computed thermodynamic overpotentials for the OER, surface charging relations and properties of active sites depending on the potential-dependent degree of surface deprotonation. These results pave the way for more realistic simulations of electrochemical systems.

The outcome of this thesis enables improved and more accurate treatments of atomic-scale processes at electrochemical interfaces at reasonable computational cost. Providing a sound methodological basis, the investigated methods allow going beyond previous computational studies in terms of the description of electrochemical conditions. These methodologies, although still far from being able to self-consistently account for all relevant electrochemical phenomena, should lead to improved understanding of electrochemical materials. In this way, they help develop improved catalyst materials for energy devices that are required for implementing the energy transition.

Zusammenfassung

Für den Übergang zu einem nachhaltigen Energiesystem werden leistungsstarke und kostengünstige Energiespeicher- und -umwandlungsgeräte, wie Batterien, Brennstoffzellen und Elektrolyseure, benötigt. Die Leistungsfähigkeit dieser Geräte hängt in erster Linie von den Eigenschaften der verwendeten Elektrokatalysatormaterialien ab. Um elektrochemische Geräte zu entwickeln, die gesellschaftliche, ökonomische und ökologische Anforderungen erfüllen können, müssen Aktivität, Langzeitstabilität und Kosten von Katalysatormaterialien verbessert werden. Dazu müssen die relevanten elektrochemischen Prozesse erheblich besser verstanden werden.

Der Großteil dieser elektrochemischen Prozesse findet an der Grenzfläche zwischen einer festen Elektrode und einem flüssigen Elektrolyten statt. Die Modellierung dieser Grenzfläche auf atomarer Ebene kann wichtige Einblicke in strukturelle, elektronische und elektrostatische Eigenschaften liefern. Allerdings ist die selbstkonsistente Modellierung der beiden Seiten der Grenzfläche sowie ihrer nichtlinearen Wechselwirkungen eine große Herausforderung. Bestehende computergestützte Methoden sind in ihrer Genauigkeit und/oder Effizienz begrenzt. Ziel dieser Arbeit ist es, einige der Einschränkungen bestehender Methoden zu beheben und akkurate computergestützte Methodiken für eine realistische Beschreibung der lokalen Reaktionsbedingungen an der elektrochemischen Grenzfläche sowie elektrokatalytischer Prozesse zu entwickeln.

Wir konzentrieren uns auf zwei Aspekte: (1) die effiziente und exakte Berechnung der elektronischen Struktur von Materialien mit stark korrelierten Elektronen, wie d- oder f-Elektronen, und (2) die selbstkonsistente Beschreibung von Phänomenen an elektrochemischen Grenzflächen, unter Berücksichtigung des Einflusses einer Elektrolytlösung und eines Elektrodenpotentials. Zu diesem Zweck wurden in dieser Arbeit zwei Methoden im Detail untersucht: (1) der DFT+U-Ansatz zur Beschreibung stark korrelierter Elektronen und (2) die kürzlich entwickelte Effective screening medium reference interaction site method (ESM-RISM) für die Beschreibung elektrochemischer Grenzflächen.

Die durchgeführten Untersuchungen ermöglichten es uns, einen verbesserten DFT+U-Ansatz zur Berechnung der elektronischen Struktur von Elektrodenmaterialien zu etablieren. In dieser Methodik leiten wir den Hubbard-U-Parameter aus einer bestehenden First-Principles-Methode, der Linear-Response-Methode, ab. Außerdem verwenden wir Wannier-Projektoren anstelle von Standard-Atomorbital-Projektoren für eine genauere Berechnung der Orbitalbesetzungen. Die resultierende Methode bietet eine verbesserte Beschreibung der elektronischen Struktur verschiedener d- und f-Materialien und ermöglicht z. B. aussagekräftige Untersuchungen katalytisch aktiver Zentren in Oxid-Elektrokatalysatoren. Diese Ergebnisse zeigen, dass eine korrekte Beschreibung der elektronischen Struktur eine wichtige Voraussetzung für eine korrekte Modellierung von elektro-

chemischen Grenzflächen ist.

Bezüglich der Simulation elektrochemischer Grenzflächen wurde die ESM-RISM ausführlich getestet, validiert und für die Beschreibung von Metall/Elektrolyt-Grenzflächen angewendet. Diese Arbeit zeigt, dass die ESM-RISM eine leistungsstarke Methode zur Berechnung elektrochemischer Grenzflächen ist, wenn Wechselwirkungsparameter mit Bedacht ausgewählt und die oberflächennahe Elektrolytstruktur sorgfältig beschrieben werden. Sie kann präzise Informationen zu verschiedenen Grenzflächeneigenschaften wie Doppelschichtstruktur, elektrostatischen Grenzflächenpotentialen und Oberflächenladungsbeziehungen liefern. Insbesondere konnten wir die experimentell gemessene nicht-monotone Ladungsbeziehung der teilweise oxidierten Pt(111)/Elektrolyt-Grenzfläche reproduzieren.

Zuletzt wurden die beiden Methoden kombiniert, um NiOOH-Materialien als Katalysatoren für die elektrochemische Sauerstoffentwicklungsreaktion (OER) zu untersuchen. Diese Untersuchung war nur mit dem nicht-Standard-DFT+U-Schema möglich, da der Standard-DFT+U-Ansatz fälschlicherweise einen metallischen Zustand für dieses halbleitende Material vorhersagte. In diesem Zusammenhang diskutieren wir auch Probleme großkanonischer Ansätze zur Simulation elektrifizierter Halbleiter/Elektrolyt-Grenzflächen. Unter Berücksichtigung der lokalen Reaktionsumgebung wurden thermodynamische Überspannungen für die OER, Oberflächenladungsbeziehungen und Eigenschaften katalytisch aktiver Zentren in Abhängigkeit vom potentialabhängigen Grad der Oberflächendeprotonierung berechnet. Diese Ergebnisse ebnen den Weg für realistischere Simulationen von elektrochemischen Systemen.

Die Ergebnisse dieser Arbeit ermöglichen eine verbesserte und genauere Beschreibung von Prozessen an elektrochemischen Grenzflächen auf atomarer Ebene bei vertretbarem Rechenaufwand. Die untersuchten Verfahren bieten eine solide methodische Grundlage und gehen hinsichtlich der Beschreibung elektrochemischer Bedingungen über bisherige Studien hinaus. Obwohl diese Methoden noch weit davon entfernt sind, alle entscheidenden elektrochemischen Phänomene konsistent zu beschreiben, führen sie zu einem besseren Verständnis elektrochemischer Materialien. Auf diese Weise tragen sie dazu bei, verbesserte Katalysatormaterialien für Energiegeräte zu entwickeln, die für die Energiewende erforderlich sind.

Acknowledgments

First of all, I would like to express my deepest gratitude to my supervisors, Prof. Michael Eikerling and Dr. Piotr Kowalski. I could not have undertaken this journey without you. Thank you both for always being available, helpful, inspiring and encouraging. Thank you, Michael, for keeping an eye on the progress of my research and guiding me through the exciting world of computational electrochemistry, with a “sense of realism”. Thank you, Piotr, for introducing me to various computational methodologies, advising me about preparing scientific papers and presentations, and involving me in collaborations.

I am also very grateful to Prof. Axel Groß and Prof. Bernd Friedrich for being part of the board of examiners.

I thank all members of the IEK-13 for the warm and open atmosphere, stimulating discussions and delicious cakes. In particular, I would like to thank Prof. Jun Huang, Dr. Zhengda He, Dr. Mohammad J. Eslamibidgoli, Oskar Cheong, Yin-Ying Ting, Alison Shad, Thomas Bornhake, Yufan Zhang and Xinwei Zhu for valuable advice, explanations and inspirations, help with data analysis, and proofreading of this thesis. Special thanks go to Binny Alangadan Davis for sharing the office, and to Sandra Müller and Matthias Roß for keeping the institute running. Thank you all for being so knowledgeable and so enjoyable to work with.

Outside the IEK-13, I had the pleasure of working with Dr. Zhoaming Zhang, Dr. Gabriel Murphy, Prof. Minoru Otani, Bart Verlinden and Dr. Maximilian Schalenbach. These collaborations very much enriched my research experience.

I would like to acknowledge the computational resources provided on the supercomputers in Jülich and Aachen by the Jülich-Aachen Research Alliance. I am also thankful to the HITEC Graduate School for inspiring workshops, networking events and practical sessions in science communication.

Last but not least, I thank my husband, Tobias, for everything, ranging from scientific discussion to childcare. Without your support, this thesis would literally not exist.

Contents

List of figures

List of Tables

List of abbreviations

AIMD	ab initio molecular dynamics
AMF	around mean field
AO	atomic orbital
bcc	body centered cubic
CHE	computational hydrogen electrode
cLDA	constrained local density approximation
CMD	classical molecular dynamics
cRPA	constrained random phase approximation
CSM	continuum solvation model
DFT	density functional theory
DFT+*U*	density functional theory plus Hubbard *U* correction
DOS	density of states
ECI	electrochemical interface
ESM	effective screening medium
ESM-RISM	effective screening medium reference interaction site method
fcc	face centered cubic
FLL	fully localized limit
GGA	generalized gradient approximation
hcp	hexagonal closed packed
HS	high-spin
IFF	interface force field
IHP	inner Helmholtz plane
jDFT	joint density functional theory
KS	Kohn–Sham
LDA	local density approximation
LJ	Lennard-Jones
LS	low-spin
ML	monolayer
OER	oxygen evolution reaction
OHP	outer Helmholtz plane
PEM	polymer electrolyte membrane
PB	Poisson–Boltzmann
PBE	Perdew–Burke–Ernzerhof
PBEsol	PBE functional revised for solids

PDOS	projected density of states
pzc	potential of zero charge
revPBE	revised Perdew–Burke–Ernzerhof
RHE	reversible hydrogen electrode
RISM	reference interaction site method
SHE	standard hydrogen electrode
SPC	simple point-charge
TIP5P	transferable intermolecular potential with 5 points
UFF	universal force field
WF	Wannier function
XPS	X-ray photoelectron spectroscopy
ZPE	zero-point energy

1. Introduction

1.1. Electrochemistry as a pillar of the energy transition

Minimizing the impact of energy production and usage on environment and climate is one of the main societal challenges nowadays. The energy system of the future must be sustainable, that means eco-friendly and clean, but also economically viable and socially responsible. Production of energy from renewable resources, like water, wind or solar power, is one way to replace the current fossil fuels-based economy [1]. However, these resources have intermittent character. Energy storage and conversion will thus play a vital role in sustaining a continuous energy supply. For example, electricity can be stored in batteries [2] or converted to hydrogen gas to be used as chemical energy storage or industrial feedstock [3]. Conversion devices are also required for any attempts to convert environmentally harmful carbon dioxide (CO_2) into value-added products [4].

To realize the energy transition in the near future, existing technologies must be further improved. In this regard, electrochemical devices such as batteries, electrolysers and fuel cells (see Figure 1.1) are foreseen as drivers of the energy transition [5]. Rechargeable batteries allow to store electrical energy by converting it to chemical energy (charging) and back to electricity (discharging) through redox reactions. Batteries play an important role in the energy transition, allowing to store electricity produced from renewable sources to use it later or at another location. Electrolysers are devices in which compounds, e.g. water or CO_2, are split into their constituent elements by electrolysis, i.e. by applying an electric current. They contribute to storing renewable energy, for example in the form of hydrogen gas (so-called power-to-gas technologies). To implement the reverse process, i.e. produce electricity from the hydrogen gas in presence of an oxidizing agent like oxygen gas, fuel cells are employed. Fuel cells are key components of, for instance, hydrogen-fuelled vehicles.

To improve the performance and reduce the cost of electrochemical devices, the underlying electrochemical processes must be well understood. Electrochemistry is the scientific discipline that studies the coupling of electrical and chemical processes which are key for energy devices, e.g. reversible reactions of lithium ions in rechargeable batteries [6], reduction of CO_2 to various chemicals or fuels like carbon monoxide, methane or formic acid [4], and oxygen and hydrogen conversion reactions that are crucial in common fuel cells [7].

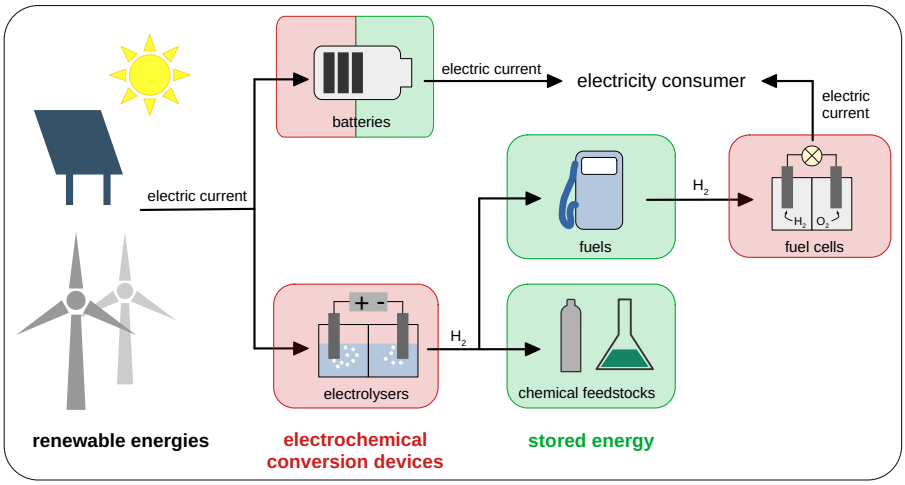

Figure 1.1.: Electrochemical devices, like batteries, electrolysers and fuel cells, make it possible to convert renewable energies to stored energy, fuels or chemical feedstocks.

In order to make the technologies competitive for use at large scale as part of a sustainable energy landscape, the underlying electrochemical reactions need to proceed with high efficiency. The reactions are accelerated by electrocatalysts to ensure this high efficiency. For example, hydrogen gas can be efficiently produced at a platinum catalyst surface. In addition, the energy devices must be stable over a long lifetime, inexpensive, safe and non-toxic. Thus, the aim is to use electrocatalyst materials with high electrochemical activity and stability during operation, and made of elements that are highly abundant and cheap.

In the last decades, electrocatalyst design and selection has become a highly active field of research, with many breakthroughs but also many open challenges. In order to make further progress, the fundamental understanding of the basic electrochemical processes has to be substantially improved. Only with a solid scientific basis it will be possible to rationalize why existing materials work well or not, to improve existing materials and to identify new promising ones. Electrochemistry can be seen as the fundamental discipline to provide important, and much-needed, technological breakthroughs – as has been realized by chemist and Nobel laureate Wilhelm Ostwald already 130 years ago [8]. Understanding the functioning and performance, but also ageing and failure of energy materials, means taking into consideration a large variety of electrochemical phenomena, which impact the electrochemical reactions. As will be demonstrated in this thesis, atomic-scale simulations can substantially contribute to an enhanced understanding of key electrochemical processes.

1.2. Fundamentals of electrocatalysis

The underlying electrochemical reactions in energy storage and conversion devices are electron transfer reactions: chemical bonds are cleaved and formed, and electrons are transferred from or to an electrode [9]. In oxidation reactions, electrons are released by some chemical species; in reduction reactions, electrons are taken up. In an electrochemical device, both reactions happen simultaneously, but at different electrodes (cathode and anode) and are thus spatially separated.

Electrocatalysts are employed to increase the rate of electrochemical reactions by reducing the activation barriers [9]. For example, the hydrogen evolution and oxygen reduction reactions in fuel cells are typically catalyzed by platinum catalysts. The catalyst itself is not consumed during the reaction and can thus fulfill its role for many reaction cycles. The reacting species adsorb at the catalyst surface, which controls bond formation and cleavage. Electrocatalysts are also electrodes [10]. They transport the reacting electrons to the counter electrode, closing the electric circuit in an electrochemical device. Next to the electrodes, electrochemical devices contain an electrolyte, which serves as a medium for ion transfer. In this thesis, we only consider solid electrodes and liquid electrolytes. Electrocatalysis at solid/liquid interfaces brings together principles of heterogeneous catalysis (taking place in vacuum) and electrified interfaces (see Section 1.3).

The ideal electrocatalyst (see Figure 1.2) is efficient (yields high reaction rates), selective (catalyzes only the wanted reaction and prevents side reactions) and stable (does not undergo chemical or structural transformations during numerous catalytic cycles). In addition, it must be non-toxic, affordable and composed of materials that are available in large amounts for large-scale technological applications. At the microscopic scale, the ideal catalyst has a high density of active sites and a large active surface area. It offers a reaction path with low activation energy and high electrical conductivity in order to effectively transport electrons. Because catalyst materials for future energy economy are to be fabricated at large scale, they should have low environmental impact at all life stages, from mining to production to disposal or recycling processes.

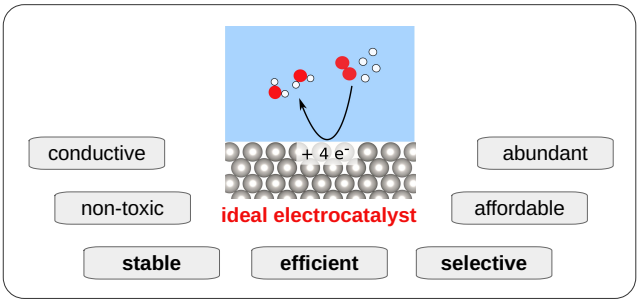

Figure 1.2.: Properties of the ideal electrocatalyst. These properties are mainly determined by the catalyst's chemical composition, particle shape and size, as well as interactions with the catalyst support.

Various kinds of materials can be manufactured as electrocatalysts. These include metals and metal oxides, carbon-based materials like carbon nanotubes and metal-organic frameworks. Electrodes are often multi-component or coated materials. In order to assure good electrical conductiv-

ity and reduce the loading of expensive catalyst particles, while maintaining a large active surface area, catalysts are usually supported, e.g. by carbon or alumina [11].

Understanding the catalytic behavior of materials to improve their performance includes analyzing and comparing their activities towards the relevant electrochemical reaction. Focusing on specific reaction steps facilitates this analysis. A widespread concept in chemical reaction kinetics is the *rate-determining step* (RDS), also called rate-limiting step. The RDS is the slowest elementary step of a multistep reaction, which determines the overall reaction rate [10]. It is usually the step with the highest activation barrier [9]. In electrochemistry, the RDS is determined by Tafel slope analysis. From the thermodynamic point of view, the *potential-determining step* (PDS), the reaction step with the most positive Gibbs free energy and thus most unfavorable equilibrium potential, is an important parameter [12]. It is closely connected to the thermodynamic overpotential, which is defined as the minimal overpotential required to make all reaction steps exergonic. The PDS is often used instead of the RDS to select an optimal catalyst [13]. It can be readily obtained from free energy profiles calculated by quantum mechanical methods (see application in Chapter 6). Both concepts, RDS and PDS, are highly simplified and based on assumptions that do not always hold in (electro)chemical reactions [14]. To overcome these issues, the *rate-determining term* (RDT) has been introduced [14]. It accounts for more characteristics of kinetics and thermodynamics, for instance, the potential-dependent adsorbate coverage. As a result, the RDT provides good estimates of potential-dependent Tafel slopes and volcano plots.

A few other principles exist that facilitate the analysis of electrochemical activities [15]. According to *Sabatier's principle* [16, 17], the bonding strength of an adsorbate (reactant) at a catalyst surface must be "just right". Too weak bonding will lead to too few molecules adsorbed and reacting, while too strong bonding will prevent the product from desorbing, leading to blocking of the surface and slowing down the reaction. When plotting the reaction rate vs. the bonding strength, one obtains a volcano-like curve [18], with the optimal catalyst located at the maximum. *Volcano plots* have been used for analysis and optimization of various electrocatalysts, but such concepts have to be employed carefully [19]. They rely on the idea of using a microscopic quantity (fundamental property), a so-called *activity descriptor*, to describe the macroscopic performance (functional property) of a catalyst. An interaction energy is usually used as the descriptor [20]. Using activity descriptors reduces the dimensionality of the problem, which is of great importance for, for example, catalyst design and selection based on high-throughput screening or artificial intelligence [21].

This dimensionality reduction is possible since activity-determining properties of catalysts are often related by the *Brønsted–Evans–Polanyi (BEP) relation* or by *scaling relations*. The BEP relation [22, 23] is a linear relation between activation energy and reaction energy of dissociative adsorption, i.e. between the adsorption strength of reaction intermediates and their reactivity. Scaling relations, on the other hand, are often identified for multistep electrochemical reactions. For instance, the adsorption energies of different intermediates are often linearly correlated, e.g. in the oxygen evolution reaction (OER) [24, 25].

Another very popular descriptor for catalysts including d-elements is the d-band center, based on the *d-band model* developed by Nørskov et al. [26–28]. This model relates adsorption energies to the metal's density of d-states. For example, an upshift in the d-band center pushes the antibonding

d-band–adsorbate states above the Fermi level, so that they are less occupied and the metal–adsorbate interaction is stronger. The bonding strength can then be related to the catalytic activity via Sabatier's principle. This simple model works remarkably well in predicting trends in reactivity among transition metals (e.g. [27, 29–32]). It can also explain effects of tensile strain or stress, e.g. for impurity atoms included in a matrix of larger atoms [33, 34].

In summary, a few catalyst properties can be enough to determine its activity. It is thus very important to derive these descriptors with high accuracy in theoretical models and simulation approaches. But even then, using descriptors is often not sufficient to explain catalytic activities and a detailed description of the local reaction conditions at the electrode/electrolyte interface is required. Both aspects are aims of this thesis.

1.3. Electrochemical solid/liquid interfaces

In electrochemical devices, the catalysts are integrated into an arrangement of layers, each with specific functionalities. As an example, the membrane electrode assembly in a polymer electrolyte membrane (PEM) fuel cell is shown in Figure 1.3 [7]. Reacting oxygen (O_2) and hydrogen (H_2) gases reach the catalyst layers via gas diffusion layers. Between the two catalyst layers, the PEM ensures separation of the electrodes and prevents gas flow as well as direct electron flow between them, while conducting protons. The catalyst layer itself is a nanoporous network that contains carbon support particles, platinum catalyst nanoparticles, ionomer and water. The support particles ensure electrical conductivity, whereas the platinum particles represent the actual catalytically active material. They are distributed in the form of nanoparticles to achieve high active surface areas, while keeping the content of costly platinum low. The ionomer ensures proton conduction while impeding electron transfer and gas diffusion. Water is the product of the oxygen reduction reaction and provides channels for proton conduction. Within this setup, the reacting species (O_2 and H_2 gases, electrons and protons) have access to the reaction sites at the catalyst surface, while the product water can travel from the catalyst to the outlet.

At the microscale, the platinum catalyst is in direct contact with a liquid, namely water containing ions (mostly protons in PEM fuel cells). The actual electrochemical reactions thus take place at this solid/liquid interface, which is called the *electrochemical interface* (ECI) or *electrode/electrolyte interface*.[1] Understanding the electrochemical reactions and other phenomena occurring at this interface is of great importance for understanding and improving the performance of electrochemical devices such as fuel cells. The electrolyte solution itself is often an acidic aqueous solution, like in PEM fuel cells, or an alkaline aqueous solution, like in the case of water splitting reactions catalysed by NiOOH compounds [35]. Similarly, the catalysts applied in CO_2 electrolysers are usually in contact with an aqueous electrolyte solution, but also organic electrolytes are applied [36].

[1] What is called "electrolyte" or "electrolyte solution" in this thesis is this ion-containing solvent, not to be mistaken with the electrolyte in the PEM.

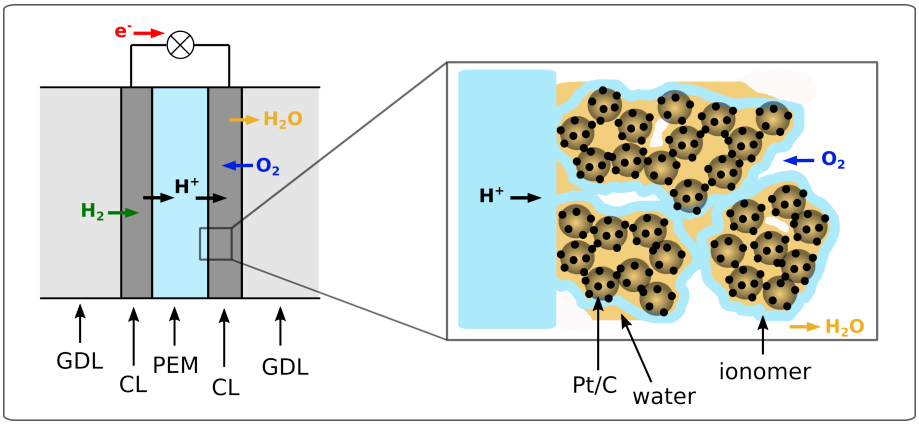

Figure 1.3.: Schematic of a PEM fuel cell (left) and detailed view of the catalyst layer (right). The fuel cell comprises gas diffusion layers (GDL), catalyst layers (CL) and the polymer electrolyte membrane (PEM). Inside the catalyst layer, there are agglomerates of carbon-supported platinum nanoparticles (Pt/C), surrounded by ionomer skins (shown in light blue). Pores are partly filled with water (shown in light orange). The size of the agglomerates is 40-80 nm [37]. The figure shows that platinum catalyst surfaces are in contact with an aqueous solution.

In electrochemical devices an electrode potential is applied to enable and facilitate electrochemical reactions. As a result, the electrode/electrolyte interface is electrified and charged. That means that the electrode surface bears an excess charge, which is balanced by a charge of equal magnitude, but opposite sign, in the electrolyte solution [10] (see Figure 1.4). The region containing the two layers of opposite charges is called the *electrical double layer*. On the solution side, mobile electrolyte ions can arrange in specific layers, named after early models by Helmholtz (see below). The potential at which the surface charge is zero is called the *potential of zero charge* (pzc).

The electrode and electrolyte regions differ in the type of conduction: the charge at the electrode surface is an electronic charge, whereas the charge in the solution is an ionic charge. For metallic electrodes, due to the high electrical conductivity, the electronic charge is confined in a narrow region of ca. 1 Å thickness at the surface [10]. In the electrolyte, the carrier concentration is smaller compared to metals and the screening region is about 5-20 Å thick (the thicker the lower the concentration of electrolyte ions) [10].

The resulting electrostatic potential profile is a key interface property. It influences, for example, the interaction of reacting ions with the surface. The variation in electrostatic potential is of the order of 1 V and occurs over a very narrow region at the interface of a few Å thickness. As a result, ECIs are characterized by extremely high electric fields of up to 10^9 V/m. Another important interface property is the surface dipole moment. Since the electronic density of a metal electrode extends into the electrolyte phase (spillover effect), a surface dipole arises that is oriented perpendicular to the surface plane [10]. The resulting surface potential is of the order of 1 V.

Depending on the applied electrode potential and resulting electric field, the electrolyte ions at the ECI arrange (see Figure 1.4) and alter the structure of the electrical double layer [38–42]. Another important effect of the applied potential is the reorientation of polar solvent molecules,

e.g. water [43, 44], as a function of potential. The applied potential also affects the electrode's electronic structure and surface structure, like chemisorption state [45] and adsorbate bonding strength [46, 47]. The applied potential thus has very high impact on local reaction conditions (see Section 1.4).

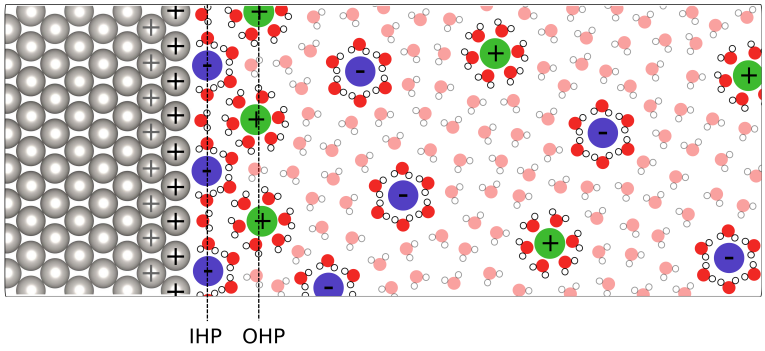

Figure 1.4.: The electrode/electrolyte interface. The electrode (here a single crystal metal, grey atoms) is shown at the left side, whereas the electrolyte aqueous solution is shown at the right side. The figure shows specifically adsorbed anions and oriented adsorbed water molecules directly at the surface, as well as solvated ions further away. Inner (IHP) and outer (OHP) Helmholtz planes are defined in the text.

In order to rationalize the impact of double layer properties on electrochemical reactions at the ECI, different models for the double layer have been developed. The first model is more than 150 years old: the Helmholtz model [48] describes the interface as a plate capacitor consisting of one layer of charges in the electrode and one rigid layer of counterions in the electrolyte solution. A linear potential profile between the two plates results from this configuration. Gouy and Chapman [39, 40] extended the Helmholtz model by replacing the rigid layer of ions by a diffuse layer, resulting in an exponential behavior for the electric potential at the interface. The electrolyte solution is represented by point charges placed in a dielectric continuum. The model is limited to low electrolyte concentrations and low interface charges, because otherwise the ion concentration at the interface becomes unphysically large and the electrode–ion gap very small. Stern [41] solved this problem by combining the Gouy–Chapman model with the Helmholtz model: a first rigid layer of ions (called Helmholtz plane) is adjacent to a diffuse layer of ions, defining a distance of closest approach for the ions to the surface. The model was further refined by Grahame [42]. In his model, a first layer of adsorbed solvent molecules together with specifically adsorbed ions (solvated ions which lost their solvation shell) build the inner Helmholtz plane (IHP) (see Figure 1.4). Solvated ions and the second solvent layer constitute the outer Helmholtz plane (OHP), next to which the diffuse layer of ions can be found. These different double layer models result in different behaviors of the interface capacitance, as will be described below (see Section 1.4 and Figure 1.7).

Further solvent effects, namely the orientation of solvent molecules at the interface in response to a surface charge, have been included by Bockris et al. [49]. Solvent orientation and polarization also have strong effects on the solvent permittivity (dielectric constant). More recent double layer models additionally include electronic effects of the electrode, first in a jellium approach [50, 51],

and nowadays usually by employing density functional theory (DFT). Double layer studies shifted to be based on first principles simulations (see Section 1.5).

So far, we have focused on interfaces of metallic electrodes. However, many interesting electrocatalyst materials have semiconducting properties, e.g. transition metal oxides like NiOOH. Semiconducting phases can also be oxide films that appear at metal electrodes due to surface oxidation. These materials potentially show different double layer properties. In contrast to metal/electrolyte interfaces, properties of semiconductor/electrolyte interfaces are to a high degree determined by the electronic properties of the electrode. Semiconductors are characterized by band gaps between ca. 1 and 3 eV. At semiconductor/electrolyte interfaces, an applied potential induces downward or upward bending of valence and conduction bands [10, 52–54]. The potential at which the bands are flat is called the *flat band potential*, and corresponds to the pzc in metal/electrolyte systems. As a consequence of band bending, accumulation or depletion of charge carriers is found (see Figure 1.5). The accumulation or depletion region is called the *space charge layer* and is up to 100 nm thick. In this region, the carrier concentration is typically very low. Consequently, in a charged semiconducting electrode, the charge is not localized in direct vicinity of the surface (as observed in metals). The largest part of the potential drop at the interface occurs in the space charge layer due to the low conductivity even of doped semiconductors. Atomic-scale simulations of semiconductor/electrolyte interfaces will also be part of this thesis.

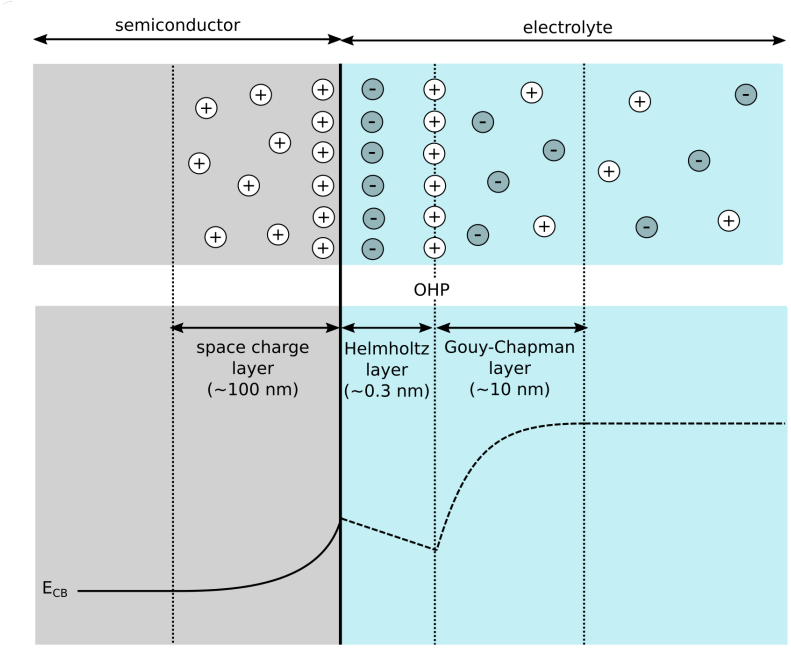

Figure 1.5.: The semiconductor/electrolyte interface. Top: possible charge carrier distribution. Bottom: conduction band (CB) energy (full line) and potential distribution in the electrolyte (dashed line). OHP indicates the outer Helmholtz plane.

1.4. Local reaction conditions

A large variety of properties and phenomena (e.g. structural, dynamic, electronic and electrostatic phenomena) arise at the ECI and determine the conditions under which electrochemical reactions take place [55], called *local reaction conditions* (or local reaction environment). It is crucial to correctly capture local reaction conditions in electrochemical simulations, since they have significant effects, for instance on the availability of catalytically active sites or on the stability of reaction intermediates, and, therefore on the catalytic activity of a material. This usually means to go beyond descriptor-based studies. One of the aims of this thesis is to improve the description of local reaction conditions in atomic-scale simulations. An overview of important atomic-scale interface properties is given here and in Figure 1.6.

The properties of an ECI are determined, first of all, by its atomic structure. The atomic structure can have an impact on the number of active sites and thereby directly influence a material's catalytic activity. The electrode's structure can deviate from the ideal structure by surface reconstructions, steps, defects, formation of surface layers or chemisorption of atoms or molecules. The structure of the electrolyte solution is determined by the positions and orientations of solvent molecules and electrolyte ions (e.g. related to concentration gradients in an electric field or mass transport limitations). The result is the structure of the electrical double layer. The structure of the solution phase is highly dynamic, including translational, rotational and vibrational movements.

Next to the atomic structure of the system, the electronic structure of electrode and electrolyte, including electron spillover effects at the interface, has an important effect on catalytic activity. It is primarily determined by the phases' chemical compositions. Electronic structure becomes apparent in spatial electron density distributions and energy levels of electronic states, and resulting spin and oxidation states.

As described in Section 1.3, the electrode potential has huge impact on atomic and electronic structures at the ECI. In addition, dielectric and polarization responses of the electrolyte solution are particularly relevant when dealing with charged interfaces. The applied potential also plays an important role in the capacitive behavior of the interface (see below). Thus, this quantity impacts the local reaction conditions severely and thereby the stability of reactants, intermediates and products and resulting catalytic activities.

Overall operation conditions like temperature, pressure, concentrations or pH value add to the list of interrelated factors determining the reaction conditions. On slightly larger time and length scales, processes like transport of reactants and products or diffusion of intermediates come into play. Likewise, degradation of materials, like oxide layer formation at platinum surfaces [56], are important effects for the long-term use of materials.

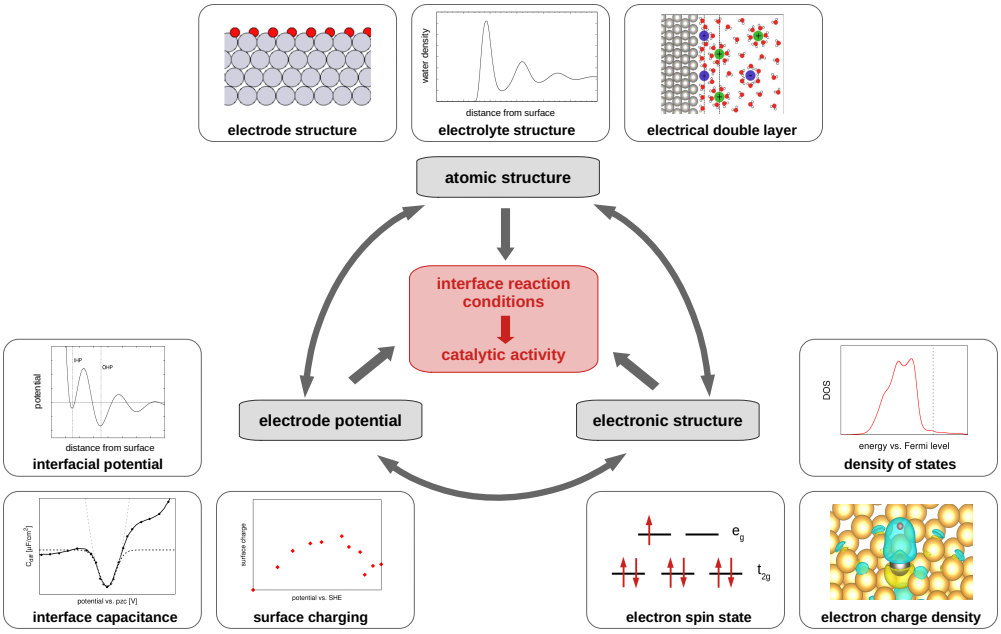

Figure 1.6.: Factors determining local reaction conditions at electrochemical interfaces and ways to probe them (small figures). Atomic structure, electronic structure and electrode potential are interdependent and need to be treated self-consistently in simulations. The focus is on the properties that will be simulated in the scope of this thesis.

One variable that is particularly relevant in the context of local reaction conditions is the *double layer capacitance* (or interface capacitance). The electrical double layer acts as a parallel plate capacitor. The capacitance specifies how much charge σ it stores at a certain applied potential ϕ:

$$C = \frac{\sigma}{\phi}\,. \tag{1.1}$$

The variation of surface charge per unit area σ with varying potential ϕ is described by the differential capacitance

$$C_{\text{diff}} = \frac{d\sigma}{d\phi}\,. \tag{1.2}$$

The double layer capacitance is of the order of magnitude of 10 μF/cm^2 for metal/electrolyte interfaces. It can be measured by impedance spectroscopy, cyclic voltammetry or electrocapillarity measurements [57, 58], but it can also be derived from DFT-based methods or theoretical models (see Chapter 5).

In general, the capacitance is not independent of potential, as assumed in the above equations, but shows characteristic behavior for different potentials. Each double layer model described above provides a capacitance curve with specific features, according to the phenomena included in the respective model. Figure 1.7 shows the constant double layer capacitance from the Helmholtz model. The Gouy–Chapman model includes the experimentally observed minimum at the pzc, but provides infinitely high capacitances for small or large potentials. The combination of both models,

the Stern model, allows the capacitance to level off for small or large potentials. The experimental curve is satisfactorily reproduced by the Grahame model, including asymmetry of the curve due to different behavior of anions and cations (cations have a more compact solvation shell, whereas anions lose their shell more easily and can then be closer to the surface). This indicates that the double layer capacitance can serve as a fingerprint for a specific ECI. Information that can be obtained from such a curve (or a set of curves) includes size, valence and concentration of electrolyte ions, solvent dielectric constant, orientation of solvent molecules, pzc or flat band potential, and different electron densities at the electrode surface (e.g. due to different crystal facets, resulting in different surface dipoles and shift of the pzc). Further, there are attempts to deconvolute the double layer capacitance (e.g. [59–62]). This results in contributions from different spatial regions of the interface, for example quantum (contribution of electrode's electronic structure), adsorbate, gap (between electrode and electrolyte), solvent and ionic contributions [59]. Each of these has a typical dependence on potential, and the smallest capacitance dominates the total interface capacitance.

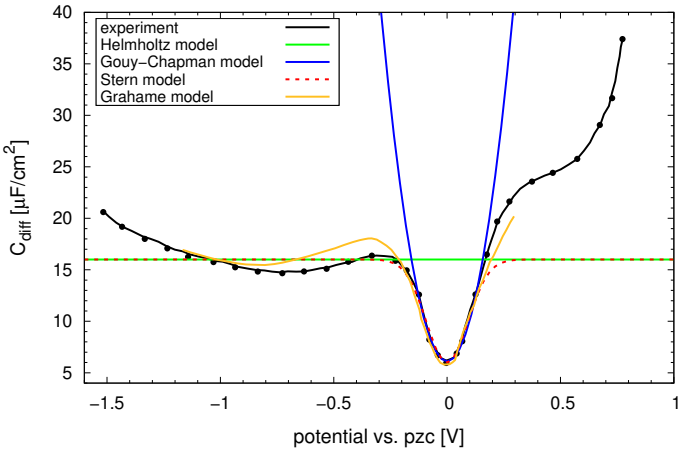

Figure 1.7.: Differential capacitance from different double layer models and experiment (adapted from ref. [63]). Experimental data [64] and Grahame model data [42] are for a mercury electrode in 0.001 mol/L NaF solution.

Due to its meaningfulness, the double layer capacitance has been used to validate computational and theoretical interface models [55, 65, 66]. The same holds for the relation between surface charge and potential, the so-called *surface charging relation*. The double layer capacitance can be determined in a simple approximation from the slope of a linear surface charging relation. Nonlinear surface charging relations can indicate specific adsorption at the surface (see Chapter 5 for the example of Pt(111)/electrolyte interfaces).

The space charge layer at semiconductor/electrolyte interfaces has a very small capacitance (0.001 to 1 μF/cm^2) due to its large thickness and low carrier concentration [54]. Since it is much smaller than the double layer capacitance in the electrolyte region, the space charge capacitance dominates the total capacitance of these interfaces [54]. This is in contrast to metal/electrolyte inter-

faces. Instead of capacitive charging, other forms of charging, like ionic or acid-base responses of oxide or hydroxide surface groups, could be dominating when applying an electrode potential or modifying the pH [67] (see Chapter 6 for the example of NiOOH(001)/electrolyte interfaces).

A self-consistent model of an electrochemical system is required to obtain valid results for local reaction conditions at ECIs [55]. This is because many interface properties are interdependent and coupled in a non-linear way. For example, the applied potential determines the arrangement of ions at the charged interface; at the same time, the ion arrangement has an effect on the potential profile. Building such a self-consistent model is a huge challenge for modeling approaches [55]. This thesis tries to address this challenge using methods of computational electrochemistry (see next sections).

1.5. Atomic-scale simulations of electrochemical interfaces

Atomic-scale simulations are very powerful tools enabling to decode ECIs at the atomic level. This thesis uses methods based on quantum mechanics as well as classical or continuum simulation methods. Because of the high computational demand of such simulations, these are limited to very short time scales (maximum of nanoseconds with classical methods, picoseconds with quantum mechanical methods). For the same reason, many aspects of ECIs must be simplified or neglected in the simulation workflow. For example, catalyst-support interactions are typically neglected, and perfect crystal surfaces are considered without any steps or defects [47, 68–70]. The challenge we tackle in this work is to find a computational methodology that can capture the relevant aspects, be computationally feasible and produce meaningful predictions of catalyst performance.

Methods originating from gas phase simulations, i.e. heterogeneous catalysis, are often adopted for electrochemical systems, but neglect important characteristics of ECIs, namely the local reaction environment. Two factors are commonly identified that make the description of ECIs more complex compared to surface science studies in vacuum: presence of the electrolyte solution and of the applied electrode potential, which together determine the formation of the electrical double layer (see Section 1.3). Since electric fields are localized in the electrochemical double layer directly at the interface [42], quantum mechanical simulations usually account for just one electrode and its local electrolyte environment.

For describing ECIs and local reaction conditions in atomic-scale simulations, a set of resulting interface properties is typically monitored (see examples in Figure 1.6). These include distribution functions, like radial or angular distribution functions, to describe the atomic structure of the dynamic electrolyte. The position of electrolyte ions is reflected by local electrolyte concentration and local pH. The electronic structure can be characterized by densities of states, band structure plots, band gap values, work function values, oxidation and spin states, or charge density visualizations, showing for example surface dipoles. Electrostatics can be characterized by a potential profile for a test charge across the interface, or potential values at the inner and outer Helmholtz planes. Combining the influence of electrode potential and pH value on phase stability results in Pourbaix diagrams. When considering electrochemical reaction paths, variables to monitor can be activation

energies or thermodynamic overpotentials.

In first principles electrochemistry approaches[2], the solid electrode is most commonly described at the level of density functional theory (DFT), whereas different approaches are adopted for the liquid electrolyte (see section 1.5.2). Figure 1.8 shows that computational approaches use different combinations of electrolyte and potential treatments. Currently, a universal method that self-consistently describes all coupled phenomena and resulting local reaction conditions at the interface does not exist [55, 59, 71–73]. In the following, state-of-the-art methods for the atomic-scale simulation of ECIs are reviewed. Comprehensive reviews on the topic can be found e.g. in refs. [55, 59, 74–79].

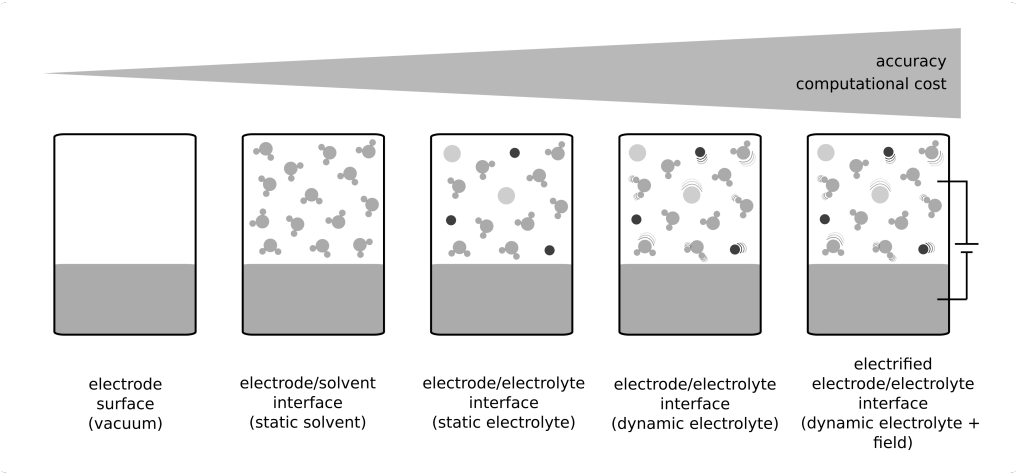

Figure 1.8.: Hierarchy of computational models for electrochemical interfaces. The solvent can be treated by an explicit, implicit or hybrid model (see Figure 1.9). Mixtures of setups shown here are often used in practice, e.g. static electrolyte with applied field.

1.5.1. Simulation methods for electrodes

Solid electrodes can be effectively computed using DFT, usually with computationally efficient exchange-correlation functionals in the generalized gradient approximation (GGA). However, electrodes in electrochemical devices often contain transition metals as active elements, and these elements contain strongly correlated electrons. Strongly correlated electrons (typically, d- or f-electrons) are poorly described by standard GGA functionals, but their description can be improved either by applying computationally intensive hybrid functionals or by adding a Hubbard U correction term to the GGA functional in the so-called DFT+U approach [80–82]. The computational cost of the latter method is comparable to calculations with GGA functionals. An important aspect of the DFT+U method is the choice of the Hubbard U parameter. For example, its value depends on the oxidation state of the respective species [83], a key variable in electrochemical reactions. Various

[2]It is sometimes discussed if DFT can be termed an “ab initio” or “first principles” method. These types of quantum chemistry methods rely only on laws of nature and physical constants, without introducing any assumptions or parameters. In practical implementations of DFT, the choice of approximation for the exchange-correlation functional (see Chapter 2) typically introduces some empiricism. However, both terms will still be used in this thesis, since the functionals employed here, e.g. PBEsol, were designed based on purely theoretical considerations.

aspects leading to accurate DFT+*U* simulations of metals and metal oxides will be investigated and substantially improved in this thesis (see Chapters 3 and 4).

Computation of electrodes involves accounting for the electrode potential, i.e. simulating charged electrodes. While experiments are typically conducted at constant electrode potential, standard DFT calculations are more easily performed at constant charge, i.e. with a fixed number of electrons. This makes the application of an external potential in a DFT calculation less straightforward. Several schemes have been developed (see e.g. ref. [74] for an overview). In addition to the approaches described in the following, which reduce the electrochemical system to just one half-cell, an electrode potential can also be applied in a two-electrodes setup. These approaches use classical force fields [84], finite field methods [85–87] or a doped semiconducting counter electrode [88].

A very simple and thus widely used potential application scheme is the computational hydrogen electrode (CHE) scheme introduced by Nørskov et al. [12]. Here, the effects of an applied potential are introduced only after the actual DFT calculation by adding a potential term to energies of electron transfer steps (see Section 2.1.3 for details on the CHE formalism). The surface remains uncharged at all potentials, and variations in the interface structure caused by the applied potential and interactions between the field and adsorbate dipoles are neglected. This can yield e.g. wrong adsorption energies for intermediates that are sensitive to the interfacial electric field [89, 90]. Despite these crude approximations for the interface description, the CHE has been routinely applied, on many occasions with success, for prediction of various properties of electrochemical systems, including trends in electrochemical activity and mechanistic details of electrochemical reactions (e.g. [12, 91–95]), or to generate Pourbaix diagrams [90, 96–99]. The CHE can also be readily combined with machine learning to speed-up materials screening [100, 101]. The generalized CHE (GCHE) [102] includes the solvent structure and some field effects at the interface. However, the interface is still treated as uncharged.

In grand canonical schemes (e.g. [96, 103–107]), the number of electrons in the DFT system can vary freely, so that the chemical potential of electrons is constant, as in experimental conditions. Adding or subtracting electrons can be realized in potentiostat schemes [103, 108, 109], which implement the charge variation in the self-consistent field procedure of the DFT calculation. In combination with a suitable counter charge distribution in the electrolyte, meaningful charging effects and electric fields at the interface can be obtained [104, 110, 111].

Charged electrodes, in a periodic DFT setup, require placement of an appropriate counter charge to establish electroneutrality of the simulation cell and ensure convergence of energy terms. Different schemes have been applied (see ref. [59] for an overview), including placement of a uniform background charge [112, 113], charge sheet [114, 115] or counter ions [116–119]. The counter charge can also be described by the Poisson–Boltzmann approach, which computes the ionic distribution as a function of potential (see Section 1.5.2). The most realistic electric field and charge distributions can be obtained in schemes where the electrode charge is balanced by the variable (self-consistently determined) electrolyte charge [65, 104, 111].

Furthermore, simulating electrified interfaces requires the definition of a potential reference, so

that the computed Fermi level (electron chemical potential) or work function can be related to an experimental potential scale. The referencing can be based on computed pzcs [120], on an internal reference [121], on the inner potential of an electrolyte solution [122], or on the absolute standard hydrogen potential [123]. Another option is to relate the electrode potential to an experimental scale via a potential-dependent interface property, like the oxygen coverage of Pt(111) [44, 124] or degree of deprotonation of nickel oxyhydroxides [125].

1.5.2. Simulation methods for liquid electrolytes

The electrolyte solution at an ECI can be aqueous, e.g. dilute salts, acids or bases [126, 127], or non-aqueous, e.g. organic solvents [126, 128–130] or ionic liquids [130–134]. This thesis will only deal with aqueous electrolyte solutions, as relevant for example in platinum catalyst layers in PEM fuel cells (see Section 1.3). In aqueous solutions, hydrogen bonds are the dominant type of intermolecular interactions. Local reaction conditions at solid/liquid interfaces depend on the dielectric response (screening) of the solvent as well as on the ionic response of electrolyte ions at the applied electrode potential (see Section 1.4). Including only a pure solvent without electrolyte ions, as it is sometimes done in simulations to reduce the complexity of the problem, neglects important characteristics of the interface.

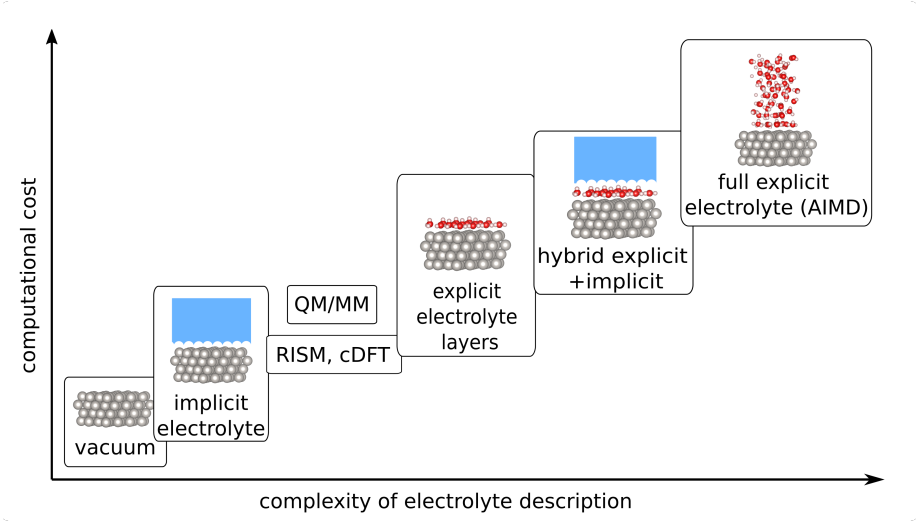

Figure 1.9.: Hierarchy of electrolyte descriptions, indicating the complexity as well as computational cost of each approach. To be combined with approaches in Figure 1.8. The electrode is always assumed to be described by DFT (classical molecular dynamics is not considered). Abbreviations are defined in the text.

Describing the dynamics and numerous possible configurations of solvent molecules and electrolyte ions at relevant operation temperatures is essential to obtain a realistic picture of the liquid phase. Thermodynamic sampling and statistical averaging of these configurations are important aspects in interface modeling. The main types of methods for the description of electrolytes in

DFT-based simulations are visualized in Figure 1.9. These approaches will be described briefly in the following. Several reviews exist about the topic, e.g. refs. [59, 77, 135].

Ab initio molecular dynamics (AIMD) simulations [136] likely provide the most complete picture of structure and dynamics at the electrode/electrolyte interface at the desired temperature. In these simulations, the forces used to generated particle trajectories are computed from DFT. With AIMD, for example, the detailed water structure and dynamics [69], surface adsorbate coverage [137] and interfacial charge redistribution and potential [138] at metal/water interfaces can be studied. However, with the entire system treated at the level of DFT, these simulations are extremely costly. In addition, very large time and length scales are necessary to obtain equilibrated and sufficiently sampled electrolyte distributions [139]. Electrolyte ions are often neglected in AIMD simulations since they would require very large simulation cells.

Often, just a few layers of electrolyte solution next to the electrode can be described in AIMD simulations due to computational constraints. This makes the solution structure prone to artificial boundary effects at the electrolyte/vacuum boundary. A few layers of explicit (AIMD) electrolyte solution, e.g. near-surface water molecules, can be combined with a continuum description (see following sections) for the bulk electrolyte, named hybrid or microsolvation schemes or cluster-continuum modeling [71, 140–142]. The explicit electrolyte layers or solvation shells around reacting molecules are also often treated in a static DFT calculation instead of AIMD [140, 143, 144]. While saving much computational effort, this treatment neglects the dynamic character of the electrolyte solution and solvent reorganization upon charge transfer [145, 146].

Quantum mechanics/molecular mechanics (QM/MM) schemes treat parts of the system, e.g. the electrode plus some electrolyte layers, by DFT, and the rest of the system by classical molecular dynamics (CMD) [147–151]. CMD simulations rely on parameterized interactions in force fields and are computationally very efficient, so that significantly larger length and time scales can be simulated compared to AIMD. However, CMD simulations do not account for electronic structure, so that reactions of electrolyte molecules or solvent dipoles are not accessible. Additionally, there are open questions for the interface between QM and MM regions [147, 152], so that works using QM/MM schemes are rather sparse in electrochemical applications.

In contrast to schemes with explicit solvent and electrolyte particles, continuum (or implicit) solvation models (CSMs) [65, 66, 153–160] conduct statistical averaging by replacing the electrolyte solution by a uniform polarizable medium. The solvent is mainly characterized by a dielectric function, switching its value from solvent to solute regions. Solvent-specific properties are parameterized [59, 161]. While making these models very efficient, this limits their applicability for charged interfaces, since CSMs were mostly originally designed for solvation of small organic, neutral solutes [66]. In CSMs, information on the solvent ordering and orientation at the interface is lost. Solvent electronics are not described, so that all electroactive molecules need to be computed explicitly at the quantum mechanical level. Comparison to AIMD results has shown that the most frequently used CSMs do not yield more accurate adsorption and solvation energies than vacuum descriptions for metal/water interfaces, since hydrogen bonds and competitive water adsorption are not described [162]. CSMs also have weaknesses in describing the capacitive behavior of an ECI [59, 65]. For example, most CSMs underestimate the surface charge as a function of applied

potential [66]. The interfacial capacitance depends on the width of the electrode–electrolyte gap and thereby on the cavity parameterization [163].

Electrolyte ion distributions as a function of potential are commonly described by Poisson–Boltzmann (PB) approaches in implicit electrolyte models [164]. PB models determine the ionic distribution under potential self-consistently. The lineralized PB model reduces the complexity and computational cost for small potentials. It is applied for example in the widely used VASPsol implementation [165, 166]. To solve the issue of unphysically high ion concentrations at ECIs, the modified PB (mPB) model [164, 167] introduces a packing limit for ions. This model is more suitable for high ionic concentrations and high surface charge densities or fields.

Statistical distributions of solvent and electrolyte species can be obtained from models that rely on integral equations theory of liquids, as the reference interaction site method (RISM) [168], or on classical DFT (cDFT), as in joint density functional theory (jDFT) [120, 169, 170]. These models do not explicitly define a cavity and are therefore also called non-cavity-based models. RISM calculations require the choice of suitable interaction parameters for the interaction between electrolyte species [122] (e.g. from a classical water model, see Chapter 5), whereas jDFT requires the construction of classical density functionals for the liquid [171–173]. Details about the RISM theory are given in Section 2.2.2.

1.5.3. Simulation methods for electrochemical interfaces

A prerequisite for a consistent and accurate interface description is a good choice of methods for treating the charged electrode and electrolyte sides (see previous sections). But this is by far not enough; the electrode and the electrolyte solution need to be properly coupled to obtain a complete picture of the ECI. All interface phenomena are interdependent and influence each other, giving rise to notable challenges for simulations. To date, there is no method that can describe all properties of the ECI self-consistently at the desired computational cost and accuracy [55, 59, 71–73]. In principle, AIMD simulations with applied potential could capture all phenomena, including the effects of surface electronic and adsorption state, electrolyte structure and orientation and chemical reactions at the level of DFT. However, this approach is infeasible due to extremely high computational effort, which would increase even more by introducing a charge optimization cycle for an electrified interface. Feasible descriptions of the entire interface therefore often rely on combinations of DFT with continuum solvation methods, like DFT combined with CSM or mPB approaches [105, 114, 174], on the effective screening medium reference interaction site method (ESM-RISM) [104] or on joint density functional theory (jDFT) [120].

Mean-field descriptions of the electrolyte solution, like in DFT+CSM/mPB, do not yield details of the fluid distributions at the ECI. They usually employ grids of constant charge calculations to model the electrode potential together with different counter charge methods (e.g. Gaussian-shaped counter charge layers [105]) to ensure electroneutrality and reproduce the electrolyte charge screening. These methods have been employed to compute pzcs, electrostatic potential, surface structure, surface dipoles, charge redistribution and double layer capacitance at ECIs [105, 174].

In contrast, the ESM-RISM and jDFT yield more detailed structural information for the electrolyte solution (see Section 1.5.2). In jDFT, an electron density functional for the electrode and a classical density functional for the electrolyte solution are joined in a single variational principle [169]. The computed electrolyte density, dielectric and screening properties lead to pzc values and capacitive properties of the interface [120]. The ESM-RISM combines a RISM description of the electrolyte solution with a DFT description of the electrode in mixed boundary conditions, both parts being coupled by an interaction potential. The method can provide information on the structure of the electrical double layer at applied potentials. It has been applied previously to platinum catalysts to obtain electrolyte distribution functions and the interfacial electrostatic potential, yielding local reactions condition at reaction planes like the OHP [124]. It has provided potential- and pH-dependent binding energies of CO at copper surfaces [175], as well as the pH-dependence of the free corrosion potential derived from grand potentials [176]. It has also been applied to study layered or intercalation materials in a solvent phase [177–179], as well as interface capacitances [175, 176]. The ESM-RISM will be used extensively in this thesis to obtain local reaction conditions at metal/electrolyte as well as semiconductor/electrolyte interfaces (see Chapters 5 and 6). Details on the method can be found in Section 2.3.

For DFT simulations of charged semiconductor/electrolyte interfaces (see Figure 1.5), two additional challenges arise: firstly, the space charge layer (up to 100 nm thick) is thicker by orders of magnitude than slab models used for DFT calculations of surfaces, so that only a small part of this layer can be captured. Secondly, the Fermi level shows a discontinuity related to the semiconductor's band gap [180]. This discontinuity is a problem for grand canonical DFT approaches since these rely on the linear relation between Fermi level and applied potential to model electrified interfaces. As a consequence, for semiconducting electrodes, potentials falling in the band gap region are not accessible in grand canonical methods.

For these reasons, atomic-scale simulations of electrified semiconductor/electrolyte interfaces are scarce with many of them published only very recently. Continuum models [181, 182] can represent the full thickness of the space charge layer, but lack all electronic structure information, as discussed above. Finite-field DFT simulations have been employed to study electrified semiconductor/electrolyte interfaces [183, 184], but rely on a different DFT formalism than commonly employed. In implementations of jDFT, a potential can be applied also to semiconducting electrodes via a separate electron bath with fixed chemical potential [180]. The constant inner potential method [107] avoids the Fermi level discontinuity problem by referencing the electrode potential to the potential in the bulk electrode instead of the Fermi level. However, the mentioned DFT methods do not address the problem of the huge space charge layer thickness. In Chapter 6 of this thesis, the capabilities of the grand canonical ESM-RISM will be evaluated for simulating a semiconductor/electrolyte interface.

For all kinds of ECIs, the main drawback of the methods described above, except for AIMD, is that they are not reactive or dynamic. Charge or atom transfer between electrode and electrolyte phases cannot be described. Therefore, important contributions to the interface dipoles and to the capacitance might not be captured. The same holds for spontaneous (electro)chemical reactions of solvent and electrolyte species with the electrode surface or among each other, that require dy-

namic simulations at sufficiently long time scales. Moreover, all models contain parameters (e.g. charge density thresholds for the dielectric cavity [105] or pair interaction parameters [104]) that need to be carefully adapted to the interface in question. Future methods could rely on reactive versions of models that couple DFT to CSMs or RISM or on powerful interface functionals. Increasing computational power meanwhile increases the possible scope of AIMD simulations. Combining simulations with theoretical concepts can greatly enhance the understanding of interface phenomena [55]. Recent works also propose to replace standard Kohn–Sham DFT by computationally efficient orbital-free DFT [185], after improving the limited accuracy of the method. In addition, machine learning approaches hold great potential for computational electrochemistry [186], either by accelerating simulations, e.g. via on-the-fly machine learning force fields for AIMD [187], or by replacing explicit simulations completely by data-driven approaches [188].

1.6. Aims of this thesis

To successfully realize the energy transition, we urgently need improved catalyst materials for energy applications at the large scale. In order to improve their performance, cost and long-term stability, we have to improve our understanding of their properties at the atomic scale. This applies in particular to properties of the electrochemical interface (ECI), since decisive catalytic processes take place there. Computational electrochemistry has good prospects for suggesting new materials or improving existing ones, especially when combined with experimental studies or theoretical models. However, still, major methodological developments are required. Atomic-scale methods for description of ECIs need to be improved in terms of accuracy, efficiency and predictive power.

Three main challenges can be formulated for computation of ECIs: (1) computing the interface under an applied electrode potential, and pinning this potential to an experimental scale; (2) incorporating electrostatic and electronic electrolyte effects and realizing thermodynamic sampling of electrolyte configurations; (3) describing the non-linear coupling of interface phenomena at the electrode/electrolyte boundary. As described above, a plethora of interface models exists, all with very different assumptions, accuracy, range of applicability and efficiency.

However, existing methods are either too computationally demanding or too inaccurate to provide a self-consistent description of all relevant interface properties. For example, ab initio molecular dynamics methods have prohibitive computational cost when applied to sufficiently large time and length scales. On the other hand, computationally efficient continuum solvation models lack an electronic description of the electrolyte solution and thus have limited accuracy. Computational methods specifically designed for electrochemical applications also have strong limitations. Many of them rely on a constant double layer capacity and assume a linear dependence of electrochemical properties on the electrode potential, so that they are applicable only near the pzc (e.g. [189, 190]), even though this is not the relevant potential range for electrochemical reactions. Another major shortcoming is that many studies are based on the computational hydrogen electrode (CHE), entirely neglecting the reaction environment at the interface. However, local reaction conditions directly influence the catalyst's performance (e.g. by determining how much reactant is available at the interface) and should therefore be included to make impactful predictions for cat-

alytic activities. A valid interface description also includes a computationally feasible and accurate electronic structure description of the electrode, since electrochemically active *d*-electrons pose a fundamental challenge to DFT-based methods.

Computational electrochemistry is a very active field of research, and new methodological developments are constantly emerging. This thesis contributes to this research flow by investigating some key challenges related to the atomic-level computation of ECIs. The overall goal of this thesis is to describe local reaction conditions at ECIs of technologically relevant electrocatalysts by applying state-of-the-art first principles methods. We aim to explicitly include electrochemical conditions to obtain a more realistic description of catalytic properties. We intend to make the best possible use of available methods in order to go beyond simplified or "black box" ways of applying them and to be able to describe complex electrochemical systems. This requires a detailed understanding of well-established as well as cutting-edge methods regarding underlying assumptions, functionality and applicability. Therefore, this thesis also comprises an extensive model validation and improvement part.

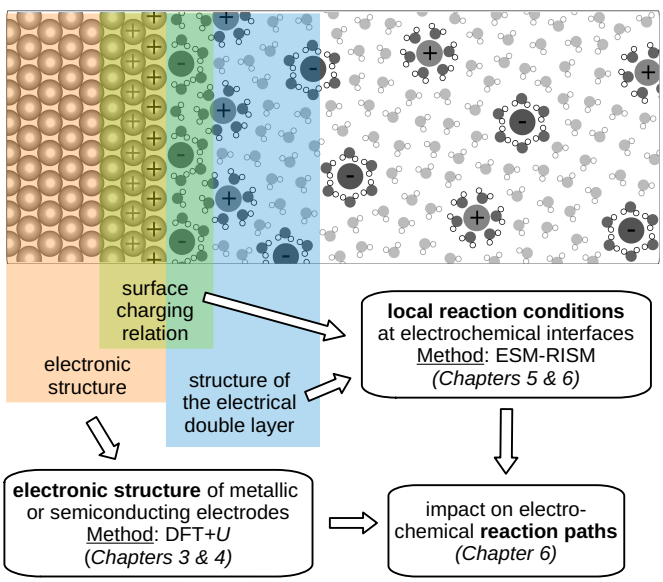

Figure 1.10.: Topics of this thesis. The figure shows the interface properties whose computation we aim to improve. Compare to Figure 1.4 for the representation of the electrochemical interface.

This thesis addresses two highly relevant aspects for computation of ECIs (see Figure 1.10): (1) the correct computation of electronic structure of various electrode materials, including those with strongly correlated electrons; (2) the self-consistent computation of ECIs, including the effects of electrode potential and electrolyte and the non-linear coupling between all involved parts of the system. Two methods are studied in detail for these purposes: (1) the DFT+*U* approach, an efficient method for electronic structure calculations of systems with strongly correlated electrons; (2) the ESM-RISM, a recently developed method for description of ECIs. Combining both methods

allows to describe relevant materials properly, as shown for NiOOH in Chapter 6 of this thesis. The aim is to establish applicable, i.e. reliable and accurate, but at the same time efficient, methods for descriptions of various ECIs. This includes metallic or semiconducting electrodes as well as acidic or alkaline aqueous electrolytes. We will thoroughly evaluate how to correctly apply these methods and what their limitations are, and introduce some improvements, before applying them to non-trivial ECIs.

Concerning the DFT+U approach, we target a parameter-free variant of this method which yields correct electronic properties for metals as well as semiconductors. The DFT+U method is regarded as the gold standard for computation of strongly correlated electrons, but we stress that it should not be applied blindly. We will evaluate different existing methods to derive the Hubbard U parameter from first principles, with focus on a linear response scheme [191]. We will show that the choice of projection operator to compute the occupations of strongly correlated orbitals is crucial to reach agreement of the electronic structures with experimental data. We will evaluate our variant of the method for different materials containing strongly correlated d- and/or f-electrons. Establishing a reliable electronic structure method for electrocatalyst materials, this part of the thesis can also be perceived as a precondition for the part following thereafter.

The ESM-RISM as a method to describe ECIs has been proposed and implemented by Nishihara and Otani [104] in 2017. It seems to be a promising method to tackle the challenges of interface descriptions and obtain a reasonable representation of local reaction conditions, including both electrolyte and electrode potential at reasonable computational cost. But to date, the ESM-RISM is far from being applied routinely. We intend to evaluate if it works reliably also for complex interfaces and which interface properties can be obtained. We will apply the method in detailed studies of Pt/electrolyte and NiOOH/electrolyte interfaces. Taking into account the results for electronic structure from the enhanced DFT+U scheme described above, we will compute local reaction conditions and an electrochemical reaction path. We will focus on electrolyte and double layer structures, surface charging relations, interface potentials, and characterization of active sites. We are interested in the impact of the enhanced interface description on these properties and compare to other first principles methods, experimental data and theoretical models.

The ultimate goal of this thesis is to improve the description of local reaction conditions in atomic-scale simulations. In summary, we aim to validate existing methods, improve upon their weaknesses and exploit their specific strengths. We then realize detailed and meaningful studies of ECIs relevant for energy materials.

During this doctoral project, several publications and contributions to publications emerged (see also List of publications B). These works constitute the main parts of this thesis, as indicated at the beginning of each chapter. This thesis is structured as follows: Chapter 2 presents the theoretical basics and computational methods used in the thesis. In Chapters 3 and 4, we demonstrate and apply the enhanced DFT+U scheme for electronic structure calculations of d- and f-element materials. Afterwards, Chapter 5 presents thorough validation and application of the ESM-RISM to metal/electrolyte interfaces. Chapter 6 combines both DFT+U and ESM-RISM to understand catalytic properties of highly relevant NiOOH catalysts. The thesis ends with conclusions and outlook for future work in Chapter 7.

2. Computational Methods

2.1. Computing electrode materials

2.1.1. Density functional theory

All simulations executed in this thesis involve calculations performed with density functional theory (DFT). Nowadays, DFT is the most widely applied quantum mechanical method for computation of the electronic structure of materials and related physical and chemical properties. The fundamentals and most important aspects of DFT are described in the following section. Comprehensive descriptions can be found in various textbooks, e.g. in refs. [192, 193].

The Schrödinger equation. In principle, the complete quantum mechanical solution of an N electrons problem can be obtained by solving the Schrödinger equation [194]. Its time-independent form is an eigenvalue equation involving the Hamiltonian $\hat{H}$, the wave function ψ (containing all information on the system), and the total energy of the system E:

$$\hat{H}\,\psi = E\,\psi\,. \tag{2.1}$$

The Hamiltonian comprises kinetic energy (operator $\hat{T}$) and potential energy (operator $\hat{V}$) terms. For a system made up of N electrons and M nuclei of mass M_X and nuclear charge Z_X, it reads (in atomic units):

$$\begin{aligned}
\hat{H} &= \hat{T} + \hat{V} && (2.2)\\
&= \hat{T}_e + \hat{T}_N + \hat{V}_{eN} + \hat{V}_{ee} + \hat{V}_{NN} && (2.3)\\
&= -\sum_i^N \frac{1}{2}\nabla_i^2 - \sum_A^M \frac{1}{2M_A}\nabla_A^2 - \sum_i^N\sum_A^M \frac{Z_A}{r_{iA}} + \sum_i^N\sum_{j>i}^N \frac{1}{r_{ij}} + \sum_A^M\sum_{B>A}^M \frac{Z_A Z_B}{r_{AB}}\,, && (2.4)
\end{aligned}$$

where r_{xy} denotes the distance between particles x and y (electrons or nuclei).

It is possible to solve the Schrödinger equation analytically for the hydrogen atom, and numerically for systems with a few electrons (e.g. the helium atom [195]) or for the simple case of the homogeneous electron gas [196], but it is unsolvable for more complex systems. Therefore, different approximations were introduced. A very prominent approximation is the Born–Oppenheimer approximation [197]. It separates the motions of heavy nuclei (considered stationary) from the ones of much lighter electrons by assuming that the time scales of these two types of motions are very different. Consequently, the total wave function can be approximated as the product of electronic and nuclear wave functions, and the kinetic energy term of the nuclei can be neglected in the

Hamiltonian. Additionally, the nuclei–nuclei interaction is treated as a constant term. The resulting Hamiltonian reads:

$$\hat{H} = \hat{T}_e + \hat{V}_{eN} + \hat{V}_{ee} \ . \tag{2.5}$$

Still, this equation is practically unsolvable. The most common approximation enabling its solution is the Hartree–Fock (HF) approximation [198]. As a mean field method, it assumes independently moving electrons in an average field produced by all the particles of the system. Its solution is reduced to the computation of a single Slater determinant (product of single-particle functions) as an approximation for the N-electrons wave function. Nevertheless, the HF method is computationally demanding, as it scales as N^3 to N^4. In addition, the approximation itself is not accurate enough to enable meaningful computational analysis of the majority of problems. However, it results in reasonable estimates of ionization energies [199], and we utilize this fact in the research presented in Chapter 4. Extensions of HF that account for so-called electronic correlations, such as Møller–Plesset perturbation theory to second order (MP2), configuration interaction (CI) and coupled cluster (CC) methods scale very badly with the number of electrons and are currently applied only to very simple molecular systems [200]. The field of computational quantum chemistry would not be successful without the emergence of DFT and its numerical solutions, which are much more efficient than wave function theory methods.

Hohenberg–Kohn theorems and Kohn–Sham equations. In DFT, the many-body problem described by the Schrödinger equation and the wave function, which has $3N$ spatial coordinates, is reduced to a three-dimensional problem by using the electronic density as fundamental property instead. This is possible thanks to the first Hohenberg–Kohn theorem [201], which states that in the ground state, the electron density $\rho_0(\boldsymbol{r})$ uniquely determines the external potential V_{ext} (also called nuclei-electron potential) and therefore the system's total energy. The ground state energy E_0, a unique functional of the electron density, can be written as [193]

$$E_0 = E[\rho_0(\boldsymbol{r})] = \int \rho_0(\boldsymbol{r}) V_{\text{ext}} d\boldsymbol{r} + T[\rho_0(\boldsymbol{r})] + V_{ee}[\rho_0(\boldsymbol{r})] \ . \tag{2.6}$$

Here, the first term represents the potential energy due to electron–nuclei interactions, $T[\rho_0(\boldsymbol{r})]$ is the kinetic energy of electrons and $V_{ee}[\rho_0(\boldsymbol{r})]$ is the potential energy due to electron–electron interactions.

Hohenberg and Kohn formulated a second theorem, stating that the energy of a system is minimized by the ground state electron density [201]. This variational principle means that any trial electron density yields higher energy than the ground state energy:

$$E[\rho_0(\boldsymbol{r})] \leq E[\rho_{\text{trial}}(\boldsymbol{r})]. \tag{2.7}$$

This represents a basic principle behind any DFT-based computational scheme. However, the exact dependence of E on the electronic density ρ is generally unknown. The major obstacle is the lack of accurate or even reasonable approximations for the kinetic energy functional. This led to the introduction of a one-electron wave-functions-based approach in practical calculations. To build up the electron density of the interacting N-electrons system, Kohn and Sham introduced N

one-particle equations with an effective potential $V_{\text{eff}}(\boldsymbol{r})$ [202]. These Kohn–Sham equations have the form:

$$\left(-\frac{1}{2}\nabla^2 + V_{\text{eff}}(\boldsymbol{r})\right)\psi_i(\boldsymbol{r}) = \varepsilon_i\,\psi_i(\boldsymbol{r})\;, \tag{2.8}$$

where $\psi_i(\boldsymbol{r})$ are single-electron wave functions (orbitals). The effective potential is given by:

$$V_{\text{eff}}(\boldsymbol{r}) = V_{\text{ext}}(\boldsymbol{r}) + \int \frac{\rho(\boldsymbol{r})}{|\boldsymbol{r}-\boldsymbol{r}'|}d\boldsymbol{r}' + V_{\text{xc}}[\rho(\boldsymbol{r})]\;. \tag{2.9}$$

Here, the second term accounts for the electrostatic electron–electron interactions, whereas $V_{\text{xc}}[\rho(\boldsymbol{r})]$ is the so-called exchange-correlation potential. The latter is defined as the derivative of the exchange-correlation energy E_{xc} with respect to the electron density:

$$V_{\text{xc}}[\rho(\boldsymbol{r})] = \frac{\delta E_{\text{xc}}}{\delta\rho}\;. \tag{2.10}$$

The effective potential V_{eff} is used in the Kohn–Sham equations 2.8, which are solved to obtain the orbitals $\psi_i(\boldsymbol{r})$. According to equation 2.9, V_{eff} depends on the electron density, but electron density and orbitals are also related according to:

$$\rho(\boldsymbol{r}) = \sum_i^N |\psi_i(\boldsymbol{r})|^2\;. \tag{2.11}$$

Due to these mutual dependencies, in practical implementations the Kohn–Sham equations require iterative solution until self-consistency is reached.

Approximations of the exchange-correlation functional. In general, DFT is an exact theory which is equivalent to the Schrödinger formulation. However, its main limitation is that the explicit form of the exchange-correlation functional, and thus E_{xc}, remain unknown. Various approximations have been developed for the exchange-correlation functional, introducing some degree of empiricism. The so-called "Jacob's ladder" of DFT [203] arranges existing approaches for the exchange-correlation functional according to the expected accuracy. The simplest approximation, and the basis for more complex functionals, is the local density approximation (LDA), which is a generalized version of the exact solution for the homogeneous electron gas. The corresponding exchange-correlation energy is given by:

$$E_{\text{xc}}^{\text{LDA}}[\rho(\boldsymbol{r})] = \int \epsilon_{\text{xc}}[\rho(\boldsymbol{r})]\rho(\boldsymbol{r})\,d\boldsymbol{r}\;. \tag{2.12}$$

Here, ϵ_{xc} is the exchange-correlation energy per particle of the homogeneous electron gas with electron density $\rho(\boldsymbol{r})$. Although the LDA was found to perform reasonably well, for instance in description of lattice parameters of simple solids [204], functionals that account for spatial variations of the electron density are needed for more accurate solutions.

For this purpose, density gradients are included. This leads to the next class of density functionals, so-called generalized gradient approximations (GGA) functionals, e.g. PW91, PBE, revPBE, RPBE and PBEsol [205, 206]. Some of them will be applied in this thesis. In GGA schemes, the exchange-

correlation energy reads:

$$E_{\mathrm{xc}}^{\mathrm{GGA}}[\rho(\boldsymbol{r})] = \int \epsilon_{\mathrm{xc}}[\rho(\boldsymbol{r}), \nabla\rho(\boldsymbol{r})]\rho(\boldsymbol{r})\, d\boldsymbol{r} \ . \tag{2.13}$$

So-called meta-GGA functionals, like TPSS and SCAN, additionally include second derivatives of the electron density [207, 208].

The next step on Jacob's ladder is dedicated to hybrid functionals. In these, to further improve the accuracy, a certain percentage a of the exact exchange energy (usually 20-25 % of exchange given by the Hartree–Fock approximation) is included [209, 210]:

$$E_{\mathrm{xc}}^{\mathrm{hybrid}}[\rho(\boldsymbol{r})] = aE_{\mathrm{x}}^{\mathrm{HF}} + (1-a)E_{\mathrm{x}}^{\mathrm{DFT}} + E_{\mathrm{c}}^{\mathrm{DFT}} \ . \tag{2.14}$$

These functionals are particularly useful for computing properties of molecules. Double-hybrid functionals additionally split the correlation energy into parts from DFT and from second-order perturbation theory [211].

With a reasonable choice of exchange-correlation functional depending on the studied system, such as GGA-type functionals for periodic solids, DFT is able to make very useful predictions for total energies, lattice parameters, vibrational frequencies, etc. For special types of interactions, correction schemes have been introduced, most prominently dispersion corrections for non-covalent interactions [212, 213].

Implementation for periodic solids. Crystalline solids are characterized by their periodic arrangement of atoms [214]. In quantum mechanical calculations, they are considered as infinite periodic arrays of atoms. Periodic boundary conditions are usually employed, i.e. infinitely repeating a 3D unit cell of suitable symmetry in all spatial directions.

For simplicity, calculations for periodic solids are done in reciprocal space. It can be reached from real (direct) space by Fourier transform. A special unit cell of the crystal in reciprocal space is the Brillouin zone. High-symmetry points in the first Brillouin zone are denoted by special letters that are used e.g. in band structure representations. The center of the first Brillouin zone is the Γ-point.

In quantum calculations of solids, the translationally symmetric crystal is described by a periodic nuclear attraction potential $V(\boldsymbol{r})$

$$V(\boldsymbol{r}+\boldsymbol{T}) = V(\boldsymbol{r}) \ , \tag{2.15}$$

where $\boldsymbol{T}$ is a lattice translation vector. For a periodic potential, the solutions of the Schrödinger or Kohn–Sham equations have a special form. Specifically, the translational symmetry requirement is fulfilled by Bloch functions. Following Bloch's theorem [215], Bloch functions are products of a plane wave $e^{i\boldsymbol{k}\cdot\boldsymbol{r}}$ and a lattice-periodic function $u_{\boldsymbol{k}}(\boldsymbol{r})$:

$$\Psi^{\boldsymbol{k}}(\boldsymbol{r}) = e^{i\boldsymbol{k}\cdot\boldsymbol{r}} \cdot u_{\boldsymbol{k}}(\boldsymbol{r}) \ \text{ with } \ \boldsymbol{r} \in V_{\text{primitive unit cell}} \ . \tag{2.16}$$

Here, $\boldsymbol{k}$ is the wave vector, which can be expressed in reciprocal lattice vectors. A very suitable option to create a basis set for solid state quantum calculations are plane waves. Plane waves are

inherently periodic and fulfill Bloch's theorem (eq. 2.16). Using Fourier expansions for the potential energy and the wave function, the wave function $\phi^k(\boldsymbol{r})$ becomes

$$\begin{aligned}\phi^k(\boldsymbol{r}) &= \sum_{\boldsymbol{G}} C(\boldsymbol{k}-\boldsymbol{G}) e^{i(k-G)\cdot r} \\ &= \left(\sum_{\boldsymbol{G}} C(\boldsymbol{k}-\boldsymbol{G}) e^{-iG\cdot r}\right) e^{ik\cdot r} \\ &= u_{\boldsymbol{k}}(\boldsymbol{r})\ e^{i\boldsymbol{k}\cdot\boldsymbol{r}}\ .\end{aligned} \tag{2.17}$$

It can be shown that $C(\boldsymbol{k}-\boldsymbol{G})e^{-iG\cdot r}$ is again a lattice-periodic function, denoted $u_{\boldsymbol{k}}(\boldsymbol{r})$. In this way, the plane wave form of a Bloch function has been created. The issue of infinitely many possible $\boldsymbol{G}$ vectors is solved by introducing a cutoff energy E_{cut} that determines the maximum value of $|\boldsymbol{G}|$ and thereby the quality of the basis set:

$$\frac{\hbar^2|\boldsymbol{k}+\boldsymbol{G}|^2}{2m_e} \leq E_{\text{cut}}\ . \tag{2.18}$$

Plane wave basis sets are used in combination with so-called pseudopotentials [216, 217]. In pseudopotentials, the presence of computationally demanding but chemically inactive core electrons is approximated by an effective potential. Only valence electrons, which dominate the chemical properties, are computed explicitly. Besides, pseudo-wave functions with significantly fewer nodes and thus smaller cutoff energies (smaller basis sets) are used to describe the valence electrons, which further reduces the computational cost. Outside a pre-defined cutoff radius, the all-electron and the pseudo-wave functions are identical. The most prominent types of pseudopotentials are norm-conserving and ultrasoft potentials, the latter relaxing the norm-conserving constraint (the total integrated electronic density within a cutoff region has to match the all-electron electron density), which requires a smaller plane wave energy cutoff and thus reduces the computational cost.

To obtain electronic properties from a DFT calculation, finite integrals over the Brillouin zone in reciprocal space must be computed. These integrals are computed numerically using a finite number of k-points. One way to choose such a k-point mesh was proposed by Monkhorst and Pack [218]. The method uses shrinking factors that generate a uniform subsectioning of the reciprocal lattice vectors. The k-point density serves as a quality measure, but the k-point mesh is in general subject to convergence tests.

DFT calculations of crystal surfaces use slab models. In these, a few layers are cut out of the bulk crystal along the desired crystallographic direction, as determined by the Miller (hkl) indices. Since most DFT codes still apply periodic boundary conditions in all three spatial directions, a sufficiently thick vacuum layer is introduced between the slabs to avoid spurious interactions between them.

2.1.2. DFT+*U* approach

As described before, DFT is a very powerful and widely-used tool for electronic structure calculations. However, the approximations for the exchange-correlation functional are based on properties of delocalized systems such as the uniform electron gas, and therefore have shortcomings when it comes to highly localized electrons, such as electrochemically active *d*-electrons in transition metals. These electrons are commonly assumed to be strongly correlated, meaning that their behavior is coupled, usually by strong Coulomb repulsion. These particles cannot be described accurately by mean field theories of non-interacting particles, like Kohn–Sham DFT. Strongly correlated electrons typically are *d*- or *f*-electrons. Here, a large number of electrons are confined to spatially localized orbitals. This is the case in transition metals or rare earth cations. For these materials, standard DFT calculations often result in qualitatively wrong electronic structure predictions, yielding metallic states for wide band gap compounds [219].

The use of hybrid exchange-correlation functionals is one way to overcome this problem by correcting the delocalization error, but these are computationally very demanding, making most calculations unfeasible. A computationally inexpensive and thus widely applied alternative, accounting for strong electronic correlations, is a combination of DFT with a Hubbard *U* model, known as the LDA+*U* or DFT+*U* approach [219–222]. It was originally introduced by Anisimov and coworkers, and is extremely popular in solid state calculations nowadays. Comprehensive reviews of the method can be found in refs. [223, 224].

In the DFT+*U* approach, the strong Coulomb interactions and correlations between electrons are described by the Hubbard model [225], whereas the rest of the electrons are described by standard DFT. The total DFT+*U* energy can be written as

$$E^{\mathrm{DFT+U}}[\rho(\boldsymbol{r}), \{n_{Im\sigma}\}] = E^{\mathrm{DFT}}[\rho(\boldsymbol{r})] + E^{\mathrm{Hub}}[\{n_{Im\sigma}\}] - E^{\mathrm{dc}}[\{N_{I\sigma}\}] \,, \tag{2.19}$$

where $E^{\mathrm{DFT}}[\rho(\boldsymbol{r})]$ denotes the total DFT energy as a functional of the electron density ρ, E^{Hub} is the on-site Hubbard interaction energy, and E^{dc} avoids double counting of the on-site interaction, which is included in both E^{DFT} and E^{Hub}. $n_{Im\sigma}$ denotes the orbital occupation for atom I with electrons of spin σ and magnetic quantum number m. The term $N_{I\sigma}$ corresponds to $\sum_m n_{Im\sigma}$. The energy expression was formulated in detail by Anisimov and co-workers in their seminal papers [221, 222].

Liechtenstein et al. [226] introduced a rotationally-invariant formulation of DFT+*U*. A simplified formulation was proposed by Dudarev *et al.* [227], where the energy terms become:

$$\begin{aligned} E^{\mathrm{Hub}}[\{n_{Im\sigma}\}] - E^{\mathrm{dc}}[\{N_{I\sigma}\}] &= \sum_{I,\sigma} \frac{U_I^{\mathrm{eff}}}{2} \left(n_{Im\sigma} - n_{Im\sigma}^2\right) \\ &= \sum_{I,\sigma} \frac{U_I^{\mathrm{eff}}}{2} \mathrm{Tr}\left(\boldsymbol{n}_{Im\sigma}(1 - \boldsymbol{n}_{Im\sigma})\right) \,. \end{aligned} \tag{2.20}$$

$\mathrm{Tr}(\boldsymbol{n}_{Im\sigma})$ denotes the trace of the orbital occupation matrix $\boldsymbol{n}_{Im\sigma}$. The Hubbard *U* parameter used here is an effective $U_I^{\mathrm{eff}} = U_I - J_I$, where J_I is the exchange term. In the following, *U* will be used as a shorthand notation for the effective U_I^{eff}.

The DFT+U approach can also be seen as a correction scheme for the spurious curvature of the DFT total energy to restore the piecewise linear behaviour of the exact energy (see Figure 2.1). As suggested by equation 2.20, the Hubbard energy is a penalty, scaled by the U parameter. When applied for fractional occupations, it forces the orbital occupations to integer values and brings the total energy as a function of electrons closer to the exact relation, thus remedying an important shortcoming of DFT.

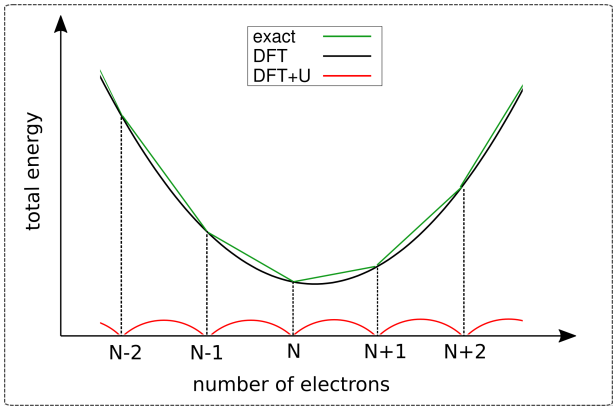

Figure 2.1.: Total energy as a function of number of electrons. The DFT+U correction is shown in red. It corresponds to the difference between the DFT curve and the exact energy and recovers the piecewise linear behavior of the exact energy.

Choice of the Hubbard U parameter. In the DFT+U scheme, the Hubbard U parameter describes the effective Coulomb on-site electron–electron interaction. Using the DFT+U method thus requires a suitable value for the U parameter (and, in some cases, also for the exchange interaction parameter J [191, 228]). Often, the parameter is taken from literature or fitted to obtain a known value of a material's property, e.g. the band gap or lattice parameters [229–234]. But a variety of methods have also been proposed to derive the parameter from first principles, making DFT+U a parameter-free technique. These are summarized in the following, based on our discussion in ref. [235].

The U parameter can be obtained from the difference in total energy of electronic configurations with the number of d- or f-electrons increased and decreased by one [220, 236–239]. This is based on the concept that U corresponds to the energy cost of the reaction $2d^n \rightarrow d^{n-1} + d^{n+1}$. Another *ab initio* approach to obtain the U paramter and the corresponding exchange term J relies on molecular orbitals from unrestricted Hartree–Fock calculations and the relation of the U and J parameters to the Coulomb and exchange integrals evaluated in this basis [240, 241]. The U parameter can also be calculated from the average on-site Coulomb matrix elements computed in a maximally localized Wannier functions basis set [238]. An accurate but computationally intensive method is based on the constrained Random Phase Approximation (cRPA) [228, 242–244], very popular in the dynamical mean field theory (DMFT) community. It allows to account for or exclude different screening channels in the evaluation of the Hubbard U parameter, an important aspect broadly discussed in the context of Hubbard U parameters derivation by different methods [191,

228, 245]. Alternatives to cRPA are based on linear response theory.

The linear response approach. A computationally efficient method to compute the Hubbard U parameter is to use the linear response method, which is one of the implementations of the constrained LDA (cLDA) theory [191]. In the linear response approach, the d- or f-state occupation number is artificially changed, i.e. perturbed. The U parameter is then calculated from the total energy variation with respect to the change in the occupation number of the considered d- or f-orbitals. With perturbation α_I, the U parameter is calculated from the interacting and non-interacting response functions χ_{IJ} and χ^0_{IJ}, which are defined for atomic sites I and J as [191]:

$$\chi_{IJ} = \frac{\partial^2 E}{\partial\alpha_I \partial\alpha_J} = \frac{\partial n_I}{\partial\alpha_J} \,, \qquad \chi^0_{IJ} = \frac{\partial^2 E^{\mathrm{KS}}}{\partial\alpha^{\mathrm{KS}}_I \partial\alpha^{\mathrm{KS}}_J} = \frac{\partial n_I}{\partial\alpha^{\mathrm{KS}}_J} \,. \tag{2.21}$$

Here, E^{KS} denotes the total energy of the non-interacting Kohn–Sham system that needs to be subtracted to avoid rehybridization effects when varying the occupations. The Hubbard U parameter for site I is finally computed from the inverse response matrices as

$$U = (\chi_0^{-1} - \chi^{-1})_{II} \,. \tag{2.22}$$

In practice, the U parameter is computed in a supercell approach, using exactly the same chemical system to which the U correction is going to be applied. This is important, since the parameter depends on the geometric environment and the oxidation state of the atom [83, 191, 246]. In a first step, a well converged, self-consistent DFT calculation for the unconstrained system is performed. In the next step, small potential shifts α, both positive and negative, are applied on each non-equivalent site, perturbing only one site at a time. Then, the variation of the occupations n_I for all sites is computed, considering two cases: (1) when allowing the system to screen the perturbation and (2) without allowing this readjustment. Taking the respective derivatives leads to the density response matrices (eq. 2.21), based on which the U parameter is derived.

The Hubbard U parameter can be refined in a self-consistent approach by restarting the procedure, applying the obtained U values, such that properties reach internal consistency, as proposed by Cococcioni and de Gironcoli [191]. It has also been proposed to derive a self-consistent U_{scf}, extrapolated from a series of U_{out} computed from linear response applying different U_{in} in the perturbation procedure (see Chapter 4 for an example) [247]. This can be of importance when the electronic structure from a DFT and a DFT+U description differ significantly. Besides the derivation method, the obtained U values will depend on the supercell size, the computational setup (k-mesh, pseudopotential, etc.), the employed exchange-correlation functional and the projector used for the d- or f-orbitals [191, 223].

A related method for derivation of the Hubbard U parameter, also based on linear response theory, is density-functional perturbation theory (limited to first order perturbations) [248]. It allows to use primitive cells instead of supercells and thereby reduces the computational cost compared to the cLDA method. The resulting U values are the same as the ones obtained with the linear response

method.

Orbital projectors in DFT+*U*. As can be seen from equation 2.20, in order to compute the Hubbard energy, next to the U parameter, we need to know the orbital occupations of the d- or f-orbitals (those on which the U correction will act). These are usually computed from the underlying delocalized electron density by projections of the respective electronic wave functions onto projector functions, also called Hubbard projectors [224]. Obtaining the occupations is closely related to selecting the states to which the Hubbard correction should be applied (the "correlated subspace") out of a set of potentially mixed or hybridized states. Different choices can be made for the projectors [191, 249], including widely applied atomic orbitals and less commonly applied Wannier functions. The projectors are more or less suitable for specific systems and can severely impact the results of DFT+U calculations, as will be discussed in this thesis (see Chapters 3 and 4). The projector functions should not be confused with the basis set used in the DFT calculations, e.g. the plane wave basis set used in this thesis.

Atomic orbitals are functions that describe the behavior of electrons in atoms and are thus a natural choice for a localized basis. In this thesis, Wannier functions will be extensively used, which represent a full set of orthogonal functions. Wannier functions can be chosen in many ways. For example, maximally localized Wannier functions (MLWFs) are constructed in a way that they are localized in space, minimizing the spread of the functions [250, 251]. By their center and shape, Wannier functions often offer a good representation of localized crystal orbitals. The exact form of Wannier functions depends on the so-called "energy window", i.e. the range of energy bands included in their construction. The use of Wannier functions is also a common procedure to separate (disentangle) bands [251], and to treat states of mixed character [252]. An overview of the application of Wannier functions in the DFT$+U$ scheme is given by Himmetoglu et al. [223].

Double counting corrections. In equation 2.19, the double counting correction term appears, which avoids double counting of interactions included in both DFT and Hubbard energy terms. The E^{dc} term accounts for the contribution of correlated electrons to the DFT energy, but is not uniquely defined and represents an unresolved challenge for DFT+U schemes [223, 224]. There are two common extreme variants of double counting corrections, called the "fully localized limit" (FLL) [253] and the "around mean field" (AMF) [254, 255] versions. The full description of the two formalisms can be found in ref. [223]. The FLL favors orbitals that are either completely filled or completely empty, by penalizing deviations from integer occupations, and is suitable for solids with a band gap. In contrast, the AMF favors uniform occupations by penalizing deviations of the occupations from the mean value, which is a more suitable description for metals. The FLL is most commonly implemented, including in the QuantumESPRESSO code [256] used in this thesis.

2.1.3. Computational hydrogen electrode

The simplest and most widely used scheme to perform quantum mechanical calculations in electrochemical conditions is the computational hydrogen electrode (CHE) [12] (see also Chapter 1). In this method, at standard conditions, the following equilibrium is assumed between the solvated

proton, electron and hydrogen gas:

$$\mu_{H^+} + \mu_{e^-} = \frac{1}{2}\mu_{H_2(gas)} \ , \tag{2.23}$$

where the μ_i denote the chemical potentials. With this, calculation of the solvation energy of the proton in water is avoided and only the gas phase energy of H_2 is needed for the estimates, which can be easily computed with DFT. At non-standard conditions, the effects of pH value and electrode potential U_{SHE} are included by slight modifications of equation 2.23:

$$\mu_{H^+} + \mu_{e^-} = \frac{1}{2}\mu_{H_2(gas)} - eU_{SHE} - k_B T \ln(10)\text{pH} \ , \tag{2.24}$$

where e is the electron charge and k_B is the Boltzmann constant.

Making use of the this relation, the change in the Gibbs free energy during an electrochemical reaction can be estimated from:

$$\Delta G \approx \Delta E_{DFT} + \Delta\text{ZPE} - T\Delta S + eU_{SHE} \ , \tag{2.25}$$

with the DFT energy, E_{DFT}, the zero point energy, ZPE, and the entropy contribution, $T\Delta S$. The effect of an applied potential is accounted for by the eU_{SHE} term, which is added for electron transfer steps. The potential is thus not an explicit variable in the DFT calculation. Sampling over electrolyte configurations is also neglected.

After computing Gibbs free energy differences for all i steps of a multistep electrochemical reaction according to equation 2.25, the thermodynamic overpotential, μ, can be estimated, using ΔG of the potential-determining step [3]:

$$\mu = \frac{\max(\Delta G_i)}{e} - 1.23\text{V} \ . \tag{2.26}$$

This estimate holds for the oxygen evolution reaction with a standard potential of 1.23 V.

2.2. Computing liquid electrolytes

The most intuitive way to represent a liquid solution in atomic-scale simulations is by computing each atom explicitly. For the sake of efficiency, however, most applied solvation models are based on a polarizable continuum and a cavity-based description for the solute in solvent (see Chapter 1). A different approach relies on using the probabilistic structure of a solvent via pair distribution or correlation functions [135, 257, 258]. These functions give the probability of finding an atom at a certain distance from a reference atom. They are obtained from the integral equation theory of liquids, based on statistical mechanics. In the resulting computational schemes, statistical solvent distributions are considered instead of explicit solvent molecules. This makes the calculations much more efficient, but also allows to consider effects of liquid structure. Below we present the basics of the reference interaction site method (RISM), which we tested and applied for simulations of electrochemical interfaces in the scope of this thesis (see Chapters 5 and 6).

2.2.1. Ornstein–Zernike equation

Pair distribution functions can be obtained by solving the Ornstein–Zernike equation [257, 259], given a pair interaction potential. The Ornstein–Zernike equation is an analytical equation originating from statistical mechanics, which connects total correlation functions, $h(r_{ij})$, and direct correlation functions, $c(r_{ij})$, between three particles at distances r_{ij} (see Figure 2.2). Assuming a simple homogeneous liquid with spherically symmetric solvent molecules, thus neglecting the orientational degrees of freedom, the equation reads:

$$h(r_{12}) = c(r_{12}) + \rho \int \mathrm{d}r_3 \, c(r_{13}) h(r_{32}) \, , \tag{2.27}$$

where ρ is the liquid density. The second term describes the indirect contribution, namely the influence of particle 1 on particle 2 via particle 3. Since the Ornstein–Zernike equation involves two unknowns, a second, independent equation is required to solve it, called the closure relation [257]. The closure relation is an approximation and typically contains a pair interaction potential, and thus some "physical information". Different types of closure relations are in use, e.g. the hypernetted-chain approximation [257], the Percus–Yevick approximation [260] and the partially linearized Kovalenko–Hirata model, which is a combination of the former ones and a partially linearized variant of the hypernetted-chain approximation [261].

In the limit of low liquid densities, the pair distribution function $g(r_{12}) = h(r_{12}) + 1$ is given as:

$$g(r_{12}) = \exp\left(-\frac{u(r_{12})}{k_\mathrm{B}T}\right) \, , \tag{2.28}$$

where $u(r_{12})$ is the pair interaction potential, e.g. a Lennard–Jones type potential. For higher densities, the relation is modified according to:

$$g(r_{12}) = \exp\left(-\frac{u(r_{12})}{k_\mathrm{B}T} + h(r_{12}) - c(r_{12}) + B(r_{12})\right) \, . \tag{2.29}$$

The exact form of the bridge functional $B(r_{12})$ is unknown and the form used depends on the choice of closure relation (e.g. $B(r_{12}) = 0$ for the hypernetted-chain approximation). The set of equations is usually solved in Fourier space, where it takes a simple form, not requiring integration.

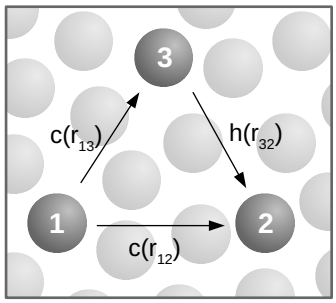

Figure 2.2.: Direct and indirect contributions to the total correlation function. Gray circles represent the liquid particles. $c(r_{ij})$ and $h(r_{ij})$ denote direct and total correlation functions, respectively (see also eq. 2.27).

2.2.2. Reference interaction site models

The Ornstein–Zernike equation as written in equation 2.27 is a simplified form of the full six-dimensional equation (three degrees of freedom for positions and three degrees of freedom for orientations) required to describe correlations between molecules in more complex liquids. In order to solve the full molecular Ornstein–Zernike equation for systems of interest, approximations are necessary. Based on the work of Chandler and Andersen [168], a group of methods have been developed for this purpose. These are called reference interaction site models or reference interaction site methods (RISM). RISM approaches model solvent molecules as sets of interacting sites, yielding distribution functions for inter- and intramolecular site–site interactions.

1D-RISM. One of the RISM approaches is the 1D-RISM, a solvation model that relies on site–site correlation functions. In this scheme, the solute is split into a set of (atomic) sites, which interact with sites of the solvent. A set of one-dimensional integral equations is then solved, assuming spherical symmetry of the interacting sites and using a radial average of correlation functions, so that orientational degrees of freedom vanish. This makes the 1D-RISM computationally very efficient. However, the approach does not account for spatial correlations of the solvent density around the solute, thus it does not represent the three-dimensional solvent structure.

3D-RISM. To cure the described drawback of the 1D-RISM, the three-dimensional generalization of the RISM (3D-RISM) was introduced by Beglov and Roux [262]. In contrast to the 1D-RISM, the solute is not considered as a set of sites in the computation of correlation functions, but as a single site. A partial integration over orientational degrees of freedom is performed and a set of three-dimensional integral equations is solved. The so-obtained three-dimensional correlation functions yield a detailed solvation structure around the solute. The 3D-RISM equations for solvent sites γ and α read:

$$h_\gamma(\boldsymbol{r}) = \sum_{\alpha}^{\#\text{ solvent sites}} \int \mathrm{d}\boldsymbol{r}' c_\alpha(\boldsymbol{r}')\, \chi_{\alpha\gamma}(\boldsymbol{r}-\boldsymbol{r}')\,, \tag{2.30}$$

where $\chi_{\alpha\gamma}$ is the solvent susceptibility. It represents the bulk solvent correlations and can be

obtained from a 1D-RISM calculation for a given solvent (for details see ref. [135]). The 3D-RISM is more commonly used compared to the 1D-RISM due to the enhanced accuracy, although it is computationally more demanding (by a factor of ca. 100 [258]).

In contrast to cavity-based continuum solvation models, the RISM provides more detailed structural information about the solvent, however in a statistically averaged way (not every particle is considered separately). In this way, the motion of solvent species is also averaged out, using the equilibrium spatial distribution. The RISM is classified as less coarse-grained compared to continuum solvation models that rely on a polarizable continuum [77]. It can provide thermodynamic quantities like the solvent free energy as a function of liquid density as well as total and direct solvent particle correlation functions.

2.3. Computing electrochemical interfaces: effective screening medium reference interaction site method

The reference interaction site method (RISM), as presented in the previous section, can be combined with a DFT description of a solute molecule or solute surface. Within such a scheme, solvent distribution and electronic structure of the solute are converged simultaneously. Depending on the geometry of the solute, there are different variants of these hybrid methods.

The 3D-RISM has been combined with different implementations of DFT [104, 261, 263], resulting in the 3D-RISM-SCF scheme. It is used to describe solvated molecules (or surfaces, if these are represented as many-atom clusters). Solvated surfaces or solid/liquid interfaces, in contrast, are best simulated in mixed boundary conditions (open boundary conditions in the direction perpendicular to the surface and periodic boundary conditions in the other spatial directions). In order to make use of mixed boundary conditions for the RISM, the Laue-RISM was introduced [104]. It reformulates the RISM correlation functions in the Laue representation. In order to implement mixed boundary conditions also for a DFT calculation using plane waves and pseudopotentials, the Laue-RISM has been combined with the effective screening medium (ESM) approach [114], resulting in the so-called ESM-RISM [104]. The ESM approach can provide different kinds of boundary conditions, replacing the periodic images of a simulation cell by the “medium”, which can be vacuum, a metal or a continuum solvent. This results in a non-repeated slab setup in the direction perpendicular to the surface slab. The ESM approach applies the Green’s functions technique to solve Poisson’s equation of electrostatics in the whole studied region, including the “media”. In the ESM-RISM, only the vacuum/slab/vacuum configuration of the ESM is used, which becomes vacuum/slab/solvent when combined with the RISM. More details on the geometric setup for ESM-RISM calculations can be found in Chapter 5.

In the ESM-RISM, the interactions between electrolyte particles as well as those between electrode and electrolyte particles are described by pair interaction potentials. In the ESM-RISM implementation used in this thesis, the interaction potential $u(r_{12})$ (see eq. 2.29) is of Lennard-Jones (LJ)

type mixed with Coulomb interactions. For the interaction between particles 1 and 2, it reads:

$$u(r_{12}) = 4\epsilon_{12}\left[\left(\frac{\sigma_{12}}{r_{12}}\right)^{12} - \left(\frac{\sigma_{12}}{r_{12}}\right)^{6}\right] + \frac{q_1 q_2}{r_{12}}\,, \tag{2.31}$$

where ϵ is the depth of the potential well, σ is the distance at which the particle–particle potential energy is zero, related to the size of the particles, and q is the charge of the particle. Parameters for interactions between different particle types are obtained from Lorentz–Berthelot mixing rules: $\sigma_{12} = \frac{\sigma_1+\sigma_2}{2}$ and $\varepsilon_{12} = \sqrt{\varepsilon_1 \varepsilon_2}$ [264]. The choice of interaction parameters is very important, as will be discussed in Chapter 5 of this thesis. For the electrode–electrolyte interaction, the Coulomb term becomes $-q_1 v_{\mathrm{DFT}}$, with v_{DFT} being the sum of the Hartree potential and the local potential calculated by DFT [104].

The free energy A of a system in the ESM-RISM is given as [104]

$$A = E_{\mathrm{solute(DFT)}} + \Delta\mu_{\mathrm{solvent}}\,, \tag{2.32}$$

where $E_{\mathrm{solute(DFT)}}$ is the total DFT energy of the solute and $\Delta\mu_{\mathrm{solvent}}$ is the RISM free energy of solvation. For electrochemical interfaces, the ESM-RISM provides total energies, including RISM solvation energy, pair distribution functions and the interfacial electrostatic potential profiles. These properties allow to characterize local reaction conditions at the interface.

The ESM-RISM also allows computation of charged slabs, i.e. to model interfaces under an applied potential. This is because any excess charge is fully compensated by the electrolyte charge of equal size and opposite sign. Charged slabs are computed in the constant bias potential scheme ("potentiostat") of Bonnet et al. [109], which is implemented together with the ESM-RISM and allows to apply an electrode potential at an electrode/electrolyte interface in grand canonical conditions. The system is coupled to an electron reservoir and thus realizes constant chemical potential instead of constant number of electrons. The grand potential, Ω, with

$$\Omega = A - \mu\Delta N \tag{2.33}$$

is minimized. Here, μ is the chemical potential of electrons (Fermi energy) and ΔN is the excess number of electrons at a specific potential μ, compared to a neutral slab. A desired electrode potential can be reached by specifying a target Fermi energy, since a shift in the Fermi energy, $\Delta\mu$, corresponds to a shift in the electrode potential of $\Delta\varphi = -\Delta\mu/e$. This target Fermi energy is reached in a fictitious charge particle (FCP) dynamics scheme by adapting the slab charge. As a potential reference, the electrostatic potential in the bulk electrolyte is used.

2.4. Software and computational details

The DFT calculations presented in this thesis were performed with the QuantumESPRESSO package (version 6.1 or higher) [256]. QuantumESPRESSO is an open-source software package designed for DFT-based electronic structure calculations and provides a variety of tools for post-

processing and data analysis. It has numerous unique functionalities that enable key research presented in this thesis, including the DFT+U method and the ESM-RISM. It also scales well on high-performance computing infrastructure. The code is specifically designed for solid state calculations and uses a plane wave basis set and pseudopotentials.

Details on the computational setup and parameters used in the calculations reported in the different parts of this thesis will be given in the respective chapters. In general, plane wave cutoff, pseudopotential and k-point mesh are very important parameters determining the accuracy of DFT calculations and have been tested accordingly. Convergence tests have been conducted in order to obtain a reasonable compromise of computational effort and accuracy. The same holds for the size and structural arrangements of the computed models, e.g. the thickness of surface slabs.

3. Computation of *d*-/*f*-element oxides

In this chapter, we apply the DFT+U method to d- and/or f-element oxides containing strongly correlated electrons. The aim is to establish a reliable, accurate and computationally efficient method for computing the electronic structure of electrodes and other energy materials. We show that the DFT+U approach should not be used as a black box, but requires careful considerations regarding the choice of the Hubbard U parameter and projectors for occupations of d- or f-orbitals. We call the resulting methodology the parameter-free DFT+U(WF) approach. We obtain very satisfying results for structural and electronic properties of the investigated oxides. The next chapter will provide a more systematic investigation and application of the parameter-free DFT+U(WF) approach to pure d-metals.

This chapter is based on my contributions to three published research articles:

- G. L. Murphy, Z. Zhang, R. Tesch, P. M. Kowalski, M. Avdeev, E. Y. Koo, D. J. Gregg, P. Kegler, E. V. Alekseev, B. J. Kennedy, *Tilting and Distortion in Rutile-Related Mixed Metal Ternary Uranium Oxides: A Structural, Spectroscopic, and Theoretical Investigation*, Inorg. Chem., 60, 4, 2246, 2021. (Section 3.2. My contribution: the computational part of the study.)
- T. Connor, O. Cheong, T. Bornhake, A. C. Shad, R. Tesch, M. Sun, Z. He, A. Bukayemsky, V. L. Vinograd, S. C. Finkeldei, P. M. Kowalski, *Pyrochlore Compounds From Atomistic Simulations*, Front. Chem. 9, 733321, 2021. (Section 3.3. My contribution: derivation of Hubbard U parameters for stoichiometric pyrochlores.)
- Z.-D. He, R. Tesch, M. J. Eslamibidgoli, M. H. Eikerling, P. M. Kowalski, *Low-spin state of Fe in Fe-doped NiOOH electrocatalysts*. Nat. Commun. 14, 3498, 2023. (Section 3.4. My contribution: derivation of Hubbard U parameters and application of the DFT+U(WF) method for computation of electronic structure of NiOOH compounds.)

The work resulting in these contributions was performed by myself under the guidance of Dr. Piotr Kowalski, utilizing the expertise from prior studies performed by him and his group (as cited in the text). Experimental data on AUO_4 monouranates were provided by Dr. Gabriel L. Murphy and Dr. Zhaoming Zhang. Further simulations on pyrochlores, using the Hubbard U parameters derived by myself, were performed by the other authors of the second listed research article. Follow-up simulations based on the electronic structure results for β-NiOOH were performed mainly by Dr. Zhengda He.

3.1. Introduction

As described in Chapter 2, computing the electronic structure of materials with d- or f-electrons requires methods beyond the standard DFT approach, due to the strong electronic correlations. This applies to electrodes at electrochemical interfaces, which are often oxides (e.g. lithium intercalation electrodes or nickel oxide electrodes), as well as other energy materials, like solid state materials considered for immobilization of radionuclides in nuclear waste management. These are studied in this chapter, whereas pure metals will be studied in Chapter 4.

We aim to establish an accurate electronic structure method for electrodes, an important prerequisite for modeling electrochemical interfaces. For this purpose we test potential improvements in the DFT+U method, as a follow-up of previous studies on computation of f-elements-bearing materials (e.g. Romero et al. [246], Beridze and Kowalski [265]). The DFT+U is computationally inexpensive and therefore widely used, sometimes blindly, as the standard method for oxides containing strongly correlated electrons.

We show here that, to obtain high-quality data, the DFT+U approach needs to be applied with care. We present thorough considerations concerning the choice of Hubbard U parameter, the choice of orbital projectors and the role of the Hubbard energy term. By comparing to high-quality experimental data obtained from our collaboration partners, we could introduce some improvements, and these aspects are now routinely applied in Dr. Kowalski's research group. The results are accurate atomic and electronic structures.

The Hubbard U parameter is determined in various ways (see Chapter 2), often empirically. In this thesis, the Hubbard U parameter is derived from the linear response method introduced by Cococcioni and de Gironcoli [191] in 2005 (see Chapter 2 for the theoretical background on DFT, DFT+U and the linear response scheme). Since this method is based on first principles, we denote our variant of DFT+U the "parameter-free DFT+U" approach. When using Wannier functions (WF)-based projection operators, we denote this by "DFT+U(WF)". The parameter-free DFT+U method has been regularly used before, including by Dr. Kowalski's group [246, 265–267], but the DFT+U(WF) method only sporadically [268]. In particular, the latter variant has not been studied systematically and thus is missing a solid justification or clear test-case demonstrating the advantages of the method. Providing these is the aim of this as well as the following chapter of this thesis.

3.2. Parameter-free DFT+*U* for mixed *d*-/*f*-uranium oxides

Mixed transition metal-uranium oxides are relevant materials for nuclear waste forms [269, 270]. Knowledge of their phase transformations is relevant e.g. for safe disposal of spent nuclear fuel. Here, we study the structures and phase transitions of AUO_4 monouranates (with A = β-Cd, Mn, Co, Mg, β-Ni), which are not yet fully understood.

High-precision measurements have been performed by our collaboration partners [271, 272] in order to uncover structures, phase transitions and uranium oxidation states in these oxides. These

measurements show that β-$CdUO_4$ adopts a high-symmetry structure of space group $Cmmm$, whereas all other AUO_4 have a lower-symmetry $Ibmm$ structure. Both structures are based on the rutile structure, but differ in tilting of the AO_6 octahedra (see Figure 3.1). The tilting is caused by a size mismatch between A^{2+} and U^{6+} cations, and the extension of the tilt depends on the relative ionic radii of A^{2+} and U^{6+} cations (see Figures 7 and 9 in ref. [271]). Transitions to the $Cmmm$ structure have been observed for $MnUO_4$ and $CoUO_4$ at elevated temperatures.

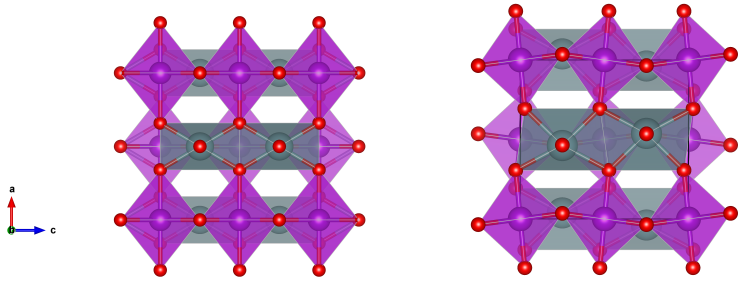

(a) $Cmmm$ (b) $Ibmm$

Figure 3.1.: Monouranate AUO_4 structures in (a) high-symmetry $Cmmm$ and (b) lower-symmetry $Ibmm$ space groups. Purple, grey and red spheres represent A, U and O atoms, respectively. Purple and grey polyhedra represent AO_6 and UO_6 octahedra, respectively. See ref. [271] for representations from other spatial directions.

This work employs first principles calculations to support the conclusions from the measurements, since differences between the $Cmmm$ and $Ibmm$ structures are subtle. The standard DFT+U approach incorrectly predicts the $Cmmm$ structure as the most stable structure for all the considered compounds. Establishing reliable modeling approaches for actinide materials is important, since experimental investigations are limited by the radioactive nature of the samples. However, modeling these materials is challenging due to possible strong spin-orbit coupling, the unique chemistry of uranium and the uranyl group and exotic bonding characters of actinide elements involving $5f$-orbitals [273, 274]. Here, we focus on testing the applicability of the DFT+U approach for the AUO_4 compounds. These structurally simple compounds represent an interesting test system for the DFT+U approach, since they contain both d- and f-electrons. We show how the standard DFT+U approach fails here and propose alternatives, allowing for characterization of these systems which is consistent with experiments.

3.2.1. Computational details and derivation of Hubbard *U* parameters

The DFT+U calculations adopted the setup that was applied successfully in previous studies of AUO_4 compounds [266–268, 275]. The calculations were performed with the PBEsol exchange-correlation functional [276], which is known to provide better structural description than the PBE functional [205]. We used a $4\times4\times4$ Methfessel–Paxton k-point mesh [277] and a plane wave cutoff of 70 Ry. Core electrons were described by ultrasoft pseudopotentials, whereas the valence electrons were computed explicitly, namely Cd ($4d5s$), Mn ($3s3p3d4s$), Co ($3d4s$), Mg ($3s$), Ni

($3d4s$), U ($6s6p6d5f7s$) and O($2s2p$). The calculations for systems containing d-elements were spin-polarized. The Hubbard U parameters for A^{2+} and U^{6+} cations were derived using the linear response method [191] (see Chapter 2). The obtained values are given in Table 3.1. The U values derived here are consistent with previously derived parameters for U^{6+} compounds [266–268, 275].

compound	$U(U^{6+})$ [eV]	$U(A^{2+})$ [eV]
β-$CdUO_4$	2.6	4.0
$MnUO_4$	2.7	4.4
$CoUO_4$	2.7	5.2
$MgUO_4$	2.6	–
β-$NiUO_4$	2.6	6.6

Table 3.1.: Hubbard U parameters for A^{2+} and U^{6+} cations in AUO_4 compounds, derived from the linear response scheme. As Mg is not a d-element, for $MgUO_4$ the Hubbard correction was applied to U atoms only. Table reprinted with permission from [271]. Copyright 2021 American Chemical Society.

The AUO_4 structures were computed in supercells containing 4 formula units. Different pressures were applied, ranging from 0 to 20 GPa, in order to access different unit cell volumes and lattice parameters. Geometry optimizations were performed for lattice parameters as well as atomic positions. They were considered to reach equilibrium when the tolerances on forces and pressure were below 0.005 eV/Å and 0.01 GPa, respectively. Calculations with Wannier function projectors were single point calculations using the experimentally determined structures. They used localized Wannier functions as generated by the "Poor Man's Wannier scheme" (pmw.x tool) in QuantumESPRESSO. In contrast to maximally localized Wannier functions (MLWFs) [250, 251], this tool applies a simplified way of localizing the Wannier functions, projecting onto a pre-defined set of local orbitals [278]. The energy window to which the Wannierization procedure was applied (the strongly correlated d- and f-bands) was specified manually by selecting the corresponding band range.

3.2.2. Phase stability and structural distortions from an enhanced DFT+*U* scheme

From standard DFT+U relaxations, the undistorted $Cmmm$ structure is obtained as the most stable AUO_4 structure for all five A cations (see Figure 3.3). This is in disagreement with experimental findings and shows that the standard DFT+U method, considered as the current "gold standard" for computation of uranium oxide materials, fails here. However, we were able to conduct a more in-depth analysis, based on the complete set of measured structural data.

Figure 3.2 shows that we could induce the distortion to the $Ibmm$ structure by applying pressure to the systems, i.e. forcing the unit cell volumes to shrink. The obtained distortion–volume relationships match the experimental results (red diamonds in Figure 3.2) qualitatively. However, the systems' energies increase significantly with decreasing volume (see Figure 3.3). This indicates that the distorted structures would be less stable than the high-symmetry $Cmmm$ structure, i.e. that

the distortion can be induced in simulations but would not be stable. Finding an explanation for this apparent inconsistency compared to experiments led us to analyze orbital occupations in the mixed d-/f-oxides. As described in Chapter 2, atomic orbitals (AO) are commonly employed as projection operators to obtain occupations of d- or f-orbitals, and these were also applied here in the first step. It is well known that these often yield spurious fractional orbital occupations [223, 249]. Table 3.2 reports that, in particular, occupations of uranium $5f$-orbitals are far from the expected values when computed with AO projectors. These spurious occupations yield an unrealistically large so-called Hubbard energy, which artificially increases the system's total energy [223, 249]. In reality, such a contribution should be rather negligible.

	A^{2+} d-occ.			U^{6+} f-occ.		
	AO	WF	expected	AO	WF	expected
$MnUO_4$	5.4	4.8	5	4.0	0.2	0
$CoUO_4$	7.3	6.8	7	4.0	0.3	0
$MgUO_4$	–	–	0	4.0	0.0	0
β-$NiUO_4$	8.4	7.9	8	4.0	0.4	0

Table 3.2.: d- and f-orbital occupations obtained for the AUO_4 $Ibmm$ structures from DFT+U calculations using atomic orbitals (AO) and Wannier functions (WF) as projectors. Table reprinted with permission from [271] (extracted from Table S5). Copyright 2021 American Chemical Society.

To circumvent this problem, we removed the unrealistic Hubbard energy term by setting it to zero. Figure 3.3 and the energy differences in Table 3.3 illustrate that, with this approach, the distorted $Ibmm$ structures stabilize for all the AUO_4 compounds except β-$CdUO_4$, reproducing exactly the experimentally observed structural types. The volumes corresponding to the energy minima fit the experimental volumes reasonably well (see Table 3.3). Extracting the distortions at these minimum energy volumes (see Figure 3.2) results in values that match the experimental ones satisfactorily (see also Table 3.3). The corresponding tilt angles decrease with increasing ionic radii of the A^{2+} cations, in agreement with the experimental trend (see Table 2 and Figure 7 of ref. [271]). Experimental unit cell volumes and distortions are slightly expanded by thermal motion, compared to DFT+U calculations which are always performed at 0 K. We note that standard DFT ($U = 0$) calculations also resulted in distortions, but the agreement with the experimentally measured structural parameters is much worse than in the corrected DFT+U calculations (see Table S4 in the Supplementary Information of ref. [271]).

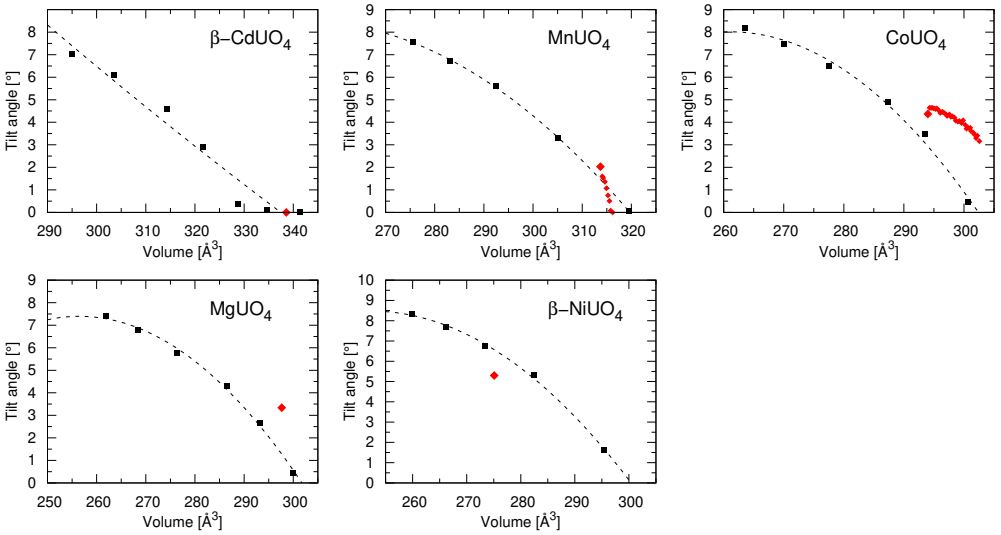

Figure 3.2.: Simulated (black squares) and measured (red diamonds) tilt angles of the UO_6 octahedra in the AUO_4 compounds. The black dashed lines represent parabolic fits to the computed data and should be used as guides to the eye. Reprinted with permission from [271]. Copyright 2021 American Chemical Society.

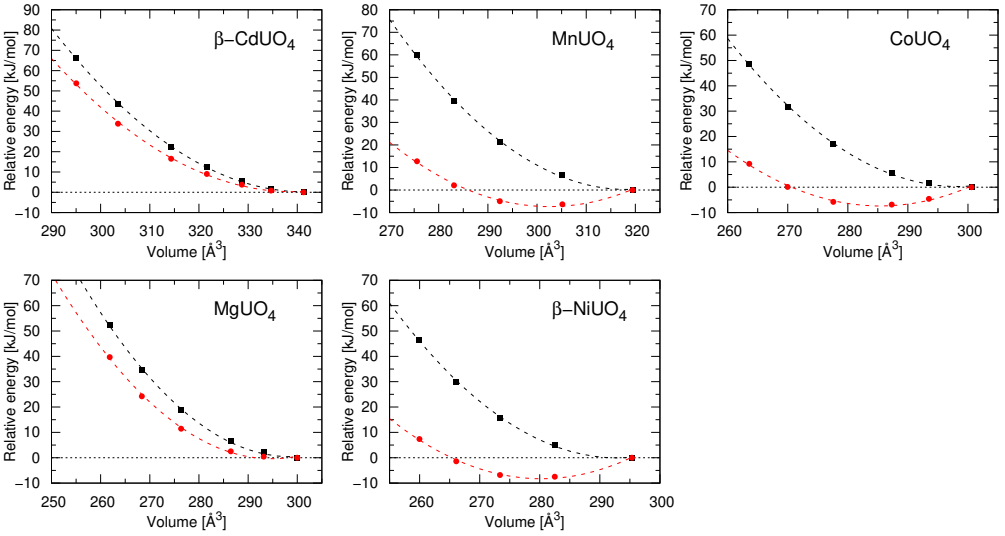

Figure 3.3.: Relative energies between the $Ibmm$ and $Cmmm$ structures computed for the AUO_4 compounds with the standard DFT+U approach (black squares) and by subtracting the Hubbard energy term (red circles). The dashed lines represent parabolic fits to the computed data, and the red dashed lines were used to derive the equilibrium volumes. Reprinted with permission from [271]. Copyright 2021 American Chemical Society.

compound	method	*a* [Å]	*b* [Å]	*c* [Å]	volume [Å^3]	dist. U^{6+} [Å]	dist. O^{2-} [Å]	ΔE [kJ/mol]	ΔE w/o E_{Hubb} [kJ/mol]	ΔE WF [kJ/mol]
β-$CdUO_4$	exp. $Cmmm$	7.02	6.85	3.52	169.3	0	0			
	comp. $Cmmm$	7.05	6.87	7.04/2	341.3/2	0	0	0	0	0
$MnUO_4$	exp. $Ibmm$	6.75	6.65	6.99	313.7	0.1027	0.0743			
	comp. $Cmmm$	6.82	6.69	7.02/2	320.0/2	0	0	0	0	0
	comp. $Ibmm$	6.64	6.54	6.96	302.5	0.1641	0.1754	+8.19	−7.39	+1.30
$CoUO_4$	exp. $Ibmm$	6.50	6.51	6.96	294.0	0.2104	0.1962			
	comp. $Cmmm$	6.60	6.52	7.01/2	300.6/2	0	0	0	0	0
	comp. $Ibmm$	6.44	6.39	6.92	285.4	0.2221	0.2128	+6.93	−7.41	−4.28
$MgUO_4$	exp. $Ibmm$	6.60	6.52	6.92	297.6	0.1517	0.1583			
	comp. $Cmmm$	6.63	6.51	6.95/2	300.0/2	0	0	0	0	0
	comp. $Ibmm$	6.58	6.47	6.93	294.7	0.0893	0.0921	+0.99	−0.41	−0.20
β-$NiUO_4$	exp. $Ibmm$	6.38	6.37	6.76	275.1	0.2431	0.2259			
	comp. $Cmmm$	6.55	6.50	6.95/2	295.9/2	0	0	0	0	0
	comp. $Ibmm$	6.40	6.39	6.85	280.2	0.2327	0.2180	+6.78	−8.29	−3.18

Table 3.3.: Measured and computed structural parameters (lattice parameters *a*, *b*, *c*, unit cell volumes, distortions of U^{6+} and O^{2-} ions) and energies of the AUO_4 compounds. Energy differences (per formula unit) use the $Cmmm$ structure as a reference (0 kJ/mol). O^{2-} distortion is reported for these oxygen atoms moving along the same crystallographic direction as U^{6+}. Table reprinted with permission from [271]. Copyright 2021 American Chemical Society.

3.2.3. Alternative approach using Wannier function projectors

A more rigorous approach that corrects the unwanted orbital occupation behavior is to replace AO projectors to represent the *d*- and *f*-orbitals by localized Wannier functions (WF). This approach will be denoted "DFT+*U*(WF)" in the following. As will be shown, it yields an improved description of the system's electronic structure instead of only correcting the effects on energies by manually subtracting the Hubbard energy term after running the calculation. The DFT+*U*(WF) approach has been employed before for uranium oxides and resulted in negligible occupations of unoccupied orbitals and improved description of high resolution X-ray absorption near edge structure (HR-XANES) spectra [268]. The reason is that Wannier functions more adequately represent the shape of *d*- or *f*-orbitals in solids. It is well known that the choice of projector functions significantly affects the results of DFT+*U* calculations [249, 279–281].

When applying the DFT+*U*(WF) scheme to the AUO_4 compounds, we also obtain occupations much closer to the expected ones, in particular for the $5f$-orbitals of U^{6+} cations (see Table 3.2). As can be seen from Table 3.3, the DFT+*U*(WF) approach results in correctly predicted phase stability for most AUO_4 compounds, since the Hubbard energy term is now mostly close to zero. The wrong prediction for $MnUO_4$ is attributed to weaknesses of the Poor Man's Wannier scheme in selecting the relevant *d*- or *f*-bands (see Chapter 4) and can be corrected by manually removing the remaining Hubbard energy contribution. Note that the DFT+*U*(WF) calculations could only be performed using the experimental structures (or, alternatively, those resulting from the previous analysis by subtracting the Hubbard energy). Geometry relaxations, obtaining the distorted structures directly, were not possible since forces are currently not implemented for this scheme.

3.3. Parameter-free DFT+*U* for structural properties of pyrochlore compounds

The DFT+*U* method with *U* parameters derived from first principles [191] was also applied by our group to study various properties of pyrochlore compounds, more specifically zirconate pyrochlores ($Ln_2Zr_2O_7$, with Ln = La, Ce, Pr, Nd, Pm, Sm, Eu, Gd) [282]. These lanthanide-containing compounds are relevant e.g. as ionic conductors [283] or for nuclear waste disposal [284]. From the methodological side, the aim was to evaluate if the DFT+*U* approach can provide highly accurate structural properties for these compounds.

It was shown before that the DFT+*U* approach with the *U* parameter derived from linear response in combination with the PBEsol exchange correlation functional [276] is successful in computing structural properties of Ln-containing orthophosphates [246, 285]. Correctly taking into account the $4f$-electrons is important (there are no d-electrons in Zr^{4+}). It was also found that the *U* parameter should be derived for the element and structure in question [246]. Therefore, in the first step, the Hubbard *U* parameter was derived for the series of Ln cations in $Ln_2Zr_2O_7$ from the linear response scheme [191] (see Chapter 2). The computational setup was similar to the one used for AUO_4 compounds (see Section 3.2, for details see the original paper [282]).

Ln	$U(Ln^{3+})$ in $Ln_2Zr_2O_7$	$U(Ln^{3+})$ in $Ln_2Zr_2O_7$ [286]	$U(Ln^{3+})$ in $LnPO_4$ [246]
La	2.8		3.2
Ce	3.7		3.6
Pr	4.3		4.1
Nd	5.0		4.9
Pm	5.1		5.5
Sm	6.3	6.5	6.6
Eu	7.6		8.1
Gd	3.9	3.4	3.4

Table 3.4.: Hubbard *U* parameters for Ln^{3+} cations in zirconate pyrochlore compounds ($Ln_2Zr_2O_7$) derived from linear response here and in literature [286], as well as parameters from literature for lanthanide orthophosphates ($LnPO_4$) [246] for comparison. All values in eV. Data originally published in ref. [282], distributed under the terms of the Creative Commons Attribution License (CC BY).

The resulting *U* parameters are shown in Table 3.4. They are consistent with previous derivations for $Ln_2Zr_2O_7$ pyrochlores [286] and lanthanide phosphates ($LnPO_4$) [246]. With increasing atomic number and thus increasing occupation of $4f$-orbitals, the *U* values increase, indicating increasing electronic correlations, as expected. The Gd^{3+} cation breaks this trend and shows a reduced *U* parameter, most probably related to its half filled $4f$-shell ($4f^7$ valence electron configuration). Values for the lanthanide phosphates (see Table 3.4) are for the same oxidation state of Ln, but for a different chemical environment, so they cannot be expected to agree perfectly with values for the pyrochlores; but they show the same trend. They have shown to give reliable results for computation of structural properties [246]. *U* parameters derived for lanthanide compounds from spectroscopy methods are typically higher than those obtained here (up to $U = 10$ eV) [287, 288].

It has also been argued that the linear response method [191] results in too small U values for f-elements due to the strong coupling of f-electrons to d- and s-electrons [289]. These contributions are included in the perturbed charge occupation during the U derivation procedure (see Chapter 2) and might falsify the resulting U parameter. On the other hand, computational studies use very different sets of U parameters successfully. U parameters for different compounds or computational setups should not be directly compared anyways, but derived for each system of interest [191]. The parameters used here will be evaluated in the following.

The results from work performed by Dr. Kowalski's group (see ref. [282]) show that the parameter-free DFT+U, using the U parameters derived here, yields very accurate results for structures of the stoichiometric $Ln_2Zr_2O_7$ pyrochlores as well as actinide-doped $Nd_2Zr_2O_7$ pyrochlores. Depending on the Ln^{3+} cation, the PBEsol+U functional can outperform the pure PBEsol functional when comparing to experimental lattice parameters corrected for thermal expansion (see Figure 2 in ref. [282]). The average error for both is around 0.04 Å, which is much better than the PBE functional [205] with an error of 0.12 Å. Note that here we do not systematically compare DFT+U results to DFT ($U = 0$) or to DFT+U results computed with differently obtained U parameters. However, it can be concluded that the parameter-free DFT+U approach is a highly reliable tool for predicting structural properties of the pyrochlore compounds. Going beyond standard atomic orbital projectors does not seem to be necessary for derivation of structural properties.

3.4. DFT+*U* with Wannier projectors for nickel oxides

The DFT+U(WF) method was also applied to β-NiOOH compounds, namely in a joint study in Dr. Kowalski's group considering Fe-doped NiOOH materials (denoted "Fe:NiOOH") [290] as well as for studying catalytic properties of β-NiOOH materials in electrochemical conditions (see Chapter 6 of this thesis). These layered materials are of relevance as catalysts for the oxygen evolution reaction (OER) (see Chapter 6 for details on structure and applications).

3.4.1. Selecting the Hubbard *U* parameter

We first derived the Hubbard U parameter for Ni^{3+} and Fe^{3+} cations from the linear response method [191] (see Chapter 2). Details on the computational setup can be found in ref. [290]. Table 3.5 shows U values around 8 eV for Ni^{3+}. Fe^{3+} has a U value between 3 and 4 eV in the high-spin (HS) state, whereas the value increases to ca. 6 eV for the low-spin (LS) state, where some orbitals are doubly occupied (d^5 configuration in octahedral coordination) and thus stronger electron correlations can be expected.

compound	spin state (Ni^{3+})	spin state (Fe^{3+})	U(Ni^{3+})	U(Fe^{3+})
β-NiOOH	HS	–	7.7 / 8.1	–
β-Fe:NiOOH	HS	HS	7.8 / 8.1	3.6
β-Fe:NiOOH	HS	LS	8.0 / 8.9	6.1
β-FeOOH	–	HS	–	3.1

Table 3.5.: Hubbard U parameters derived from the linear response scheme for Ni^{3+} and Fe^{3+} cations in β-MOOH (PBEsol functional). All values in eV. HS = high-spin, LS = low-spin. Several reported values for Ni^{3+} correspond to different sites of the crystal structure.

The linear response method has also been used by Li and Selloni [291] to derive U parameters for various (mixed) Ni-Fe oxides, which were adopted in many studies thereafter [70, 90, 292]. Their parameter of 3.3 eV for Fe agrees with the one derived for HS Fe^{3+} here (LS Fe^{3+} is usually not considered) and values derived for other iron oxides are also around 4 eV [191, 241, 293]. In contrast, the value obtained here for Ni^{3+} is significantly larger than 5.5 eV from Li and Selloni [291]. The correct U parameter to be used for Ni^{3+} is discussed in the literature. Besides the beforementioned value of $U = 5.5$ eV [291], linear response calculations have also resulted in larger values of 6.6 eV [294–296]. The correct value of the Hubbard U parameter for Ni cations has also been discussed for similar Ni oxide compounds like NiO. Large U values of 7-8 eV have been reported [81, 297], but have been related to missing self-screening of d-electrons [297, 298]. From their linear response scheme, Cococcioni and de Gironcoli [191] themselves obtain $U = 4.6$ eV for NiO, which is close to the values of ca. 5.3 eV that are commonly used [299, 300] and recommended based on agreement with experimental data, e.g. magnetic and optical properties [298]. However, it has also been reported that $U > 8$ eV is required to match the experimental band gap and thus an intermediate value of $U = 6.3$ eV was used [301].

In principle, a U parameter around 8 eV for Ni^{3+} cations, as obtained here from linear response, could be a suitable choice for our computational setup (pseudopotentials, energy cutoff, orbital projectors, DFT software), even if other studies obtain much smaller values. However, based on the above discussion, besides the U parameters from Table 3.5, we also tested $U = 5$ eV for Ni^{3+} cations. We found that the U value of 5 eV is indeed more suitable to reproduce the experimental band gap of β-NiOOH [302–304] and we thus adopt this value in the following. A discussion about why U values from linear response can be larger than expected can be found in Chapter 4.

One single U parameter of 5 eV will also be employed in our follow-up studies using β-NiOOH surface slabs (ref. [290] and Chapter 6). It is known that, strictly speaking, the U parameter differs for bulk and surface sites [305] and for different oxidation states [83, 282]. However, using a specific U for each cation site is not a practical scheme since the total DFT energy depends on the U value and thus building energy differences involving two different slab models (as necessary e.g. when computing reaction energies) would not be possible. The effect is expected to be negligible.

3.4.2. Choice of orbital projectors and results for electronic structure

We found that, when computed with standard atomic orbitals (AO) projectors (see Chapter 2), β-NiOOH has metallic properties. As illustrated in Figure 3.4(a), the band gap is zero in this case. This result has been obtained before by other DFT($U = 0$) and DFT+U studies [306, 307]. Hybrid functionals [307, 308] and the G_0W_0 approach [306] were able to correct his behavior, but are computationally prohibitively costly. We could recover the band gap in reasonable agreement with experimental values (1.7-3.75 eV [302–304]) by using our DFT+U(WF) approach (see Figure 3.4(b)). The errors in electronic structure with AO projectors are again related to orbital occupations that deviate significantly from the expected ones (see Table 2 in ref. [290]), which is improved with WF projectors.

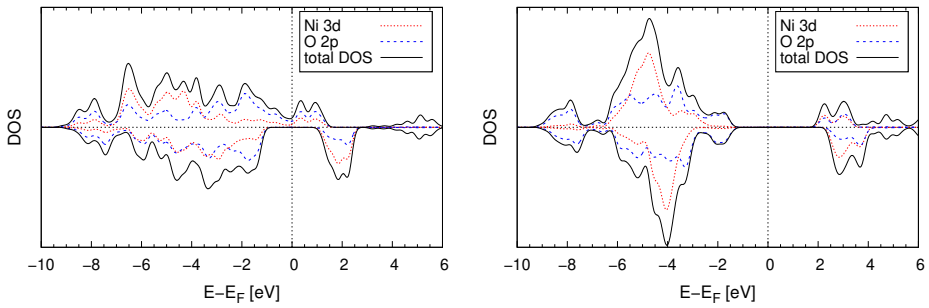

(a) AO (b) WF

Figure 3.4.: Densities of states of β-NiOOH(001) surfaces around the Fermi level, computed with atomic orbitals (AOs) vs. Wannier function (WFs) projectors in DFT+U ($U = 5$ eV). The spin down component is plotted with negative sign. Selected projected DOS (Ni $3d$, O $2p$ states) are also shown.

For constructing WF projectors, we again used the "Poor Man's Wannier" scheme in Quantum-ESPRESSO. This scheme requires to select the bands to which the Wannierization procedure should be applied, namely the Ni and/or Fe $3d$-bands. However, since only one band range can be specified and the $3d$-states mix with O $2p$-states (see Figure 3.4), this band choice is not straightforward. We selected the band range that gave d-occupations closest to the expected 0 or 1 and minimal resulting Hubbard energy. This procedure gave very satisfying results here (see also total occupations in Table 2 in ref. [290]), despite the pronounced mixing of d- and s-states. However, a more rigorous approach for band disentanglement would be desirable.

The electronic structure correctly represented by DFT+U(WF) enabled follow-up studies of the spin state of Fe dopant atoms in β-NiOOH and the resulting enhanced catalytic activity towards the OER [290]. These studies showed that, at low concentrations, Fe species are in the low-spin state. This is consistent with the measured metal-oxygen bond lengths and solubility limit of Fe in NiOOH, which is related to the low-to-high-spin transition. Fe low-spin species have also been reported in experimental studies [309]. Based on this, thermodynamic overpotentials for the OER could be derived (see Table 7 in ref. [290]), which are in excellent agreement with experimental values [290].

The impact of including an electrochemical environment in the DFT calculations will be studied in detail in Chapter 6.

3.5. Conclusion

In this chapter, we applied the parameter-free DFT+U and DFT+U(WF) methods to d- and/or f-element oxides with very satisfying results regarding atomic structures, phase stability, and electronic properties like band gaps. We showed that these approaches are reliable and versatile, but cannot be used as black boxes. By comparing to high-quality experimental data, we were able to improve over the "standard" DFT+U method. Atomic orbital projectors can be sufficient, depending on the material and target properties (e.g. for accurate structural properties of pyrochlores), but in general Wannier projectors are needed to obtain realistic d- or f-orbital occupations. As a result, an excellent electronic structure description was obtained for Fe:NiOOH materials, which enabled a high-level study of Fe spin states which would not have been possible otherwise. The computation of electronic structure of f-elements could be more intricate (see e.g. discussion in ref. [289]) and gives room for many studies related to the DFT+U approach, but this is not the focus of this thesis.

Concerning the choice of Hubbard U parameter, it should be kept in mind that the U value depends on the exact computational setup, like the choice of exchange-correlation functional, projectors or pseudopotentials [191]. Different U values can be required to obtain valid results for different setups, so that the parameter should be derived for each setup individually. Therefore, comparing to U values derived in other studies is not easily possible, but rather ranges and trends should be compared. The focus should be on verifying if the results obtained with the respective setup are valid and accurate. U parameters derived from first principles (like from the linear response scheme) should be preferred over semi-empirical values in principle, since they are potentially more accurate. However, it does not make sense to stick to such a value if results are obviously far from experiment or there is a clear reasoning indicating the applied approximation to be not fully valid (as observed here for β-NiOOH, where d-electrons of Ni are not fully localized).

The DFT+U(WF) approach is currently limited by the manual choice of bands to which the Wannierization scheme is applied, which might in principle be problematic if d- or f-bands mix with other states. In addition, forces are currently not implemented in the WF scheme. The method of manually subtracting the Hubbard energy term *a posteriori* is a very simple, but effective correction scheme that can serve as a workaround.

After showing the advantages of the parameter-free DFT+U and DFT+U(WF) schemes for applications to oxides, we will discuss its application to pure d-metals in the next chapter. We will study the U parameter derivation and application of the WF scheme systematically. A more detailed discussion on the applicability of the DFT+U method, comparison to other U parameter derivation methods, the problem of "too high" U parameters obtained sometimes from linear response, and d-band properties resulting from the WF scheme will be provided.

4. Computation of *d*-metals

In this chapter, we provide a more detailed analysis of the parameter-free DFT+U(WF) approach introduced in the previous chapter for reliable electronic structure computations. After discussing metal oxides in the previous chapter, the focus is now on pure transition metals. We compare Hubbard U parameters derived from different methods for all $3d$-, $4d$- and $5d$-transition metals, and provide details about some aspects of the U derivation in the linear response scheme. In a systematic investigation, we compare the performance of the DFT ($U = 0$) approach and different variants of the parameter-free DFT+U approach for lattice parameters, work functions, magnetic moments and d-band properties. We also discuss different double counting corrections in DFT+U and their applicability to metals. We show that the standard version of the DFT+U approach miscalculates the positions of d-band centers, but much better agreement with experiment is obtained when applying the DFT+U(WF) scheme. The findings of this chapter are highly relevant for computation of electronic structure of electrodes as part of electrochemical interfaces, as will be done in the following chapters.
This chapter is adapted from work previously published in the research article R. Tesch and P. M. Kowalski, *Hubbard U parameters for transition metals from first principles*, Phys. Rev. B 105, 195153, 2022. Sections 4.3 and 4.8 contain some additional data and analyses. The work presented here was performed by myself under the guidance of Dr. Piotr Kowalski.

4.1. Introduction

In the previous chapter, we successfully applied the parameter-free DFT+U and an improved scheme, the DFT+U(WF) approach, to d- and f-element oxides. In this chapter, we extend our analysis to pure d-metals, which are very relevant materials in electrocatalysis, for example platinum nanoparticles as catalysts in fuel cells. Describing their electronic structure accurately and efficiently is of utmost importance.

Metals are commonly described by the DFT method (Hubbard parameter $U = 0$), with typically good results e.g. for d-band properties [310]. However, metals also contain strongly correlated d-electrons, so that the DFT+U approach, if properly applied, should be suitable to describe their electronic structure. In addition, a consistent approach that can be used for both metals and metal oxides is desirable. We discuss the applicability of different flavors of DFT+U to metals in detail in Section 4.8.

Here, we systematically compute the Hubbard U parameter for all $3d$-, $4d$- and $5d$-transition metals from the linear response scheme (see Chapter 2) and discuss details of the derivation procedure.

We then compare them to an estimate based on comparison of Hartree–Fock and DFT eigenvalues and to values derived in literature by the constrained random phase approximation (cRPA). Systematic applications of the linear response method to charge-neutral pure transition metals are rare, especially for $4d$- and $5d$-metals. However, the exact values of U used for these systems are relevant, since they affect the positions of their d-bands, which are used in assessing adsorption behaviour and thereby catalytic activity [33].

Based on the derived U values, we discuss the performance of the parameter-free DFT+U method for the prediction of structural and electronic properties and compare to DFT calculations with $U = 0$. Systematic investigation of the impact of the Hubbard U correction on the computed properties of transition metals has not been performed before.

Note that we call here "self-consistent DFT+U" what we called "parameter-free DFT+U" in Chapter 3. The latter would be a more consistent choice, since the former is used with different meanings in the literature (compare refs. [191, 247]). However, for consistency with the published article [235], we stick to the first notation.

4.2. Computational details

All calculations were performed with the QuantumESPRESSO software package [256]. Ultrasoft and norm-conserving pseudopotentials were used to describe the core electrons with no differences in computed parameters. We applied plane wave energy cutoffs of 50 Ry and 150 Ry for ultrasoft and norm-conserving pseudopotentials, respectively. We used the PBEsol exchange-correlation functional [276] with some comparative calculations performed with the PBE functional [205]. The PBEsol functional has been specifically used as it results in much better prediction of structural parameters [276] and thus allows for more meaningful comparison with experimental lattice parameters. A Monkhorst–Pack [218] k-point mesh of $8\times8\times8$ (or comparable for non-cubic cells) was applied to assure converged results. All structures were optimized with convergence thresholds of 10^{-5} Ry and 10^{-4} Ry/a_0 (where a_0 is the Bohr radius) for energy and forces, respectively. Except for a few magnetic cases (Cr, Mn, Fe, Co, Ni), all metals were computed as spin-unpolarized. All $3d$-, $4d$- and $5d$-transition metals were considered in their most common, low-temperature crystal structures (see also Table A.1), i.e. fcc for Ni, Cu, Rh, Pd, Ag, Ir, Pt and Au; bcc for V, Cr, Fe, Mn, Nb, Mo, Ta and W; and hcp for Sc, Ti, Co, Y, Zr, Tc, Ru, Lu, Hf, Re and Os. For those $3d$-metals that show magnetic properties in their crystalline bulk phases, magnetic states were additionally considered; namely ferromagnetic (FM) states for Mn, Fe, Co and Ni and an antiferromagnetic (AFM) state for Cr [228].

As done in Chapter 3, the Hubbard U parameter was derived by applying the linear response method of Cococcioni and de Gironcoli [191]. These calculations were performed in $2\times2\times2$ supercells, which we found to be well converged in terms of system size. We note that there are differences between our applied procedure and that of the cRPA method regarding accounting for screening. While the cRPA method implicitly accounts for the sp-screening, it excludes the d-d-self-screening (the value computed in such a way is taken as the Hubbard U parameter) [228].

On the other hand, the linear response method does not require any *a priori* assumption about screening [191]. The standard DFT+U calculations discussed here were performed in the fully localized limit (FLL) double counting scheme, as opposed to the around mean field (AMF) approach [255, 311] (see Chapter 2). As an alternative to the standard atomic orbitals set of d-orbital projectors for the DFT+U calculations, we used localized Wannier functions. This was done with the aid of the "Poor Man's Wannier scheme" as implemented in the QuantumESPRESSO package (pmw.x tool) [278] (see also Chapter 3), excluding the 4s-states from the procedure. All calculations involving the Wannier functions-based representation were performed as single point calculations using geometries from standard atomic orbital-based DFT+U calculations. This is because forces are currently not implemented for such a computational setup in the standard release of the QuantumESPRESSO package. The Wannierization scheme was not used in the calculation of Hubbard U parameters.

In order to calculate work functions, surfaces were represented by slabs of 5 atomic layers thickness. We applied a 30 Å thick vacuum layer between the periodically repeated slabs. The k-point mesh for surface calculations was $8\times8\times1$. To preserve the bulk environment at the bottom of the slab, the two bottom layers were fixed during geometry optimization.

4.3. Variants of Hubbard *U* parameter derivation

In the literature, some variants of deriving the U parameter within the linear response approach have been proposed (see Chapter 2). Cococcioni and de Gironcoli [191] proposed to refine the parameter by restarting the derivation procedure applying the U parameter obtained in the previous iteration, until consistency is reached. We tested this procedure for selected transition metals, but the effect on U was small (maximally 0.2 eV, but typically below 0.1 eV).

Furthermore, Kulik et al. [247] proposed another "self-consistent" procedure, extrapolating U from a series of U_{out} computed from linear response applying different U_{in} in the perturbation procedure. Commonly, the U_0 value is used (where $U_{\text{in}} = 0$), but they proposed to use U_{scf} which is the intercept of the fit line. We also tested this approach here and the results are shown in Figure 4.1 for two examples. Mostly, the difference between U_0 and U_{scf} is around 0.1 eV, with exceptions of 0.2 eV (see the case of W in Figure 4.1(b)). Differences between U_0 and U_{scf} can be much larger, especially when the electronic structure differs significantly between DFT and DFT+U. This is not the case here.

In the systematic derivations presented here, we do not use these two self-consistent procedures for the sake of simplicity. The effects on the U value are small for d-metals and trends are not affected.

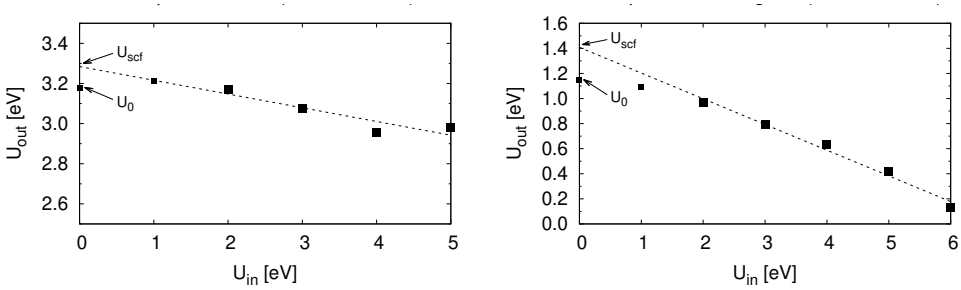

(a) fcc Pt (b) bcc W

Figure 4.1.: Determination of U_{scf} according to Kulik et al. [247], shown here for fcc Pt and bcc W metals. Big symbols: data points are included in the linear fit, small symbols: data points are not included.

The U parameter can also be derived from density-functional perturbation theory [248] (see Chapter 2) implemented in the hp.x code in QuantumESPRESSO (available as of version 6.4). We also tested this code for a few examples. As expected, the results are identical to the ones from the standard linear response scheme. Since we found that we do not need large supercells in the linear response procedure, the hp.x code does not have any advantages, and we do not use it here. However, the results confirmed that our linear response setup was sound.

4.4. Hubbard *U* parameters from the linear response scheme

Figure 4.2 shows the Hubbard U parameters derived by the linear response approach (denoted by the more general term "constrained local density approximation" (cLDA) here), together with the theoretical and experimental reference data. $3d$-metals show the largest U values, and U decreases with increasing d-element row number. This effect has also been observed for the U parameters calculated with the cRPA method [228] and reflects the higher degree of localization of $3d$-states. The calculated U parameters exhibit strong trends along the d-element rows. The U values are smaller than 1 eV for early transition metals, and increase continuously with filling of the d-shell. Such a trend is expected due to the increasing number of d-electrons. The increase in nuclear charge and the resulting stronger localization of d-orbitals also contributes to the rise in correlation effects. The same trend is visible in the series of U parameters computed by Şaşıoğlu et al. [228] with the cRPA method. The trend of increasing U with increasing d-shell filling, seen in both computed data sets, is in line with the experimental data [312–315], independent cLDA derivations [239, 245, 316, 317] and calculations by other *ab initio* methods [317].

Our calculations show that spin-polarization has a strong effect on the U parameter for the magnetic $3d$-elements. Except for the case of antiferromagnetic Cr, all magnetic states show significantly smaller U values than the non-magnetic cases, by 0.7 to 2.2 eV. This effect cannot be explained by changes in the lattice parameters, which results in much smaller variations of the derived U parameter values (ca. 0.1 eV). The cRPA study by Şaşıoğlu et al. [228] does not show so pronounced differences between the magnetic and non-magnetic states.

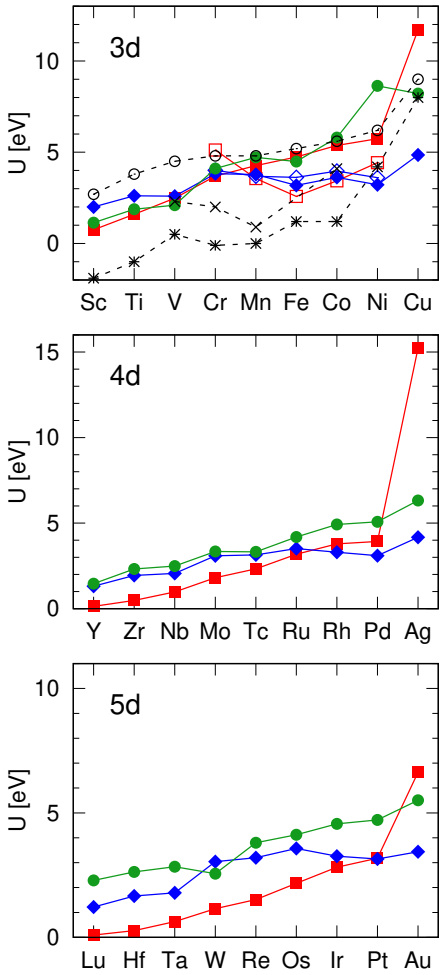

Figure 4.2.: The Hubbard U parameters for $3d$-, $4d$- and $5d$-transition metals. The different symbols denote the results obtained with: the cLDA method (red filled and open squares for non-magnetic and magnetic metals, respectively), the d-band center shifts between HF and DFT methods (green circles for non-magnetic metals), the cRPA method by Şaşıoğlu et al. [228] (blue filled and open diamonds for non-magnetic and magnetic metals, respectively), the cLDA method by Nakamura et al. [239] (open circles). The black symbols represent the experimental values (the measured correlation energy deduced from Auger and XPS spectroscopy) of de Boer et al. [312], Sawatzky and Post [313], Antonides et al. [314] (stars) and Kaurila et al. [315] (crosses, with uncertainty at the level of ± 0.4 eV). We note, however, that an exact correspondence between the measured and computed values is not expected and we provide these values only for qualitative comparison. All the reported data are also provided in Table A.2. Reprinted with permission from [235]. Copyright 2022 American Physical Society.

The largest differences between the Hubbard U parameters obtained with the cLDA and cRPA methods are for Cu, Ag and Au, i.e. the latest transition metals, with the cLDA method resulting in significantly larger values that are well out of the trends clearly formed by all other members of the series (see Figure 4.2). Such large, and usually not applied U parameters were also obtained in previous cLDA studies for these elements. For Cu Nakamura et al. [239] obtained 9.0 eV and Schnell et al. [238] report a very large value of 18.2 eV, although the latter value may be overestimated because of computing a one-atom unit cell. Cu, Ag and Au have completely filled d-shells and the cLDA approach is known to give unreasonable results for such cases [228, 244]. This may happen because the polarization of d- to non-d-orbitals is not correctly captured by the cLDA approach for atoms with completely filled d-shell. The reason is that hopping between, for instance, $3d$- and non-$3d$-states is cut off due to the constrained (maximum) $3d$-electron number on the completely filled d-site [244]. This may also lead to incorrect screening [228]. On the other hand, the experimental value of 8.0 eV [315] obtained for Cu from Auger spectroscopy indicates larger U values for late transition metals, as compared to the other transition metals. These values will be validated later by comparison of the calculated electronic density of states (DOS) with X-ray photoelectron spectroscopy (XPS) data. In the next section we present another, independent, estimate of Hubbard U parameters for transition metals which is based on Hartree–Fock calculations.

4.5. Hubbard *U* parameters using Hartree–Fock results as a reference

We propose here that an estimate of the Hubbard U parameter could be made using the Hartree–Fock (HF) method. HF is an exact method for the exchange part of the electronic interaction, but does not account for the correlations. However, comparing to DFT, HF results in reasonable estimates of eigenvalues. For instance, by applying Koopmans' theorem [199], HF reproduces the experimental ionization potentials of single atoms with relative errors of only $\sim$1 eV [318]. On the other hand, DFT heavily underestimates the eigenvalues, including the one of the highest occupied orbital, which should correspond to the ionization energy. The standard DFT+U method could be seen as a cure for such a deficiency [191]. In principle it shifts the occupied electronic levels by $-0.5\,U$ [227]. Thus, we assumed that the Hubbard U parameter can be estimated from a similar shift of DFT vs. HF eigenvalues:

$$0.5U = \epsilon_{\mathrm{DFT}} - \epsilon_{\mathrm{HF}}\,, \tag{4.1}$$

where ϵ_{DFT} and ϵ_{HF} are the DFT and HF eigenvalues, respectively. To our knowledge, such an approach has not been used before, although Schnell et al. [238] used similar reasoning to explain the difference between the eigenvalues computed for selected metals with Hartree and unscreened Hartree–Fock approximations.

Such a derivation based on the comparison of DFT and HF results to obtain the U parameter seems contradictory, as the DFT+U method is expected to correct for electronic correlations effects, neglected completely by the HF method. However, it is well known that, for instance, the PBE0 exchange-correlation functional [209] corrects the DFT (PBE) prediction for strongly correlated ele-

ments (e.g. [265, 319]), while having the same description of correlation as the PBE functional and differing only by the exchange part (by mixing HF with PBE exchange) [209, 320]. It has also been realized that the DFT+U approach provides a better description of exchange than DFT, by reducing the self-interaction problem [321]. In our estimate, HF results serve only as a reference that gives a more realistic estimate of orbital energies.

Table 4.1.: The Hubbard U parameter estimated from the differences between Hartree–Fock and DFT d-orbitals eigenvalues, by considering the shift of the highest occupied level (high.occ.) and the shift of the d-band center ($d$bc).The last row represents the same estimate for the lowest occupied valence s-states ($4s$, $5s$ and $6s$). The U values computed with the cLDA and cRPA methods are reported for comparison. All values are in eV. Data for more transition metals is available in Table A.2. Reprinted with permission from [235]. Copyright 2022 American Physical Society.

	Ti	V	Cu	Mo	Rh	Ag	W	Pt	Au
structure	hcp	bcc	fcc	bcc	fcc	fcc	bcc	fcc	fcc
cLDA	1.6	2.5	11.7	1.8	3.8	15.2	1.2	3.2	6.6
cRPA [228]	2.6	2.6	4.9	3.1	3.3	4.2	3.0	3.2	3.4
HF (high.occ.)	3.8	3.5	5.0	−0.1	3.7	3.5	4.6	2.6	1.1
HF ($d$bc)	1.9	2.1	8.2	3.3	4.9	6.3	2.6	4.7	5.5
HF (s-states)	11.4	12.6	11.1	12.4	12.1	9.5	12.3	12.5	11.1

In the first step we thus compared the HF eigenvalues of the highest occupied d-orbitals with the ones derived by DFT and interpret differences as a shift by $-0.5\,U$. In Table 4.1 we compare the so-derived U parameter to the estimates by cLDA and cRPA. For fcc metals, with the exception of Au, the HF estimate matches the U values derived from cRPA and/or cLDA surprisingly well. This may be related to the fact that fcc metals are always late transition metals. For bcc and hcp metals, HF values are slightly larger than cRPA values, and much larger than cLDA values. For Mo, the method results in a small negative value.

In the second step, we made the same estimate, but by comparing the differences in the positions of d-band centers obtained from the DFT and HF simulations. With such an approach we account for the cumulative relative shifts of all the d-states. For most of the cases, the resulting U values provided in Table 4.1 and in Figure 4.2 are larger than the estimate based solely on the highest occupied eigenvalues, but more consistent with the cLDA and cRPA results. In fact, the trends of increasing U parameter values along the d-elements series are well captured. Surprisingly, such a HF-based estimate matches the results of the cRPA method for early $3d$- and $4d$-transition metals well.

We were particularly interested in the estimate for Cu, Ag and Au, in order to understand the differences in results from the cLDA and the cRPA methods (see Figure 4.2), and to check if with the HF-based derivation, we could validate large U values for these elements. We obtained U parameters of 5.0 eV and 8.2 eV for Cu and 3.5 eV and 6.3 eV for Ag with the HF estimates from the highest occupied level and the d-band center shifts, respectively, which are consistent with the values computed by the cRPA method, but far smaller than the cLDA values. This estimate thus independently shows that the cLDA method indeed overestimates the Hubbard U parameter values

for transition metal elements with completely filled d-shells. We also note that the HF estimate for Au of 1.1 eV, based on the highest occupied level only, is much smaller than the values obtained by cRPA or cLDA methods. However, the HF estimate of 5.5 eV based on the position of the d-band center falls between the cLDA and the cRPA values, which is similar to the case of Cu. Our exercise thus shows that the HF-based calculations are useful for estimating Hubbard U parameters.

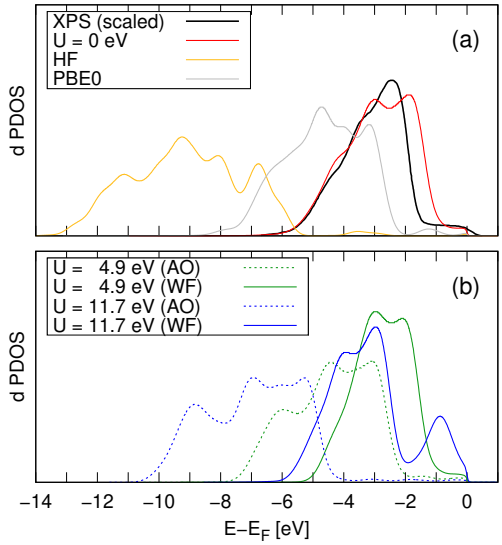

Figure 4.3.: Projected d-orbitals density of states for fcc Cu metal: (a) computed with the standard DFT ($U = 0$), hybrid functional (PBE0) and Hartree–Fock (HF) methods, as well as measured by XPS [310], and (b) computed with DFT+U and different projections of the d-states occupation: atomic orbitals (AO), Wannier functions (WF). Gaussian smearing of 0.03 Ry has been used to match the experimental band broadening. The XPS data are scaled vertically to match the intensity of the computed d-band. Reprinted with permission from [235]. Copyright 2022 American Physical Society.

However, the HF method does not provide perfect description of the electronic states of d-metals. When comparing the density of states (DOS) computed for Cu (see Figure 4.3) to the reference data, we notice that our DFT results agree with other DFT calculations [238, 322, 323]. Experimental spectra [322–324] show that plain DFT calculations match the experimental d-band position well, as observed here. In contrast, our HF DOS shows the d-band far away (ca. 10 eV) from the Fermi level. Similarly, unscreened HF calculations by Schnell et al. [325] show the Cu $3d$-band at 22 eV below the Fermi level and far distant from the $4sp$-states. The authors attribute the difference in HF and DFT DOS to the electronic self-interaction, which is correctly treated in HF, but not in DFT [325].

In order to validate the Hubbard U parameter values obtained with different methods, in the next section we test the performance of the DFT+U method for prediction of a set of physical parameters.

4.6. Evaluation of Hubbard *U* parameters

It is well known that different derivation methods can result in differences in the derived Hubbard *U* parameters [191, 279]. The reason for that is, for instance, the use of different projectors for the determination of occupations of orbitals of interest (e.g. *d*-orbitals) [191, 326]. As pointed out by Cococcioni and de Gironcoli [191] and stressed in Chapter 3, the best approach is to self-consistently apply the same method to derive the *U* parameter and to perform the follow-up calculations of targeted properties. We thus applied our derived *U* values for calculating lattice parameters, *d*-bandwidths and *d*-band centers for all *d*-transition metals as well as work functions for selected cases. The resulting values are compared to those computed by standard DFT calculations and by DFT+*U* calculations with the *U* parameters derived by the cRPA method [228], keeping in mind that the cRPA values were derived using a computational setup and software that are different from the ones applied here.

One important aspect of DFT+*U* calculations is the double counting scheme applied in the calculations (see Chapter 2). The applicability of the DFT+*U* approach in the FLL scheme (favoring full electron localization) is discussed in the literature [191, 311] and often the AMF scheme (favoring orbital occupations close to the average electronic density) is suggested as a correct approach for computation of metals [311]. More details will be discussed in Section 4.8. Here we focus on the results computed within the standard FLL variant, since the AMF scheme results in a solution equivalent to standard DFT ($U = 0$) for uniform occupations of *d*-orbitals (because Hubbard energy and potential terms cancel [255]). This is also particularly important because of the widespread usage of the FLL scheme.

		DFT	DFT+*U* (cLDA)	DFT+*U* (cRPA)
Ti	hcp (*a*)	−1.29	−0.65	−0.19
	hcp (*c*)	−1.48	−0.71	−0.17
V	bcc	−2.18	−2.15	−2.15
Cu	fcc	−0.77	+0.61	−0.27
Zr	hcp (*a*)	−1.21	−1.16	−0.98
	hcp (*c*)	−0.21	−0.22	−0.24
Mo	bcc	−0.26	−0.70	−0.98
Rh	fcc	−0.39	−1.15	−1.06
Ag	fcc	−0.04	+1.31	+0.35
W	bcc	−0.33	−0.64	−1.09
Os	hcp (*a*)	−0.23	−0.76	−1.11
	hcp (*c*)	+0.23	−0.44	−0.83
Pt	fcc	+0.41	+0.02	+0.02
Au	fcc	+0.76	+1.22	+0.99

Table 4.2.: Relative errors in % of computed lattice parameters for selected *d*-metals obtained with different computational methods, taking the experimental values as a reference [327, 328]. The full table is available in Table A.3. Reprinted with permission from [235]. Copyright 2022 American Physical Society.

Table 4.2 shows the signed relative errors of computed lattice parameters for selected d-metals in different crystal structures (the full table is available in Table A.3). The reference experimental values were corrected for thermal expansion effects using the measured linear thermal expansion coefficients [328]. Because we applied the PBEsol exchange-correlation functional that by design gives good predictions for lattice parameters of solids, the standard DFT gives good results for most of the considered metals. The DFT+U calculations with the U parameter derived by either the cLDA or the cRPA methods show very similar performance. Agreement with the experimental values is best for fcc and bcc, and slightly worse for hcp structures. We obtained larger errors for magnetic cases, which are related to wrongly reproduced magnetic moments for Cr and Mn, as discussed below. Overall, most of the lattice parameters are predicted with relative errors smaller than 2 %, which is in the usual accuracy range of DFT methods [329]. The lattice parameters of some metals (e.g. Fe, Pd and Pt) are surprisingly well predicted by the DFT+U calculations.

Table 4.3 summarizes the absolute magnetic moments per atom for all the considered magnetic 3d-metals. The best results are obtained with the standard DFT method. There is no significant difference in magnetic moments computed with the DFT+U(cLDA) and DFT+U(cRPA) methods, but these values are severely overestimated for Cr and Fe. We note that FM bcc Mn, which is a high-temperature phase of Mn, shows a similar behavior, but experimental reference is missing for this compound. The overestimation of magnetic moments leads to unreasonably large errors in lattice constants of up to 10 % (see Table A.3). The standard DFT+U method favors integer orbital occupations (0 or 1) and localization of electrons, and therefore is known to overestimate magnetic moments [330–332]. This may also be seen as an artifact of applying the FLL version of DFT+U, and could be reduced when applying the AMF approach. For the other magnetic elements (Co and Ni), which have higher d-occupations, the differences between the DFT and DFT+U values are less pronounced, and the agreement with experiment is rather good.

	Cr AFM bcc	Mn FM bcc	Fe FM bcc	Co FM hcp	Ni FM fcc
DFT	±0.50	0.59	2.13	1.63	0.63
DFT+U(cLDA)	±3.80 (5.1)	3.89 (3.6)	2.56 (2.6)	1.63 (3.4)	0.62 (4.4)
DFT+U(cRPA)	±3.60 (4.0)	3.89 (3.7)	2.66 (3.6)	1.63 (4.0)	0.63 (3.6)
exp. spin magn. mom.	±0.59 [333]		2.13 [334]	1.53 [334]	0.57 [334]

Table 4.3.: Computed and measured magnetic moments per atom in μ_B for magnetic 3d-metals (using atomic orbital projectors). The U parameter values (in eV) used in the calculations are given in parentheses. The cRPA U parameters are these of Şaşıoğlu et al. [228]. The experimental value reported for AFM Cr is the total magnetic moment, which includes the orbital magnetic moment. The spin magnetic moment should be slightly smaller. Reprinted with permission from [235]. Copyright 2022 American Physical Society.

	Cu(111)	Ag(111)	Pt(111)	Mo(110)	W(110)	MAD
DFT	5.01	4.66	5.82	4.67	4.95	0.15
DFT+U(cLDA)	4.93 (11.7)	4.58 (15.2)	6.19 (3.2)	4.68 (1.8)	5.01 (1.2)	0.17
DFT+U(cRPA)	4.98 (4.9)	4.64 (4.2)	6.19 (3.2)	4.68 (3.1)	5.00 (3.0)	0.15
exp.	4.94 [310], 4.98 [335]	4.74 [335]	5.93 [310, 336]	4.95 [335]	5.25 [335]	

Table 4.4.: Computed and measured work functions for selected closest-packed metal surfaces (using atomic orbital projectors). The mean absolute deviation (MAD) is reported for each method. The U parameter values used in the calculations are given in brackets. The cRPA U parameters are taken from [228]. All values are in eV. Reprinted with permission from [235]. Copyright 2022 American Physical Society.

The computed work functions of selected closest-packed crystal surfaces (i.e. (111) for fcc and (110) for bcc structures) are provided in Table 4.4. These values were obtained by taking the difference of the surface Fermi energy and the reference electrostatic potential in the middle of the vacuum region. The computed work functions are in most cases smaller than the experimental values. This is consistent with previous calculations using GGA and meta-GGA functionals [337, 338]. The effect is more pronounced for bcc(110) than for fcc(111) surfaces, with maximal deviations from the experimental values of 0.3 eV. The effect of applying the U correction is small in most cases. This is expected for d-metals, as the DFT+U correction simultaneously shifts the energies of the d-band and the Fermi level, leaving the density of states at the Fermi level unaffected. Except for the case of Pt(111), all computational methods yield very similar values, with larger differences from the measured values than between the methods. The similar values of mean absolute error show that all the methods perform similarly well. Moreover, for the bcc(110) surfaces, the DFT+U(cLDA) and DFT+U(cRPA) approaches result in nearly identical work functions values even though the U parameter values differ significantly.

In the next step we computed the d-bandwidths and d-band centers for all considered metals. We defined the d-band center as the centroid of the d-band and considered two cases: (1) the occupied states (up to the Fermi level) and (2) the entire d-band width. When computing the d-bandwidths, we defined the upper and lower limits of the band at points where the d-states DOS is only 5 % of the maximum band height. This was done to avoid counting of spurious, minor d-contributions. For spin-polarized metals we considered the sum of spin-up and spin-down components.

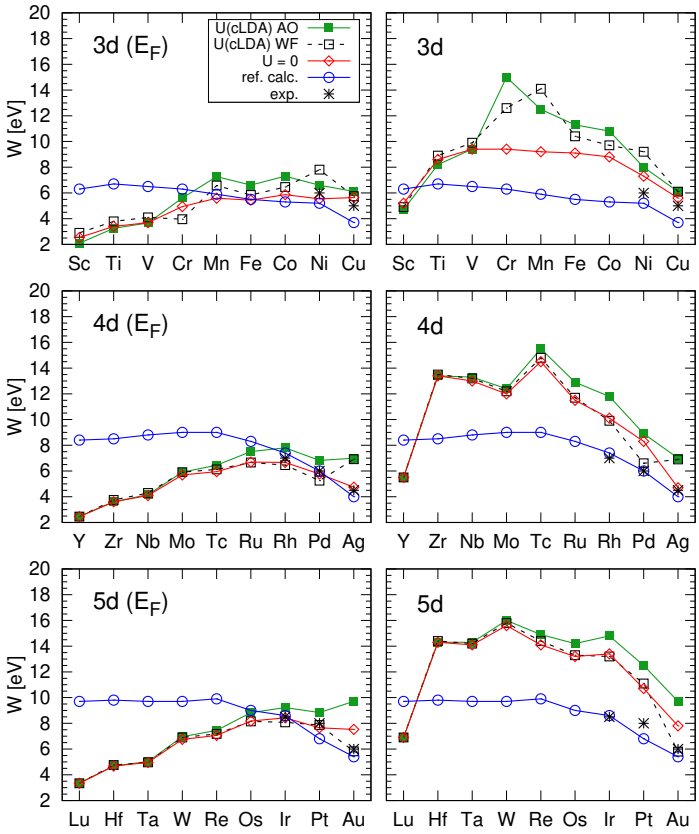

Figure 4.4.: d-bandwidths W (derived considering: only the occupied part of the d-band (left panels) and the entire d-band width (right panels)), derived as described in the text. Magnetic states of Cr, Mn, Fe, Co and Ni metals are considered. Computed reference data (ref. calc.) are taken from Şaşıoğlu et al. [228]. Experimental reference data are taken from Hüfner et al. [323] for Ni, Cu and Ag and from Smith et al. [339] for Rh, Pd, Ir, Pt, and Au. AO and WF indicate calculations performed with atomic orbitals and Wannier functions as projectors, respectively. Uncertainty of the measured values is in the order of ± 1 eV, and arises mainly due to unclear definitions of the band limits. All the reported data are also provided in Table A.4.

As shown in Figure 4.4, all methods indicate that $3d$-metals (except for AFM Cr and FM Mn) have the narrowest bands compared to their isovalent analogues, while $5d$-metals have the broadest bands. Along the d-metals series, the bandwidth increases from the start to the middle of the series and slightly decreases for the later transition metals. Data in Figure 4.4 indicate also that the DFT+U(cLDA) method results in broader bands than the standard DFT approach. This effect can also correspond to a shift of the occupied and unoccupied parts of the band to lower and higher energies, respectively. For all the magnetic $3d$-metals, the U correction produces a shift of the spin-up and the spin-down bands relative to each other, broadening the bands.

Our computed bandwidths are consistent with the DFT+U calculations of Cococcioni [340] for Fe bulk, indicating an increase of ca. 2 eV when applying the DFT+U method. The direct comparison to the set of calculated bandwidths of Şaşıoğlu et al. [228], as shown in Figure 4.4, is not

straightforward, since those data were produced applying an unspecified definition of the bandwidth. Figure 4.4 also shows known measured bandwidths [323, 339]. Because XPS measures occupied states, these can be compared to the computed results that account for the occupied part of the d-band only (left panels of Figure 4.4). The agreement with these experimental data is better in the case of DFT than DFT+U(cLDA). On the other hand, other spectroscopic studies show that for late transition metals, the d-bands become narrower with increasing the metal's valence electron number in all periods [339, 341–343]. This trend is also captured in our calculations. We are not aware of similar experimental data for early transition metals, which would be required for more in-depth analysis.

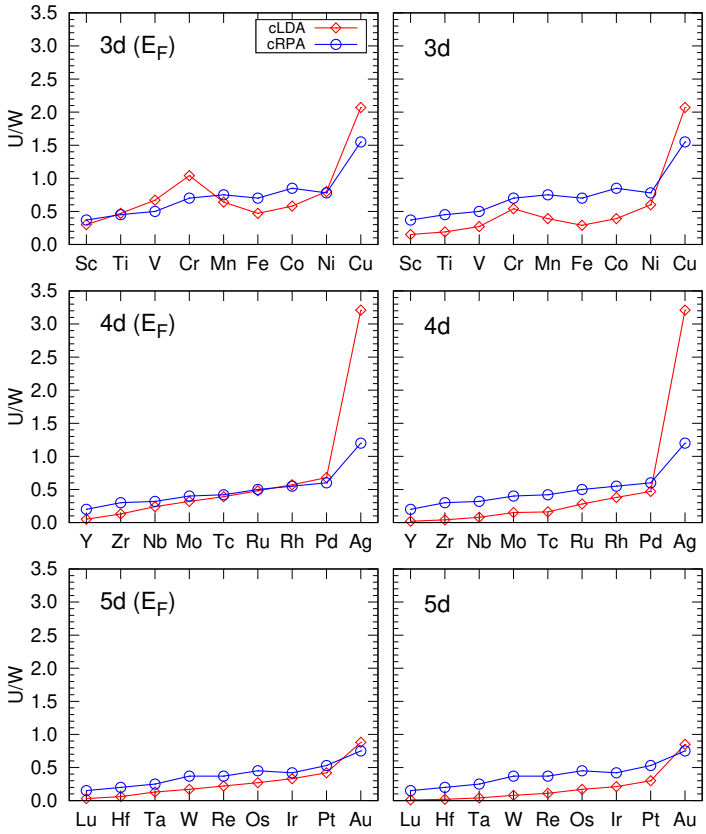

Figure 4.5.: U/W ratio computed with the cLDA and cRPA [228] Hubbard U parameter values. The bandwidths W are those from standard DFT calculations (U = 0), to allow a straightforward comparison to the cRPA reference data [228] computed in such way. These were derived considering: only the occupied part of the d-band (left panels) and the entire d-band width (right panels). Magnetic states of Cr, Mn, Fe, Co and Ni metals are considered. Reprinted with permission from [235]. Copyright 2022 American Physical Society.

The ratio of computed U values and the bandwidths, U/W, is shown in Figure 4.5. This parameter was used by Şaşıoğlu et al. [228] to assess the strength of the electron correlation for the different metals. In agreement with those results, in our calculations the so-defined correlation strength

increases along the d-metals series with $3d$-metals having the largest U/W ratios. This is because $3d$-metals have smaller bandwidths and slightly larger U parameters. The magnetic $3d$-metals, except for AFM Cr, stand out by relatively small U/W ratios, thereby significantly differing from the non-magnetic metal equivalents. Due to the large derived U parameters, Cu and Ag have huge U/W ratios. This does not necessarily reflect strongly correlated electronic structure, as these elements have completely filled d-shells.

Figure 4.5 shows that strong correlations (U/W $>$ 1) do not occur for the transition metals. Nevertheless, we decided to test the DFT+U method for all transition metals, since it is not clear at which point the correlations start to play a significant role [255].

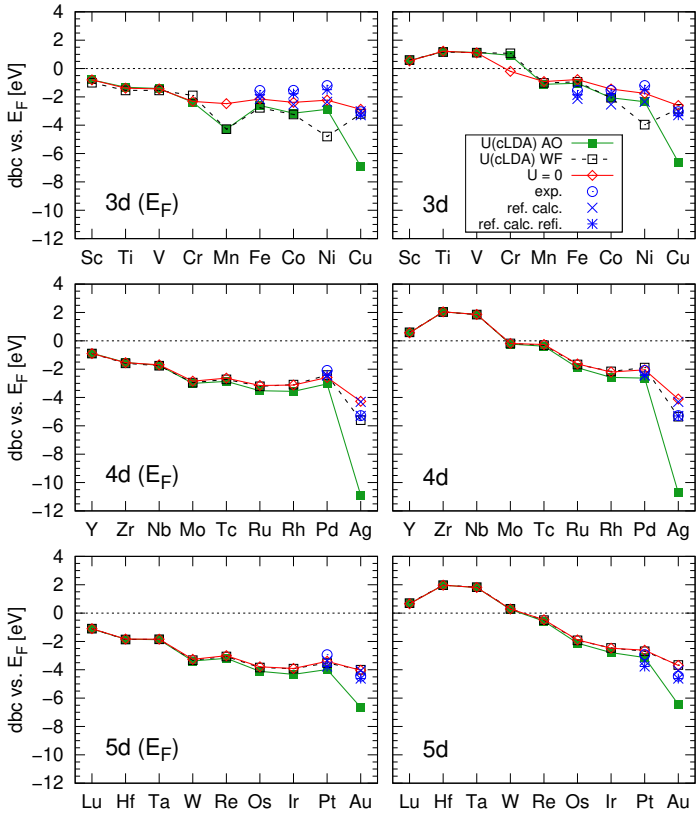

Figure 4.6.: Position of the d-band center ($d$bc) with respect to the Fermi level, derived considering: only the occupied part of the d-band (left panels) and the entire d-band width (right panels). Magnetic states of Cr, Mn, Fe, Co and Ni metals are considered. Experimental XPS data (with maximal uncertainty of $\pm$0.1 eV), calculated reference data (standard (ref. calc.) and refined (ref. calc. refi., see the text for explanation)) are taken from Hofmann et al. [310] for Fe, Co, Ni, Cu, Pd, Ag, Pt and Au and from Smith et al. [339] for Rh and Ir metals. Refined DFT calculations of Hofmann et al. [310] are given by blue stars. More details are provided in Table A.5. Reprinted with permission from [235]. Copyright 2022 American Physical Society.

Due to the popularity of the d-band model [26, 33], which relates the d-band center to the adsorption properties on metal surfaces (see Chapter 1), there exist multiple studies of d-band centers

of different transition metals surfaces [33, 337, 344]. These show clearly that the d-band center continuously shifts to lower energies along the d-series, with exceptions only for Ni, Pd and Pt [337, 344]. All studies demonstrate that the 11-valence electrons metals (especially Ag) have very small d-band center energies. Very similar trends are observed in computational [310] and experimental [310, 341, 342] studies of bulk d-metals. The calculated d-band centers are shown in Figure 4.6. The shift to lower energies is reproduced by all the applied methods. Hofmann et al. [310] calculated DOS and d-band centers using the standard DFT method. However, in order to better match the measured spectra, they refined their DOS by varying the e_g to t_{2g} orbitals relative contribution ratio and/or applying an offset (represented as "reference refined calculation" in Figure 4.6). We note that the difference between bare and refined values is large for Ag.

When applying the Hubbard U correction within the standard FLL scheme, the d-band centers shift significantly to lower energies, and the shift is proportional to the U value. The effect reflects a downward energy shift of occupied bands (by $-0.5\,U$) within the DFT+U framework. However, the experimental reference is matched much better by the standard DFT results. In particular, as compared to the experimental reference, the DFT+U(cLDA) results in large shifts of d-band center energies for Cu, Ag and Au, in part due to the contribution of s-states to the DOS at the Fermi level (see Figure 4.7) [345, 346]. The problem of DFT+U methods in reproducing spectra of transition metals has been noticed before [191, 347]. Interestingly, hybrid functionals also have problems in describing metals [348–351], attributed to problems with the HF exchange term. Our simulations of Cu with the hybrid PBE0 functional show the shift and mismatch between computed and experimental data (see Figure 4.3). We will elaborate more on this issue in the next section. We note, however, that the shift of the d-band has been eliminated by applying the AMF version of the DFT+U method [191] (see also Section 4.8). Nevertheless, this problem may also be related to the incorrect representation of d-orbitals in metals by atomic d-orbitals used in the projection of d-orbitals occupations, which we discuss in the next section.

4.7. Wannier projectors as orbital projectors

Although the DFT+U(cLDA) method reproduces the periodic trend of d-band center energies, the absolute energies differ from the measured values by ca. 1.5 eV and by several eV for Cu, Ag and Au. The experimental bandwidths are also not well matched by the DFT+U(cLDA) calculations (see Figure 4.4). Surprisingly, for metals such as Cu, the standard DFT+U(cLDA) method results in a shift of the d-levels, but not of the Fermi level itself. To find the reason for such an unexpected behavior we considered the projected density of states. As is shown in Figure 4.7, the states at the Fermi level remain unshifted, comparing to the large shift of the d-band, and they represent a hybrid of d-and s-states. We observe the same behavior for Ag and Au metals. It may in part originate from the atomic orbitals representation of the d-orbitals that is used in the projection of d-orbitals occupations in the DFT+U method. The d-orbitals in metals are different from the equivalent orbitals in isolated atoms, and the usage of an incorrect projector may result in formation of an artificial hybrid orbital at the Fermi level, which could affect the electronic structure computed with the DFT+U method. On the other hand, it is well known that metals such as Cu possess s-like

contributions at the Fermi level [345, 346].

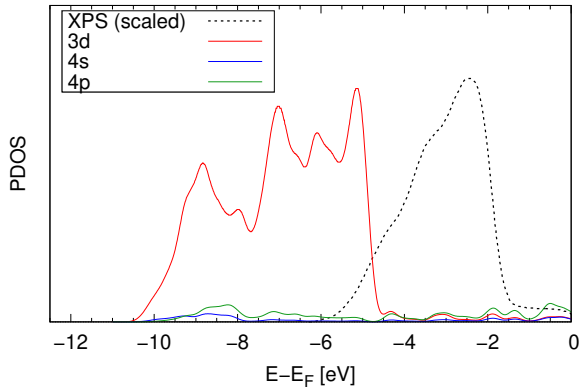

Figure 4.7.: Projected density of states for fcc Cu computed with the PBEsol+U(cLDA) method (atomic orbitals as projectors, $U = 11.7$ eV), with Gaussian smearing of 0.015 Ry. The results show a clear hybrid spd-state between the main d-band and the Fermi level. XPS data are taken from [310] and scaled vertically to match the intensity of the computed d-band. Reprinted with permission from [235]. Copyright 2022 American Physical Society.

The results of DFT+U calculations depend on the choice of projector functions [249, 279–281]. We address this issue by representing the d-orbitals in metals by Wannier functions, as has been done for strongly correlated orbitals in oxides in Chapter 3 (DFT+U(WF) approach). As mentioned before, Kvashnina et al. [268] have shown that Wannier functions improve the match of the f-electrons DOS to the experimental HR-XANES spectra of various uranium oxides. Here we test if similar improvement could be obtained for d-electrons DOS and its match to the measured XPS spectra.

We applied localized Wannier functions (as obtained from the "Poor Man's Wannier scheme") and obtained a localized basis of orthonormal orbitals to use as projectors of d-orbitals occupations in the DFT+U method. We constructed the respective representations of d-states in the Wannier scheme by picking the corresponding band indices. This procedure allowed us to separate s- and p-contributions from the d-bands. As mentioned in Chapter 3, however, the current implementation of Wannier orbitals does not allow to effectively separate the bands according to their s-, p- or d-character.

The projected densities of states for the d-bands calculated with atomic orbitals (AO) and Wannier functions (WF) as projectors are shown for selected elements in Figure 4.8, together with the experimental reference. The XPS experimental data of Hofmann et al. [310] were measured using Al Kα radiation and include s- and p-contributions, but these are very small [310]. The absolute intensities of computed DOS and XPS data in Figure 4.8 are arbitrary and should not be directly compared. This is because of the decrease of relative intensity of XPS bands towards lower energies [310, 339] that is attributed to a variation of the photoionization cross section across the d-band [352]. Moreover, electrons of e_g symmetry have higher transition probabilities than t_{2g} electrons [353].

The bands calculated with the DFT+U method with WF as projectors are much closer in position to the standard DFT and experimental bands (see Figures 4.6 and 4.8). The effect is distinct for Cu, Ag and Au, with their large U parameters computed with the cLDA approach. The DFT+U(cLDA) method with WF projectors is also able to reproduce the experimental d-band center for Ag, the case for which the standard DFT failed. In contrast, the WF-based calculations make the prediction for Ni worse. This only happens for the magnetic case, with the non-magnetic solution showing the same improvement as seen for other metals. This results from general problems in computing the magnetic states with the DFT+U method (like for the case of Cr, see Table 4.3).

The use of WF projectors improves the capability of the DFT+U scheme for prediction of d-band centers. Nevertheless, the standard DFT bands still fit the XPS data best. Interestingly, the hybrid functionals also produce significant, unwanted shifts (see Figure 4.3). We stress that the DFT+U method corrects only the d-states. Our HF calculations also indicate the need for a correction of the energies of s-states (see estimation of U parameter values for the lowest occupied valence s-states in Table 4.1). Similarly, we observe a significant shift of the energies of 4s-states in our calculations of Cu (by 2.2 eV) and calculations of MgB_2 metals by Gao et al. [351] using the PBE0 hybrid functional. Such an unaccounted effect should strongly affect the relative positions of d-band and Fermi level, and potentially influence the agreement with XPS spectra[1]. On the other hand, the AMF implementation of DFT+U could be an alternative to improve spectral properties (see also next section).

[1] Unfortunately, it is not possible to apply a U correction to more than one orbital (l quantum number) of the same element in the current release of the QuantumESPRESSO package (version 6.5).

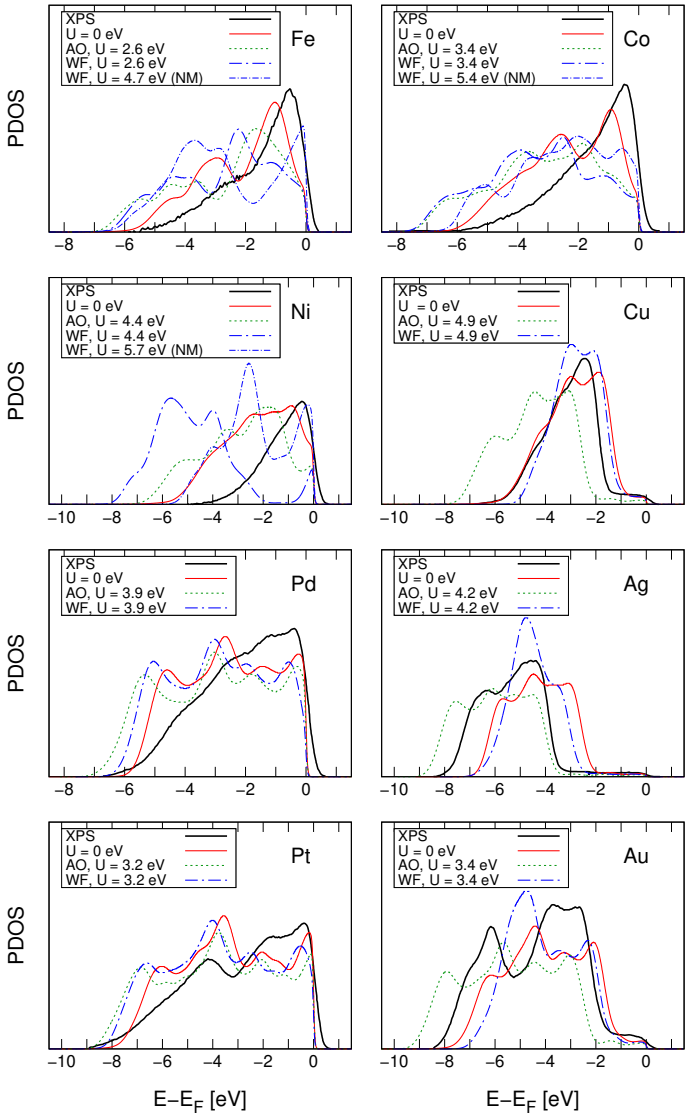

Figure 4.8.: Projected d-orbitals density of states for selected metals, computed with different projections of d-states occupation: atomic orbitals (AO), Wannier functions (WF). Gaussian smearing of 0.03 Ry has been applied to match the experimental band broadening. Magnetic and non-magnetic states of Fe, Cr and Ni metals are considered. XPS data are taken from [310] and are rescaled vertically to match the intensity of the computed d-bands. The reference experimental spectra agree well with earlier measurements by Hüfner et al. [323], Smith et al. [339], Höchst et al. [354]. Our computed DOS for $U = 0$ (DFT approach) agree well with the calculations by Hofmann et al. [310]. Reprinted with permission from [235]. Copyright 2022 American Physical Society.

4.8. Impact of double-counting correction and applicability of DFT+*U* to metals

The DFT+U method has been occasionally used in studies of Fe, Co and Ni [191, 331, 355], but in general, the standard DFT ($U = 0$) is most commonly used to describe pure transition metals (e.g. Hofmann et al. [310]). Jain et al. [356] demonstrated empirically that the standard DFT computation of metals results in much better formation enthalpies of transition metal oxides, although the application of the DFT+U method has been shown to be essential for the considered oxide phases. On the other hand, a DFT+U description of metallic (sub)systems might be required for mixed metal/oxide compounds, like metal electrodes with surface oxide layers. Computation of oxidation reaction paths could also require metals to be computed at the DFT+U level to ensure comparability of the obtained energies (which are known to depend on the U value). Independently of its necessity or importance, when properly applied, the DFT+U method should give good results also for pure metal systems [340]. The magnitude of the U parameters obtained here for metals indicates that electrons are indeed strongly correlated, at least for intermediate and late transition metals.

The application of the DFT+U method for weakly correlated (early) d-metals is debated [357], but the line between weakly and moderately correlated systems is not clearly defined. Instead, for weakly correlated metals, the mentioned AMF version of the DFT+U method [358] (see Chapter 2) has been proposed, and shown to give good results [191]. This seems obvious when considering the formalisms of the two double counting flavors [223], the AMF favoring complete electron delocalization and uniform occupations and the FLL favoring full electron localization and occupations of 1 or 0. The two schemes thus represent the extreme limits. It has also been demonstrated that the real solution may be better represented by a hybrid between the two extremes [255], with the AMF and FLL approaches more appropriate for metals with small ($U < 2$ eV) and large ($U > 2$ eV) Hubbard U parameter, respectively.

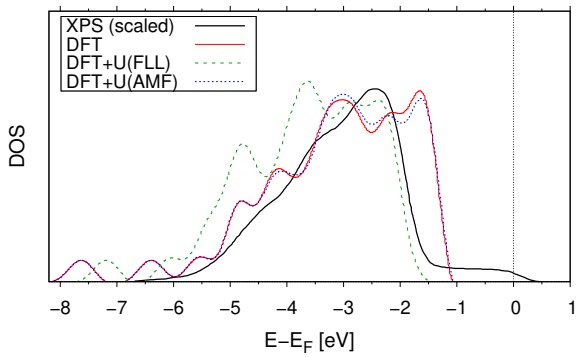

Figure 4.9.: Total density of states for fcc Cu, as computed with standard DFT ($U = 0$) and DFT+U ($U = 4.9$ eV) with different double counting corrections (FLL and AMF). XPS data are from [310] and scaled and shifted vertically.

So far, in this thesis we used the FLL double counting scheme for describing metals. Only the FLL,

but not the AMF scheme is implemented in most DFT codes, including QuantumESPRESSO. For a brief evaluation of both FLL and AMF schemes, we switched to the Abinit code [359, 360]. The computational settings were the same as before, except that we had to use PAW potentials [361] instead of the ultrasoft pseudopotentials. The results are shown in Figure 4.9 for Cu. It can be clearly seen that the DFT+U(AMF) scheme almost perfectly reproduces the standard DFT result, as expected for a metallic system. In contrast, the DFT+U(FFL) scheme results in a DOS shifted to lower energies by 0.5 to 1 eV. The overall agreement with the experimental XPS data is similar for all presented schemes. The best approach for future work would be to evaluate both double counting schemes for each application; if the AMF scheme is not implemented, the FLL scheme in combination with the DFT+U(WF) approach presented above proved to be a valid alternative also for pure metals.

4.9. Conclusion

In this chapter, we carried out a detailed electronic structure study for all $3d$-, $4d$- and $5d$-transition metals. We carefully considered details of the Hubbard U parameter derivation from the linear response implementation of the cLDA method, including system and method dependence of the U value and self-consistent procedures to obtain the U parameter. Systematically derived U parameters from linear response compare reasonably well to those obtained with the cRPA method, but show a more pronounced trend along the periodic series. This underlines the necessity of using different values of U parameters for different d-elements. We observe that for metals with fully occupied d-shell (Cu, Ag, Au), the cLDA method overestimates the Hubbard U parameters, which is a known feature of the method and attributed to incomplete removal of self-screening. Values consistent with the cLDA and cRPA methods were also obtained with the HF-based estimate proposed here, and allow for validation of cRPA or cLDA results for the disputed cases.

We evaluated the performance of the DFT and DFT+U methods for prediction of a set of physical parameters of metal bulk phases and surfaces. In general, the benefit of applying the Hubbard U correction depends on the element, the property under consideration and the applied DFT+U scheme. The considered DFT+U schemes differ in the choice of orbital projectors (atomic orbitals or Wannier functions) and double counting correction (FLL or AMF variant). It is important to stress that in the widely used FLL double counting scheme, the U parameter directly affects the position of the d-band, which is often used as an indicator for adsorption behavior and catalytic activity.

When computing d-band properties of transition metals with FLL DFT+U, we observed a shift of the d-band to lower energies compared to experimental XPS spectra. Interestingly, we found a very similar behavior for hybrid density functionals. This is to a large extend corrected when Wannier functions (WFs) are used as projectors in the determination of occupations of d-orbitals. Wannier projectors indeed seem to provide a more realistic representation of orbitals in metals (as it was the case for metal oxides in Chapter 3). It is well known that the choice of projector functions significantly affects the results of DFT+U calculations, but the systematic and routine-type application of WF projectors is new. The mentioned shift in the d-band is not expected in the AMF implementation of DFT+U, which is often referred to as a more appropriate method for

computation of metals.

The DFT+U(WF) approach evaluated here lacks an implementation of forces as well as a rigorous approach to disentangle d- and s- (or other) states for applying the Wannierization procedure, as mentioned already in Chapter 3. The Wannier90 program [362] could be a way to achieve this, but this was beyond the scope of this thesis.

Assessing whether the electronic structure is correctly described (e.g. by analyzing the DOS) is very important in any DFT study, and we showed that the DFT+U approach should not be applied blindly. Various variants of the approach were presented here that can be the best choice for the system in question. A correct description of metal d-bands is extremely important, since they are often used as descriptors for catalytic activity, like in the famous d-band model [27, 33]. As described, the U parameter and projectors directly affect the position of the d-band. Our analysis provides a solid basis for the correct computation of electronic structure of metals and metallic surfaces, which is of utmost importance in, for example, computational catalysis.

5. Computation of electrochemical interfaces

In this chapter, we intensively test and validate the recently developed ESM-RISM for computation of electrochemical interfaces. The method combines a grand canonical DFT or DFT+*U* description of the electrode with an implicit description of the electrolyte in the RISM framework, thus including both electrolyte and electrode potential effects. We show that the ESM-RISM yields reliable interface descriptions, when geometric setup, interaction parameters and description of the near-surface electrolyte structure are carefully considered. We apply the method to the simple Au(111)/electrolyte interface as well as to the more complex partially oxidized Pt(111)/electrolyte interface. We obtain descriptions of local reaction conditions at the interfaces, including double layer structure, electrostatic interface potentials and surface charging relations. In particular, we can reproduce the peculiar non-monotonic charging relation of the Pt(111)/electrolyte interface. We conclude that the ESM-RISM is a powerful method for computation of electrochemical interfaces. It will be applied in the following chapter to model an electrochemical reaction at technologically relevant nickel (oxy)hydroxide catalysts.
This chapter is adapted from the following research articles:

- P. M. Kowalski, T. Bornhake, O. Cheong, N. Dohrmann, A. L. Koch Liston, A. Shad, S. K. Potts, R. Tesch, Y.-Y. Ting, *Fundamentals of Energy Storage from First Principles Simulations: Challenges and Opportunities*, Front. Energy Res. 10, 1096190, 2023. (Section 5.2. My contribution: interface description for the Au(111)/electrolyte interface.)
- R. Tesch, P. M. Kowalski, M. H. Eikerling, *Properties of the Pt(111)/Electrolyte Electrochemical Interface Studied with a Hybrid DFT—Solvation Approach*, J. Phys.: Condens. Matter, 33, 444004, 2021. (Section 5.3)

The work presented in this chapter was performed by myself under the guidance of Prof. Michael Eikerling and Dr. Piotr Kowalski. The mean field model for the Pt(111)/electrolyte interface was developed and implemented mainly by Prof. Jun Huang. Classical molecular dynamics simulations, shown in Appendix B for comparison, were run by Oskar Cheong.

5.1. Introduction

As described in Chapter 1, a self-consistent approach to describe electrochemical interfaces (ECIs) at sufficient accuracy and at reasonable computational cost is still missing [55, 59]. In order to model local reaction conditions at ECIs, the applied electrode potential as well as electrolyte solution need to be taken into account. Existing methods have been reviewed in Chapter 1.

Here, we adopt the effective screening medium reference interaction site method (ESM-RISM) developed by Nishihara and Otani [104] a few years ago (see Chapter 2). This method combines a DFT description of the solid electrode with an integral equation-based solvation model, namely the RISM, for the electrolyte region. The ESM-RISM can yield important information about local reaction conditions via electrolyte distribution functions and local electrical potentials, also including the effects of an applied potential in a grand canonical potentiostat scheme.

The ESM-RISM has been applied previously to successfully simulate electrochemical systems (e.g. [122, 175–177]). The method seems to have numerous advantages [104, 114]: it self-consistently accounts for solvent, pH, temperature, and electrode potential. Charge neutrality is always ensured with the counter charge placed properly in the electrolyte region, and the potential in the bulk electrode serves as a potential reference. In addition, the method is efficient due to the classical electrolyte treatment and mixed boundary conditions that allow for relatively small DFT simulation cells. In the following, we will evaluate if these advantages persist in practical applications of the method.

We apply the ESM-RISM to the interfaces between charged Au(111) and Pt(111) electrode surfaces and aqueous acidic electrolyte solutions. The Au(111)/electrolyte interface serves as a simple test system, whereas the Pt(111)/electrolyte interface is known to have complex potential-dependent properties and thus serves as a more challenging test system. We thoroughly study the geometric arrangement of the solid electrode and liquid electrolyte in the simulation cell, making the model applicable for our use, and parameterization of the water and interface models, as well as the required splitting of the system into quantum mechanically and classically treated parts. Based on this, we compute various interface properties, such as electrolyte structure and electrostatic potential profiles. One focus will be on computing surface charging relations, which are a very important interface property [363], e.g. determining electrostatic interactions with electrolyte ions, and can serve as a fingerprint of a specific interface (see Chapter 1). A key result in this regard is the non-monotonic charging relation for the Pt(111)/electrolyte interface, which was for the first time obtained from first principles.

We show that the ESM-RISM reproduces key interface properties and local reaction conditions like local potential, electrolyte ions concentrations, structure of the electrical double layer and capacitive behavior. Comparing to explicit simulations of the interface and a theoretical model, we discuss strengths and limitations of the ESM-RISM for description of ECIs. This analysis enables us to productively use the ESM-RISM in studies of other relevant catalyst/electrolyte interfaces (see Chapter 6).

5.2. Properties of the Au(111)/electrolyte interface

Here, we apply the ESM-RISM to model the electrified interface between a Au(111) electrode and a 0.1 mol/L aqueous HCl solution. This system represents a simple test system, since the Au(111) surface is not covered by adsorbates in the relevant potential range, as shown by cyclic voltammetry [364]. The interaction between water and gold surfaces is known to be rather weak [365].

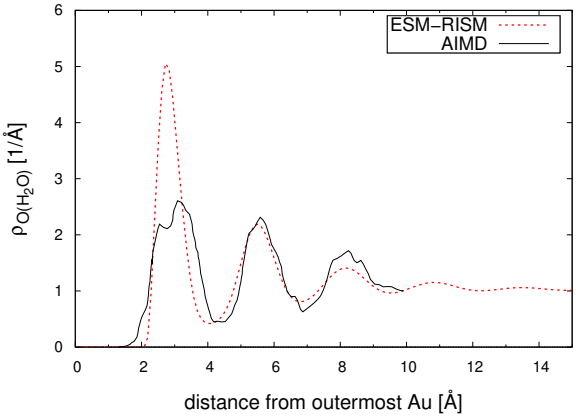

Figure 5.1.: Water density distribution functions at the Au(111)/water interface computed with the ESM-RISM as a function of the distance from the outermost layer of Au atoms. The position of water molecules is represented by the position of water oxygen atoms. AIMD data were taken from ref. [366].

For the Au electrode, we used the PBE exchange-correlation functional [205], with the optimized lattice constant of bulk Au of 4.17 Å. The Au(111) surface was modeled by slabs of six layers thickness (with the two bottom layers fixed to the bulk structure) and a 1×1 surface unit cell. A $12\times12\times1$ k-point mesh [218] and a plane wave energy cutoff of 60 Ry were employed. The Au pseudopotential was ultrasoft with the $6s^15d^{10}$ electrons computed explicitly. The computational setup for the ESM-RISM was equivalent to what is described in detail in Section 5.3.1. The Lennard-Jones parameters for Au atoms used in the ESM-RISM calculations were $\sigma = 2.629$ Å and $\epsilon = 5.29$ kcal/mol [367]. We checked that these values result in a water density profile that matches the AIMD data of Goldsmith et al. [366] (see Figure 5.1).

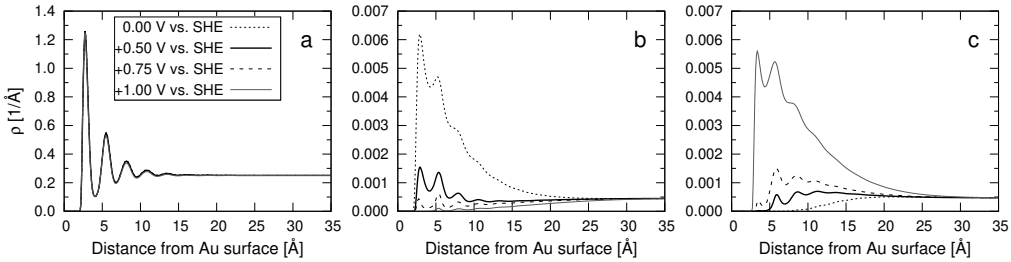

Figure 5.2.: Density profiles for electrolyte species (c(HCl) = 0.1 mol/L) at the Au(111)/electrolyte interface at different electrode potentials. Different panels show results for: (a) water molecules, (b) H_3O^+ electrolyte ions and (c) Cl^- electrolyte ions. Different lines represent the results computed with the ESM–RISM at different electrode potentials. The potential of zero charge (pzc) is located at 0.5 V vs. SHE [368]. Reprinted with permission from [369], published by Frontiers Media S.A. under the Creative Commons Attribution License.

Figure 5.2 shows the surface structure of the electrolyte solution as represented by density distribution functions of water and electrolyte ions. For example, the near-surface structure of water

solvent shows alternating shells of water, as observed in AIMD simulations [366]. One can clearly observe the effects of the applied potential and resulting surface charge on excess or depletion of ions near the interface, as expected from electrostatic arguments. This also means that the electrode charge is correctly balanced by the arrangement of electrolyte ions in the solution (as opposed to, for example, uniform counter charge schemes).

The relation between the surface charge and applied potential is approximately linear (see Figure 5.3). This is expected because in the considered potential range, the Au(111) surface is characterized by the formation of the electrical double layer and not covered by adsorbed species [364]. Other computational studies have derived very similar charging relations [120, 366] (see Figure 5.3). The trends are consistent with the experimental findings of linearly decreasing (i.e. opposite) charge at the outer Helmholtz plane [370]. The double layer capacitance, as derived from the slope of the linear fit, is 23.4 μF/cm^2 and compares well to the experimental [371, 372] and other computational [105, 110, 366] results.

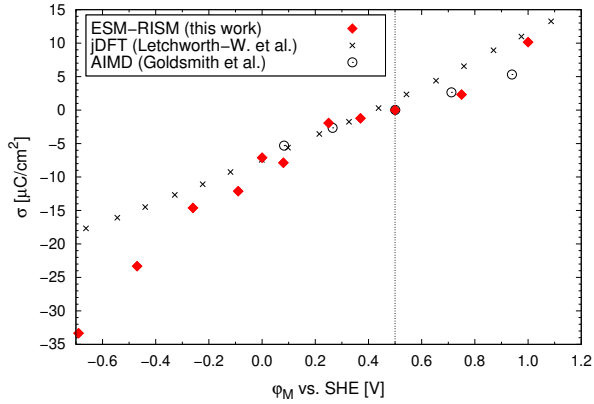

Figure 5.3.: The computed surface charge vs. the applied electrode potential for the Au(111)/electrolyte interface in 0.1 mol/L aq. HCl solution (our data), in pure water by Goldsmith et al. [366] and in an electrolyte of 1 mol/L ionic strength by Letchworth-Weaver and Arias [120]. The vertical dashed line shows the pzc assumed here (0.5 V vs. SHE [368]). Reprinted with permission from [369], published by Frontiers Media S.A. under the Creative Commons Attribution License.

In summary, the ESM-RISM yields the expected results for electrolyte structure and capacitive behavior of this simple metal/electrolyte interface. This paves the way for applications of the method to more complex interfaces.

5.3. Properties of the Pt(111)/electrolyte interface

Next, we apply the ESM-RISM to the interface between a partially oxidized Pt(111) electrode and an aqueous acidic electrolyte solution. This interface is of particular relevance, since platinum (Pt) catalysts are widely used, e.g. in PEM fuel cells (see Chapter 1). In these devices, the catalyst

nanoparticles are in direct contact with an acidic electrolyte solution. Due to the technological relevance, the Pt(111)/electrolyte interface has been intensively studied [373–376].

Depending on the applied potential and electrolyte composition, the Pt(111) surface is known to be covered by varying types and amounts of adsorbates [45, 377]. Between potentials of ca. 0.1 and 0.4 V vs. reversible hydrogen electrode (RHE), hydrogen adsorption is dominant, whereas oxygen species adsorb at potentials between ca. 0.6 and 0.8 V vs. RHE (in 0.1 mol/L $HClO_4$ solution) [45]. At larger potentials, the surface is known to dissolve due to formation of surface oxide [56, 378]. The adsorption has an impact on local reaction conditions, as reflected for example by the peculiar non-monotonic surface charging relation [379] (see below for detailed discussion). Based on the amount of available data and its complexity, the Pt(111)/electrolyte interface represents an excellent test case for the ESM-RISM.

5.3.1. Computational details

We computed clean as well as partially oxidized Pt(111) surfaces in pure water and aqueous HCl electrolyte. All calculations were performed with the plane wave QuantumESPRESSO software package, version 6.4 [256], modified by Nishihara and Otani [104] to implement the ESM-RISM interface model. We used the PBE exchange-correlation functional [205] to directly compare our results with previous studies of Fernandez-Alvarez and Eikerling [124]. For systems with explicit water we used the revPBE exchange-correlation functional [380] in conjunction with the D3 dispersion correction [212]. This functional is known to give very similar results to the RPBE-D3 functional [381, 382], which reliably describes water structures at the Pt(111)/water interface [383]. However, the latter functional is not implemented in the standard version of QuantumESPRESSO. Core electrons were described by ultrasoft pseudopotentials, with the Pt $6s^1 5d^9$, O $2s^2 2p^4$ and H $1s^1$ electrons computed explicitly. All calculations were spin-unpolarized, with energy cutoffs of 40 Ry and 320 Ry for plane waves and charge density, respectively. Gaussian broadening by 0.015 Ry was used for orbital occupations. Geometries were optimized with convergence thresholds of 10^{-4} Ry and 10^{-3} Ry/a_0 (where a_0 is the Bohr radius) for energy and forces, respectively.

The RISM and ESM-RISM formalisms were described in detail in Chapter 2. Here, in the first step of a RISM calculation, electrolyte–electrolyte correlation functions are computed in the 1D-RISM framework [104]. When computing molecules in electrolyte solution, the 3D-RISM [384] is then used to obtain the solute–electrolyte correlations. For computation of interfaces we applied the Laue-RISM scheme in the ESM framework, called the ESM-RISM [104].

The computation of a single water molecule in aqueous solvent was performed using a cubic box of 20 Å length and the 3D-RISM framework with the Kovalenko–Hirata (KH) closure relation [261]. A single k-point (the Γ point) was used in this case. The solvent temperature was set to 300 K and the cutoff energy for solvent correlation functions was 160 Ry. Solvent water of density 1 g/cm^3 was described by the TIP5P [385] and SPC [386] water models. It should be noted that the original water models are modified in the RISM framework by adding Lennard-Jones (LJ) parameters of $\varepsilon = 0.046$ kcal/mol and $\sigma = 1.0$ and 1.8 Å at the H and oxygen lone pair (L) sites, respectively [122, 387–389]. The LJ parameters for the solute water molecule were $\varepsilon_O = 0.1554$ kcal/mol, $\sigma_O = 3.166$ Å

[390], $\varepsilon_H = 0.0460$ kcal/mol and $\sigma_H = 1.0$ Å. Convergence thresholds for the 1D-RISM and 3D-RISM were 10^{-8} Ry and 10^{-6} Ry, respectively.

Interface calculations were performed in a vacuum/slab/electrolyte configuration (see Figure 5.4). In the direction perpendicular to the metal slab, the DFT unit cell is bounded by effective screening media (vacuum in this case) at both ends. The metal slab adjoins vacuum at its left side; at its right side, the electrolyte region extends, starting from the position set by the `laue_starting_right` parameter. The electrode/electrolyte interface is located at the metal slab's right side in this asymmetric setup. Beyond the DFT cell, the electrolyte region extends further, as determined by the `laue_expand_right` parameter.

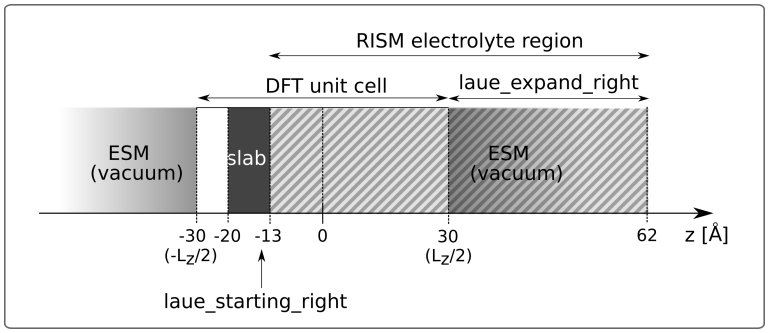

Figure 5.4.: Schematic representation of the computational setup for ESM-RISM calculations of an electrochemical interface. The simulated system consists of a vacuum region, a metal slab and an electrolyte region. The schematic also indicates the regions for the effective screening medium (ESM) at both sides of the DFT unit cell as well as the metal slab position in the DFT unit cell. The scale shows the dimensions of the respective regions as used in this work. Reprinted with permission from [391], published by IOP Publishing under the Creative Commons Attribution 4.0 licence.

Converged interfacial properties were obtained with a DFT cell length of 60 Å (see also Figure B.2). The left vacuum region was 10 Å thick. The right solvent region was extended beyond the DFT cell by ∼32 Å, i.e. up to ∼75 Å from the Pt surface slab (see also Figure B.3). Vacuum layers as well as dipole correction schemes are not needed in the ESM scheme, because the simulation cell is not periodically repeated in the direction perpendicular to the slab. If not explicitly mentioned in the text, the parameter limiting the extend of the solvent region slab-sided (`laue_starting_right`) was set between the two outermost atomic layers of the Pt slab, as suggested by Haruyama et al. [122] (see also discussion in Appendix B and below). Optimized Pt bulk lattice constants of 3.981 and 3.996 Å were used in calculations with the PBE and revPBE-D3 functionals, respectively.

The Pt(111) surface was modeled by slabs of four layers thickness. The two bottom layers were fixed to bulk positions. The computed surface unit cell was a $2\sqrt{3} \times 2\sqrt{3}$ cell with 12 surface Pt atoms. A Monkhorst–Pack [218] k-point mesh of $4\times4\times1$ was applied. Surface coverage with oxygen species was modeled by adding varying numbers of adsorbed oxygen atoms in the fcc hollow sites of Pt(111), using coverages of 0 to 3/4 monolayer (ML). The oxygen atoms were evenly distributed on the surface sites. The electrolyte region was filled by either pure water (described by the TIP5P model) or by aqueous HCl with a concentration of 0.1 or 1 mol/L. The closure relation,

solvent temperature, solvent correlation functions cutoff and RISM convergence thresholds were the same as in the case of the solvated water molecule. Different LJ parameters were used for solute Pt and O atoms (see Table 5.2), as will be described in Section 5.3.2. LJ parameters for the electrolyte ions Cl^- and H_3O^+ were $\varepsilon_{Cl} = 0.1001$ kcal/mol, $\sigma_{Cl} = 4.4$ Å [392], $\varepsilon_O = 0.1554$ kcal/mol, $\sigma_O = 3.166$ Å [393], $\varepsilon_H = 0.0460$ kcal/mol and $\sigma_H = 0.4$ Å [393].

In calculations with one water layer computed explicitly by DFT, we used an ice-like hexagonal bilayer water structure with H-up and H-down structural arrangements. In both cases, 8 water molecules were added per surface unit cell, resulting in a water coverage of 2/3 ML (see Figure 5.7). LJ parameters for the explicit O and H atoms of these water molecules were the same as in the pure water simulations.

Simulations with applied potential were performed in a grand canonical ensemble [109] (see Chapter 2). The convergence threshold for the forces in the fictitious charge particle (FCP) relaxation was set to 0.01 eV. The electrostatic potential in bulk electrolyte served as a potential reference. The referencing to the SHE potential scale will be described below.

5.3.2. Building a reliable interface model with the ESM-RISM

Water model

The accurate description of electrolyte–electrolyte interactions is a prerequisite for the correct description of electrode/electrolyte interfaces. Therefore, we first computed properties of pure water solvent. This basic inspection does not involve an interface, but serves to test the water model used in the RISM for consistency. Describing the structure of water is a challenge in itself for molecular simulations [394–396]. To test the performance of the RISM, in the first step we computed a single, solvated (hydrated) water molecule. We calculated water–water pair distribution functions (with 1D-RISM) and hydration free energies of the water molecule (with 3D-RISM). The resulting pair distribution functions are shown in Figure 5.5. They show the typical qualitative features of the hydrogen bonded network in water [397], yet deviate visibly from experimental results in terms of peak positions and peak shapes. Our results are consistent with other RISM studies of water [384, 398]. We note the significant offset between computed and measured maxima of O–O pair distribution functions. This occurs because water in the first hydration shell exhibits structural ordering which cannot be preserved with the statistical averaging involved in a RISM calculation. Comparison to classical molecular dynamics (CMD) simulations with the same water models (see Figure B.1) shows that the deficiency in describing the water structure is indeed related to the RISM, and not to the water model itself. To adequately represent the structural organization and electrostatic properties of water, water molecules of the first hydration shell have to be treated explicitly at the level of quantum mechanical calculations.

Hydration free energies play an important role in electrochemical systems and should be reproduced with sufficient accuracy by a chosen water model [122]. As shown in Table 5.1, hydration free energies computed with the RISM using the TIP5P water model agree better with experiment than those computed with the simpler SPC model. Therefore, we used the TIP5P model in the

subsequently reported studies.

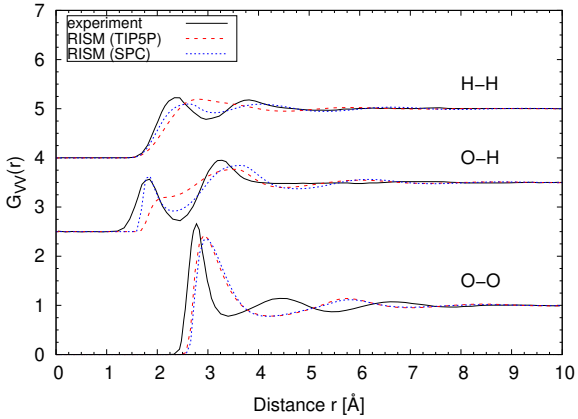

Figure 5.5.: Water–water pair distribution functions computed with the 1D-RISM applying the TIP5P and SPC water models. Neutron scattering experimental data [397] are shown for comparison. Reprinted with permission from [391], published by IOP Publishing under the Creative Commons Attribution 4.0 licence.

Table 5.1.: Hydration free energies of a water molecule in implicit water solvent computed with the 3D-RISM with different water models. Reprinted with permission from [391], published by IOP Publishing under the Creative Commons Attribution 4.0 licence.

Method	Hydration free energy [kcal/mol]
3D-RISM SPC	-4.1
3D-RISM TIP5P	-5.2
3D-RISM SPC [104]	-4.2
experiment [399]	-6.3

ESM-RISM electrode–electrolyte model

Several parameters have to be set in the ESM-RISM approach so that it will provide consistent and insightful results for the Pt(111)/electrolyte interface. These include the simulation cell size, the width and starting position of the solvent region (see Figure 5.4) and the LJ parameters for interactions between electrode and electrolyte.

Too small simulation cell and/or solvent region sizes can affect interfacial properties such as electrostatic potential profiles (see Figures B.2 and B.2). This is because in small model systems direct correlation functions are truncated at too short distances [104]. We therefore used large DFT unit cells of 60 Å length with the solvent region expanding $\sim$32 Å further, beyond the DFT cell.

Another important ESM-RISM input parameter, which is discussed in the literature [122, 124], is the starting position of the solvent region at the right side of the slab in the vacuum/slab/electrolyte setup (`laue_starting_right`, see Figure 5.4). An infinitely high potential wall prevents the solvent from extending to the left of this point. The actual electrode–electrolyte separation distance (or gap

width) is determined by the LJ interaction between electrode atoms and electrolyte species. The statistical distribution of solvent and electrolyte is an outcome of the self-consistent solution of the Ornstein–Zernike equation, as implemented in the RISM. The `laue_starting_right` parameter should be located close to the interface, on the electrode side, preferably between the first and second layers of atoms in the metal slab [122]. In contrast, when the `laue_starting_right` parameter is set too far from the Pt surface, an artificial vacuum between slab and solvent is created (see Figure B.4), which has a significant impact on interfacial solvent distribution functions (see Figure B.4), interfacial potential (see Figure B.5) and other computed interface properties. The relative position of electrode and electrolyte is of utmost importance for electrochemical interfaces [59, 400, 401] and therefore should be carefully computed.

An energy minimization procedure has been used in the literature to determine the parameter `laue_starting_right` [124]. The ESM-RISM solvation energy as a function of `laue_starting_right` shows a clearly discernible minimum (see Figure B.5). The increase in solvation energy with increasing `laue_starting_right` is induced by too large (and thus unfavorable) electrode–electrolyte separation. On the other hand, the solvation energy increase with decreasing `laue_starting_right` is probably related to a very small (and unphysical) amount of solvent that extends into the metal slab, despite the infinitely high repulsive wall, experiencing highly repulsive interactions. This puts energy minimization procedures to find the correct `laue_starting_right` [124] into question. As can be seen from Figures B.4, B.5 and B.6, the value of `laue_starting_right` that would result from an energy minimization procedure is too large and introduces the aforementioned artificial vacuum layer between slab and solvent. We stress that in this work, the `laue_starting_right` parameter is not obtained from an energy minimization procedure, but set between the two outermost atomic layers of the Pt slab. The electrode–electrolyte gap is then computed self-consistently within the RISM and affected only by the choice of LJ interaction parameters (see below). The size of the electrode–electrolyte gap and the interfacial concentrations of electrolyte species also depend on the oxygen coverage at the Pt(111) slab. This effect is also taken into account self-consistently by the LJ interaction. With the outlined setup, we were able to reliably simulate the properties of the Pt(111)/electrolyte interface and to assess the performance of the ESM-RISM for this system.

In the ESM-RISM, both the electrolyte–electrolyte and electrode–electrolyte interactions are described by classical interaction potentials (eq. 2.31). For the electrolyte species, both LJ parameters and charges for the Coulomb interaction are those of the modified TIP5P water model or taken from the literature for the electrolyte ions (see Section 5.3.1). The Coulomb interactions between the charges on the electrolyte species and on the electrode atoms depend on the charge density within the electrode computed by DFT [104]. In contrast, the LJ parameters of electrode atoms (Pt, O) have to be chosen manually. These parameters determine the electrode–electrolyte gap and the distribution of electrolyte at the interface via the correlation functions and closure relation. The choice of LJ interaction parameters for electrode atoms is not straightforward, since these are generally not transferable from one system to another. There is also only limited information on these parameters [367, 402]. We therefore tested different LJ parameterizations for the Pt atoms (see Table 5.2) and compared electrolyte distribution functions at the Pt(111)/water interface to AIMD

data [69, 403]. Fitting of LJ parameters to AIMD distribution functions is one way to improve the accuracy of the ESM-RISM. Such an approach has been used recently to derive the LJ parameters for a Cu(100) electrode [175].

Table 5.2.: Different applied Lennard-Jones (LJ) parameters for the electrode Pt atoms. Reprinted with permission from [391], published by IOP Publishing under the Creative Commons Attribution 4.0 licence.

	ε_{Pt} [kcal/mol]	σ_{Pt} [Å]
Interface Force Field (IFF) [367, 402]	7.80	2.53
Universal Force Field (UFF) [404]	0.08	2.45
Pt–Xe interaction [122]	1.66	2.65

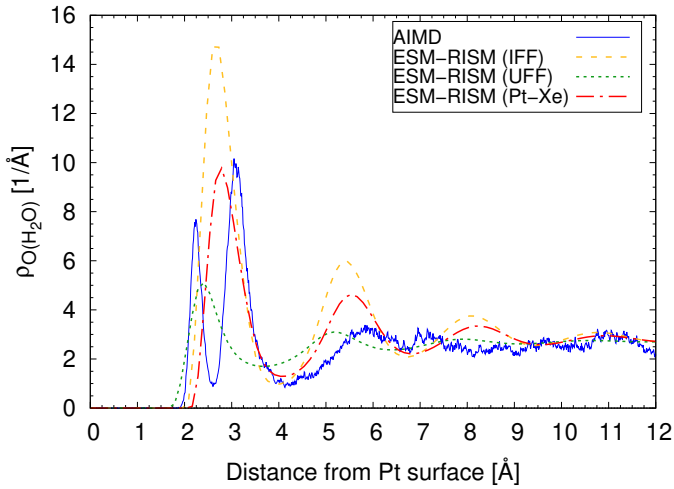

Figure 5.6.: Water density distribution functions at the Pt(111)/water interface computed with the ESM-RISM using different LJ interaction parameter sets for Pt (see Table 5.2). The water density distribution is a function of the distance from the outermost layer of Pt atoms. The position of water molecules is represented by the position of water oxygen atoms. AIMD data were taken from refs. [69, 403]. ESM-RISM calculations were performed at 300 K solvent temperature.

Figure 5.6 shows the interfacial water distribution functions computed with the different LJ parameter sets (see Table 5.2) and with AIMD simulations [69, 403]. These are plane-averaged density profiles, where the absolute values refer to the area of our surface unit cell, which is 82.34 Å. The ESM-RISM cannot reproduce the double peak structure (between 2 and 4 Å) obtained by AIMD [69, 137, 403, 405, 406]. This is because the double peak reflects the structured surface water layer that cannot be reproduced by a microscopically averaging integral equation approach as implemented in the RISM. Nevertheless, the overall shape of the distribution function is reproduced reasonably well, with the best match obtained with the LJ parameterization of Haruyama et al. [122], which had been used in the work of Fernandez-Alvarez and Eikerling [124], and was also used in all subsequently discussed calculations of this study. The width of the Pt(111)–water gap is very similar to the AIMD result (ca. 2 Å). The surface water layer in the ESM-RISM exhibits one

broad peak. Although it cannot quantitatively reproduce the bilayer AIMD feature (see discussion in the next section), its height and width are well consistent with the AIMD distribution, showing that the averaged near-surface water density and total width of the near-surface water layer are comparable. Overall, as in the pure water case (see Figure 5.5), the accuracy of the results is limited by the statistical character of the RISM: deviations from reference data are caused by local structuring of water that cannot be captured in this scheme. We also note that the simple LJ interaction potential is not optimal to describe the interatomic interactions quantitatively, and more sophisticated interatomic force-field schemes could further improve the performance of the ESM-RISM.

5.3.3. Quantum mechanically and classically treated parts of the system

Interface water structure

As seen before in Figure 5.6, the ESM-RISM (just like classical MD simulations, see Figure B.7) cannot resolve the double peak in the water density distribution at the Pt(111)/water interface that was obtained with AIMD simulations [69, 137, 405, 406]. This makes the ESM-RISM less useful for the computation of surface reactions, where the arrangement of water molecules around adsorbed electroactive reactants plays a vital role. One solution for more accurate modeling of electrochemical reactions in these cases is to explicitly simulate the reactants with their hydration shell. The problems of implicit water models with the adequate description of solvent effects at interfaces have already been realized in previous studies [66, 142, 162, 407, 408]. We thus tried to account for the local solvent effects within the ESM-RISM by including the first interfacial water layer into the explicitly treated DFT region.

The explicit water layer was modeled by a static ice-like hexagonal water bilayer, a model which is commonly employed in DFT calculations of the wetted Pt(111) surface [68, 409, 410]. Such a structure with 2/3 ML water coverage has been observed experimentally at low temperature and in the case of a single surface water layer formed in ultrahigh vacuum [411]. These studies determined the water layer to be almost flat, representing more of a monolayer than a bilayer. Static DFT studies reproduce this small water layer thickness [412, 413]. In contrast, AIMD simulations, that were performed at room temperature [69, 137, 405, 406], show the clear double peak (as depicted in Figure 5.6). We also notice that the areas of the two peaks composing the double peak are not identical, which is inconsistent with the perfect ice-like hexagonal water bilayer, where one half of the water molecules lie flatly on the surface and another half adsorb with H pointing towards the surface (H-down) or away from it (H-up). AIMD simulations show dynamic exchange between these two groups of water molecules [69] and between H-up and H-down configurations [406]. Sakong and Groß [69, 403] also observed rapid exchange of water molecules between the structured dynamic bilayer and the continuous, fluid-type water distribution (at distances larger than 4 Å).

Static DFT calculations cannot capture the dynamic nature of surface water layers. We thus considered the H-up and H-down configurations (see Figure 5.7) as limiting cases. Our focus was on the general effect of the explicit treatment of surface water molecules on interfacial properties computed by the ESM-RISM. Figure B.8(a) shows that with static ESM-RISM calculations a struc-

tured first interfacial water layer is reproduced reasonably well, with the double peak feature, which, however, does not exactly match the AIMD result. Nevertheless, the implicit water distribution couples smoothly to the explicit part and the second solvent peak (around 6 Å from the Pt surface) matches the AIMD results well (better than in simulations without the explicit water layer). The Pt–O(H_2O) distances in H-up and H-down configurations are slightly different, which is reflected by different positions of the double peaks using the two models. The true water orientation probably lies between these two limiting cases. These ESM-RISM calculations do not capture the exact separation between the two parts of the AIMD double peak. We notice, however, that reduced peak distances have been observed in other low temperature studies (far below 300 K), both experimental and computational [411–413], and may therefore be attributed to missing effects of thermal motion. ESM-RISM calculations thus yield an electrode–solvent gap that is slightly too large, which could affect computed interfacial properties. For comparison, we performed calculations with the z-coordinates of the oxygen atoms of the surface water bilayer fixed to the AIMD Pt-O(H_2O) distances. Figure B.8(b) shows that the so-obtained water distribution beyond the explicit layer (the part modeled by RISM) differs only slightly from that obtained using aforementioned setups.

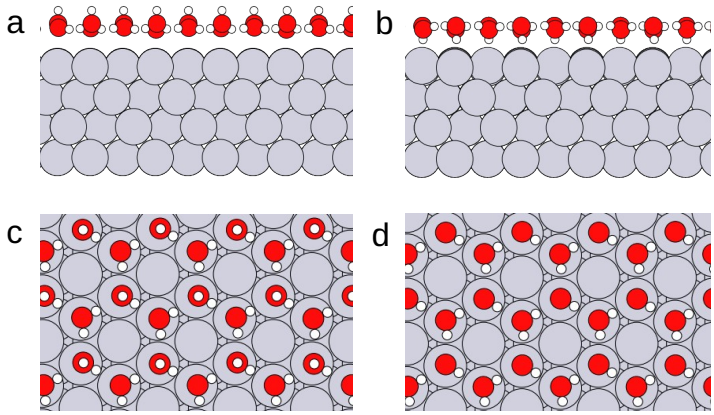

Figure 5.7.: Explicit surface water layer configurations, side and top views, for (a,c) H-up and (b,d) H-down configurations. Reprinted with permission from [391], published by IOP Publishing under the Creative Commons Attribution 4.0 licence.

Electrostatic potential at the interface

Figure B.9 illustrates the impact of the explicit water layer on the interfacial potential profile. Explicit treatment of near-surface water molecules leads to more pronounced peaks in electric potential. The potential at the outer Helmholtz plane (OHP) is also severely affected (see also Section 5.3.4). Fixing the positions of explicit water molecules to the AIMD positions results in a different potential profile (see Figure B.9(b)), which reflects the distinct double peak in the surface water distribution (see Figure B.8(b)). On the other hand, the potential profile beyond the explicit layer is hardly affected; it depends mainly on the position of the outer layer of the explicit double peak, which is very similar for both setups. The orientation of the hydrogen atoms (H-up vs. H-down) has a much larger effect on the potential profile beyond $\sim$3.5 Å from the Pt surface.

An explicit water layer is also important to reproduce the measured decrease of the work function of the wetted Pt(111) surface [414–416]. As shown in Table 5.3, the implicit RISM solvent alone underestimates the change in the work function. This is due to the missing effects of surface water dipole orientation and polarization, i.e. interfacial charge transfer between surface water and Pt, which is captured only when the surface water molecules are computed explicitly [368, 410, 416]. Indeed, the best result is obtained with an explicit water layer in H-up configuration. The difference in the predicted work function shift with H-up and H-down explicit water layers arises from different dipole orientations in the two model cases, as found in other DFT studies [410, 416]. It dominates over the polarization effects for H-up and H-down configurations [416]. Nevertheless, AIMD simulations indicate that, when performing time averaging over different water configurations realized in the simulations, and thus averaging the dipole orientation, the polarization contribution is also an important factor [368].

Table 5.3.: Work function change vs. vacuum for the Pt(111) surface in water solvent. The work function is computed here as the difference between the Fermi level of the surface slab and the electrostatic potential in bulk solvent. This procedure deviates from the original definition of the work function, which defines it as the energy required to take an electron from the bulk of the metal to (electric-field free) vacuum. Reprinted with permission from [391], published by IOP Publishing under the Creative Commons Attribution 4.0 licence.

Setting	$\Delta\Phi$ [eV]
Implicit water	-0.23
Implicit + 1 explicit layer (H-up)	-1.25
Implicit + 1 explicit layer (H-down)	-0.26
Experiment	-1.02 [414], -1.2 [415]

The above discussion indicates that explicit treatment of the surface water layer is required to obtain a correct interfacial water structure with the ESM-RISM. Describing the interaction between Pt and near-surface water molecules at the level of DFT is crucial in order to reproduce the realistic surface structure and interfacial electrostatic potential. The impact of the explicit water layer on other properties of the interface region will be discussed in the next section.

5.3.4. Potential at the outer Helmholtz plane

Experiments show that with an increase in applied electrode potential, an oxide layer forms at the Pt(111) surface [45]. It is thus important to take into account the oxygen coverage to correctly model electrochemical reactions at the Pt(111) surface. It impacts the electrolyte interfacial structure, solvent molecule orientation and local electrostatic potential. When computing the potential at the outer Helmholtz plane we therefore considered partially oxidized Pt(111) surfaces with oxygen coverages between 0 and 2/3 ML. The electrolyte consists of aqueous HCl with a concentration of 0.1 mol/L.

The theoretical description of electrocatalytic reactions requires knowledge of the electrostatic potential profile across the interface. The inner Helmholtz plane (IHP) is the first layer of adsorbed

water and specifically adsorbed electrolyte ions, which is represented by the first peak in the solvent distribution functions in the ESM-RISM (see e.g. Figure 5.6). The outer Helmholtz plane (OHP) is constituted by the first layer of non-specifically adsorbed (solvated) ions and the second water layer at the interface, and therefore is represented by the second peak in solvent distribution functions. The Helmholtz planes are important reaction planes for electrochemical reactions and the electrochemical conditions at their positions have to be known precisely. The potential at the OHP depends on near-surface solvent and electrolyte distribution and orientation, as well as on the oxygen coverage of Pt(111) and the metal surface charge. It is thus a suitable property to probe local reaction conditions at the interface. Therefore, we evaluated the interfacial potential profile computed by the ESM-RISM. We note that results of similar evaluations have been published before [124, 377] and here we compare our results with the outcome of those studies. Figure 5.8 shows the way the potential at the OHP is determined from the local interfacial potential profile. Our aim here is to assess the impact of ESM-RISM input variables and explicit treatment of surface water molecules on the value of the potential at the OHP.

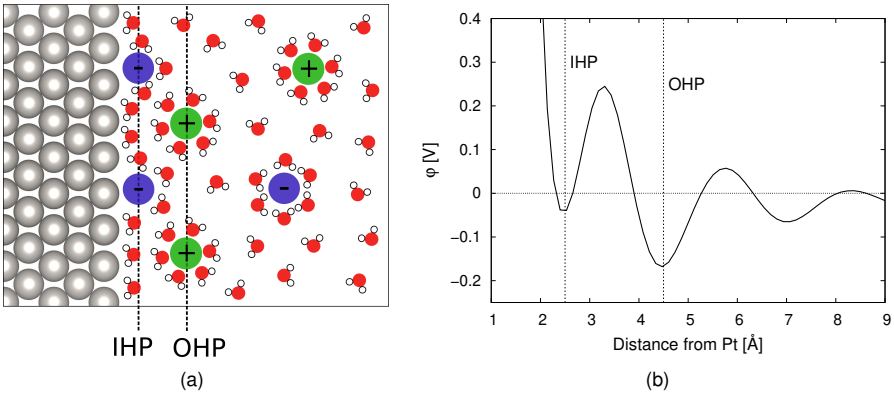

Figure 5.8.: (a) Schematic representation of inner (IHP) and outer (OHP) Helmholtz planes at the Pt(111)/electrolyte interface. (b) Plane-averaged local potential at the bare Pt(111)/electrolyte interface, computed with the ESM-RISM. Reprinted with permission from [391], published by IOP Publishing under the Creative Commons Attribution 4.0 licence.

Figure 5.9 shows the electrostatic potential at the outer Helmholtz plane as a function of oxygen coverage. We note that different adsorption geometries of adsorbed oxygen atoms result in slightly different values of potential at the OHP as computed with the ESM-RISM (± 0.05 V). However, the trends as a function of potential are not affected. The potential at the OHP vs. oxygen coverage shows a non-monotonic behavior, as observed in previous DFT studies [124] and a mean-field approach by Huang et al. [44]. The differences from the previously published ESM-RISM results in ref. [124] stem from differences in the computational setup, namely from differences in the starting position of solvent, as we discussed in Section 5.3.2.

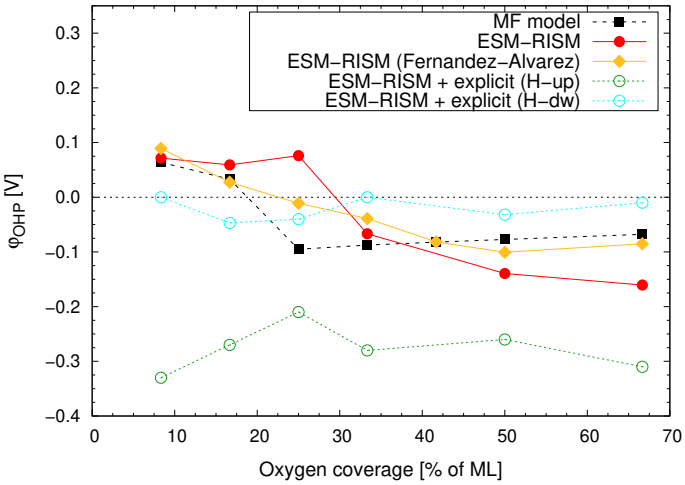

Figure 5.9.: Potential at the outer Helmholtz plane for the oxidized Pt(111)/electrolyte interface (c(HCl) = 0.1 mol/L). Mean field (MF) model by Huang et al. [377]. ESM-RISM results (implicit electrolyte only) with smaller DFT cell length and `laue_starting_right` parameter obtained from energy minimization by Fernandez-Alvarez and Eikerling [124]. Curves obtained with one explicitly treated water layer in H-up and H-down configurations are shown as well. Reprinted with permission from [391], published by IOP Publishing under the Creative Commons Attribution 4.0 licence.

Figure 5.9 also illustrates the influence of an explicitly treated surface water layer on the outer Helmholtz potential. For the H-up configuration, the absolute potential at the OHP is much larger than in case of the H-down configuration and in the calculations with implicit electrolyte only. The explicit computation of the interfacial water structure seems to have a major impact on the electrolyte ion distribution near the interface and thus on the corresponding interfacial potential profile. As discussed before, the H-up and H-down structures can be considered as limiting cases of the real structure; the realistic outer Helmholtz potential is thus expected to lie between the H-up and H-down results. The overall agreement with the mean field model is not improved by the inclusion of the explicit water layer. This can be related to the fact that the explicit layer in our simulation setup does not contain charged species, which would significantly contribute to shaping the structure of the double layer. More sophisticated modeling is required to understand the differences between the results from the different approaches.

As shown in Figure 5.9, the different setups including calculations with the explicit water layer result in different values of the potential at the OHP. However, all predictions show a non-monotonic behavior, which is also seen in the measured metal charging relation [379]. This shows that the potential-dependent oxygen coverage at Pt(111) causes the peculiar non-monotonic effects on the interfacial potential. Note that the potential at the OHP as considered here is an average over the plane perpendicular to the Pt surface. Variations in this plane are of course possible, but not resolved here. This is one aspect that hinders a more detailed comparison between the results from different simulation setups and models. To include the effects of an applied potential – beyond the resulting oxygen coverage – we applied the ESM-RISM potentiostat to perform grand canonical

calculations, as described in the next section.

5.3.5. Grand canonical ESM-RISM simulations and metal charging relation

Table 5.4.: Oxygen coverage as a function of the applied electrode potential as computed by the mean field model by Huang et al. [377]. The pzc is 0.3 V vs. SHE. 1 monolayer (ML) of oxygen coverage corresponds to 12 adsorbed atoms per unit cell. Reprinted with permission from [391], published by IOP Publishing under the Creative Commons Attribution 4.0 licence.

# ads. O atoms	coverage [% of ML]	φ_M vs. SHE [V]
0	0	0.30
0	0	0.45
0	0	0.55
1	8.3	0.65
2	16.7	0.73
3	25.0	0.85
4	33.3	0.90
6	50.0	0.96
8	66.7	1.00
9	75.0	1.10

We used the potentiostat scheme included in the ESM-RISM implementation, which allows to apply a potential in the grand canonical ensemble and thus compute realistic electrochemical interfaces at a given electrode potential [109]. In this framework, the resulting charge of the metal slab is compensated by the electrolyte charge of equal size and opposite sign.

For the case of the partially oxidized Pt(111)/electrolyte interface, the oxygen coverage can be pinned to the metal potential by using the experimental surface coverage-vs-potential data [124, 377]. Following the mean field model [377], we assume that the uncharged bare Pt(111) surface corresponds to the potential of zero charge (pzc), which is 0.3 V vs. SHE. The functional relationship between oxygen coverage and potential is summarized in Table 5.4. Only when taking into account both the applied potential and the corresponding oxygen coverage, the realistic conditions at the Pt(111)/electrolyte interface can be reproduced. The calculations with applied potential were performed here assuming implicit aqueous HCl electrolytes with concentrations of 0.1 and 1 mol/L.

Charge analysis of the oxidized Pt(111) surface slabs showed that charges are entirely located at surface Pt atoms and adsorbed O atoms. This corresponds to the expected and realistic charge distribution.

Figure 5.10 shows the computed surface ion density profiles for the different applied potentials for Cl^- and H_3O^+ ions in the electrolyte. As reported above for the Au(111)/electrolyte interface, the different peaks represent the alternating charged layers of electrolyte ions at the interface. The obtained trends clearly reflect the electrostatic effects of the positive slab charge (representing the positively charged Pt electrode). For example, a depletion of H_3O^+ ions in the interface region with increasing positive electrode charge is clearly visible.

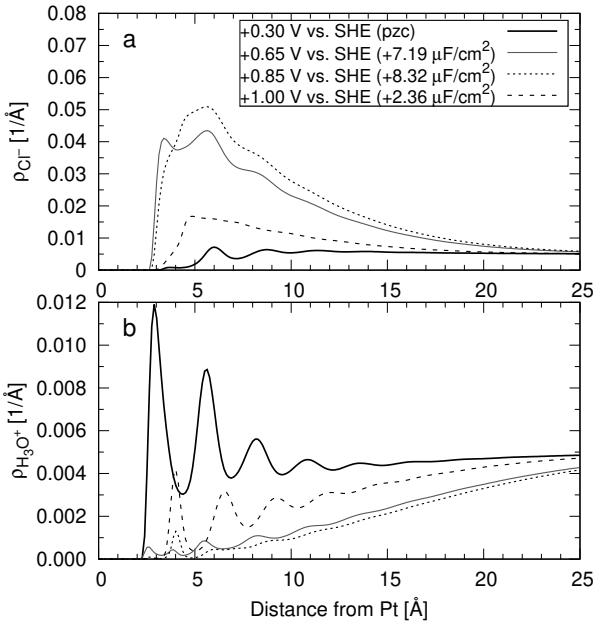

Figure 5.10.: Density profiles for (a) Cl^- and (b) H_3O^+ electrolyte ions (c(HCl) = 0.1 mol/L) at the Pt(111)/electrolyte interface computed with the ESM-RISM at different electrode potentials. Surface charges per area are given in brackets. The Pt(111) surface is partially oxidized according to the applied potential; for coverages see Table 5.4. Data for all computed potentials are available in Figures B.10 and B.11. Reprinted with permission from [391], published by IOP Publishing under the Creative Commons Attribution 4.0 licence.

The electrode charges per area of the oxidized Pt(111) surface at different potentials are shown in Figure 5.11. The metal charge as a function of the electrode potential exhibits a non-monotonic trend, which was also observed in seminal experiments by Frumkin and Petrii [379]. Vital features of the so-called surface or metal charging relation, i.e. σ plotted as a function of φ_M, are in agreement with predictions by the mean-field (MF) model of Huang et al. [44] (dashed lines in Figure 5.11) and experimental data [379]. As the electrode potential increases from the pzc, the surface charge density increases monotonically, reaching a maximum at 0.8 V vs. SHE (at 0.55 V vs. SHE in the original MF model [44], black dashed line in Figure 5.11). Upon further increase of φ_M, σ decreases to a minimum at 1.0 V vs. SHE (0.8 V vs. SHE in the original MF model). This decrease in surface charge allows electrolyte cations, like H^+ ions, to approach the surface at elevated potentials, instead of being repelled for electrostatic reasons. These local reaction conditions are crucial e.g. for oxygen redox reactions, which use H^+ as a reactant. This is an additional hint that the surface charging relation must follow a non-monotonic trend. We notice that the second pzc, as measured [379] and reproduced by the MF model [44], is not seen with the ESM-RISM.

For comparison, Figure B.12 depicts the metal charging relation for the non-oxidized Pt(111)/electrolyte interface. For the bare electrode surface, a linear metal charging relation is obtained, as obtained above for the Au(111)/electrolyte interface. This behavior reflects charge accumulated in the double layer and is well consistent with the double layer charge contribution to the total charge,

as modeled by Huang et al. [44]. At small electrode potentials (below ca. 0.6 V vs. SHE, where the oxygen coverage is zero), the double layer capacitance for the Pt(111)/electrolyte interface can be estimated from the slope of the metal charge per area vs. applied potential. This simple estimate yields an interfacial capacitance of 24 μF/cm^2 for an electrolyte concentration of 0.1 mol/L. This value is in agreement with the experimental value of 20 μF/cm^2 [57] and results of other computational studies [120]. As shown already for the Au(111)/electrolyte interface, the ESM-RISM reproduces the linear capacitive response of metals that are not covered with adsorbates. We note, however, that bare Pt(111) surfaces do not exist in the full potential range considered here, but only below ca. 0.6 V vs. SHE.

Huang et al. [44] attributed the non-monotonic charging behaviour, with a second pzc at about 0.75 V vs. SHE, to the impact of surface oxide dipoles. Our results from the ESM-RISM support this interpretation, since without the surface oxide layer the peculiar non-monotonic shape of the metal charging relation is not reproduced (see Figure B.12). The decrease in surface charge could be related to increasing shielding of electrolyte ions by increasing amounts of oxygen species at the surface. Balancing of surface charge by electrolyte ions is hindered by the oxide layer, so that the surface charge cannot increase. Further, in the MF model, the increase in charge for potentials higher than 0.8 V vs. SHE is explained by saturation of oxide species at the Pt surface [44]. The quantitative disagreement in metal charging relations between the ESM-RISM and the original MF model indicates that potential effects are screened differently in the two approaches. In this regard, the blue dashed line in Figure 5.11 illustrates the sensitivity of the interfacial potential distribution and surface charging to the parameterization of the MF model. With a decreased parameter for the fractional charge number of the oxide dipole, the MF model can be reparameterized such that the surface charges agree with those from the ESM-RISM. More recent studies also show that this parameter should be smaller than in the original MF model [417], and our ESM-RISM results confirm this. As a first principles approach, the ESM-RISM can also be used to validate the MF model and its parameterization.

Still, differences between the ESM-RISM and the MF model in potential screening by the oxide layer, but also by the layer of interfacial water dipoles or the diffuse ionic layer are possible and should be evaluated in more detail in follow-up studies. Both, the ESM-RISM and the MF model rely on assumptions and approximations about structural organization and polarization effects in the interface region. These assumptions will have to be scrutinized and fine-tuned in future work. However, the quantitative agreement between the approaches that has been achieved to date is encouraging. The crucial role of surface oxide formation in determining interface properties and local reaction conditions is clearly evident.

An additional analysis shows that including the electrolyte solution in the ESM-RISM simulations indeed is crucial, as expected. As shown in Figure 5.11, neglecting the electrolyte solution leads to surface charges that are about two orders of magnitude too small. We also note that the metal charging relation was computed successfully, although we did not include explicit water layers in these calculations, i.e. detailed features of the near-surface water structure were not resolved (see above). When including explicit water layers, another problem arises: electrolyte ions are excluded from this water layer, so that they cannot come arbitrarily close to the metal surface. This would

potentially lead to a spurious charging behavior of the interface.

Future studies should include the possibility of other electrolyte species to adsorb at the surface. For example, Cl^- ions are known to adsorb at Pt(111), potentially competing with oxygen species [418]. Cl^- ions are also present in our ESM-RISM simulations, but were treated as part of the RISM region and thus could not adsorb at the surface in our setup.

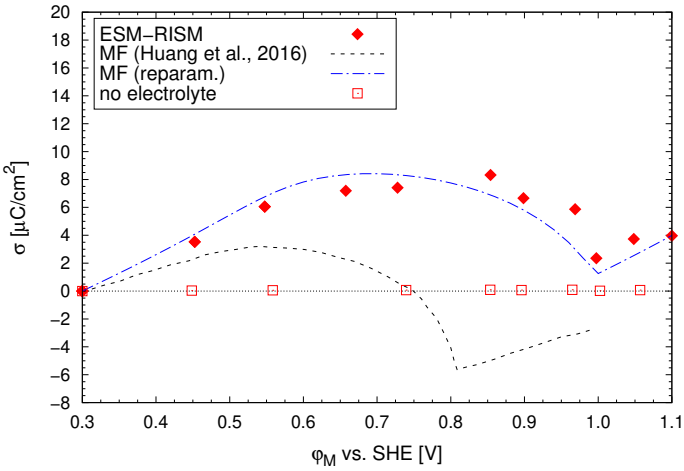

Figure 5.11.: Surface charge vs. electrode potential for the oxidized Pt(111)/electrolyte interface with 0.1 mol/L HCl concentration. The oxygen coverages for the different potentials are those from Table 5.4 (slight deviations arise from the charge optimization procedure). For potentials higher than 1.0 V vs. SHE, we performed calculations with oxygen coverages of both 66.7 % and 75.0 %, because oxygen coverages larger than 66.7 % tend to favor Pt dissolution [56, 378]. The impact on the results was insignificant. Data for the mean-field model (MF) by Huang et al. [44] at pH 1.2 (black dashed line) and from the MF model reparameterized with a smaller fractional charge number of the oxide dipole (blue dashed line). The square symbols show data computed in the grand canonical ESM framework, but without the RISM electrolyte (in vacuum).

5.4. Conclusion

We presented an in-depth evaluation of the abilities of the ESM-RISM to reproduce properties of ECIs. As demonstration cases, we studied the interfaces between Au(111) as well as partially oxidized Pt(111) surfaces and acidic aqueous electrolytes, computing properties that reflect local reaction conditions at the interfaces. The grand canonical potentiostat enabled us to model the interface under applied potential, not restricted to potentials around the pzc.

We have shown that interface properties are highly sensitive to the choice of geometric setup for the calculation and choice of interaction parameters. The results depend on the parameterization of the electrode–electrolyte interactions, described with Lennard-Jones potentials in the ESM-RISM, which determine for example the electrode–electrolyte gap. The interaction parameters were selected to reproduce the AIMD interfacial solvent density profiles. We also demonstrated for the

Pt(111)/electrolyte interface that the structured interfacial water layer has to be explicitly computed at the level of DFT in order to capture detailed features of the interfacial electrolyte structure. The implicit electrolyte, as modeled by the RISM, smoothly couples to the explicit water layer and such a hybrid approach consistently describes the electrolyte structure. We were thus able to identify a setup in which the ESM-RISM gives reliable results, which was adopted in follow-up studies (see Chapter 6).

In contrast to standard cavity-based continuum solvation models, the ESM-RISM provides more realistic electrolyte distribution functions at the interface. The method also accounts for the electrolyte pH and temperature, while being computationally relatively efficient. The method proved to be well suited to control the electrode potential and describe the chemisorption and charging state of the interface, while the potential-dependent oxygen coverage of the Pt(111) surface had to be included manually. The potential in the bulk electrolyte served as a reference potential and could be related to the SHE scale via the potential-dependent oxygen coverage or the computed pzc. The counter charge is correctly represented by electrolyte ions, so that we were able to obtain the structure of the electrical double layer at the charged interface. Regarding electrochemical parameters, the ESM-RISM framework reproduces the effect of a surface oxide layer on the outer Helmholtz potential. By accounting for the oxide layer, we were able to reproduce the non-monotonic metal charging relation that is known from experiments for the partially oxidized Pt(111)/electrolyte interface.

The main drawback, next to the dependence on parameterization, is that the RISM is an implicit electrolyte model that does not provide any information on the electronic configuration of the electrolyte and its structure is described only in an average, statistical way. Electroactive molecules that undergo reactive processes at the metal surface must be considered explicitly at the quantum mechanical level, i.e. as part of the DFT region. However, AIMD simulations based on the ESM-RISM are prohibitively costly for the studied interfaces.

The question arises if the ESM-RISM can be termed a self-consistent interface model. The method couples electrode and electrolyte regions by a Lennard-Jones plus Coulomb interaction potential, resulting for example in the correct electrode–electrolyte gap. Electrolyte, pH, T, and electrode potential are treated self-consistently. Nevertheless, effects like adsorption of electrolyte species at the electrode demand more sophisticated simulations or need to be included manually. However, including all these effects, the method is superior to many other, more simplified, DFT-based interface methods.

The thorough testing of the ESM-RISM for the two metal/electrolyte interfaces indicates that when correctly set up, this method can result in a quantitative level prediction of properties of ECIs. This includes the structure of the double layer, the interfacial potential variation and the surface charging relation. Comparison with independent theoretical models and explicit simulations of the interface showed strengths and limitations of the ESM-RISM for modeling of ECIs.

6. Properties of NiOOH electrocatalysts in electrochemical conditions

In this chapter, we combine the two approaches studied in this thesis, the DFT+U(WF) approach and the ESM-RISM, to investigate nickel oxyhydroxide (NiOOH) surfaces as catalysts for the alkaline oxygen evolution reaction (OER). Our aim is to contribute to an improved understanding of factors influencing the catalytic activity by describing the catalyst/electrolyte interface under electrochemical reaction conditions as accurately as possible. This study was possible only with the DFT+U(WF) approach, since the standard DFT+U approach incorrectly predicted a metallic state for this semiconducting material. We focus on the effects of including an electrolyte solution and an electrode potential in the simulations by the grand canonical ESM-RISM and compare to simulations with the simple computational hydrogen electrode (CHE) scheme. We discuss thermodynamic overpotentials for the OER and surface charging relations for the semiconductor/electrolyte interface. We show that double layer charging seems to be of minor importance, so that the CHE scheme gives satisfying results for overpotentials. In contrast, potential-dependent surface deprotonation causes significantly varying local properties near the catalytically active sites. Our studies provide a solid basis for follow-up studies of complex NiOOH/electrolyte interfaces.
The research described in this chapter was performed by myself under the guidance of Dr. Piotr Kowalski and Prof. Michael Eikerling. Dr. Zhengda He and Dr. Mohammad J. Eslamibidgoli assisted with the initial setup for simulations of β-NiOOH interfaces and performed the simulations of reaction free energies in vacuum reported in ref. [290] and used here for comparison.

6.1. Introduction

The oxygen evolution reaction (OER) is a technologically highly relevant electrochemical reaction, e.g. as part of the water splitting reaction for hydrogen production. However, more active and stable catalyst materials need to be found for this reaction, since existing ones show slow kinetics or poor long-term stability [419]. Nickel (oxy)hydroxide materials are considered as promising catalysts for the OER in alkaline conditions due to their high efficiency and Earth-abundance, as opposed to e.g. Pt or IrO_2 catalysts. But to date, they also exhibit large overpotentials and poor long-term stability [420]. Recent research efforts try to overcome these problems.

This research is complicated by the fact that nickel (oxy)hydroxide materials are very complex ma-

terials with many phenomena potentially influencing the catalytic activity. Open questions concern e.g. the bulk and surface structure, the role of defects, the OER mechanism and the catalytically active phase [421]. Nickel (oxy)hydroxides can exist in four different layered phases which transform into each other under electrochemical conditions, as depicted in Bode's diagram [422]: β-Ni(OH)$_2$, β-NiOOH, γ-NiOOH and α-Ni(OH)$_2$. As done before in DFT studies [70, 90], we here use the simpler β-NiOOH phase to model the catalytically active [294] γ-NiOOH phase, which is too complex to model due to intercalated water layers.

DFT-based studies of β-NiOOH have difficulties to correctly represent the band gap of the material (experimental value: 1.7–3.75 eV [302–304]) even with the DFT+U method and relatively large Hubbard U parameter values. Computationally demanding hybrid functionals are required to correctly capture the electronic structure. In Section 3.4 of this thesis, we showed that the DFT+U(WF) can be used alternatively and enabled breakthrough studies of Fe spin states in Fe-doped β-NiOOH [290]. Only with a correct electronic structure description, the analyses performed in this chapter became possible, since we needed to correctly capture the semiconducting state of β-NiOOH. As a semiconductor/electrolyte interface, the β-NiOOH(001)/electrolyte interface studied here will have different properties from a metal/electrolyte interface. For example, electrolyte ion distributions in the interface region differ, because of the diffuse charge distribution in the semiconducting electrode (see Chapter 1).

In this chapter, we combine the two methods studied so far, the DFT+U(WF) approach and the ESM-RISM, to study β-NiOOH(001)/alkaline electrolyte interfaces. Both methods proved to be accurate and relatively efficient in the previous chapters, so that we hope to gain an enhanced understanding of interface processes and effects on catalytic activity of β-NiOOH. We will analyze the importance of potential and electrolyte effects on the OER. Our aim is to consistently describe the state of the catalyst and related local reaction conditions under electrochemical conditions, including potential-dependent surface deprotonation. We will also compare the grand canonical ESM-RISM to the simple computational hydrogen electrode (CHE) approach.

6.2. Computational details

The simulations were performed with the ESM-RISM [104] both with and without applied potential. The ESM-RISM setup was adopted from Chapter 5. The DFT cell height in z-direction was 40 Å. The Lennard-Jones parameters for Ni ($\epsilon = 5.65$ kcal/mol and $\sigma = 2.274$ Å) were selected from the Interface Force Field [367] and resulting surface water distribution functions showed to agree well with AIMD simulations [423]. The other parameters were the same as in Chapter 5. The electrolyte was a 0.1 mol/L KOH solution, corresponding to typical experimental conditions [125, 424, 425]. The electrolyte was simulated at 300 K. Electrode potentials computed with the grand canonical ESM-RISM potentiostat [109] were related to the SHE scale by subtracting the absolute potential of the SHE, 4.44 eV [123], from the computed work function of the respective OER intermediate and adding this constant to the potential vs. pzc.

We used the PBE functional [205] in the DFT+U(WF) scheme described in Chapter 3 with $U = 5$ eV.

Electronic structure results for β-NiOOH were described in detail in Section 3.4. We first relaxed the structures with atomic orbital projectors. In a second step, single point calculations with Wannier projectors were performed using the "Poor Man's Wannier scheme" (pmw.x tool) provided by QuantumESPRESSO. The bands for the Wannierization procedure were chosen such that the d-orbital occupations were closest to the expected ones. We employed ultrasoft pseudopotentials with the following valence electrons computed explicitly: Ni $3d^8 4s^2$, O $2s^2 2p^4$ and H $1s^1$. Including $3s$ and $3p$ electrons for Ni did not affect our results. The plane wave cutoff was 80 Ry and the k-point mesh was a $4\times4\times1$ Monkhorst–Pack mesh [218]. The calculations were spin-polarized.

The β-NiOOH(001) surface (also called β-NiOOH(0001) surface in the literature) was modeled by 3-layers slabs with a 2×2 surface unit cell (see Figure 6.1). The (001) facet has been found to be the predominant surface configuration under electrochemical conditions [306, 426]. The slab setup was asymmetric, with the RISM electrolyte on the right side of the slab only (compare to Figure 5.4). The OER was modeled only on this side of the slab. Deprotonation was modeled by removing one or two hydrogen atoms per surface unit cell. Water and hydrogen molecules were computed in cubic boxes of 20 Å side length and at the Γ point. The atomic structures were relaxed until thresholds of 10^{-4} Ry and 10^{-3} Ry/a_0 (where a_0 is the Bohr radius) were obtained for energy and forces, respectively.

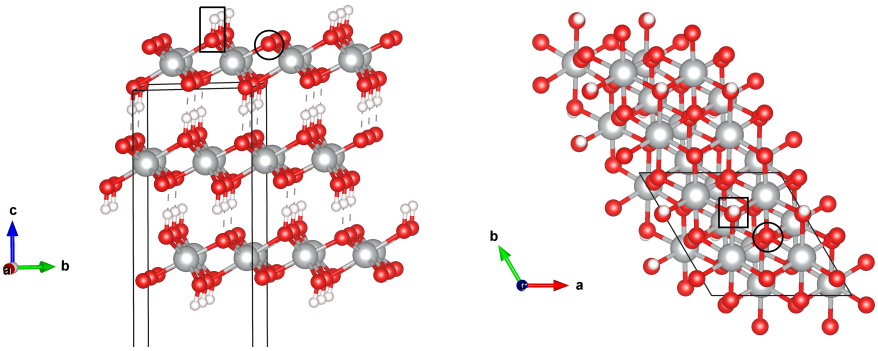

(a) side view (b) top view

Figure 6.1.: 3-layers stoichiometric β-NiOOH(001) slab model used in the DFT+U calculations. Red: oxygen, white: hydrogen, grey: nickel atoms. Black lines: unit cell (DFT simulation cell). Black circles and rectangles indicate the reaction sites for the R1 and R2 OER paths, respectively (see eqs. 6.2 and 6.3).

6.3. Electrolyte effects on reaction free energies and overpotentials

First, we aimed to study effects of an alkaline electrolyte, as simulated by the RISM, on predictions for catalytic activity. For this purpose, we computed reaction free energies and thermodynamic overpotentials for the two most plausible reaction paths of the OER catalyzed by β-NiOOH(001) electrodes. Even if the thermodynamic overpotential, derived from the potential-determining step

(PDS) is not always a reliable measure for reaction rates and catalytic activity (see Chapter 1), it allows to readily compare simulations without and with electrolyte effects included. Potential effects were included using the CHE scheme.

The overall reaction equation for the OER, assuming a 4-electron transfer mechanism, is

$$2\,H_2O \longrightarrow O_2 + 4\,H^+ + 4\,e^- \,. \tag{6.1}$$

Various reaction mechanisms have been proposed for this reaction [421]. For the β-NiOOH(001) facet, two of them, involving lattice oxygen atoms, have been studied in detail by Rajan et al. [70] and in our previous work [290]. Within these paths, we only considered the first two reaction steps, since one of these was identified to be the PDS or to have a reaction energy very close to the one of the PDS [70]. The considered reaction paths are formulated here in alkaline conditions, as present in experiments, where * denotes an adsorption site on the surface:

Reaction path 1 (R1):

$$\begin{aligned} &\text{step 1: } {}^*O + OH^- \longrightarrow {}^*OOH + e^- \\ &\text{step 2: } {}^*OOH + OH^- \longrightarrow {}^*O_2 + H_2O + e^- \end{aligned} \tag{6.2}$$

Reaction path 2 (R2):

$$\begin{aligned} &\text{step 1: } {}^*OH + OH^- \longrightarrow {}^*O + H_2O + e^- \\ &\text{step 2: } {}^*O + OH^- \longrightarrow {}^*OOH + e^- \end{aligned} \tag{6.3}$$

Note that the *O and *OH intermediates involved in step 1 of the R1 and R2 paths, respectively, both correspond to the stoichiometric β-NiOOH(001) surface, but the following reactions occur at different reaction sites (see Figure 6.1).

The CHE formalism and the derivation of thermodynamic overpotentials were described in Chapter 2. The CHE scheme is typically formulated in acidic conditions and relies on the relation

$$\mu_{H^+} + \mu_{e^-} = \frac{1}{2}\mu_{H_2(gas)} - eU_{SHE} \,. \tag{6.4}$$

The same relation can be used in alkaline media, when assuming equilibrium between water and dissociated ions. For example, for a reaction step like

$${}^*O + OH^- \longrightarrow {}^*OOH + e^- \,, \tag{6.5}$$

the reaction free energy is computed as:

$$\Delta G = \mu_{{}^*OOH} + \mu_{e^-} - \mu_{{}^*O} - \mu_{OH^-} \tag{6.6}$$

$$= \mu_{{}^*OOH} - \mu_{{}^*O} - \mu_{OH^-} + \mu_{e^-} \,. \tag{6.7}$$

Assuming an equilibrium $H_2O(l) \longleftrightarrow OH^- + H^+$, we can use:

$$\mu_{H_2O(l)} = \mu_{OH^-} + \mu_{H^+} \tag{6.8}$$

$$= \mu_{OH^-} - \mu_{e^-} + \mu_{H^+} + \mu_{e^-} \tag{6.9}$$

$$\Leftrightarrow \mu_{OH^-} - \mu_{e^-} = \mu_{H_2O(l)} - (\mu_{H^+} + \mu_{e^-}) \tag{6.10}$$

With this, we are able to formulate the reaction free energy in terms of μ_{H+} and μ_{e^-}, thus using the CHE formalism to include potential effects in alkaline media. For the above example reaction (eq. 6.5), the reaction free energy thus reads:

$$\Delta G = \mu_{*OOH} - \mu_{*O} - \mu_{H_2O} + (\mu_{H^+} + \mu_{e^-}) \tag{6.11}$$

$$= \mu_{*OOH} - \mu_{*O} - \mu_{H_2O} + (\frac{1}{2}\mu_{H_2} - eU_{SHE}) \, . \tag{6.12}$$

Reaction free energies were computed from equation 2.25, in analogy to what we did in ref. [290]. The values for zero point energy and entropy contributions were taken from ref. [12]. The results are reported in Table 6.1, together with the thermodynamic overpotentials η computed in the CHE framework. The latter were obtained by subtracting 1.23 V from the reaction free energy of the PDS, divided by the electron charge e (see equation 2.26).

Table 6.1.: Gibbs free energies of reaction, ΔG, and thermodynamic overpotentials, η, for the first steps of the OER at the β-NiOOH(001) surface, in vacuum and in RISM aq. 0.1 mol/L KOH electrolyte. Values in eV. $\Delta\Delta G$ denotes the difference between energies in vacuum and in electrolyte.

OER path	step	ΔG (vacuum)	ΔG (electrolyte)	$\Delta\Delta G$
R1	1	2.72	3.16	+0.44
		(η = 1.49 V)	(η = 1.93 V)	
	2	1.74	1.61	−0.13
R2	1	1.17	1.28	+0.11
	2	2.22	2.57	+0.35
		(η = 0.99 V)	(η = 1.34 V)	

The values for ΔG obtained here for the vacuum case differ slightly from those in ref. [290], since ESM-RISM calculations were performed with an asymmetric surface slab. The PDS is the first reaction step for the R1 path and the second reaction step for the R2 path, as obtained in ref. [290]. Rajan et al. [70] found the PDS to be the first reaction step also for the R2 path, but with a difference of only 0.03 eV in reaction free energy compared to the second step. The PDS does not change when including the alkaline electrolyte in the simulation, but the thermodynamic overpotentials increase significantly by ca. 0.4 V. These overpotentials are much larger than measured ones of 0.5-0.7 V [294, 427]. It should also be kept in mind that thermodynamic overpotentials are not equivalent to kinetic overpotentials, but provide only a lower bound. Simulations in vacuum provide results closer to the measurements. This can be attributed to error cancellation in vacuum simulations or to deficiencies of the RISM electrolyte description (see below).

Similarly, for the R2 reaction path, the sum of the reaction energies of the two reported steps is

expected to be close to 3.2 eV, related to the scaling relation between the adsorption energies of OH and OOH species known from DFT calculations [428]. Our value computed in vacuum calculations is close to this, but the RISM electrolyte increases the sum to 3.85 eV. Solvation typically does not have such a large effect on this relation [429, 430].

The RISM electrolyte description yields contributions to reaction free energies between -0.13 and $+0.44$ eV. These numbers are much larger than those obtained from continuum solvation models (CSMs). With a water solvent description by the VASPsol model, Rajan et al. [70] obtained an energy contribution of just 0.09 eV for the β-NiOOH(001) system. Other studies have shown that the effects of continuum water descriptions are generally small and often do not even offer an improved description compared to vacuum studies [162]. In contrast, explicit water models produce reaction energy contributions for oxygen redox reactions at NiOOH phases between 0.2 and 0.7 eV [292, 431, 432]. Explicit water models capture effects of surface polarity and direct interaction with the solvent much better than CSMs. However, the implicit and explicit models cited so far focused on the water description and neglected electrolyte ions. Martirez and Carter [433] included electrolyte ions in the implicit model in their study of β-NiOOH and obtained surface energies that were close to those obtained with an explicit model. Electrolyte ions can have significant effects on reaction energies, in particular at high pH and high concentrations. This could be one explanation for the large energy contributions we obtain in our ESM-RISM calculations, where electrolyte ions are included as a substantial part of the model and can also correctly form the electrical double layer, i.e. localize or deplete at the interface. On the other hand, these large energy contributions could also be related to unphysical behavior of this model. For example, it uses the same Lennard-Jones interaction parameters for electrode oxygen atoms in all considered intermediates, regardless of the charge or chemical connectivity (e.g. OH, OOH, O^-).

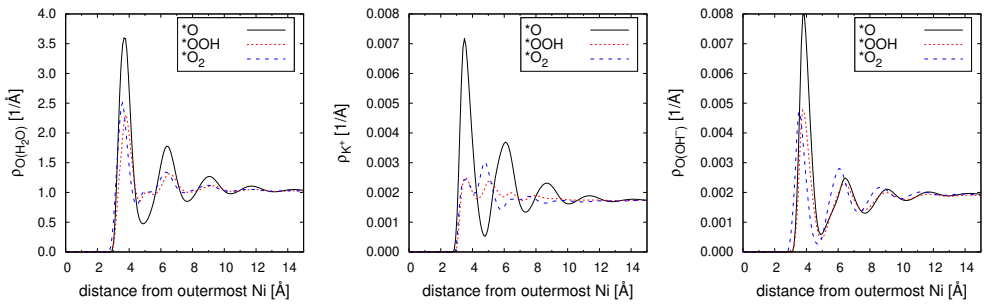

(a) H_2O molecules (b) K^+ cations (c) OH^- anions

Figure 6.2.: Electrolyte distribution functions for all computed intermediates of the R1 path of the OER catalyzed by β-NiOOH(001) in aq. 0.1 mol/L KOH solution.

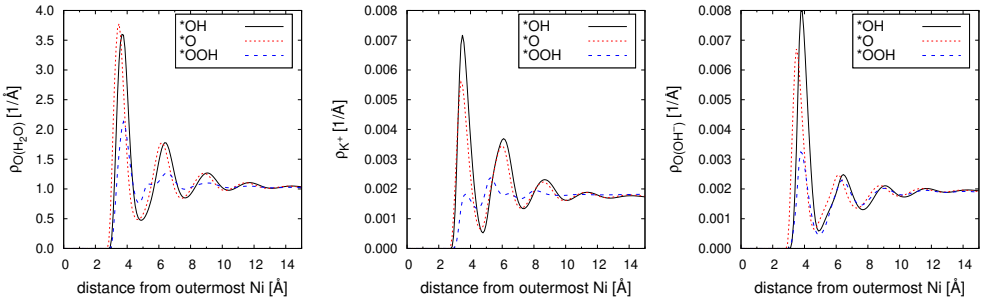

(a) H_2O molecules (b) K^+ cations (c) OH^- anions

Figure 6.3.: Electrolyte distribution functions for all computed intermediates of the R2 path of the OER catalyzed by β-NiOOH(001) in aq. 0.1 mol/L KOH solution.

To assess whether the RISM electrolyte description is consistent with our expectations, we show electrolyte distribution functions for all OER intermediates in Figures 6.2 and 6.3. They exhibit the typical oscillating behavior as described in Chapter 5. Electrolyte structures are significantly altered for the different OER intermediates, in particular for the *OOH and $*O_2$ intermediates. This is also translated to solvation energies and thus OER reaction energies. Solvation energies from the ESM-RISM calculations indicate that the *OOH intermediate is less stabilized by solvation than the other intermediates, reflected in the reaction energies in Table 6.1. Reaction steps with this intermediate as a product are hindered, whereas the second step of the R1 path, where this intermediate disappears, is facilitated. The stoichiometric β-NiOOH(001) structure is most stabilized by solvation among all intermediates, so that the PDS (the first reaction step in both paths) becomes more difficult in electrolyte solution and the overpotentials increase. Rationalizing these observations in terms of electrolyte structure, the *OOH intermediate, with the peroxo group extending relatively far into the electrolyte, might destroy the network of water molecules as described by the RISM, thus resulting in the destabilization. As discussed in Chapter 5, the water network is in principle represented by the RISM, but detailed features of near-surface water are not well represented. Electronic effects like polarization of electrolyte species are also neglected.

A detailed comparison of electrolyte descriptions by different models, including AIMD simulations, would be required to access the correctness of RISM solvation effects. Including explicit water layers, computed at the level of DFT, is very important, since only this allows to model interactions between the polar β-NiOOH(001) surface and electrolyte species in detail [423]. However, these simulations are computationally very demanding and were beyond the scope of this thesis. In AIMD simulations of electrolyte solutions, the description of electrolyte ions is difficult to realize, since the respective concentrations require very large simulation cells, making the calculation even more costly. An important strength of the ESM-RISM is the inclusion of electrolyte ions at reasonable computational cost.

6.4. Explicit potential application and comparison to the CHE approach

After evaluating the electrolyte effects on OER overpotentials, we were also interested in explicit potential effects (beyond the CHE scheme). We thus applied a range of potentials to all considered OER intermediates in the grand canonical scheme, obtaining surface charging relations. Where possible, we then explicitly applied the overpotentials obtained from our CHE calculations and analyzed potential effects e.g. on the double layer structure. We stress that the CHE relies on crude approximations in the interface description (most importantly, the surface is uncharged), but we assume it to yield at least a reasonable approximation for the realistic overpotentials. Comparisons to calculations with charged surfaces are discussed below.

Surface charging relations

Figures 6.4 and 6.5 show the surface charging relations for the intermediates of the R1 and R2 OER paths, respectively. Except for the R1 $*O_2$ intermediate (see Figure 6.4(c)), which is computed to be metallic, all systems show a discontinuity in the charging relation: in a certain potential range, the surface charge does not increase with increasing potential. This is the expected Fermi level discontinuity related to the semiconductor's band gap (see Chapter 1). The Fermi level as the highest occupied energy level does not change in a certain potential range [180], since no electrons can be taken up by or released from the system, because no electronic states are available at the corresponding energy due to the band gap. The magnitude of the "band gap region" in the charging relation is indeed similar to the computed band gap (see Figure 3.4(b)), e.g. around 3 eV for the stoichiometric β-NiOOH(001) surface. This expected behavior is only obtained when computing the electrode at the DFT+U(WF) level. With atomic orbital projectors, a metallic state is obtained and the charging relation is continuous (see Figure 6.4(a) for an example). This underlines the importance of using Wannier projectors for obtaining the correct electronic structure and correct resulting properties of this material.

Our calculations also indicate that the overpotential approximated by the CHE scheme (dashed vertical lines in Figures 6.4 and 6.5) can fall into the described "band gap region". For these target potentials, the grand canonical potentiostat scheme is not applicable, since the target potentials are not accessible by modifying the surface charge. Grand canonical DFT approaches rely on the linear relation between Fermi level and applied potential, which is disrupted by the Fermi level discontinuity. This has been realized before [107], complicating the simulation of electrified semiconductor/electrolyte interfaces. Here, we were able to compute only a single reaction step at the electrode potential predicted by the CHE, namely the first reaction step of the R1 OER path (see below). However, the question arises if potentials that fall into the "band gap region" are actually meaningful. In an experimental setup, any electrode potential can be applied (the potential is continuous), but in the "band gap region", it is questionable if the potential has any effect. The electrode cannot take up or release charge and remains at the same charging state. Still, other effects of potential could be relevant, e.g. surface deprotonation (see next section).

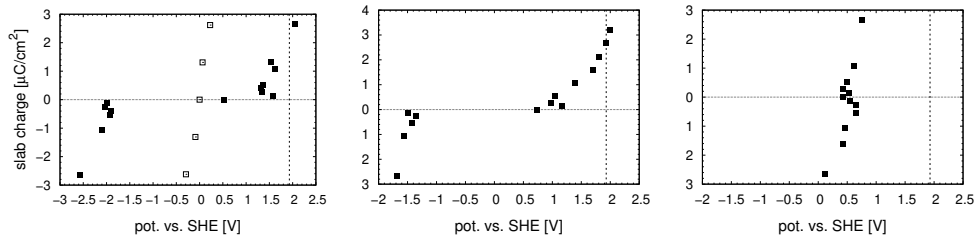

(a) *O (b) *OOH (c) *O_2

Figure 6.4.: Charging relations for β-NiOOH(001)/0.1 mol/L aq. KOH interfaces for the different intermediates of the R1 OER path. The vertical dashed lines mark the overpotentials obtained from simple CHE analysis, namely $\eta = 1.93$ V vs. SHE. Open symbols in (a) are computed with the DFT+U approach and atomic orbital projectors (instead of Wannier function projectors).

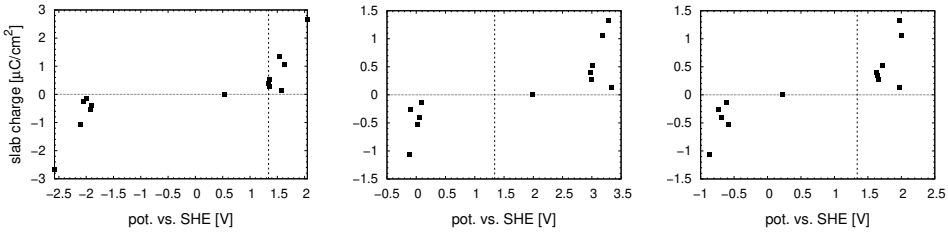

(a) *OH (b) *O (c) *OOH

Figure 6.5.: Charging relations for β-NiOOH(001)/0.1 mol/L aq. KOH interfaces for the different intermediates of the R2 OER path. The vertical dashed lines mark the overpotentials obtained from simple CHE analysis, namely $\eta = 1.34$ V vs. SHE.

Nevertheless, further aspects in simulating the electrified semiconductor/electrolyte interface might be problematic. As mentioned in Chapter 1, a thick space charge layer (thickness up to 100 nm) is expected in the semiconductor electrode at applied potential, only a small part of which is described by the thin slab model (thickness around 10 Å) used here. This can potentially lead to wrong descriptions of interface properties and catalyst activity, but the extend of the effect is difficult to estimate. In contrast to what is expected, a Löwdin charge analysis shows that the slab charge localizes at the outermost atoms (as observed and expected for metals). We still continued our analysis here in the grand canonical ESM-RISM, selecting those systems that we could compute at an applied potential, because our focus was on computation of the local environment at the ECI.

Comparison of CHE approach and grand canonical ESM-RISM

To evaluate the performance of the CHE scheme and the benefit of applying the more sophisticated ESM-RISM potentiostat, we compare the respective results in terms of reaction free energies, double layer structure and electrostatic interfacial potentials. We studied the cases of the R1 *O intermediate (identical to the R2 *OH intermediate) and the R1 *OOH intermediate, since the surface charging relations showed that these can be computed in the grand canonical potentiostat at the

desired potentials (1.93 and 1.34 V vs. SHE, respectively). In the CHE scheme, the systems are neutral and the potential is only applied by an additive term to reaction free energies after running the actual DFT calculation. In contrast, in the ESM-RISM potentiostat calculation, the systems are charged. The CHE overpotentials serve here as a first approximation to the realistic overpotential; effects of the explicitly applied potential like surface restructuring or surface dipoles are expected to modify the system in such a way that another, deviating overpotential may become necessary to drive the OER. In principle, a self-consistent approach would be necessary.

Our analysis shows that the structure of the electrode and the water solvent, as described by the RISM, are the same for the CHE and the potentiostat calculations. Interface potentials differ by ca. 0.2 V. Significant changes are observed for the distributions of electrolyte ions at the interface, as expected from neutral vs. charged calculations. The electrical double layer (as a response to interface charging) is not represented in the CHE calculations. The reaction free energy for the first step of the R1 path changes from 3.16 to 3.25 eV, when explicitly computed at the potential of 1.93 V vs. SHE. This change of ca. 0.1 eV is much smaller than the average electrolyte effect and falls into the uncertainty range of the computed values and experimental overpotentials.

We conclude that the CHE gives reasonable estimates of overpotentials for the considered β-NiOOH(001), as has been confirmed by comparison to experimental overpotential values and concluded from previous CHE studies (see previous section). We could not see a benefit of using a grand canonical potentiostat for this aspect. The effects of double layer charging seem to be insignificant, while other effects of an applied potential could be more relevant (see following section). Only slight effects of including a local electric field have been found before [434]. We note that the importance of correctly describing the electronic structure is unaffected, even if the correct representation of the resulting surface charging relation and related capacitive behavior might be of secondary importance. This is supported by previous studies which have shown that hybrid DFT functionals, which yield the correct electronic structure like the DFT+U(WF) approach used here, yield superior results to standard GGA functionals for OER reaction energies [70] .

6.5. Potential-dependent deprotonation and properties of active sites

The β-NiOOH(001) surface is known to release protons (deprotonate) with increasing applied potential [125]. As we learned from our simulations of Pt(111)/electrolyte interfaces (see Chapter 5), the potential-dependent surface state is highly important, e.g. for the charging behavior of the surface. Since OER mechanisms are often assumed to have a deprotonation step as a first step (see also eqs. 6.2 and 6.3), increasing degrees of deprotonation make the material potentially more catalytically active. Deprotonated sites can be treated as catalytically active sites. Therefore, next to the double layer charging studied in the previous section, we study this very important effect with the grand canonical ESM-RISM. Local properties and reaction conditions at deprotonated sites are particularly interesting and we studied these as a function of the degree of deprotonation.

Surface charging relation including potential-dependent deprotonation

The quantitative relation between potential and degree of deprotonation is not known from experiment [125], but we used data from DFT calculations instead [90] (computed with an explicit water layer and accounting for a dipole correction). These are shown in Table 6.2.

Table 6.2.: Degree of deprotonation of the β-NiOOH(001) surface as a function of potential. In this work, only three degrees of deprotonation were considered, due to the limited size of the surface unit cell.

potential vs. SHE [V]	stable degree of deprot. [90]	degree of deprot. used here
< 1.1	stoich.	stoich.
1.1-1.2	16.7 %	
1.2-1.5	50 %	50 %
1.5-1.6	83.3 %	
> 1.6	fully deprot.	fully deprot.

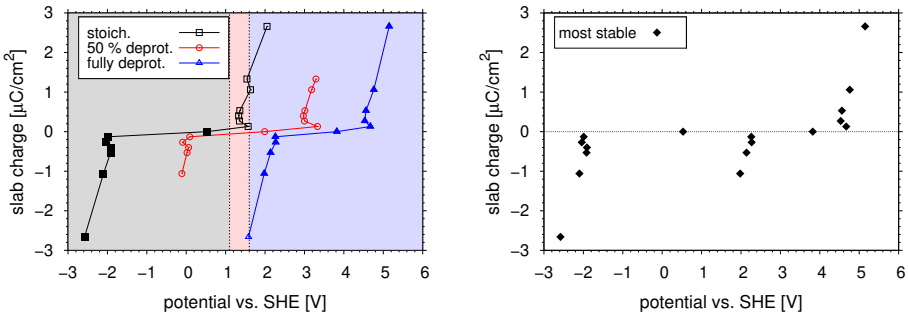

(a) all (b) most stable

Figure 6.6.: Charging relation of the β-NiOOH(001)/0.1 mol/L aq. KOH interface including potential-dependent deprotonation. (a) Filled regions: stability range of respective deprotonation state (according to Table 6.2). Full symbols: most stable deprotonation state at this potential. Lines are guides to the eye. (b) The final charging relation (extracted from (a)), depicting only the most stable deprotonation state.

We first derived the surface charging relation, including the potential-dependent deprotonation. This means that for each potential region, the surface charge of the existing degree of deprotonation (according to Table 6.2) is reported. The same technique was applied previously for the charging relation of the partially oxidized Pt(111) surface (see Chapter 5). As illustrated in Figure 6.6(b), this results in a jump in the charging relation around 1 V vs. SHE. This means that the charging relation is substantially modified by deprotonation. Ionic or acid-base behavior of the surface is very important next to capacitive double layer charging, and even more relevant in the potential region between 1 and 3 V vs. SHE, the catalytically relevant region for the OER. This is not surprising when recalling that deprotonation changes the charge of the surface by 1 e per 4 Ni surface atoms, whereas the charge introduced by applying a potential is around 0.02 e per 4 Ni surface atoms. Knijff et al. [67] call this situation a “protonic double layer”, attracting electrolyte ions

to compensate the ionic surface charge. They also point out that this protonic double layer at metal oxide interfaces can accumulate charges that are an order of magnitude larger than double layer charges at metal/electrolyte interface. However, surface deprotonation is typically not considered in computational studies of the OER. Surprisingly, our study of the OER paths (see above) gave the expected trends, even when neglecting the deprotonation and resulting large ionic surface charge.

Local properties of deprotonated sites

Next, we analyze changes in local properties with increasing degree of deprotonation, to better characterize the active surface and sites for the OER. Figure 6.7 shows electrolyte distribution functions for the different systems. Note that, for simplicity, these calculations were done at the pzc, although, as mentioned above and included in Figure 6.6, the degrees of deprotonation are stable at different potentials.

The deprotonation changes the structure of water solvent just very slightly. For the electrolyte ions, the effects are more pronounced due to electrostatic reasons: the surface becomes negatively charged with increasing degree of deprotonation. However, the effect on the distribution of K^+ cations is unexpected, since the near-surface cation concentration becomes smaller with increasingly negatively charged surface. One explanation could be that the concentration follows the anion concentration, so that local charge separation remains moderate. The near-surface distribution of OH^- anions responds to the surface charging in the expected way: the negatively charged surfaces repel the anions and the anion concentration becomes smaller with increasing degree of deprotonation. OH^- ions are consumed in the OER (see eqs. 6.2 and 6.3). However, relatively small concentrations should be sufficient for the reaction, which is a rare event on atomic-level time scales. The OH^- distribution functions directly reflect the local pH, which is here shown to change as a consequence of deprotonation. According to our results, a local pH results which stabilizes the deprotonated surface state. At the same time, the pH is also known to increase the OER activity [125, 421], potentially by favoring deprotonation. Varying the pH in the simulation and observing the effect on deprotonation would also be readily possible with the ESM-RISM.

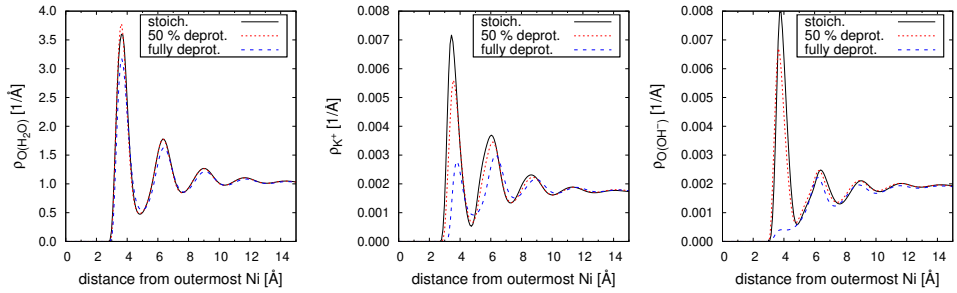

(a) H_2O molecules (b) K^+ cations (c) OH^- anions

Figure 6.7.: Electrolyte distribution functions at the β-NiOOH(001)/0.1 mol/L aq. KOH interface at different degrees of deprotonation as a function of distance from the surface. The subfigures show distribution functions for (a) water molecules, (b) K^+ electrolyte ions and (c) OH^- electrolyte ions.

Figure 6.8 shows that changes in interfacial potential upon deprotonation are quite significant, with differences of up to 1 V between the curves. The peak around 2 Å is related to the hydrogen atoms and naturally vanishes with increasing degree of deprotonation. At the same time, the oscillations in the electrolyte region get less pronounced. These significant differences potentially have an impact on local reaction conditions, like the approach of charged species to the surface, and thus the catalytic activity of β-NiOOH, and should therefore be carefully considered in simulations.

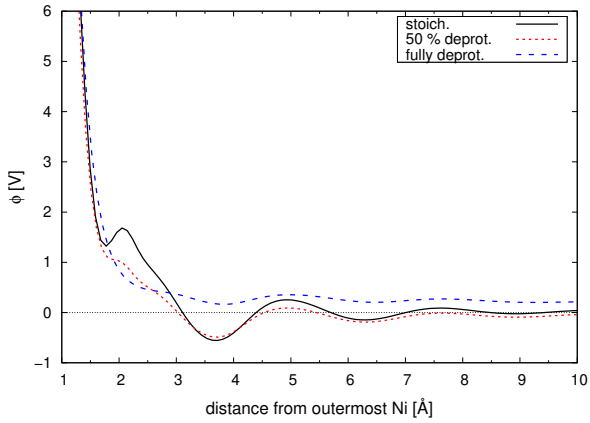

Figure 6.8.: Interface potential at the β-NiOOH(001)/0.1 mol/L aq. KOH interface for different degrees of deprotonation as a function of distance from the surface.

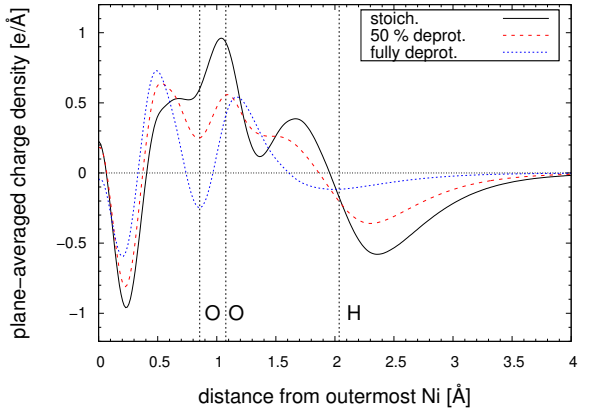

Figure 6.9.: Plane-averaged charge densities for the β-NiOOH(001)/0.1 mol/L aq. KOH interface at different degrees of deprotonation. Dashed vertical lines indicate atomic positions for the stoichiometric surface (O layers shift to the left by 0.2-0.4 Å for the deprotonated cases).

Figure 6.9 shows the plane-averaged charge density along the surface normal for the surface regions of the three systems with different degrees of deprotonation. Atomic charge densities of Ni, O and H atoms sitting at the same sites as in the surface slab were subtracted to remove this background charge. Positive values indicate regions with accumulation of (negative) charge, as

seen clearly for the region where surface oxygen atoms are located. Between the atomic layers, e.g. between Ni and O planes, the charge density is negative, indicating a depletion of charge. For the deprotonated cases, the charge density shifts closer to the Ni atoms, as the whole slab contracts slightly. The negative peak at largest distances, related to the surface hydrogen atom (being gradually released) becomes smaller with increasing degree of deprotonation, as expected. Many feature of the surface structure mix in this representation (e.g. there are two types of surface oxygen groups, O and OH, depending on the degree of deprotonation). The surface dipole moment condenses this information into a more approachable quantity, and will be discussed next.

Dipole moment shifts with respect to the stoichiometric system, $\Delta\mu$, were computed from work function shifts, $\Delta\Phi$, according to

$$\Delta\mu = -\epsilon_0 A \frac{\Delta\Phi}{e} , \tag{6.13}$$

where ϵ_0 is the vacuum permittivity, e is the electron charge and A is a dipole density factor (here the surface area per Ni–O dipole). This yields the dipole moment contributions along the surface normal, because only this direction contributes to the work function. Work functions were computed from the difference between the Fermi level of the surface slab and the electrostatic potential in bulk solvent[1]. As shown in Table 6.3, the work function shifts obtained here compare reasonably well to those computed by Eslamibidgoli et al. [90] with an explicit water layer at the surface. As reported before [90, 423], the work function as well as absolute values of the dipole moment at the β-NiOOH(001) surface increase with increasing degree of deprotonation. Dipole moments are directed from the negative charge to the positive charge, i.e. pointing towards the surface. Our computed orbital occupations, as well as 3D visualizations of charge density differences, show that for each removed hydrogen atom, one Ni^{3+} cation becomes a Ni^{4+} cation, giving an electron to the surface oxygen site which has released the hydrogen atom. The surface termination becomes $NiOO^{-}$. Experimental studies have also assumed negative charge at the surface oxygen site (active site) [125], although it is not clear if the active site is really an O^{-}. In any case, the higher charging of the Ni and O sites explains the increase in dipole moment with increasing degree of deprotonation.

Table 6.3.: Work function differences and dipole moment differences vs. the stoichiometric system for the β-NiOOH(001) surface at different degrees of deprotonation.

degree of deprot.	$\Delta\Phi$ [eV]	$\Delta\Phi$ [eV] [90]	$\Delta\mu$ [D]
stoich.	0	0	0
50 %	+1.46	+1.58	−0.29
fully deprot.	+3.29	+2.77	−0.66

The surface dipole moment interacts with the electric field at the interface. This effect is included in our grand canonical ESM-RISM studies, in contrast to many other studies, which either neglect the effect [12] or include it by an additional term [90]. Studies with compared to those without the dipole moment–field interaction included have concluded that the deprotonation is facilitated by

[1] Strictly speaking, the work function is a vacuum property (the energy required to take an electron from the metal bulk phase to vacuum), but can be used here as a useful measure.

this interaction [90]. The deprotonation and negatively charged surface sites have been reported to increase the material's OER activity [125] by favoring the formation of subsequent OER intermediates (see eqs. 6.2 and 6.3). These are very important aspects that should be included adequately in simulations.

6.6. Conclusion

In this chapter, we studied the β-NiOOH(001) surface as a catalyst for the alkaline OER. Our focus was on the effects of including an electrolyte solution and an electrode potential in DFT simulations. We used the DFT+U(WF) approach introduced in Chapter 3, which, in contrast to standard DFT+U calculations, results in the correct electronic structure of the system.

We first computed thermodynamic overpotentials for the OER and compared to values obtained in vacuum simulations. Overpotentials obtained with a RISM electrolyte description are significantly larger than experimental values and values obtained in vacuum calculations. This is either related to the inclusion of electrolyte ions, often neglected in other studies, or to deficiencies of the electrolyte structure description by the RISM. Future studies should absolutely include an explicit electrolyte layer at the interface, computed at the DFT level, which was beyond the scope of this thesis. In addition, this chapter provides a rather simplistic analysis of the OER paths, because the focus was on methodological aspects and description of the local reaction environment. Future studies should include reaction barriers, transport effects and kinetics, e.g. via mikrokinetic modeling.

In the next step, we additionally included an explicit electrode potential using the grand canonical ESM-RISM. Computed surface charging relations showed that grand canonical approaches are limited for simulations of semiconductor/electrolyte interfaces due to the discontinuity of the charge–potential relation related to the material's band gap. In Chapter 1, existing approaches to simulate semiconductor/electrolyte interfaces were described. These have limitations due to highly simplified (continuum) descriptions of the electrolyte region or negligence of the space charge layer thickness. Another direction might be a method that separates valences electrons, described by the DFT or DFT+U approach, from conduction electrons, that are described in a jellium-like model by partial differential equations. This would enable simulations at large length scales. These difficulties for semiconductor/electrolyte interfaces might however be of minor importance, since in the mentioned "band gap region", an applied potential should not have any effect.

We found that the simple CHE approach, neglecting double layer properties, gives reasonable results. Apparently, capacitive double layer charging is of secondary importance in the considered systems and potential ranges. However, in contrast to the CHE scheme, the ESM-RISM offers a description of local reaction conditions and double layer properties and allowed us to analyze them in detail.

Similar to the Pt(111) surface investigated in Chapter 5, the β-NiOOH(001) surface changes its surface state (degree of deprotonation) with varying electrode potential. However, in contrast to the Pt(111) surface, the β-NiOOH(001) surface is not dominated by capacitive surface charging, but

ionic effects are more important. Surface deprotonation is known to occur as an effect of potential and to affect the OER activity of NiOOH materials. Our analysis has shown that the change of surface state causes jumps in the surface charging relation and significantly varying local properties near the catalytically active sites (like electrolyte ion concentrations, interface potential and surface dipole moment). The deprotonation is typically not considered in OER studies. Additionally, the local reaction environment at the active sites is rarely analyzed in so much detail as possible here with our ESM-RISM simulations. Future studies should include a similar analysis of the effects of deprotonation, which might also allow to explain further reactivity trends. A carefully prepared study including the deprotonation and its effects in an analysis of OER reactions paths and activity could yield very important understanding of this catalytic reaction.

The prospect for the future is to create a universal model of nickel (oxy)hydroxide catalysis, including phenomena like defects or transformations between the α-, β- and γ-phases. This model could benefit from combining DFT-based simulations with theoretical models, which have so far described, for instance, cation effects on the OER activity of NiOOH materials [435].

7. Conclusion and outlook

7.1. Achievements of this thesis

The aims of this thesis were to better understand the performance of atomic-scale simulation methods when applied to electrochemical systems, make methodological improvements for key aspects and improve simulation-based understanding of local reaction conditions at electrochemical interfaces (ECIs). The methodologies were successfully applied to complex catalyst/electrolyte interfaces with significant improvements in description of electronic structure, double layer properties and catalytic reaction pathways. This contributed to decoding essential atomic-level phenomena that determine the performance of energy storage and conversion devices. We focused on two aspects: (1) accurate computation of electronic structure of materials with strongly correlated electrons, and (2) self-consistent description of phenomena at ECIs. In both cases the computational efficiency was one of the main factors in selecting the computational methods.

The first part of this thesis was dedicated to establishing a reliable and computationally efficient electronic structure method for metal and metal oxide materials containing strongly correlated electrons. The DFT+U approach is a well-established and widely used approach for this purpose, but we demonstrated its serious limitations. The standard way of applying the DFT+U method is to use atomic orbitals as projectors of orbital occupations and a reasonable guess of the Hubbard U parameter. There exist, however, first principles methods that allow to compute the U values for the elements and system in question, resulting in a parameter-free DFT+U approach. In this thesis we presented a detailed derivation of U parameters for transition metals using the computationally efficient linear response approach. We compared the results with measured values and values computed with other methods, including a Hartree–Fock-based scheme for estimation of the Hubbard U parameter.

We also tested the usage of Wannier functions instead of atomic orbitals as orbital projectors in the DFT+U method. This was initially performed in close collaboration with experimental partners, having access to unique data on d-/f-elements oxides. As a result, we obtained more realistic orbital occupations and a better overall electronic structure description. This enabled correct prediction of the most stable phases of the d-/f-elements oxides, correcting the bias of metal d-bands compared to experimental spectra, as well as a meaningful investigation of catalytically active sites in oxide materials. For example, this methodology allowed decoding the role of Fe dopant atoms in the catalytic performance of NiOOH electrocatalysts, a previously unresolved problem in electrochemistry.

Combining these two aspects, we established the parameter-free DFT+U(WF) approach. We eval-

uated this method for different d- and mixed d-/f-materials computing a variety of properties and comparing to high-quality experimental data, consistently obtaining good results. For computation of metals, however, the standard DFT method still gives good results, the origin of which is not fully clear. Still, the DFT+U(WF) scheme can be useful for computing metallic (sub)systems in mixed metal/oxide compounds or in oxidation reaction paths, where it is necessary to use the DFT+U approach for the other subsystems. In addition, we discussed the less common "around mean field" (AMF) implementation of DFT+U, which might be more suitable for metals due to the delocalized character of the electrons. However, the AMF version is not commonly implemented in DFT codes, and our DFT+U(WF) method is a good alternative.

A correct description of the electronic structure of catalyst materials, as obtained with the DFT+U(WF) approach, is of upmost importance for reliable predictions of their performance. For example, the d-bands of transition metals are commonly applied as descriptors for catalytic activity. However, the value of the U parameter and the choice of orbital projectors directly affect the d-band position, so that these must be chosen properly. The improvements made here were used in later parts of this thesis for the computation of local reaction conditions at ECIs.

In the second part of this thesis, regarding the realistic and efficient computation of interface phenomena, we extensively tested, validated and applied the effective screening medium reference interaction site method (ESM-RISM). In the first step, we worked out a valid geometric arrangement for the calculations as well as physical interaction parameters, identifying a setup in which the ESM-RISM gives reliable results. We then exploited the strengths of the RISM, as an integral equation-based solvation model, to obtain the electrolyte structure at the interface via electrolyte distribution functions. However, we showed that near-surface water layers need to be treated at the quantum mechanical level to capture all structural features, slightly reducing the efficiency of the method.

We also made use of the implemented grand canonical scheme to include an electrode potential. We confirmed that the ESM-RISM is not limited to potentials close to the potential of zero charge (pzc). The potential scale was successfully related to an experimental scale via potential-dependent surface properties or the computed pzc or work function. The obtained electrode charge was located in a narrow region at the surface, as expected for a metal; the counter charge was found in the electrolyte solution in the direct vicinity to the surface, as expected from electrostatic arguments.

Combining the electrolyte and electrode potential descriptions, we computed properties of the Au(111)/electrolyte and the partially oxidized Pt(111)/electrolyte interfaces. We were able to obtain a representation of local reaction conditions via a set of successfully computed interface properties. These include the structure of the electrical double layer, the electrostatic potential at the interface, and the chemisorption and charging state of the interface, as expressed by an accurate surface charging relation. Based on these results, we identified the ESM-RISM to be a promising method for self-consistent computation of electrochemical interfaces. The fact that it includes electrode potential and electrolyte makes the method superior to many other, more simplified, interface models.

The last part of this thesis combined the two computational schemes, the DFT+U(WF) approach and the ESM-RISM, to compute catalytic properties of technologically very relevant, but also very complex, NiOOH catalysts. Electrified semiconductor/electrolyte interfaces have been rarely studied by DFT-based methods so far. In our studies, we clearly demonstrated that computations of these materials would not have been possible in a standard DFT+U scheme, since only with Wannier function projectors, we could obtain the correct semiconducting state of NiOOH. We then evaluated the importance of including electrolyte and potential effects for computation of thermodynamic overpotentials for the oxygen evolution reaction (OER) at the NiOOH(001)/electrolyte interface. We found that the effects on structural reorganization and interface potentials at the NiOOH interface are surprisingly small. Thus, the simple computational hydrogen electrode (CHE) scheme, combined with a RISM description of the electrolyte, might be a good approximation, despite its crude approximations in the interface description. This is probably related to the fact that the potential-dependent deprotonation of the NiOOH(001) surface has larger impact on the surface state than potential-induced restructuring of the interface region and capacitive double layer charging. Our analysis of local properties at active sites showed that they heavily depend on the degree of deprotonation. Including the potential-dependent surface composition is thus highly important for computation of electrochemical reaction paths.

In summary, our overall goal was to improve accuracy, efficiency and predictive power of first principles simulation methods for ECIs. We investigated two efficient methods, and substantially improved methodological aspects. More precisely, the aim of this thesis was to enhance the description of local reaction conditions at ECIs. This aim was achieved by obtaining good results for electronic structure, electrolyte and potential distributions at the interface, and resulting catalytic properties. We addressed the main challenges for computation of ECIs and made progress in overcoming these: (1) We have demonstrated limitations of the standard DFT+U scheme for metals and metal oxides and proposed a more reliable computational scheme, based on Wannier function projectors for occupations of d-states and computation of the Hubbard U parameter value from first principles. (2) We successfully computed metal electrodes under an applied electrode potential within the grand canonical ESM-RISM potentiostat, which is not limited to a narrow potential region. However, we showed that it is not easily applicable for electrode materials with a band gap. (3) We accounted for structural and electrostatic electrolyte effects in the parameterized RISM electrolyte model, which implicitly includes thermodynamic sampling of electrolyte configurations. However, electronic electrolyte effects were not considered, due to computational constraints. (4) We coupled the electrode and electrolyte regions in the ESM-RISM by a Lennard-Jones plus Coulomb interaction potential, which resulted e.g. in correct electrode–electrolyte gaps. Some coupled phenomena at the interface, like potential-dependent oxygen coverage, could be included manually. However, effects like spontaneous adsorption of electrolyte species require more sophisticated simulations.

7.2. Arising problems

The computational approaches investigated and applied in this thesis provide a significantly improved description of ECIs. However, these methods also have limitations. First, the approaches have to be applied in a thoughtful way, to avoid spurious effects. This is evident for the DFT+U method, in which inaccurate orbital projectors lead to qualitatively wrong description of the electronic structure, e.g. predicting semiconducting NiOOH as a metal. The same applies to the ESM-RISM method, the outcome of which depends on the quality of the parameterization of interactions between the electrode and electrolyte particles. Our studies contributed to uncover some of these subtle pitfalls, which have not been discussed in detail in the literature.

The parameter-free DFT+U(WF) method widely tested and applied here is only partially ready for application. First, forces are not implemented, which severely limits further testing and applications of this approach, as relaxation of ionic positions and cell parameters is a key aspect of computations of solids and interfaces. Second, although the simple band selection procedure for Wannierization implemented in the pmw.x tool gave reasonable results here, even if d- or f-bands mixed with other states, a thorough validation by comparison with results of more sophisticated band disentanglement procedures is advised.

We have demonstrated here the power of the ESM-RISM for computation of electrochemical interfaces, but we also identified a few weaknesses of this approach. First, calculations with this method are not trivial to set up, and important geometric parameters have to be carefully chosen by convergence tests. Otherwise, predictions can be wrong. In addition, interface properties, like the electrode–electrolyte gap, are sensitive to the parameterization of electrolyte–electrolyte and electrode–electrolyte interactions. These interaction parameters are known to be not readily transferable between different systems. In our studies the parameters for electrode species were selected by comparing to near-surface water structures obtained from ab initio molecular dynamics (AIMD) simulations, but these are computationally very demanding to generate. The correct parameterization is thus a limiting aspect of this method.

For the ESM-RISM, we also found that, for some systems, the DFT unit cell height must be relatively large (50 Å and larger). This makes the calculations computationally costly. Combining the ESM-RISM with AIMD simulations is thus practically infeasible. This is a serious disadvantage, since we demonstrated that near-surface water molecules need to be included in the DFT simulation to capture detailed features of the near-surface structure of an aqueous electrolyte. AIMD simulations represent an elegant way to realize proper sampling of the corresponding electrolyte configurations. Even more, they offer the advantage of including electronic electrolyte effects. On the other hand, spontaneous chemical reactions or adsorption of electrolyte species at a surface are still very difficult to capture. This is because of the long time needed for a specific phenomenon to occur as compared to very short simulation times (tens of picoseconds). Thus, the surface state (e.g. oxygen adsorption or deprotonation of the surface) has to be adjusted manually. Electrolyte ions in relevant concentrations cannot be considered in AIMD simulations, since such studies would require extremely large simulation cells. But excluding electrolyte ions from the interface region impedes correct representation of the electrical double layer and related effects. In this respect,

the ESM-RISM has an advantage over explicit simulations methods.

Going beyond metal electrodes, our simulations of semiconductor/electrolyte interfaces showed that grand canonical schemes have limitations for these types of materials, related to the band gap of the materials and corresponding Fermi level discontinuity. Assuming that potentials in the region corresponding to the band gap do not have an effect on surface charging or charge transfer, the relevant potential effects could still be simulated. However, the large thickness of the space charge and the obtained unexpected charge localization inside the semiconductor electrode pose further challenges. We hope that the simulations shown in the thesis will trigger further developments of efficient computational schemes for this type of materials.

7.3. Prospects for future work

With the advancements made in this thesis we contributed to improvements in computational description of catalytic processes at ECIs. However, to release the full power of computational methods that would lead to technological breakthroughs, computational electrochemistry needs further methodological developments, for which we hope this work represents a solid scientific basis. To conclude the thesis, we discuss perspectives for further development of the considered methods as well as potential useful applications.

The main weakness of the ESM-RISM is the lack of an explicit representation of the electrolyte atoms, including their dynamic and electronic properties. As described in the previous section, AIMD simulations could give access to these properties, but are practically infeasible due to computationally constraints. However, they may become possible with emerging machine learning force fields and the field of accelerated simulations. These advancements together with the emerging exascale computing infrastructure will enable more realistic simulations in the near future. Another improvement would be to make the ESM-RISM a reactive scheme. This might be achieved by combining it with principles of reactive force fields, such as the ReaxFF framework which allows to study potential-dependent adsorbate coverages [119, 436].

On the methodological side, we also discussed that the quality of predictions from the ESM-RISM depends on the quality of the employed interaction parameters. To improve in this very important aspect, progress in interaction parameterizations is needed. The method can benefit from advancements in the area of interface force fields, possibly also including insights from artificial intelligence approaches.

A promising path for interface modeling is to combine first principles simulation methods with theoretical models, as we did here, for instance, with a mean-field model of the Pt(111)/electrolyte interface. Theoretical models are computationally very efficient and can add important information, e.g. on the behavior of the system at larger length and time scales. Information on the reaction kinetics can be obtained from mikrokinetic modeling. Beyond the extensions of the ESM-RISM proposed above, future methods for computation of ECIs could rely on powerful interface functionals (similar to existing functionals in joint DFT), on orbital-free DFT, or on machine learning approaches. The long-term perspective is to create an efficient model with high predictive power,

so that aspects that have to be neglected currently (e.g. surface reconstructions, catalyst–support interactions, or catalyst ageing) can be included in the future.

In terms of applications, the methods presented in this thesis can be very useful for detailed studies of technologically relevant materials, since they provide a more sound methodological basis compared to standard methods. We have demonstrated that the DFT+U(WF) approach enables enhanced and computationally efficient studies of catalytic activity by providing correct electronic structures. The method could be very useful in future studies of materials that typically require the use of computationally demanding hybrid DFT functionals. The DFT+U(WF) approach can be valuable also for cases where the band gap of a material is correctly captured by the standard DFT or DFT+U approaches, since it provides more realistic orbital occupations and thus better description of oxidation states. A very important aspects is to consistently compute metals and metal oxides with the same approach within one simulation workflow, which is sometimes neglected.

The ESM-RISM has the potential to become a very useful interface model with various possible applications, when improving a few above-mentioned aspects such as the interaction parameterization and explicit computation of near-surface electrolyte layers. In combination with the DFT+U(WF), it can be used for follow-up studies of complex metal or metal oxide/electrolyte interfaces. Aspects that are very relevant and can be studied with the grand canonical ESM-RISM, but are often neglected in other DFT-based studies, include effects of potentials far from the pzc, the potential-dependent state of the surface, and comparison of capacitive vs. other (e.g. ionic) effects of surface charging. The analyses performed in this thesis indicate that the potential-dependent surface state (e.g. adsorbate coverage or degree of deprotonation) is of huge importance. Accounting for these effects can significantly advance DFT-based simulations of ECIs. The proposed simulations would contribute to gathering important information for fundamental understanding of catalytic processes. We hope that the research and advancements on computation of ECIs presented here bring us closer to accurate, self-consistent computation of electrochemical systems and computation-aided materials design for the energy system of the future.

Appendix

A. Additional computed data on atomic and electronic structure of *d*-metals

This appendix chapter provides the data published by us in the Supplementary Information to the article R. Tesch and P. M. Kowalski, *Hubbard U parameters for transition metals from first principles*, Phys. Rev. B 105, 195153, 2022 (ref. [235]). It includes the considered crystal structures for all transition metals, tabulated Hubbard U parameters depicted in Figure 4.2, the full set of computed lattice parameters and relative errors, shown partly in Table 4.2, as well as tabulated d-bandwidths and d-band centers depicted in Figures 4.4 and 4.6, respectively.

Table A.1.: Structures of the $3d$-, $4d$- and $5d$-transition metals. Reprinted with permission from [235]. Copyright 2022 American Physical Society.

# valence e^-	3	4	5	6	7	8	9	10	11
$3d$	Sc hcp	Ti hcp	V bcc	Cr bcc	Mn bcc	Fe bcc	Co hcp	Ni fcc	Cu fcc
$4d$	Y hcp	Zr hcp	Nb bcc	Mo bcc	Tc hcp	Ru hcp	Rh fcc	Pd fcc	Ag fcc
$5d$	Lu hcp	Hf hcp	Ta bcc	W bcc	Re hcp	Os hcp	Ir fcc	Pt fcc	Au fcc

Table A.2.: The Hubbard U parameters for $3d$-, $4d$- and $5d$-transition metals, obtained with the cLDA method, from the d-band center shifts between HF and DFT methods, the cRPA method by Şaşıoğlu et al. [228], the cLDA method by Nakamura et al. [239] and experiment. Both non-magnetic (NM) and magnetic (FM, AFM) calculations are reported for magnetic $3d$ metals. All values are in eV. Reprinted with permission from [235]. Copyright 2022 American Physical Society.

	cLDA	HF($d$bc)	cRPA [228]	cLDA [239]	exp.
Sc	0.8	1.1	2.0	2.7	-1.9 [312–314]
Ti	1.6	1.9	2.6	3.8	-1.0 [312–314]
V	2.5	2.1	2.6	4.5	2.3 ± 0.4 [315], 0.5 [312–314]
Cr (NM)	3.7	4.1	3.8	4.8	
Cr (AFM)	5.1		4.0		2.0 ± 0.4 [315], -0.1 [312–314]
Mn (NM)	4.3	4.7	3.8	4.8	
Mn (FM)	3.6		3.7		0.9 ± 0.4 [315], 0.0 [312–314]
Fe (NM)	4.7	4.5	3.2	5.2	
Fe (FM)	2.6		3.6		1.2 [312–314]
Co (NM)	5.4	5.8	3.6	5.6	
Co (FM)	3.4		4.0		4.1 ± 0.4 [315], 1.2 [312–314]
Ni (NM)	5.7	8.6	3.2	6.2	
Ni (FM)	4.4		3.6		4.2 [312–314]
Cu	11.7	8.2	4.9	9.0, 18.2[238]	8.0 [312–314]
Y	0.1	1.5	1.3		
Zr	0.5	2.3	1.9		
Nb	1.0	2.5	2.1		
Mo	1.8	3.3	3.1		
Tc	2.3	3.3	3.1		
Ru	3.2	4.2	3.5		
Rh	3.8	4.9	3.3		
Pd	3.9	5.1	3.1		
Ag	15.2	6.3	4.2		
Lu	0.1	2.3	1.2		
Hf	0.3	2.6	1.7		
Ta	0.6	2.8	1.8		
W	1.2	2.6	3.0		
Re	1.5	3.8	3.2		
Os	2.2	4.1	3.6		
Ir	2.8	4.6	3.3		
Pt	3.2	4.7	3.2		
Au	6.6	5.5	3.4		

Table A.3.: Lattice parameters in Å computed with different methods, using the PBEsol exchange-correlation functional, and relative errors in % w.r.t temperature-corrected experimental values and corresponding U parameters in eV. Reprinted with permission from [235]. Copyright 2022 American Physical Society.

		exp. [327]	DFT		DFT+U		DFT+U		U	U
				[%]	(cLDA)	[%]	(cRPA)	[%]	(cLDA)	(cRPA) [228]
Sc	hcp *a*	3.299	3.270	−0.86	3.304	+0.14	3.361	+1.89	0.8	2.0
	hcp *c*	5.252	5.086	−3.17	3.361	−1.96	5.313	+1.16		
Ti	hcp *a*	2.944	2.906	−1.29	2.925	−0.65	2.938	−0.19	1.6	2.6
	hcp *c*	4.670	4.601	−1.48	4.637	−0.71	4.662	−0.17		
V	bcc	3.023	2.957	−2.18	2.958	−2.15	2.958	−2.15	2.5	2.6
Cr (AFM)	bcc	2.879	2.822	−1.97	3.162	+9.83	3.114	+8.16	5.1	4.0
Mn (FM)	bcc	2.988	2.760	−7.63	3.204	+7.21	3.206	+7.30	3.6	3.7
Fe (FM)	bcc	2.856	2.794	−2.16	2.848	−0.29	2.884	+0.98	2.6	3.6
Co (FM)	hcp *a*	2.498	2.456	−1.70	2.449	−1.97	2.445	−2.15	3.4	4.0
	hcp *c*	4.055	3.955	−2.48	3.949	−2.62	3.941	−2.81		
Ni (FM)	fcc	3.510	3.465	−1.29	3.455	−1.57	3.456	−1.54	4.4	3.6
Cu	fcc	3.598	3.570	−0.77	3.620	+0.61	3.588	−0.27	11.7	4.9
Y	hcp *a*	3.636	3.603	−0.90	3.609	−0.75	3.663	+0.74	0.1	1.3
	hcp *c*	5.713	5.573	−2.46	5.579	−2.35	5.652	−1.07		
Zr	hcp *a*	3.227	3.188	−1.21	3.189	−1.16	3.195	−0.98	0.5	1.9
	hcp *c*	5.139	5.128	−0.21	5.127	−0.22	5.126	−0.24		
Nb	bcc	3.294	3.273	−0.63	3.265	−0.86	3.256	−1.13	1.0	2.1
Mo	bcc	3.142	3.134	−0.26	3.120	−0.70	3.111	−0.98	1.8	3.1
Tc	hcp *a*	2.734	2.722	−0.44	2.704	−1.10	2.698	−1.32	2.3	3.1
	hcp *c*	4.390	4.365	−0.56	4.327	−1.43	4.314	−1.73		
Ru	hcp *a*	2.699	2.689	−0.35	2.667	−1.16	2.665	−1.25	3.2	3.5
	hcp *c*	4.270	4.252	−0.43	4.211	−1.38	4.207	−1.48		
Rh	fcc	3.794	3.779	−0.39	3.751	−1.15	3.754	−1.06	3.8	3.3
Pd	fcc	3.877	3.886	+0.23	3.881	+0.10	3.881	+0.11	3.9	3.1
Ag	fcc	4.064	4.063	−0.04	4.118	+1.31	4.078	+0.35	15.2	4.1
Lu	hcp *a*	3.500	3.455	−1.29	3.457	−1.23	3.489	−0.31	0.1	1.2
	hcp *c*	5.550	5.360	−3.43	5.364	−3.37	5.416	−2.42		
Hf	hcp *a*	3.187	3.154	−1.06	3.152	−1.10	3.145	−1.34	0.3	1.7
	hcp *c*	5.043	4.981	−1.23	4.980	−1.26	4.970	−1.45		
Ta	bcc	3.299	3.269	−0.91	3.263	−1.10	3.251	−1.46	0.6	1.8
W	bcc	3.161	3.150	−0.33	3.141	−0.64	3.127	−1.09	1.2	3.0
Re	hcp *a*	2.755	2.747	−0.28	2.734	−0.73	2.720	−1.24	1.5	3.2
	hcp *c*	4.449	4.445	−0.09	4.421	−0.64	4.394	−1.25		
Os	hcp *a*	2.730	2.723	−0.23	2.709	−0.76	2.699	−1.11	2.2	3.6
	hcp *c*	4.313	4.323	+0.23	4.294	−0.44	4.277	−0.83		
Ir	fcc	3.832	3.846	+0.39	3.826	−0.16	3.823	−0.24	2.8	3.3
Pt	fcc	3.913	3.929	+0.41	3.914	+0.02	3.914	+0.02	3.2	3.2
Au	fcc	4.062	4.093	+0.76	4.112	+1.22	4.102	+0.99	6.6	3.4

Table A.4.: *d*-bandwidths calculated up to the Fermi level, as described in Chapter 5. Gaussian smearing of 0.03 Ry has been applied to match experimental band broadening. Reference calculations are for non-magnetic cases. All values are in eV. Reprinted with permission from [235]. Copyright 2022 American Physical Society.

	$U = 0$	U(cLDA) AO	U(cLDA) WF	ref. calc. [228]	exp.
Sc	2.5	2.1	2.9	6.3	
Ti	3.4	3.3	3.8	6.7	
V	3.7	3.7	4.1	6.5	
Cr (AFM)	4.9	5.6	4.0	6.3	
Mn (FM)	5.6	7.3	6.6	5.9	
Fe (FM)	5.4	6.6	5.8	5.5	
Co (FM)	5.9	7.3	6.5	5.3	
Ni (FM)	5.5	6.6	7.8	5.2	6 [323]
Cu	5.6	6.1	5.8	3.7	5 [323]
Y	2.5	2.5	2.5	8.4	
Zr	3.6	3.6	3.8	8.5	
Nb	4.1	4.2	4.3	8.8	
Mo	5.7	5.9	5.9	9.0	
Tc	6.0	6.5	6.1	9.0	
Ru	6.7	7.5	6.7	8.3	
Rh	6.7	7.8	6.5	7.4	7 [339]
Pd	5.8	6.8	5.3	6.0	6 [339]
Ag	4.7	7.0	6.9	4.0	4.5 [323, 339]
Lu	3.3	3.3	3.3	9.7	
Hf	4.7	4.7	4.8	9.8	
Ta	5.0	5.0	5.0	9.7	
W	6.8	7.0	6.9	9.7	
Re	7.1	7.5	7.2	9.9	
Os	8.2	8.8	8.2	9.0	
Ir	8.4	9.2	8.1	8.6	8.5 [339]
Pt	7.7	8.8	7.9	6.8	8 [339]
Au	7.5	9.7	5.8	5.4	6 [339]

Table A.5.: *d*-band centers w.r.t. the Fermi level, calculated up to the Fermi level, as described in Chapter 5. Gaussian smearing of 0.03 Ry has been applied to match experimental band broadening. All values are in eV. Values from [339] were calculated by us from reported experimental spectra. Reprinted with permission from [235]. Copyright 2022 American Physical Society.

	$U = 0$	U(cLDA) AO	U(cLDA) WF	exp. (XPS)
Sc	−0.8	−0.8	−1.0	
Ti	−1.4	−1.3	−1.5	
V	−1.4	−1.4	−1.5	
Cr (AFM)	−2.3	−2.4	−1.9	
Mn (FM)	−2.5	−4.3	−4.3	
Fe (FM)	−2.2	−2.6	−2.8	−1.55 [310]
Co (FM)	−2.4	−3.2	−3.2	−1.54 [310]
Ni (FM)	−2.2	−2.9	−4.8	−1.20 [310]
Cu	−2.9	−6.9	−3.2	−3.05 [310]
Y	−0.9	−0.9	−0.9	
Zr	−1.5	−1.5	−1.6	
Nb	−1.7	−1.7	−1.8	
Mo	−2.9	−3.0	−3.0	
Tc	−2.6	−2.9	−2.7	
Ru	−3.2	−3.5	−3.2	
Rh	−3.1	−3.6	−3.1	−2.71 [339]
Pd	−2.6	−3.0	−2.4	−2.09 [310], −2.21 [339]
Ag	−4.3	−10.9	−5.6	−5.28 [310], −5.33 [339]
Lu	−1.1	−1.1	−1.1	
Hf	−1.8	−1.8	−1.9	
Ta	−1.8	−1.9	−1.9	
W	−3.3	−3.4	−3.3	
Re	−3.0	−3.2	−3.1	
Os	−3.8	−4.1	−3.8	
Ir	−3.9	−4.3	−3.9	−3.59 [339]
Pt	−3.4	−4.0	−3.5	−2.94 [310]
Au	−4.0	−6.7	−4.0	−4.45 [310], −4.53 [339]

B. Additional data for the Pt(111)/electrolyte interface computed with the ESM-RISM

This appendix chapter provides the data published by us in the Supplementary Information to the article R. Tesch, P. M. Kowalski, M. H. Eikerling, *Properties of the Pt(111)/Electrolyte Electrochemical Interface Studied with a Hybrid DFT—Solvation Approach*, J. Phys.: Condens. Matter, 33, 444004, 2021 (ref. [391]). It includes data from classical molecular dynamics (CMD) simulations, effects on interface properties of geometric parameters in the ESM-RISM calculation setup, details on the explicit water layer structure, as well as additional data on electrolyte distribution densities at different potentials and surface charging.

Bulk water structure

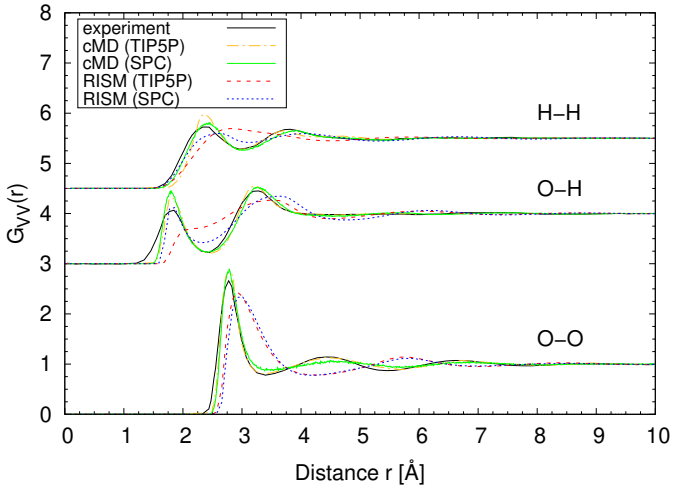

Figure B.1.: Water–water pair distribution functions computed with the 1D-RISM applying TIP5P and SPC water models. Neutron scattering experimental data [397] and classical MD (CMD) simulations are shown for comparison. Distribution functions from CMD simulation with the TIP5P water model are taken from ref. [437]. Reprinted with permission from [391], published by IOP Publishing under the Creative Commons Attribution 4.0 licence.

To assess the description of the water structure with the RISM, we first computed bulk liquid water. For comparison, Figure B.1 shows water distribution functions from classical MD (CMD) simulations

and from experiment. CMD trajectories of 1 ns length for a box of 8000 water molecules have been computed with the LAMMPS code [438] and the SPC water model [386]. Temperature and pressure were fixed to 298 K and 1 atm, respectively, by Nosé–Hoover thermostat and barostat. As mentioned in Chapter 5, the comparison between RISM and CMD water descriptions with the same water models (SPC and TIP5P [385]) shows that deficiencies in describing the water structure are due to the statistical character of RISM and not due to the water model itself.

Details on setup of ESM-RISM simulations

Several geometric parameters (see Figure 5.4 in Chapter 5) have to be chosen carefully when setting up the ESM-RISM calculations for the partially oxidized Pt(111)/electrolyte interface. Figures B.2 and B.3 show the impact of the DFT unit cell length and the expansion of the RISM electrolyte region beyond the DFT unit cell (`laue_expand_right` parameter), respectively, on the interfacial electrostatic potential. These parameters must be as large as 60 Å and 60 a_0 (where a_0 is the Bohr radius), respectively, to reach converged interface properties. The vacuum region at the left hand side of the metal slab must also be chosen wide enough (ca. 10 Å) to ensure that electronic wave functions are properly decayed to zero inside the DFT unit cell.

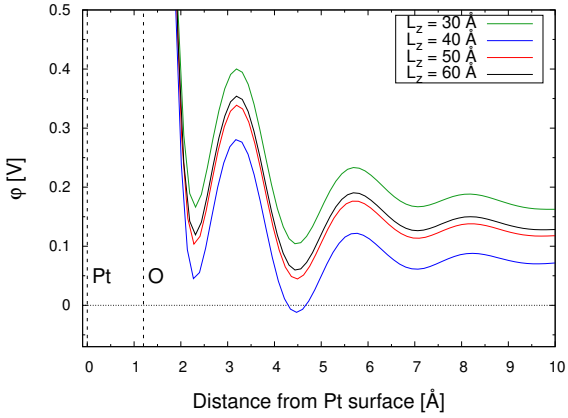

Figure B.2.: Plane-averaged electrostatic potential at the partially oxidized Pt(111)/electrolyte interface (oxygen coverage of 25 %) for different choices of the DFT cell length. The slab geometry is identical for all cases. Vertical lines indicate the positions of the outermost Pt and adsorbed O layers. Reprinted with permission from [391], published by IOP Publishing under the Creative Commons Attribution 4.0 licence.

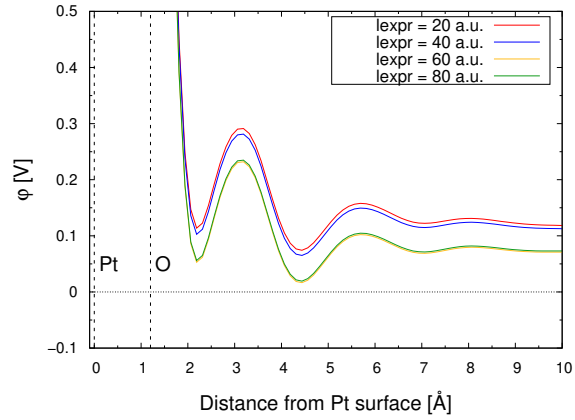

Figure B.3.: Plane-averaged electrostatic potential at the partially oxidized Pt(111)/electrolyte interface (oxygen coverage of 16.7 %) for different choices of the extension of the RISM electrolyte region beyond the DFT cell (`laue_expand_right`, "lexp"). The slab geometry is identical for all cases. Vertical lines indicate the positions of the outermost Pt and adsorbed O layers. Reprinted with permission from [391], published by IOP Publishing under the Creative Commons Attribution 4.0 licence.

Figure B.4 depicts the water density distribution at the interface for different values of the `laue_starting_right` parameter, which determines the start of the RISM electrolyte region next to the metal slab. As discussed in Chapter 5, a too large value of this parameter leads to an artificial vacuum between metal slab and electrolyte which also impacts interface properties like the interfacial electrostatic potential (see Figure B.5).

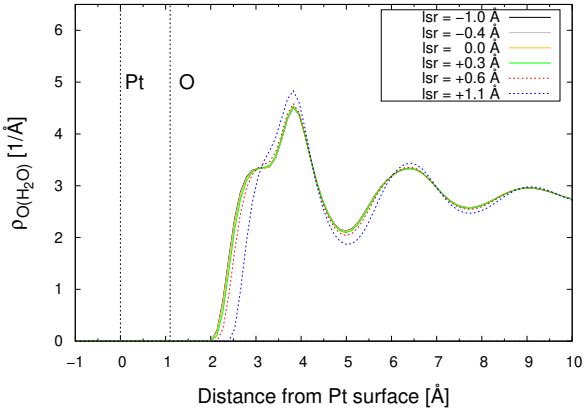

Figure B.4.: Water density distribution functions at the partially oxidized Pt(111)/electrolyte interface (oxygen coverage of 50 %) for different choices of the `laue_starting_right` ("lsr") parameter. The slab geometry is identical for all cases. Vertical lines indicate the positions of the outermost Pt and adsorbed O layers. Reprinted with permission from [391], published by IOP Publishing under the Creative Commons Attribution 4.0 licence.

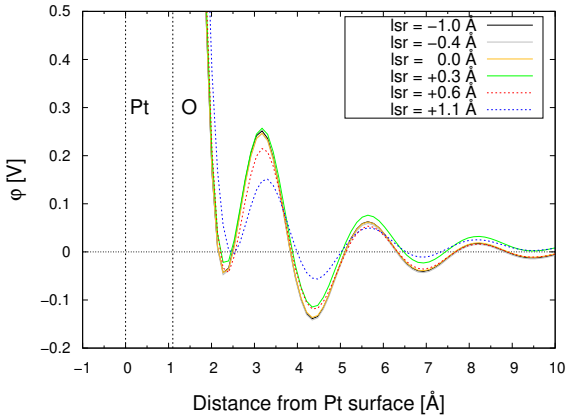

Figure B.5.: Plane-averaged electrostatic potential at the partially oxidized Pt(111)/electrolyte interface (oxygen coverage of 50 %) for different choices of the `laue_starting_right` ("lsr") parameter. The slab geometry is identical for all cases. Vertical lines indicate the positions of the outermost Pt and adsorbed O layers. Reprinted with permission from [391], published by IOP Publishing under the Creative Commons Attribution 4.0 licence.

Figure B.6 shows the solvation energy as a function of the `laue_starting_right` parameter. The energy trends for different values of `laue_starting_right` are discussed in Chapter 5. It should be stressed here that the energy increase for `laue_starting_right` smaller than 0.5 Å is due to very small amounts of solvent that extend into the metal slab and thus unphysical.

The value for `laue_starting_right` that would result from an energy minimization procedure (0.5 Å) is too large. It prevents the solvent from extending up to the Pt surface and thus causes changes in interface properties, as can be seen when comparing values from Figure B.6 to Figures B.4 and B.5. To avoid too large electrode–electrolyte separations, we chose to set the `laue_starting_right` parameter between the two outermost layers of the Pt slab, and kept this choice throughout our studies for consistency. The actual electrode–electrolyte gap is computed self-consistently from the Lennard-Jones electrode–electrolyte interaction within the RISM. Setting `laue_starting_right` inside the slab does not affect interfacial solvent densities and interfacial electrostatic potentials (see Figures B.4 and B.5). As shown in Figure B.6, the choice of `laue_starting_right` has an impact on the total energy of the system, but when using one value consistently, energy differences will not be affected.

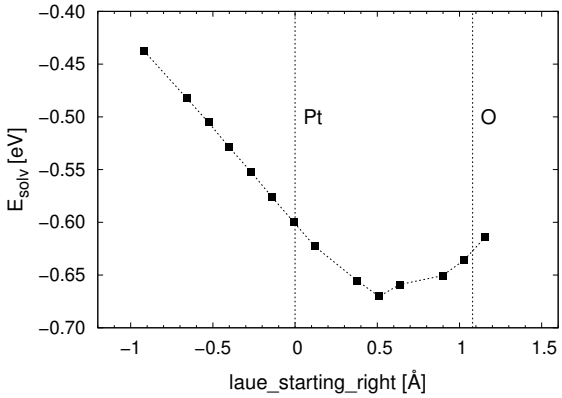

Figure B.6.: ESM-RISM solvation energy for the partially oxidized Pt(111)/electrolyte interface (oxygen coverage of 50 %) as a function of the `laue_starting_right` parameter. The slab geometry is identical for all cases. Vertical lines indicate the positions of the outermost Pt and adsorbed O layers. Reprinted with permission from [391], published by IOP Publishing under the Creative Commons Attribution 4.0 licence.

Distribution of water at the interface

Figure B.7 compares interface water density distribution functions from the ESM-RISM, as well as classical molecular dynamics simulations (CMD), to *ab initio* molecular dynamics (AIMD) literature data [69, 403]. Just like the ESM-RISM, the CMD simulation does not reproduce the AIMD near-surface double-peak, i.e. it cannot resolve the structure of the near-surface water bilayer.

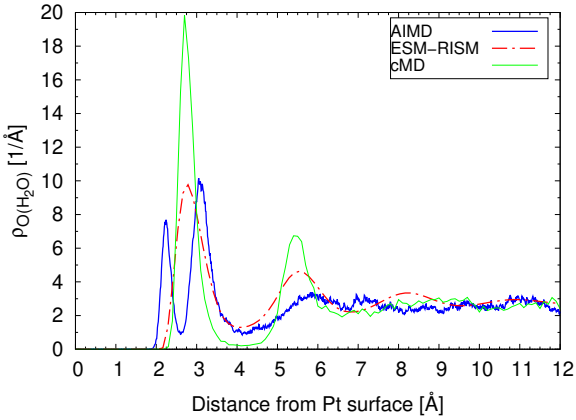

Figure B.7.: Water density distribution functions at the Pt(111)/water interface as computed by classical MD (CMD) simulation with the SPC water model [386] and the Interface Force Field [402] for Pt atoms. The simulation was performed at room temperature with 111 water molecules in the simulation cell (water density of 1 g/cm^3). ESM-RISM results and AIMD data from [69, 403] are shown for comparison. Reprinted with permission from [391], published by IOP Publishing under the Creative Commons Attribution 4.0 licence.

Figure B.8 shows water density distribution functions at the Pt(111)/water interface with one near-surface water layer computed explicitly at the level of DFT. When fully relaxing the explicit water layer in the DFT calculation, the electrode–solvent gap is slightly too large compared to AIMD. We therefore also computed a setup with the z-coordinates of water oxygen atoms (Pt–O(H_2O) distances) fixed to AIMD positions. Figure B.9 shows the corresponding plane-averaged electrostatic potential profiles. The distinct water double peak obtained by fixing the Pt–O(H_2O) distances to AIMD position is reflected here. The shoulder at the right edge of the main potential peaks for H-up configurations corresponds to the plane of up-pointing H atoms. More detailed discussion can be found in Chapter 5.

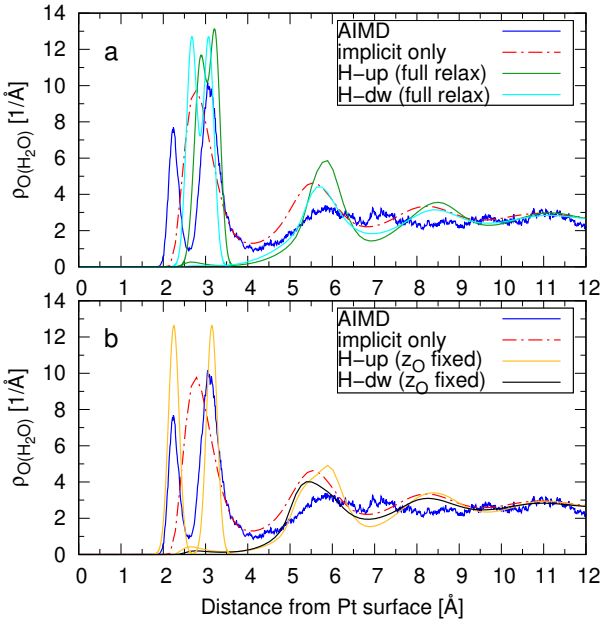

Figure B.8.: Water density distribution functions at the Pt(111)/water interface computed by the ESM-RISM with and without one explicitly computed water layer (H-up or H-down configuration). The water density distribution is a function of the distance from the outermost layer of Pt atoms. The position of water molecules is represented by the position of water oxygen atoms. Peaks for the explicit water layer (0 K, static) have been broadened by Gaussian convolution to mimic the temperature effect. The explicit water layer is (a) fully relaxed by DFT or (b) the z-coordinates of water oxygen atoms (Pt–O(H_2O) distances) are fixed to AIMD positions. AIMD data were taken from [69, 403]. Reprinted with permission from [391], published by IOP Publishing under the Creative Commons Attribution 4.0 licence.

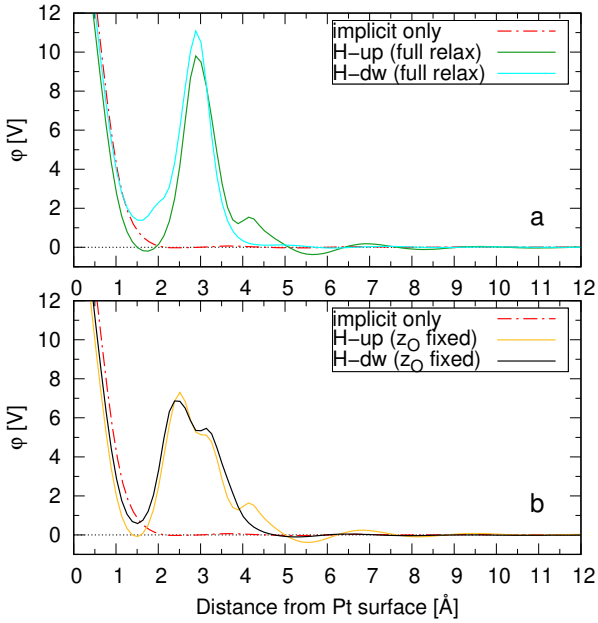

Figure B.9.: Plane-averaged electrostatic potential at the Pt(111)/water interface with and without one explicitly computed water layer. The explicit water layer is (a) fully relaxed by DFT or (b) the z-coordinates of water oxygen atoms (Pt–O(H_2O) distances) are fixed to AIMD positions. Reprinted with permission from [391], published by IOP Publishing under the Creative Commons Attribution 4.0 licence.

Ion distributions and surface charge under applied electrode potential

Figures B.10 and B.11 contain additional data lines for electrolyte ion density profiles at the charged Pt(111)/electrolyte interface that were omitted in Figure 5.10 in Chapter 5 for better readability. Data for different applied potentials in the potentiostat framework are shown. The ion densities clearly respond to the surface slab charges.

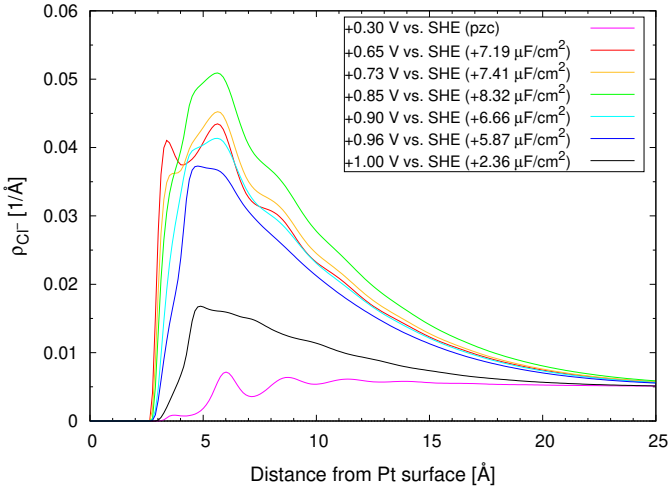

Figure B.10.: Density profile for Cl^- electrolyte ions (c(HCl) = 0.1 mol/L) computed with ESM-RISM at different electrode potentials. Slab charges per area are given in brackets. The Pt(111) surface is partially oxidized according to the applied potential; for coverages see Table 5.4. Reprinted with permission from [391], published by IOP Publishing under the Creative Commons Attribution 4.0 licence.

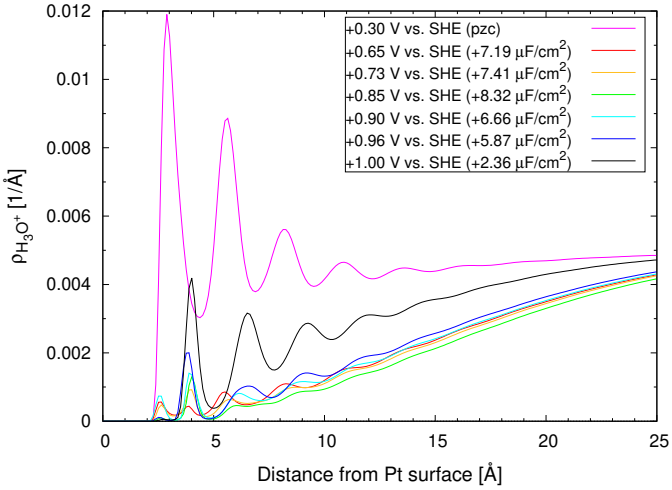

Figure B.11.: Density profile for H_3O^+ electrolyte ions (c(HCl) = 0.1 mol/L) computed with ESM-RISM at different electrode potentials. Slab charges per area are given in brackets. The Pt(111) surface is partially oxidized according to the applied potential; for coverages see Table 5.4. Reprinted with permission from [391], published by IOP Publishing under the Creative Commons Attribution 4.0 licence.

Figure B.12 depicts the Pt(111) surface charge as a function of electrode potential. In contrast to Figure 5.11 in Chapter 5, this is data for the non-oxidized Pt(111)/electrolyte interface. Without surface oxidation, a linear charging behavior is observed, as opposed to the non-monotonic metal

charging relation obtained for the partially oxidized interface.

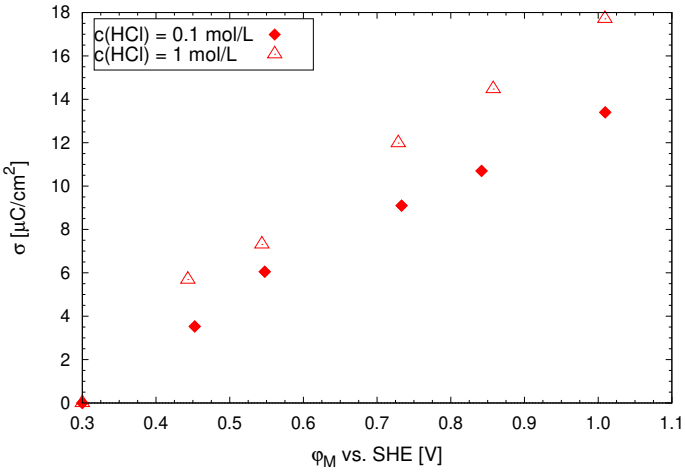

Figure B.12.: Surface charge vs. electrode potential for the non-oxidized Pt(111)/electrolyte interface with different electrolyte concentrations, as computed with the ESM-RISM. Reprinted with permission from [391], published by IOP Publishing under the Creative Commons Attribution 4.0 licence.

Bibliography

[1] IPCC. *Climate Change 2022: Mitigation of Climate Change. Contribution of Working Group III to the Sixth Assessment Report of the Intergovernmental Panel on Climate Change*. Cambridge University Press, Cambridge, UK and New York, NY, USA, 2022. doi: 10.1017/9781009157926.

[2] S. Maddukuri, D. Malka, M. S. Chae, Y. Elias, S. Luski, and D. Aurbach. *On the challenge of large energy storage by electrochemical devices*. Electrochim. Acta, 354, 136771, 2020. doi: 10.1016/j.electacta.2020.136771.

[3] M. Chatenet, B. G. Pollet, D. R. Dekel, F. Dionigi, J. Deseure, P. Millet, R. D. Braatz, M. Z. Bazant, M. Eikerling, I. Staffell, P. Balcombe, Y. Shao-Horn, and H. Schäfer. *Water electrolysis: from textbook knowledge to the latest scientific strategies and industrial developments*. Chem. Soc. Rev., 51(11), 4583–4762, 2022. doi: 10.1039/d0cs01079k.

[4] M.-Y. Lee, K. T. Park, W. Lee, H. Lim, Y. Kwon, and S. Kang. *Current achievements and the future direction of electrochemical CO_2 reduction: A short review*. Crit. Rev. Environ. Sci. Technol., 50(8), 769–815, 2019. doi: 10.1080/10643389.2019.1631991.

[5] A. Gallo, J. Simões-Moreira, H. Costa, M. Santos, and E. M. dos Santos. *Energy storage in the energy transition context: A technology review*. Renew. Sust. Energ. Rev., 65, 800–822, 2016. doi: 10.1016/j.rser.2016.07.028.

[6] M. Li, J. Lu, Z. Chen, and K. Amine. *30 Years of Lithium-Ion Batteries*. Adv. Mater., 30(33), 1800561, 2018. doi: 10.1002/adma.201800561.

[7] J. Zhang, editor. *PEM Fuel Cell Electrocatalysts and Catalyst Layers*. Springer Verlag, London, 2008. ISBN 978-1-84800-935-6. doi: 10.1007/978-1-84800-936-3.

[8] W. Ostwald. Z. Phys. Chem., 15, 409, 1894.

[9] P. W. Atkins and J. de Paula. *Physikalische Chemie*. Wiley-VCH, Weinheim, 5th edition, 2013. ISBN 978-3-527-33247-2.

[10] W. Schmickler and E. Santos. *Interfacial Electrochemistry*. Springer Berlin Heidelberg, 2010. doi: 10.1007/978-3-642-04937-8.

[11] I. C. Gerber and P. Serp. *A Theory/Experience Description of Support Effects in Carbon-Supported Catalysts*. Chem. Rev., 120(2), 1250–1349, 2019. doi: 10.1021/acs.chemrev.9b00209.

[12] J. K. Nørskov, J. Rossmeisl, A. Logadottir, L. Lindqvist, J. R. Kitchin, T. Bligaard, and H. Jónsson. *Origin of the Overpotential for Oxygen Reduction at a Fuel-Cell Cathode*. J. Phys. Chem. B, 108(46), 17886–17892, 2004. doi: 10.1021/jp047349j.

[13] M. T. M. Koper. *Analysis of electrocatalytic reaction schemes: distinction between rate-determining and potential-determining steps*. J. Solid State Electrochem., 17(2), 339–344, 2012. doi: 10.1007/s10008-012-1918-x.

[14] J. Huang, X. Zhu, and M. Eikerling. *The rate-determining term of electrocatalytic reactions with first-order kinetics*. Electrochim. Acta, 393, 139019, 2021. doi: 10.1016/j.electacta.2021.139019.

[15] J. K. Nørskov, T. Bligaard, B. Hvolbæk, F. Abild-Pedersen, I. Chorkendorff, and C. H. Christensen. *The nature of the active site in heterogeneous metal catalysis*. Chem. Soc. Rev., 37 (10), 2163, 2008. doi: 10.1039/b800260f.

[16] P. Sabatier. *Hydrogénations et deshydrogénations par catalyse*. Ber. Deut. Chem. Ges., 44, 1984, 1911.

[17] H. Ooka, J. Huang, and K. S. Exner. *The Sabatier Principle in Electrocatalysis: Basics, Limitations, and Extensions*. Front. Energy Res., 9, 2021. doi: 10.3389/fenrg.2021.654460.

[18] A. Balandin. *On the theory of the selection of catalysts*. Zh. Obshch. Khim., 16(6), 793, 1946.

[19] P. Quaino, F. Juarez, E. Santos, and W. Schmickler. *Volcano plots in hydrogen electrocatalysis – uses and abuses*. Beilstein J. Nanotechnol., 5, 846–854, 2014. doi: 10.3762/bjnano.5.96.

[20] I. A. Pašti, N. V. Skorodumova, and S. V. Mentus. *Theoretical studies in catalysis and electrocatalysis: from fundamental knowledge to catalyst design*. React. Kinet. Mech. Catal., 115 (1), 5–32, 2014. doi: 10.1007/s11144-014-0808-x.

[21] M. Wang and H. Zhu. *Machine Learning for Transition-Metal-Based Hydrogen Generation Electrocatalysts*. ACS Catal., 11(7), 3930–3937, 2021. doi: 10.1021/acscatal.1c00178.

[22] J. N. Bronsted. *Acid and Basic Catalysis.* Chem. Rev., 5(3), 231–338, 1928.

[23] M. G. Evans and M. Polanyi. *Inertia and driving force of chemical reactions*. Trans. Faraday Soc., 34, 11–24, 1938.

[24] F. Abild-Pedersen, J. Greeley, F. Studt, J. Rossmeisl, T. R. Munter, P. G. Moses, E. Skúlason, T. Bligaard, and J. K. Nørskov. *Scaling Properties of Adsorption Energies for Hydrogen-Containing Molecules on Transition-Metal Surfaces*. Phys. Rev. Lett., 99, 016105, 2007. doi: 10.1103/PhysRevLett.99.016105.

[25] K. S. Exner. *Why the breaking of the OOH versus OH scaling relation might cause decreased electrocatalytic activity*. Chem. Catalysis, 1(2), 258–271, 2021. doi: 10.1016/j.checat.2021.06.011.

[26] B. Hammer and J. K. Nørskov. *Why gold is the noblest of all the metals*. Nature, 376(6537), 238–240, 1995. doi: 10.1038/376238a0.

[27] B. Hammer and J. Nørskov. *Electronic factors determining the reactivity of metal surfaces*. Surf. Sci., 343(3), 211–220, 1995. doi: 10.1016/0039-6028(96)80007-0.

[28] J. K. Nørskov, F. Abild-Pedersen, F. Studt, and T. Bligaard. *Density functional theory in surface chemistry and catalysis*. Proc. Natl. Acad. Sci., 108(3), 937–943, 2011. doi: 10.1073/pnas.1006652108.

[29] A. Nilsson, L. G. M. Pettersson, B. Hammer, T. Bligaard, C. H. Christensen, and J. K. Nørskov. *The electronic structure effect in heterogeneous catalysis*. Catal. Lett., 100(3-4), 111–114, 2005. doi: 10.1007/s10562-004-3434-9.

[30] V. R. Stamenkovic, B. S. Mun, M. Arenz, K. J. J. Mayrhofer, C. A. Lucas, G. Wang, P. N. Ross, and N. M. Markovic. *Trends in electrocatalysis on extended and nanoscale Pt-bimetallic alloy surfaces*. Nat. Mater., 6(3), 241–247, 2007. doi: 10.1038/nmat1840.

[31] J. Greeley, T. F. Jaramillo, J. Bonde, I. Chorkendorff, and J. K. Nørskov. *Computational high-throughput screening of electrocatalytic materials for hydrogen evolution*. Nat. Mater., 5(11), 909–913, 2006. doi: 10.1038/nmat1752.

[32] X.-B. Li, T. Cao, F. Zheng, and X. Chen. *Computational Screening of Electrocatalytic Materials for Hydrogen Evolution: Platinum Monolayer on Transitional Metals*. J. Phys. Chem. C, 123(1), 495–503, 2019. doi: 10.1021/acs.jpcc.8b09301.

[33] A. Ruban, B. Hammer, P. Stoltze, H. Skriver, and J. Nørskov. *Surface electronic structure and reactivity of transition and noble metals*. J. Mol. Catal. A Chem., 115(3), 421–429, 1997. doi: 10.1016/S1381-1169(96)00348-2.

[34] M. Mavrikakis, B. Hammer, and J. K. Nørskov. *Effect of Strain on the Reactivity of Metal Surfaces*. Phys. Rev. Lett., 81, 2819–2822, 1998. doi: 10.1103/PhysRevLett.81.2819.

[35] M. Yu, E. Budiyanto, and H. Tüysüz. *Principles of Water Electrolysis and Recent Progress in Cobalt-, Nickel-, and Iron-Based Oxides for the Oxygen Evolution Reaction*. Angew. Chem. Int. Ed., 61(1), 2021. doi: 10.1002/anie.202103824.

[36] M. König, J. Vaes, E. Klemm, and D. Pant. *Solvents and Supporting Electrolytes in the Electrocatalytic Reduction of CO2*. iScience, 19, 135–160, 2019. doi: 10.1016/j.isci.2019.07.014.

[37] R. Jinnouchi, K. Kudo, K. Kodama, N. Kitano, T. Suzuki, S. Minami, K. Shinozaki, N. Hasegawa, and A. Shinohara. *The role of oxygen-permeable ionomer for polymer electrolyte fuel cells*. Nat. Commun., 12(1), 2021. doi: 10.1038/s41467-021-25301-3.

[38] H. Helmholtz. *Studien über electrische Grenzschichten*. Ann. Phys., 243(7), 337–382, 1879. doi: 10.1002/andp.18792430702.

[39] M. Gouy. *Sur la constitution de la charge électrique à la surface d'un électrolyte*. J. phys. theor. appli., 9(1), 457–468, 1910. doi: 10.1051/jphystap:019100090045700.

[40] D. L. Chapman. *LI. A contribution to the theory of electrocapillarity*. Lond. Edinb. Dublin Philos. Mag. J. Sci., 25(148), 475–481, 1913. doi: 10.1080/14786440408634187.

[41] O. Stern. *Zur Theorie der elektrolytischen Doppelschicht*. Z. Elektrochem. angew. phys. Chem., 30(21-22), 508–516, 1924. doi: 10.1002/bbpc.192400182.

[42] D. C. Grahame. *The Electrical Double Layer and the Theory of Electrocapillarity.* Chem. Rev., 41(3), 441–501, 1947. doi: 10.1021/cr60130a002.

[43] A. P. Willard, S. K. Reed, P. A. Madden, and D. Chandler. *Water at an electrochemical interface—a simulation study*. Faraday Discuss., 141, 423–441, 2009. doi: 10.1039/B805544K.

[44] J. Huang, A. Malek, J. Zhang, and M. H. Eikerling. *Non-monotonic Surface Charging Behavior of Platinum: A Paradigm Change*. J. Phys. Chem. C, 120(25), 13587–13595, 2016. doi: 10.1021/acs.jpcc.6b03930.

[45] A. Berná, V. Climent, and J. M. Feliu. *New understanding of the nature of OH adsorption on Pt(111) electrodes*. Electrochem. Commun., 9(12), 2789–2794, 2007. doi: 10.1016/j.elecom.2007.09.018.

[46] X. Yin, H. Wang, and E.-H. Han. *Effects of solvation and applied potential on the adsorption behaviors of H, O, OH and H_2O on Fe(110) surface*. Surf. Sci., 691, 121504, 2020. doi: 10.1016/j.susc.2019.121504.

[47] K. Chang, J. G. Chen, Q. Lu, and M.-J. Cheng. *Grand Canonical Quantum Mechanical Study of the Effect of the Electrode Potential on N-Heterocyclic Carbene Adsorption on Au Surfaces*. J. Phys. Chem. C, 121(44), 24618–24625, 2017. doi: 10.1021/acs.jpcc.7b07866.

[48] H. Helmholtz. *Ueber einige Gesetze der Vertheilung elektrischer Ströme in körperlichen Leitern mit Anwendung auf die thierisch-elektrischen Versuche*. Ann. Phys. Chem., 165(6), 211–233, 1853. doi: 10.1002/andp.18531650603.

[49] J. O. Bockris, M. A. V. Devanathan, and K. Müller. *On the structure of charged interfaces*. Proc. R. Soc. A: Math. Phys. Eng. Sci., 274(1356), 55–79, 1963. doi: 10.1098/rspa.1963.0114.

[50] W. Schmickler. *A jellium-dipole model for the double layer*. J. Electroanal. Chem. Interfacial Electrochem., 150(1-2), 19–24, 1983. doi: 10.1016/s0022-0728(83)80185-5.

[51] A. Kornyshev. *Metal electrons in the double layer theory*. Electrochim. Acta, 34(12), 1829–1847, 1989. doi: 10.1016/0013-4686(89)85070-4.

[52] R. Memming. *Semiconductor Electrochemistry*. Wiley-VCH, Weinheim, 2nd edition, 2015. ISBN 978-3-527-31281-8. doi: 10.1002/9783527688685.

[53] Y. V. Pleskov. *Electric Double Layer on Semiconductor Electrodes*. Springer Science+Business Media, New York, 1st edition, 1980. ISBN 978-1-4615-6686-1. doi: 10.1007/978-1-4615-6684-7.

[54] J. A. Turner. *Energetics of the semiconductor-electrolyte interface*. J. Chem. Educ., 60(4), 327–329, 1983. doi: 10.1002/qua.24521.

[55] M. J. Eslamibidgoli and M. H. Eikerling. *Approaching the self-consistency challenge of electrocatalysis with theory and computation*. Curr. Opin. Electrochem., 9, 189–197, 2018. doi: 10.1016/j.coelec.2018.03.038.

[56] A. A. Topalov, S. Cherevko, A. R. Zeradjanin, J. C. Meier, I. Katsounaros, and K. J. J. Mayrhofer. *Towards a comprehensive understanding of platinum dissolution in acidic media*. Chem. Sci., 5(2), 631–638, 2014. doi: 10.1039/c3sc52411f.

[57] T. Pajkossy and D. Kolb. *Double layer capacitance of Pt(111) single crystal electrodes*. Elec-

trochim. Acta, 46(20-21), 3063–3071, 2001. doi: 10.1016/s0013-4686(01)00597-7.

[58] M. T. Alam, M. M. Islam, T. Okajima, and T. Ohsaka. *Measurements of differential capacitance in room temperature ionic liquid at mercury, glassy carbon and gold electrode interfaces*. Electrochem. Commun., 9(9), 2370–2374, 2007. doi: 10.1016/j.elecom.2007.07.009.

[59] K. Schwarz and R. Sundararaman. *The electrochemical interface in first-principles calculations*. Surf. Sci. Rep., 75(2), 100492, 2020. doi: 10.1016/j.surfrep.2020.100492.

[60] R. Sundararaman, M. C. Figueiredo, M. T. M. Koper, and K. A. Schwarz. *Electrochemical Capacitance of CO-Terminated Pt(111) Dominated by the CO–Solvent Gap*. J. Phys. Chem. Lett., 8(21), 5344–5348, 2017. doi: 10.1021/acs.jpclett.7b02383.

[61] T. Binninger. *Piecewise nonlinearity and capacitance in the joint density functional theory of extended interfaces*. Phys. Rev. B, 103, L161403, 2021. doi: 10.1103/PhysRevB.103.L161403.

[62] C. Zhan and D. en Jiang. *Contribution of Dielectric Screening to the Total Capacitance of Few-Layer Graphene Electrodes*. J. Phys. Chem. Lett., 7(5), 789–794, 2016. doi: 10.1021/acs.jpclett.6b00047.

[63] M. Eikerling. *Theory and Simulation of Electrochemical Materials*, 2020. Lecture notes.

[64] D. C. Grahame. *Differential Capacity of Mercury in Aqueous Sodium Fluoride Solutions. I. Effect of Concentration at 25°*. J. Am. Chem. Soc., 76(19), 4819–4823, 1954. doi: 10.1021/ja01648a014.

[65] R. Sundararaman, K. Letchworth-Weaver, and K. A. Schwarz. *Improving accuracy of electrochemical capacitance and solvation energetics in first-principles calculations*. J. Chem. Phys., 148(14), 144105, 2018. doi: 10.1063/1.5024219.

[66] R. Sundararaman and K. Schwarz. *Evaluating continuum solvation models for the electrode-electrolyte interface: Challenges and strategies for improvement*. J. Chem. Phys., 146(8), 084111, 2017. doi: 10.1063/1.4976971.

[67] L. Knijff, M. Jia, and C. Zhang. *Electric double layer at the metal-oxide/electrolyte interface*. In *Reference Module in Chemistry, Molecular Sciences and Chemical Engineering*. Elsevier, 2023. doi: 10.1016/b978-0-323-85669-0.00012-x.

[68] M. J. Eslamibidgoli and M. H. Eikerling. *Electrochemical Formation of Reactive Oxygen Species at Pt(111) - A Density Functional Theory Study*. ACS Catal., 5(10), 6090–6098, 2015. doi: 10.1021/acscatal.5b01154.

[69] S. Sakong and A. Groß. *Water structures on a Pt(111) electrode from ab initio molecular dynamic simulations for a variety of electrochemical conditions*. Phys. Chem. Chem. Phys., 22(19), 10431–10437, 2020. doi: 10.1039/c9cp06584a.

[70] A. G. Rajan, J. M. P. Martirez, and E. A. Carter. *Facet-Independent Oxygen Evolution Activity of Pure β-NiOOH: Different Chemistries Leading to Similar Overpotentials*. J. Am. Chem. Soc., 142(7), 3600–3612, 2020. doi: 10.1021/jacs.9b13708.

[71] A. Roldan. *Frontiers in first principles modelling of electrochemical simulations*. Curr. Opin. Electrochem., 10, 1–6, 2018. doi: 10.1016/j.coelec.2018.03.013.

[72] O. M. Magnussen and A. Groß. *Toward an Atomic-Scale Understanding of Electrochemical Interface Structure and Dynamics*. J. Am. Chem. Soc., 141(12), 4777–4790, 2019. doi: 10.1021/jacs.8b13188.

[73] A. Groß and S. Sakong. *Modelling the electric double layer at electrode/electrolyte interfaces*. Curr. Opin. Electrochem., 14, 1–6, 2019. doi: 10.1016/j.coelec.2018.09.005. Bioelectrochemistry, Electrocatalysis.

[74] N. Abidi, K. R. G. Lim, Z. W. Seh, and S. N. Steinmann. *Atomistic modeling of electrocatalysis: Are we there yet?* Wiley Interdiscip. Rev. Comput. Mol. Sci., 11(3), 2020. doi: 10.1002/wcms.1499.

[75] A. Groß. *Structure of Electrode-Electrolyte Interfaces, Modeling of Double Layer and Electrode Potential*. In *Handbook of Materials Modeling*, pages 1439–1472. Springer International Publishing, 2020. doi: 10.1007/978-3-319-44680-6_7.

[76] X.-H. Yang, Y.-B. Zhuang, J.-X. Zhu, J.-B. Le, and J. Cheng. *Recent progress on multi-scale modeling of electrochemistry*. Wiley Interdiscip. Rev. Comput. Mol. Sci., 2021. doi: 10.1002/wcms.1559.

[77] S. Ringe, N. G. Hörmann, H. Oberhofer, and K. Reuter. *Implicit Solvation Methods for Catalysis at Electrified Interfaces*. Chem. Rev., 122(12), 10777–10820, 2021. doi: 10.1021/acs.chemrev.1c00675.

[78] M. M. Melander, T. T. Laurila, and K. Laasonen, editors. *Atomic-Scale Modelling of Electrochemical Systems*. John Wiley & Sons, Hoboken, NJ, US, 2022. ISBN 978-1-119-60561-4. doi: 10.1007/978-3-642-04937-8.

[79] S. Sakong, J. Huang, M. Eikerling, and A. Groß. *The structure of the electric double layer: Atomistic versus continuum approaches*. Curr. Opin. Electrochem., 33, 100953, 2022. doi: 10.1016/j.coelec.2022.100953.

[80] I. G. Austin and N. F. Mott. *Metallic and Nonmetallic Behavior in Transition Metal Oxides*. Science, 168(3927), 71–77, 1970. doi: 10.1126/science.168.3927.71.

[81] V. I. Anisimov, J. Zaanen, and O. K. Andersen. *Band theory and Mott insulators: Hubbard U instead of Stoner I*. Phys. Rev. B, 44, 943–954, 1991. doi: 10.1103/PhysRevB.44.943.

[82] V. I. Anisimov, I. V. Solovyev, M. A. Korotin, M. T. Czyżyk, and G. A. Sawatzky. *Density-functional theory and NiO photoemission spectra*. Phys. Rev. B, 48(23), 16929–16934, 1993. doi: 10.1103/physrevb.48.16929.

[83] M. Sun, J. Stackhouse, and P. Kowalski. *The +2 oxidation state of Cr incorporated into the crystal lattice of* UO_2. Commun. Mater., 1, 13, 2020. doi: 10.1038/s43246-020-0014-5.

[84] L. Scalfi, M. Salanne, and B. Rotenberg. *Molecular Simulation of Electrode-Solution Interfaces*. Annu. Rev. Phys. Chem., 72(1), 189–212, 2021. doi: 10.1146/annurev-physchem-090519-024042.

[85] C. Zhang and M. Sprik. *Finite field methods for the supercell modeling of charged insulator/electrolyte interfaces*. Phys. Rev. B, 94, 245309, 2016. doi: 10.1103/PhysRevB.94.245309.

[86] T. Dufils, G. Jeanmairet, B. Rotenberg, M. Sprik, and M. Salanne. *Simulating Electrochemical Systems by Combining the Finite Field Method with a Constant Potential Electrode*. Phys. Rev. Lett., 123, 195501, 2019. doi: 10.1103/PhysRevLett.123.195501.

[87] C. Zhang, T. Sayer, J. Hutter, and M. Sprik. *Modelling electrochemical systems with finite field molecular dynamics*. J. Phys. Energy, 2(3), 032005, 2020. doi: 10.1088/2515-7655/ab9d8c.

[88] S. Surendralal, M. Todorova, M. W. Finnis, and J. Neugebauer. *First-Principles Approach to Model Electrochemical Reactions: Understanding the Fundamental Mechanisms behind Mg Corrosion*. Phys. Rev. Lett., 120, 246801, 2018. doi: 10.1103/PhysRevLett.120.246801.

[89] L. D. Chen, M. Urushihara, K. Chan, and J. K. Nørskov. *Electric field effects in electrochemical CO_2 reduction*. ACS Catal., 6(10), 7133–7139, 2016. doi: 10.1021/acscatal.6b02299.

[90] M. J. Eslamibidgoli, J. Huang, P. M. Kowalski, M. H. Eikerling, and A. Groß. *Deprotonation and cation adsorption on the NiOOH/water interface: A grand-canonical first-principles investigation*. Electrochim. Acta, 398, 139253, 2021. doi: 10.1016/j.electacta.2021.139253.

[91] Z.-F. Huang, J. Wang, Y. Peng, C.-Y. Jung, A. Fisher, and X. Wang. *Design of efficient bifunctional oxygen reduction/evolution electrocatalyst: recent advances and perspectives*. Adv. Energy Mater., 7(23), 1700544, 2017. doi: 10.1002/aenm.201700544.

[92] S. Sakong, D. Mahlberg, T. Roman, M. Li, M. Pandey, and A. Groß. *Influence of Local Inhomogeneities and the Electrochemical Environment on the Oxygen Reduction Reaction on Pt-Based Electrodes: A DFT Study*. J. Phys. Chem. C, 124(50), 27604–27613, 2020. doi: 10.1021/acs.jpcc.0c09548.

[93] W. Sheng, M. Myint, J. G. Chen, and Y. Yan. *Correlating the hydrogen evolution reaction activity in alkaline electrolytes with the hydrogen binding energy on monometallic surfaces*. Energy Environ. Sci., 6(5), 1509–1512, 2013. doi: 10.1039/C3EE00045A.

[94] Z.-D. He, J. Wei, Y.-X. Chen, E. Santos, and W. Schmickler. *Hydrogen evolution at Pt(111)–*

activation energy, frequency factor and hydrogen repulsion. Electrochim. Acta, 255, 391–395, 2017. doi: 10.1016/j.electacta.2017.09.127.

[95] M. R. Singh, J. D. Goodpaster, A. Z. Weber, M. Head-Gordon, and A. T. Bell. *Mechanistic insights into electrochemical reduction of CO_2 over Ag using density functional theory and transport models*. Proc. Natl. Acad. Sci., 114(42), E8812–E8821, 2017. doi: 10.1073/pnas.1713164114.

[96] A. Groß. *Grand-canonical approaches to understand structures and processes at electrochemical interfaces from an atomistic perspective*. Curr. Opin. Electrochem., 27, 100684, 2021. doi: 10.1016/j.coelec.2020.100684.

[97] F. Gossenberger, T. Roman, and A. Groß. *Equilibrium coverage of halides on metal electrodes*. Surf. Sci., 631, 17–22, 2015. doi: 10.1016/j.susc.2014.01.021.

[98] F. Gossenberger, T. Roman, and A. Groß. *Hydrogen and halide co-adsorption on Pt(111) in an electrochemical environment: a computational perspective*. Electrochim. Acta, 216, 152–159, 2016. doi: 10.1016/j.electacta.2016.08.117.

[99] F. Gossenberger, F. Juarez, and A. Groß. *Sulfate, bisulfate, and hydrogen co-adsorption on Pt(111) and Au(111) in an electrochemical environment*. Front. Chem., 8, 634, 2020. doi: 10.3389/fchem.2020.00634.

[100] M. Zhong, K. Tran, Y. Min, C. Wang, Z. Wang, C.-T. Dinh, P. De Luna, Z. Yu, A. S. Rasouli, P. Brodersen, et al. *Accelerated discovery of CO_2 electrocatalysts using active machine learning*. Nature, 581(7807), 178–183, 2020. doi: 10.1038/s41586-020-2242-8.

[101] Z. W. Ulissi, M. T. Tang, J. Xiao, X. Liu, D. A. Torelli, M. Karamad, K. Cummins, C. Hahn, N. S. Lewis, T. F. Jaramillo, et al. *Machine-learning methods enable exhaustive searches for active bimetallic facets and reveal active site motifs for CO_2 reduction*. ACS Catal., 7(10), 6600–6608, 2017. doi: 10.1021/acscatal.7b01648.

[102] M. H. Hansen and J. Rossmeisl. *pH in Grand Canonical Statistics of an Electrochemical Interface*. J. Phys. Chem. C, 120(51), 29135–29143, 2016. doi: 10.1021/acs.jpcc.6b09019.

[103] R. Sundararaman, W. A. Goddard, and T. A. Arias. *Grand canonical electronic density-functional theory: Algorithms and applications to electrochemistry*. J. Chem. Phys., 146(11), 114104, 2017. doi: 10.1063/1.4978411.

[104] S. Nishihara and M. Otani. *Hybrid solvation models for bulk, interface, and membrane: Reference interaction site methods coupled with density functional theory*. Phys. Rev. B, 96, 115429, 2017. doi: 10.1103/PhysRevB.96.115429. and Supplementary Information.

[105] N. G. Hörmann, O. Andreussi, and N. Marzari. *Grand canonical simulations of electrochemical interfaces in implicit solvation models*. J. Chem. Phys., 150(4), 041730, 2019. doi: 10.1063/1.5054580.

[106] M. M. Melander. *Grand canonical ensemble approach to electrochemical thermodynamics, kinetics, and model Hamiltonians*. Curr. Opin. Electrochem., 29, 100749, 2021. doi: 10.1016/j.coelec.2021.100749.

[107] M. Melander, T. Wu, and K. Honkala. *Constant inner potential DFT for modelling electrochemical systems under constant potential and bias*. preprint, 2023.

[108] A. Y. Lozovoi, A. Alavi, J. Kohanoff, and R. M. Lynden-Bell. *Ab initio simulation of charged slabs at constant chemical potential*. J. Chem. Phys., 115(4), 1661–1669, 2001. doi: 10.1063/1.1379327.

[109] N. Bonnet, T. Morishita, O. Sugino, and M. Otani. *First-Principles Molecular Dynamics at a Constant Electrode Potential*. Phys. Rev. Lett., 109, 266101, 2012. doi: 10.1103/PhysRevLett.109.266101.

[110] G. Kastlunger, P. Lindgren, and A. A. Peterson. *Controlled-Potential Simulation of Elementary Electrochemical Reactions: Proton Discharge on Metal Surfaces*. J. Phys. Chem. C, 122 (24), 12771–12781, 2018. doi: 10.1021/acs.jpcc.8b02465.

[111] F. Nattino, M. Truscott, N. Marzari, and O. Andreussi. *Continuum models of the electrochemical diffuse layer in electronic-structure calculations*. J. Chem. Phys., 150(4), 041722, 2019.

doi: 10.1063/1.5054588.

[112] J.-S. Filhol and M. Neurock. *Elucidation of the Electrochemical Activation of Water over Pd by First Principles*. Angew. Chem. Int. Ed., 45(3), 402–406, 2006. doi: 10.1002/anie.200502540.

[113] A. Hagopian, M.-L. Doublet, J.-S. Filhol, and T. Binninger. *Advancement of the Homogeneous Background Method for the Computational Simulation of Electrochemical Interfaces*. J. Chem. Theory Comput., 18(3), 1883–1893, 2022. doi: 10.1021/acs.jctc.1c01237.

[114] M. Otani and O. Sugino. *First-principles calculations of charged surfaces and interfaces: A plane-wave nonrepeated slab approach*. Phys. Rev. B, 73, 115407, 2006. doi: 10.1103/PhysRevB.73.115407.

[115] Y. J. Feng, K. P. Bohnen, and C. T. Chan. *First-principles studies of Au(100)-hex reconstruction in an electrochemical environment*. Phys. Rev. B, 72, 125401, 2005. doi: 10.1103/PhysRevB.72.125401.

[116] C. D. Taylor, S. A. Wasileski, J.-S. Filhol, and M. Neurock. *First principles reaction modeling of the electrochemical interface: Consideration and calculation of a tunable surface potential from atomic and electronic structure*. Phys. Rev. B, 73, 165402, 2006. doi: 10.1103/PhysRevB.73.165402.

[117] E. Skúlason, G. S. Karlberg, J. Rossmeisl, T. Bligaard, J. Greeley, H. Jónsson, and J. K. Nørskov. *Density functional theory calculations for the hydrogen evolution reaction in an electrochemical double layer on the Pt(111) electrode*. Phys. Chem. Chem. Phys., 9(25), 3241–3250, 2007. doi: 10.1039/b700099e.

[118] J. Rossmeisl, E. Skúlason, M. E. Björketun, V. Tripkovic, and J. K. Nørskov. *Modeling the electrified solid–liquid interface*. Chem. Phys. Lett., 466(1-3), 68–71, 2008. doi: 10.1016/j.cplett.2008.10.024.

[119] L. Braunwarth, C. Jung, and T. Jacob. *Potential-Dependent Pt(111)/Water Interface: Tackling the Challenge of a Consistent Treatment of Electrochemical Interfaces*. ChemPhysChem, 24 (1), 2022. doi: 10.1002/cphc.202200336.

[120] K. Letchworth-Weaver and T. A. Arias. *Joint density functional theory of the electrode-electrolyte interface: Application to fixed electrode potentials, interfacial capacitances, and potentials of zero charge*. Phys. Rev. B, 86, 075140, 2012. doi: 10.1103/PhysRevB.86.075140.

[121] J. Cheng and M. Sprik. *Aligning electronic energy levels at the TiO_2/H_2O interface*. Phys. Rev. B, 82, 081406, 2010. doi: 10.1103/PhysRevB.82.081406.

[122] J. Haruyama, T. Ikeshoji, and M. Otani. *Electrode potential from density functional theory calculations combined with implicit solvation theory*. Phys. Rev. Materials, 2, 095801, 2018. doi: 10.1103/PhysRevMaterials.2.095801.

[123] S. Trasatti. *The absolute electrode potential: an explanatory note (Recommendations 1986)*. Pure Appl. Chem., 58(7), 955–966, 1986. doi: 10.1351/pac198658070955.

[124] V. M. Fernandez-Alvarez and M. H. Eikerling. *Interface Properties of the Partially Oxidized Pt(111) Surface Using Hybrid DFT–Solvation Models*. ACS Appl. Mater. & Interfaces, 11(46), 43774–43780, 2019. doi: 10.1021/acsami.9b16326.

[125] O. Diaz-Morales, D. Ferrus-Suspedra, and M. T. M. Koper. *The importance of nickel oxyhydroxide deprotonation on its activity towards electrochemical water oxidation*. Chem. Sci., 7, 2639–2645, 2016. doi: 10.1039/C5SC04486C.

[126] C. Zhao and W. Zheng. *A Review for Aqueous Electrochemical Supercapacitors*. Front. Energy Res., 3, 2015. doi: 10.3389/fenrg.2015.00023.

[127] Y. Yokoyama, T. Fukutsuka, K. Miyazaki, and T. Abe. *Origin of the Electrochemical Stability of Aqueous Concentrated Electrolyte Solutions*. J. Electrochem. Soc., 165(14), A3299–A3303, 2018. doi: 10.1149/2.0491814jes.

[128] K. Xu. *Nonaqueous Liquid Electrolytes for Lithium-Based Rechargeable Batteries*. Chem. Rev., 104(10), 4303–4418, 2004. doi: 10.1021/cr030203g.

[129] T. Ludwig, A. R. Singh, and J. K. Nørskov. *Acetonitrile Transition Metal Interfaces from First Principles*. J. Phys. Chem. Lett., 11(22), 9802–9811, 2020. doi: 10.1021/acs.jpclett.0c02692.

[130] M. Kar and C. Pozo-Gonzalo. *Emergence of nonaqueous electrolytes for rechargeable zinc batteries*. Curr. Opin. Green Sustain. Chem., 28, 100426, 2021. doi: 10.1016/j.cogsc.2020.100426.

[131] C. Merlet, B. Rotenberg, P. A. Madden, and M. Salanne. *Computer simulations of ionic liquids at electrochemical interfaces*. Phys. Chem. Chem. Phys., 15(38), 15781, 2013. doi: 10.1039/c3cp52088a.

[132] M. V. Fedorov and A. A. Kornyshev. *Ionic Liquids at Electrified Interfaces*. Chem. Rev., 114 (5), 2978–3036, 2014. doi: 10.1021/cr400374x.

[133] L. Yu and G. Z. Chen. *Ionic Liquid-Based Electrolytes for Supercapacitor and Supercapattery*. Front. Chem., 7, 2019. doi: 10.3389/fchem.2019.00272.

[134] D. S. Silvester, R. Jamil, S. Doblinger, Y. Zhang, R. Atkin, and H. Li. *Electrical Double Layer Structure in Ionic Liquids and Its Importance for Supercapacitor, Battery, Sensing, and Lubrication Applications*. J. Phys. Chem. C, 125(25), 13707–13720, 2021. doi: 10.1021/acs.jpcc.1c03253.

[135] R. E. Skyner, J. L. McDonagh, C. R. Groom, T. van Mourik, and J. B. O. Mitchell. *A review of methods for the calculation of solution free energies and the modelling of systems in solution*. Phys. Chem. Chem. Phys., 17(9), 6174–6191, 2015. doi: 10.1039/c5cp00288e.

[136] D. Marx and J. Hutter. *Ab Initio Molecular Dynamics: Theory and Implementation*. In J. Grotendorst, editor, *Modern Methods and Algorithms of Quantum Chemistry*, pages 301–449. NIC Series, Jülich, 2000.

[137] H. H. Kristoffersen, T. Vegge, and H. A. Hansen. *OH formation and H_2 adsorption at the liquid water–Pt(111) interface*. Chem. Sci, 9(34), 6912–6921, 2018. doi: 10.1039/c8sc02495b.

[138] J.-B. Le and J. Cheng. *Modeling electrochemical interfaces from ab initio molecular dynamics: water adsorption on metal surfaces at potential of zero charge*. Curr. Opin. Electrochem., 19, 129–136, 2020. doi: 10.1016/j.coelec.2019.11.008.

[139] S. N. Steinmann, R. Ferreira De Morais, A. W. Götz, P. Fleurat-Lessard, M. Iannuzzi, P. Sautet, and C. Michel. *Force Field for Water over Pt(111): Development, Assessment, and Comparison*. J. Chem. Theory Comput., 14(6), 3238–3251, 2018. doi: 10.1021/acs.jctc.7b01177.

[140] M. Garcia-Ratés, R. García-Muelas, and N. López. *Solvation Effects on Methanol Decomposition on Pd(111), Pt(111), and Ru(0001)*. J. Phys. Chem. C, 121(25), 13803–13809, 2017. doi: 10.1021/acs.jpcc.7b05545.

[141] B. Schweitzer, S. N. Steinmann, and C. Michel. *Can microsolvation effects be estimated from vacuum computations? A case-study of alcohol decomposition at the H_2O/Pt(111) interface*. Phys. Chem. Chem. Phys., 21(10), 5368–5377, 2019. doi: 10.1039/c8cp06331a.

[142] N. G. Hörmann, Z. Guo, F. Ambrosio, O. Andreussi, A. Pasquarello, and N. Marzari. *Absolute band alignment at semiconductor-water interfaces using explicit and implicit descriptions for liquid water*. npj Comp. Mater., 5(1), 2019. doi: 10.1038/s41524-019-0238-4.

[143] M. Fan, M. J. Eslamibidgoli, X. Zhu, S. Garbarino, A. C. Tavares, M. Eikerling, and D. Guay. *Understanding the Improved Activity of Dendritic Sn1Pb3 Alloy for the CO2 Electrochemical Reduction: A Computational–Experimental Investigation*. ACS Catal., 10(18), 10726–10734, 2020. doi: 10.1021/acscatal.0c01785.

[144] X. Nie, M. R. Esopi, M. J. Janik, and A. Asthagiri. *Selectivity of CO2Reduction on Copper Electrodes: The Role of the Kinetics of Elementary Steps*. Angew. Chem., 125(9), 2519–2522, 2013. doi: 10.1002/ange.201208320.

[145] R. A. Marcus. *On the Theory of Oxidation-Reduction Reactions Involving Electron Transfer. I*. J. Chem. Phys., 24(5), 966–978, 1956. doi: 10.1063/1.1742723.

[146] R. A. Marcus. *On the Theory of Electron-Transfer Reactions. VI. Unified Treatment for Homogeneous and Electrode Reactions*. J. Chem. Phys., 43(2), 679–701, 1965. doi:

10.1063/1.1696792.

[147] H. Lin and D. G. Truhlar. *QM/MM: what have we learned, where are we, and where do we go from here?* Theor. Chem. Acc., 117(2), 185–199, 2006. doi: 10.1007/s00214-006-0143-z.

[148] L.-P. Wang and T. V. Voorhis. *A Polarizable QM/MM Explicit Solvent Model for Computational Electrochemistry in Water*. J. Chem. Theory Comput., 8(2), 610–617, 2012. doi: 10.1021/ct200340x.

[149] Z. Rinkevicius, X. Li, J. A. R. Sandberg, K. V. Mikkelsen, and H. Ågren. *A Hybrid Density Functional Theory/Molecular Mechanics Approach for Linear Response Properties in Heterogeneous Environments*. J. Chem. Theory Comput., 10(3), 989–1003, 2014. doi: 10.1021/ct400897s.

[150] S. Dohm, E. Spohr, and M. Korth. *Developing adaptive QM/MM computer simulations for electrochemistry*. J. Comput. Chem., 38(1), 51–58, 2016. doi: 10.1002/jcc.24513.

[151] S. Naserifar, Y. Chen, S. Kwon, H. Xiao, and W. A. Goddard. *Artificial Intelligence and QM/MM with a Polarizable Reactive Force Field for Next-Generation Electrocatalysts*. Matter, 4(1), 195–216, 2021. doi: 10.1016/j.matt.2020.11.010.

[152] T. Löytynoja, X. Li, K. Jänkälä, Z. Rinkevicius, and H. Ågren. *Quantum mechanics capacitance molecular mechanics modeling of core-electron binding energies of methanol and methyl nitrite on Ag(111) surface*. J. Chem. Phys., 145(2), 024703, 2016. doi: 10.1063/1.4956449.

[153] S. Miertuš, E. Scrocco, and J. Tomasi. *Electrostatic interaction of a solute with a continuum. A direct utilizaion of AB initio molecular potentials for the prevision of solvent effects*. Chem. Phys., 55(1), 117–129, 1981. doi: 10.1016/0301-0104(81)85090-2.

[154] A. Klamt and G. Schüürmann. *COSMO: a new approach to dielectric screening in solvents with explicit expressions for the screening energy and its gradient*. J. Chem. Soc., Perkin Trans. 2, 5, 799–805, 1993. doi: 10.1039/p29930000799.

[155] J.-L. Fattebert and F. Gygi. *Density functional theory for efficientab initio molecular dynamics simulations in solution*. J. Comput. Chem., 23(6), 662–666, 2002. doi: 10.1002/jcc.10069.

[156] O. Andreussi, I. Dabo, and N. Marzari. *Revised self-consistent continuum solvation in electronic-structure calculations*. J. Chem. Phys., 136(6), 064102, 2012. doi: 10.1063/1.3676407.

[157] D. Gunceler, K. Letchworth-Weaver, R. Sundararaman, K. A. Schwarz, and T. A. Arias. *The importance of nonlinear fluid response in joint density-functional theory studies of battery systems*. Model. Simul. Mater. Sci. Eng., 21(7), 074005, 2013. doi: 10.1088/0965-0393/21/7/074005.

[158] K. Mathew, R. Sundararaman, K. Letchworth-Weaver, T. A. Arias, and R. G. Hennig. *Implicit solvation model for density-functional study of nanocrystal surfaces and reaction pathways*. J. Chem. Phys., 140(8), 084106, 2014. doi: 10.1063/1.4865107.

[159] R. Sundararaman and W. A. Goddard. *The charge-asymmetric nonlocally determined local-electric (CANDLE) solvation model*. J. Chem. Phys., 142(6), 064107, 2015. doi: 10.1063/1.4907731.

[160] R. Sundararaman, K. A. Schwarz, K. Letchworth-Weaver, and T. A. Arias. *Spicing up continuum solvation models with SaLSA: The spherically averaged liquid susceptibility ansatz*. J. Chem. Phys., 142(5), 054102, 2015. doi: 10.1063/1.4906828.

[161] O. Andreussi, N. G. Hörmann, F. Nattino, G. Fisicaro, S. Goedecker, and N. Marzari. *Solvent-Aware Interfaces in Continuum Solvation*. J. Chem. Theory Comput., 15(3), 1996–2009, 2019. doi: 10.1021/acs.jctc.8b01174.

[162] H. H. Heenen, J. A. Gauthier, H. H. Kristoffersen, T. Ludwig, and K. Chan. *Solvation at metal/water interfaces: An ab initio molecular dynamics benchmark of common computational approaches*. J. Chem. Phys., 152(14), 144703, 2020. doi: 10.1063/1.5144912.

[163] N. G. Hörmann and K. Reuter. *Thermodynamic Cyclic Voltammograms Based on Ab Initio Calculations: Ag(111) in Halide-Containing Solutions*. J. Chem. Theory Comput., 17(3),

1782–1794, 2021. doi: 10.1021/acs.jctc.0c01166.

[164] I. Borukhov, D. Andelman, and H. Orland. *Steric Effects in Electrolytes: A Modified Poisson-Boltzmann Equation*. Phys. Rev. Lett., 79, 435–438, 1997. doi: 10.1103/PhysRevLett.79.435.

[165] K. Mathew, R. Sundararaman, K. Letchworth-Weaver, T. A. Arias, and R. G. Hennig. *Implicit solvation model for density-functional study of nanocrystal surfaces and reaction pathways.* J. Chem. Phys., 140, 084106, 2014. doi: 10.1063/1.4865107.

[166] K. Mathew, V. S. C. Kolluru, S. Mula, S. N. Steinmann, and R. G. Hennig. *Implicit self-consistent electrolyte model in plane-wave density-functional theory.* J. Chem. Phys., 151, 234101, 2019. doi: 10.1063/1.5132354.

[167] J. Bikerman. *XXXIX. Structure and capacity of electrical double layer*. Lond. Edinb. Dublin Philos. Mag. J. Sci., 33(220), 384–397, 1942. doi: 10.1080/14786444208520813.

[168] D. Chandler and H. C. Andersen. *Optimized Cluster Expansions for Classical Fluids. II. Theory of Molecular Liquids*. J. Chem. Phys., 57(5), 1930–1937, 1972. doi: 10.1063/1.1678513.

[169] S. A. Petrosyan, J.-F. Briere, D. Roundy, and T. A. Arias. *Joint density-functional theory for electronic structure of solvated systems*. Phys. Rev. B, 75, 205105, 2007. doi: 10.1103/PhysRevB.75.205105.

[170] R. Sundararaman, K. Letchworth-Weaver, K. A. Schwarz, D. Gunceler, Y. Ozhabes, and T. Arias. *JDFTx: Software for joint density-functional theory*. SoftwareX, 6, 278–284, 2017. doi: 10.1016/j.softx.2017.10.006.

[171] R. Sundararaman, K. Letchworth-Weaver, and T. A. Arias. *A computationally efficacious free-energy functional for studies of inhomogeneous liquid water*. J. Chem. Phys., 137(4), 044107, 2012. doi: 10.1063/1.4737392.

[172] R. Sundararaman and T. Arias. *Efficient classical density-functional theories of rigid-molecular fluids and a simplified free energy functional for liquid water*. Comput. Phys. Commun., 185(3), 818–825, 2014. doi: 10.1016/j.cpc.2013.11.013.

[173] R. Sundararaman, K. Letchworth-Weaver, and T. A. Arias. *A recipe for free-energy functionals of polarizable molecular fluids*. J. Chem. Phys., 140(14), 144504, 2014. doi: 10.1063/1.4870653.

[174] R. Jinnouchi and A. B. Anderson. *Electronic structure calculations of liquid-solid interfaces: Combination of density functional theory and modified Poisson-Boltzmann theory*. Phys. Rev. B, 77, 245417, 2008. doi: 10.1103/PhysRevB.77.245417.

[175] S. E. Weitzner, S. A. Akhade, J. B. Varley, B. C. Wood, M. Otani, S. E. Baker, and E. B. Duoss. *Toward Engineering of Solution Microenvironments for the CO2 Reduction Reaction: Unraveling pH and Voltage Effects from a Combined Density-Functional–Continuum Theory*. J. Phys. Chem. Lett., 11(10), 4113–4118, 2020. doi: 10.1021/acs.jpclett.0c00957.

[176] K. Kano, S. Hagiwara, T. Igarashi, and M. Otani. *Study on the free corrosion potential at an interface between an Al electrode and an acidic aqueous NaCl solution through density functional theory combined with the reference interaction site model*. Electrochim. Acta, 377, 138121, 2021. doi: 10.1016/j.electacta.2021.138121.

[177] J. Haruyama, T. Ikeshoji, and M. Otani. *Analysis of Lithium Insertion/Desorption Reaction at Interfaces between Graphite Electrodes and Electrolyte Solution Using Density Functional + Implicit Solvation Theory*. J. Phys. Chem. C, 122(18), 9804–9810, 2018. doi: 10.1021/acs.jpcc.8b01979.

[178] T. A. Pham, K. E. Kweon, A. Samanta, M. T. Ong, V. Lordi, and J. E. Pask. *Intercalation of Lithium into Graphite: Insights from First-Principles Simulations*. J. Phys. Chem. C, 124(40), 21985–21992, 2020. doi: 10.1021/acs.jpcc.0c06842.

[179] S. Hagiwara, Y. Ando, Y. Goto, S. Shinoki, and M. Otani. *Electronic, adsorption, and hydration structures of water-contained Na-montmorillonite and Na-beidellite through the first-principles method combined with the classical solution theory*. Phys. Rev. Mater., 6, 025001, 2022. doi: 10.1103/PhysRevMaterials.6.025001.

[180] C. Islas-Vargas, A. Guevara-García, and M. Galván. *Electronic structure behavior of PbO_2, IrO_2, and SnO_2 metal oxide surfaces (110) with dissociatively adsorbed water molecules as a function of the chemical potential*. J. Chem. Phys., 154(7), 2021. doi: 10.1063/5.0035208.

[181] J.-Q. Li, L. Meng, M. Sprik, and J. Cheng. *Thermodynamic Investigation of Proton/Electron Interplay on the Pourbaix Diagram at the TiO_2/Electrolyte Interface*. J. Phys. Chem. C, 124 (35), 19003–19014, 2020. doi: 10.1021/acs.jpcc.0c03546.

[182] J. Yang, M. Youssef, and B. Yildiz. *Charged species redistribution at electrochemical interfaces: a model system of the zirconium oxide/water interface*. Phys. Chem. Chem. Phys., 25 (8), 6380–6391, 2023. doi: 10.1039/d2cp05566j.

[183] C. Zhang, J. Hutter, and M. Sprik. *Coupling of Surface Chemistry and Electric Double Layer at TiO_2 Electrochemical Interfaces*. J. Phys. Chem. Lett., 10(14), 3871–3876, 2019. doi: 10.1021/acs.jpclett.9b01355.

[184] M. Jia, C. Zhang, and J. Cheng. *Origin of Asymmetric Electric Double Layers at Electrified Oxide/Electrolyte Interfaces*. J. Phys. Chem. Lett., 12(19), 4616–4622, 2021. doi: 10.1021/acs.jpclett.1c00775.

[185] J. Huang. *Hybrid density-potential functional theory of electric double layers*. Electrochim. Acta, 389, 138720, 2021. doi: 10.1016/j.electacta.2021.138720.

[186] Y. Zhou, Y. Ouyang, Y. Zhang, Q. Li, and J. Wang. *Machine Learning Assisted Simulations of Electrochemical Interfaces: Recent Progress and Challenges*. J. Phys. Chem. Lett., 14 (9), 2308–2316, 2023. doi: 10.1021/acs.jpclett.2c03288.

[187] R. Jinnouchi, J. Lahnsteiner, F. Karsai, G. Kresse, and M. Bokdam. *Phase Transitions of Hybrid Perovskites Simulated by Machine-Learning Force Fields Trained on the Fly with Bayesian Inference*. Phys. Rev. Lett., 122, 225701, 2019. doi: 10.1103/PhysRevLett.122.225701.

[188] S. Zhu, K. Jiang, B. Chen, and S. Zheng. *Data-driven design of electrocatalysts: principle, progress, and perspective*. J. Mater. Chem. A, 11(8), 3849–3870, 2023. doi: 10.1039/d2ta09278f.

[189] K. Chan and J. K. Nørskov. *Electrochemical Barriers Made Simple*. J. Phys. Chem. Lett., 6 (14), 2663–2668, 2015. doi: 10.1021/acs.jpclett.5b01043.

[190] K. Chan and J. K. Nørskov. *Potential Dependence of Electrochemical Barriers from ab Initio Calculations*. J. Phys. Chem. Lett., 7(9), 1686–1690, 2016. doi: 10.1021/acs.jpclett.6b00382.

[191] M. Cococcioni and S. de Gironcoli. *Linear response approach to the calculation of the effective interaction parameters in the LDA+U method*. Phys. Rev. B, 71, 035105, 2005. doi: 10.1103/PhysRevB.71.035105.

[192] F. Jensen. *Introduction to Computational Chemistry*. Wiley-VCH, 3rd edition, 2017.

[193] W. Koch and M. C. Holthausen. *A Chemist's Guide to Density Functional Theory*. Wiley-VCH, 2nd edition, 2001.

[194] E. Schrödinger. *Quantisierung als Eigenwertproblem*. Ann. Phys., 384(4), 361–376, 1926. doi: 10.1002/andp.19263840404.

[195] H. Nakashima and H. Nakatsuji. *Solving the Schrödinger equation for helium atom and its isoelectronic ions with the free iterative complement interaction (ICI) method*. J. Chem. Phys., 127(22), 2007. doi: 10.1063/1.2801981.

[196] P.-F. Loos and P. M. W. Gill. *The uniform electron gas*. Wiley Interdiscip. Rev. Comput. Mol. Sci., 6(4), 410–429, 2016. doi: 10.1002/wcms.1257.

[197] M. Born and R. Oppenheimer. *Zur Quantentheorie der Molekeln*. Ann. Phys., 389(20), 457–484, 1927. doi: 10.1002/andp.19273892002.

[198] A. Szabo and N. S. Ostlund. *Modern Quantum Chemistry: Introduction to Advanced Electronic Structure Theory*. Dover Publications, Inc., Mineola, New York, 1st edition, 1989.

[199] T. Koopmans. *Über die Zuordnung von Wellenfunktionen und Eigenwerten zu den Einzelnen Elektronen eines Atoms*. Physica, 1(1), 104–113, 1934. doi: 10.1016/S0031-8914(34)90011-2.

[200] S. Jahn and P. M. Kowalski. *Theoretical Approaches to Structure and Spectroscopy of Earth Materials*. Rev. Mineral. Geochem., 78(1), 691–743, 2014. doi: 10.2138/rmg.2014.78.17.

[201] P. Hohenberg and W. Kohn. *Inhomogeneous Electron Gas*. Phys. Rev., 136, B864–B871, 1964. doi: 10.1103/PhysRev.136.B864.

[202] W. Kohn and L. J. Sham. *Self-Consistent Equations Including Exchange and Correlation Effects*. Phys. Rev., 140(4A), A1133–A1138, 1965. doi: 10.1103/PhysRev.140.A1133.

[203] J. P. John and K. Schmidt. *Jacob's ladder of density functional approximations for the exchange-correlation energy*. AIP Conf. Proc., 577(1), 1–20, 2001. doi: 10.1063/1.1390175.

[204] J. P. Perdew. *Climbing the ladder of density functional approximations*. MRS Bulletin, 38(9), 743–750, 2013. doi: 10.1557/mrs.2013.178.

[205] J. P. Perdew, K. Burke, and M. Ernzerhof. *Generalized Gradient Approximation Made Simple*. Phys. Rev. Lett., 77, 3865–3868, 1996. doi: 10.1103/PhysRevLett.77.3865.

[206] J. P. Perdew, J. A. Chevary, S. H. Vosko, K. A. Jackson, M. R. Pederson, D. J. Singh, and C. Fiolhais. *Atoms, molecules, solids, and surfaces: Applications of the generalized gradient approximation for exchange and correlation*. Phys. Rev. B, 46, 6671–6687, 1992. doi: 10.1103/PhysRevB.46.6671.

[207] J. Tao, J. P. Perdew, V. N. Staroverov, and G. E. Scuseria. *Climbing the Density Functional Ladder: Nonempirical Meta–Generalized Gradient Approximation Designed for Molecules and Solids*. Phys. Rev. Lett., 91, 146401, 2003. doi: 10.1103/PhysRevLett.91.146401.

[208] J. Sun, A. Ruzsinszky, and J. P. Perdew. *Strongly Constrained and Appropriately Normed Semilocal Density Functional*. Phys. Rev. Lett., 115, 036402, 2015. doi: 10.1103/PhysRevLett.115.036402.

[209] C. Adamo and V. Barone. *Toward reliable density functional methods without adjustable parameters: The PBE0 model*. J. Chem. Phys., 110(13), 6158–6170, 1999. doi: 10.1063/1.478522.

[210] J. Heyd, G. E. Scuseria, and M. Ernzerhof. *Hybrid functionals based on a screened Coulomb potential*. J. Chem. Phys., 118(18), 8207–8215, 2003. doi: 10.1063/1.1564060.

[211] S. Grimme. *Semiempirical hybrid density functional with perturbative second-order correlation*. J. Chem. Phys., 124(3), 2006. doi: 10.1063/1.2148954.

[212] S. Grimme, J. Antony, S. Ehrlich, and H. Krieg. *A consistent and accurate ab initio parametrization of density functional dispersion correction (DFT-D) for the 94 elements H-Pu*. J. Chem. Phys., 132(15), 154104, 2010. doi: 10.1063/1.3382344.

[213] A. Tkatchenko and M. Scheffler. *Accurate Molecular Van Der Waals Interactions from Ground-State Electron Density and Free-Atom Reference Data*. Phys. Rev. Lett., 102, 073005, 2009. doi: 10.1103/PhysRevLett.102.073005.

[214] C. Kittel. *Introduction to Solid State Physics*. John Wiley & Sons, 8th edition, 2005.

[215] F. Bloch. *Über die Quantenmechanik der Elektronen in Kristallgittern*. Z. Phys., 52(7), 555–600, 1929. doi: 10.1007/BF01339455.

[216] H. Hellmann. *A New Approximation Method in the Problem of Many Electrons*. J. Chem. Phys., 3(1), 61–61, 1935. doi: 10.1063/1.1749559.

[217] P. Schwerdtfeger. *The Pseudopotential Approximation in Electronic Structure Theory*. ChemPhysChem, 12(17), 3143–3155, 2011. doi: 10.1002/cphc.201100387.

[218] H. J. Monkhorst and J. D. Pack. *Special points for Brillouin-zone integrations*. Phys. Rev. B, 13, 5188–5192, 1976. doi: 10.1103/PhysRevB.13.5188.

[219] V. I. Anisimov, J. Zaanen, and O. K. Andersen. *Band theory and Mott insulators: Hubbard U instead of Stoner I*. Phys. Rev. B, 44, 943–954, 1991. doi: 10.1103/PhysRevB.44.943.

[220] V. I. Anisimov and O. Gunnarsson. *Density-functional calculation of effective Coulomb interactions in metals*. Phys. Rev. B, 43, 7570–7574, 1991. doi: 10.1103/PhysRevB.43.7570.

[221] V. I. Anisimov, I. V. Solovyev, M. A. Korotin, M. T. Czyżyk, and G. A. Sawatzky. *Density-functional theory and NiO photoemission spectra*. Phys. Rev. B, 48, 16929–16934, 1993. doi: 10.1103/PhysRevB.48.16929.

[222] I. V. Solovyev, P. H. Dederichs, and V. I. Anisimov. *Corrected atomic limit in the local-density approximation and the electronic structure of d impurities in Rb*. Phys. Rev. B, 50, 16861–16871, 1994. doi: 10.1103/PhysRevB.50.16861.

[223] B. Himmetoglu, A. Floris, S. de Gironcoli, and M. Cococcioni. *Hubbard-corrected DFT energy functionals: The LDA+U description of correlated systems*. Int. J. Quantum Chem., 114(1), 14–49, 2013. doi: 10.1002/qua.24521.

[224] M. Cococcioni. *The LDA+U Approach: A Simple Hubbard Correction for Correlated Ground States*. In E. Pavarini, E. Koch, F. Anders, and M. Jarrell, editors, *Correlated Electrons: From Models to Materials*, volume 2. Forschungszentrum Jülich, 2012. Lecture Notes of the Autumn School Correlated Electrons 2012, Jülich.

[225] J. Hubbard. *Electron correlations in narrow energy bands*. Proc. R. Soc. A: Math. Phys. Sci., 276(1365), 238–257, 1963. doi: 10.1098/rspa.1963.0204.

[226] A. I. Liechtenstein, V. I. Anisimov, and J. Zaanen. *Density-functional theory and strong interactions: Orbital ordering in Mott-Hubbard insulators*. Phys. Rev. B, 52, R5467–R5470, 1995. doi: 10.1103/PhysRevB.52.R5467.

[227] S. L. Dudarev, G. A. Botton, S. Y. Savrasov, C. J. Humphreys, and A. P. Sutton. *Electron-energy-loss spectra and the structural stability of nickel oxide: An LSDA+U study*. Phys. Rev. B, 57, 1505–1509, 1998. doi: 10.1103/PhysRevB.57.1505.

[228] E. Şaşıoğlu, C. Friedrich, and S. Blügel. *Effective Coulomb interaction in transition metals from constrained random-phase approximation*. Phys. Rev. B, 83, 121101, 2011. doi: 10.1103/PhysRevB.83.121101.

[229] G.-Y. Huang, C.-Y. Wang, and J.-T. Wang. *Detailed check of the LDA+U and GGA+U corrected method for defect calculations in wurtzite ZnO*. Comput. Phys. Commun., 183(8), 1749 – 1752, 2012. doi: 10.1016/j.cpc.2012.03.017.

[230] S. Laubach, P. C. Schmidt, A. Thißen, F. J. Fernandez-Madrigal, Q.-H. Wu, W. Jaegermann, M. Klemm, and S. Horn. *Theoretical and experimental determination of the electronic structure of V_2O_5, reduced V_2O_{5-x} and sodium intercalated NaV_2O_5*. Phys. Chem. Chem. Phys., 9, 2564–2576, 2007. doi: 10.1039/B612489E.

[231] S. Lutfalla, V. Shapovalov, and A. T. Bell. *Calibration of the DFT/GGA+U Method for Determination of Reduction Energies for Transition and Rare Earth Metal Oxides of Ti, V, Mo, and Ce*. J. Chem. Theory Comput., 7(7), 2218–2223, 2011. doi: 10.1021/ct200202g.

[232] C. W. M. Castleton, J. Kullgren, and K. Hermansson. *Tuning LDA+U for electron localization and structure at oxygen vacancies in ceria*. J. Chem. Phys., 127(24), 244704, 2007. doi: 10.1063/1.2800015.

[233] W. Chen, P. Yuan, S. Zhang, Q. Sun, E. Liang, and Y. Jia. *Electronic properties of anatase TiO_2 doped by lanthanides: A DFT+U study*. Phys. B: Condens. Matter, 407(6), 1038 – 1043, 2012. doi: 10.1016/j.physb.2012.01.085.

[234] J. T. Pegg, X. Aparicio-Anglès, M. Storr, and N. H. de Leeuw. *DFT+U study of the structures and properties of the actinide dioxides*. J. Nucl. Mater., 492, 269–278, 2017. doi: 10.1016/j.jnucmat.2017.05.025.

[235] R. Tesch and P. M. Kowalski. *Hubbard U parameters for transition metals from first principles*. Phys. Rev. B, 105, 195153, 2022. doi: 10.1103/PhysRevB.105.195153.

[236] C. Herring. *Magnetism*. pages 187–240. Academic Press: New York, 1966.

[237] B. N. Cox, M. A. Coulthard, and P. Lloyd. *A calculation of the Coulomb correlation energy, U, for transition metals in Hubbard's model*. J. Phys. F: Metal Phys., 4(6), 807–820, 1974. doi: 10.1088/0305-4608/4/6/009.

[238] I. Schnell, G. Czycholl, and R. C. Albers. *Hubbard-U calculations for Cu from first-principle Wannier functions*. Phys. Rev. B, 65, 075103, 2002. doi: 10.1103/PhysRevB.65.075103.

[239] K. Nakamura, R. Arita, Y. Yoshimoto, and S. Tsuneyuki. *First-principles calculation of effective onsite Coulomb interactions of $3d$ transition metals: Constrained local density functional approach with maximally localized Wannier functions*. Phys. Rev. B, 74, 235113, 2006. doi:

10.1103/PhysRevB.74.235113.

[240] N. J. Mosey and E. A. Carter. *Ab initio evaluation of Coulomb and exchange parameters for DFT+U calculations*. Phys. Rev. B, 76(15), 2007. doi: 10.1103/PhysRevB.76.155123.

[241] N. J. Mosey, P. Liao, and E. A. Carter. *Rotationally invariant ab initio evaluation of Coulomb and exchange parameters for DFT+U calculations*. J. Chem. Phys., 129(1), 014103, 2008. doi: 10.1063/1.2943142.

[242] M. Springer and F. Aryasetiawan. *Frequency-dependent screened interaction in Ni within the random-phase approximation*. Phys. Rev. B, 57, 4364–4368, 1998. doi: 10.1103/PhysRevB.57.4364.

[243] F. Aryasetiawan, M. Imada, A. Georges, G. Kotliar, S. Biermann, and A. I. Lichtenstein. *Frequency-dependent local interactions and low-energy effective models from electronic structure calculations*. Phys. Rev. B, 70, 195104, 2004. doi: 10.1103/PhysRevB.70.195104.

[244] F. Aryasetiawan, K. Karlsson, O. Jepsen, and U. Schönberger. *Calculations of Hubbard U from first-principles*. Phys. Rev. B, 74, 125106, 2006. doi: 10.1103/PhysRevB.74.125106.

[245] I. V. Solovyev and M. Imada. *Screening of Coulomb interactions in transition metals*. Phys. Rev. B, 71, 045103, 2005. doi: 10.1103/PhysRevB.71.045103.

[246] A. B. Romero, P. M. Kowalski, G. Beridze, H. Schlenz, and D. Bosbach. *Performance of DFT+U method for prediction of structural and thermodynamic parameters of monazite-type ceramics*. J. Comput. Chem., 35(18), 1339–1346, 2014. doi: 10.1002/jcc.23618.

[247] H. J. Kulik, M. Cococcioni, D. A. Scherlis, and N. Marzari. *Density Functional Theory in Transition-Metal Chemistry: A Self-Consistent Hubbard U Approach*. Phys. Rev. Lett., 97, 103001, 2006. doi: 10.1103/PhysRevLett.97.103001.

[248] I. Timrov, N. Marzari, and M. Cococcioni. *Hubbard parameters from density-functional perturbation theory*. Phys. Rev. B, 98, 085127, 2018. doi: 10.1103/PhysRevB.98.085127.

[249] M. Kick, K. Reuter, and H. Oberhofer. *Intricacies of DFT+U, Not Only in a Numeric Atom Centered Orbital Framework*. J. Chem. Theory Comput., 15(3), 1705–1718, 2019. doi: 10.1021/acs.jctc.8b01211.

[250] N. Marzari and D. Vanderbilt. *Maximally localized generalized Wannier functions for composite energy bands*. Phys. Rev. B, 56(20), 12847–12865, 1997. doi: 10.1103/physrevb.56.12847.

[251] I. Souza, N. Marzari, and D. Vanderbilt. *Maximally localized Wannier functions for entangled energy bands*. Phys. Rev. B, 65, 035109, 2001. doi: 10.1103/PhysRevB.65.035109.

[252] D. Novoselov, D. M. Korotin, and V. I. Anisimov. *Hellmann–Feynman forces within the DFT+U in Wannier functions basis*. J. Phys. Condens. Matter, 27(32), 325602, 2015. doi: 10.1088/0953-8984/27/32/325602.

[253] A. I. Liechtenstein, V. I. Anisimov, and J. Zaanen. *Density-functional theory and strong interactions: Orbital ordering in Mott-Hubbard insulators*. Phys. Rev. B, 52, R5467–R5470, 1995. doi: 10.1103/PhysRevB.52.R5467.

[254] M. T. Czyżyk and G. A. Sawatzky. *Local-density functional and on-site correlations: The electronic structure of* La_2CuO_4 *and* $LaCuO_3$. Phys. Rev. B, 49, 14211–14228, 1994. doi: 10.1103/PhysRevB.49.14211.

[255] A. G. Petukhov, I. I. Mazin, L. Chioncel, and A. I. Lichtenstein. *Correlated metals and the* LDA + *U method*. Phys. Rev. B, 67, 153106, 2003. doi: 10.1103/PhysRevB.67.153106.

[256] P. Giannozzi, S. Baroni, N. Bonini, M. Calandra, R. Car, C. Cavazzoni, D. Ceresoli, G. L. Chiarotti, M. Cococcioni, I. Dabo, A. D. Corso, S. de Gironcoli, S. Fabris, G. Fratesi, R. Gebauer, U. Gerstmann, C. Gougoussis, A. Kokalj, M. Lazzeri, L. Martin-Samos, N. Marzari, F. Mauri, R. Mazzarello, S. Paolini, A. Pasquarello, L. Paulatto, C. Sbraccia, S. Scandolo, G. Sclauzero, A. P. Seitsonen, A. Smogunov, P. Umari, and R. M. Wentzcovitch. *QUANTUM ESPRESSO: a modular and open-source software project for quantum simulations of materials*. J. Phys. Condens. Matter, 21(39), 395502, 2009. doi: 10.1088/0953-8984/21/39/395502.

[257] J. P. Hansen and I. R. McDonald. *Theory of Simple Liquids*. Academic, London, 1976.

[258] E. L. Ratkova, D. S. Palmer, and M. V. Fedorov. *Solvation Thermodynamics of Organic Molecules by the Molecular Integral Equation Theory: Approaching Chemical Accuracy*. Chem. Rev., 115(13), 6312–6356, 2015. doi: 10.1021/cr5000283.

[259] L. S. Ornstein and F. Zernike. *Accidental deviations of density and opalescence at the critical point of a single substance*. Proc. Acad. Sci. Amsterdam, 17, 793–806, 1914.

[260] J. K. Percus and G. J. Yevick. *Analysis of Classical Statistical Mechanics by Means of Collective Coordinates*. Phys. Rev., 110, 1–13, 1958. doi: 10.1103/PhysRev.110.1.

[261] A. Kovalenko and F. Hirata. *Self-consistent description of a metal–water interface by the Kohn–Sham density functional theory and the three-dimensional reference interaction site model*. J. Chem. Phys., 110(20), 10095–10112, 1999. doi: 10.1063/1.478883.

[262] D. Beglov and B. Roux. *An Integral Equation To Describe the Solvation of Polar Molecules in Liquid Water*. J. Phys. Chem. B, 101(39), 7821–7826, 1997. doi: 10.1021/jp971083h.

[263] H. Sato, A. Kovalenko, and F. Hirata. *Self-consistent field, ab initio molecular orbital and three-dimensional reference interaction site model study for solvation effect on carbon monoxide in aqueous solution*. J. Chem. Phys., 112(21), 9463–9468, 2000. doi: 10.1063/1.481564.

[264] H. A. Lorentz. *Ueber die Anwendung des Satzes vom Virial in der kinetischen Theorie der Gase*. Ann. Phys., 248(1), 127–136, 1881. doi: 10.1002/andp.18812480110.

[265] G. Beridze and P. M. Kowalski. *Benchmarking the DFT+U Method for Thermochemical Calculations of Uranium Molecular Compounds and Solids*. J. Phys. Chem. A, 118(50), 11797–11810, 2014. doi: 10.1021/jp5101126.

[266] G. L. Murphy, C.-H. Wang, G. Beridze, Z. Zhang, J. A. Kimpton, M. Avdeev, P. M. Kowalski, and B. J. Kennedy. *Unexpected Crystallographic Phase Transformation in Nonstoichiometric $SrUO_{4-x}$: Reversible Oxygen Defect Ordering and Symmetry Lowering with Increasing Temperature*. Inorg. Chem., 57(10), 5948–5958, 2018. doi: 10.1021/acs.inorgchem.8b00463.

[267] G. L. Murphy, C.-H. Wang, Z. Zhang, P. M. Kowalski, G. Beridze, M. Avdeev, O. Muransky, H. E. Brand, Q.-F. Gu, and B. J. Kennedy. *Controlling Oxygen Defect Formation and Its Effect on Reversible Symmetry Lowering and Disorder-to-Order Phase Transformations in Nonstoichiometric Ternary Uranium Oxides*. Inorg. Chem., 58(9), 6143–6154, 2019. doi: 10.1021/acs.inorgchem.9b00406.

[268] K. O. Kvashnina, P. M. Kowalski, S. M. Butorin, G. Leinders, J. Pakarinen, R. Bès, H. Li, and M. Verwerft. *Trends in the valence band electronic structures of mixed uranium oxides*. Chem. Commun., 54(70), 9757–9760, 2018. doi: 10.1039/c8cc05464a.

[269] P. Bots, K. Morris, R. Hibberd, G. T. W. Law, J. F. W. Mosselmans, A. P. Brown, J. Doutch, A. J. Smith, and S. Shaw. *Formation of Stable Uranium(VI) Colloidal Nanoparticles in Conditions Relevant to Radioactive Waste Disposal*. Langmuir, 30(48), 14396–14405, 2014. doi: 10.1021/la502832j.

[270] D. Akiyama, H. Akiyama, A. Uehara, A. Kirishima, and N. Sato. *Phase analysis of uranium oxides after reaction with stainless steel components and ZrO_2 at high temperature by XRD, XAFS, and SEM/EDX*. J. Nucl. Mater., 520, 27–33, 2019. doi: 10.1016/j.jnucmat.2019.03.055.

[271] G. L. Murphy, Z. Zhang, R. Tesch, P. M. Kowalski, M. Avdeev, E. Y. Kuo, D. J. Gregg, P. Kegler, E. V. Alekseev, and B. J. Kennedy. *Tilting and Distortion in Rutile-Related Mixed Metal Ternary Uranium Oxides: A Structural, Spectroscopic, and Theoretical Investigation*. Inorg. Chem., 60, 2246–2260, 2021. doi: 10.1021/acs.inorgchem.0c03077.

[272] G. L. Murphy, P. Kegler, Y. Zhang, Z. Zhang, E. V. Alekseev, M. D. de Jonge, and B. J. Kennedy. *High-Pressure Synthesis, Structural, and Spectroscopic Studies of the Ni–U–O System*. Inorg. Chem., 57(21), 13847–13858, 2018. doi: 10.1021/acs.inorgchem.8b02355.

[273] R. G. Denning. *Electronic Structure and Bonding in Actinyl Ions and their Analogs*. J. Phys. Chem. A, 111(20), 4125–4143, 2007. doi: 10.1021/jp071061n.

[274] T. Vitova, I. Pidchenko, D. Fellhauer, P. S. Bagus, Y. Joly, T. Pruessmann, S. Bahl, E. Gonzalez-Robles, J. Rothe, M. Altmaier, M. A. Denecke, and H. Geckeis. *The role of the 5f valence orbitals of early actinides in chemical bonding*. Nat. Commun., 8(1), 2017. doi: 10.1038/ncomms16053.

[275] G. L. Murphy, B. J. Kennedy, J. A. Kimpton, Q. Gu, B. Johannessen, G. Beridze, P. M. Kowalski, D. Bosbach, M. Avdeev, and Z. Zhang. *Nonstoichiometry in Strontium Uranium Oxide: Understanding the Rhombohedral–Orthorhombic Transition in $SrUO_4$*. Inorg. Chem., 55(18), 9329–9334, 2016. doi: 10.1021/acs.inorgchem.6b01391.

[276] J. P. Perdew, A. Ruzsinszky, G. I. Csonka, O. A. Vydrov, G. E. Scuseria, L. A. Constantin, X. Zhou, and K. Burke. *Restoring the Density-Gradient Expansion for Exchange in Solids and Surfaces*. Phys. Rev. Lett., 100, 136406, 2008. doi: 10.1103/PhysRevLett.100.136406.

[277] M. Methfessel and A. T. Paxton. *High-precision sampling for Brillouin-zone integration in metals*. Phys. Rev. B, 40, 3616–3621, 1989. doi: 10.1103/PhysRevB.40.3616.

[278] N. Marzari. *Maximally-localized Wannier functions*, 2021. Virtual School on Electron-Phonon Physics and the EPW code.

[279] A. Morales-García, S. Rhatigan, M. Nolan, and F. Illas. *On the use of DFT+U to describe the electronic structure of TiO_2 nanoparticles: $(TiO_2)_{35}$ as a case study*. J. Chem. Phys., 152 (24), 244107, 2020. doi: 10.1063/5.0012271.

[280] P. M. Kowalski, Z. He, and O. Cheong. *Electrode and Electrolyte Materials From Atomistic Simulations: Properties of Li_xFePO_4 Electrode and Zircon-Based Ionic Conductors*. Front. Energy Res., 9, 107, 2021. doi: 10.3389/fenrg.2021.653542.

[281] G. L. Murphy, Z. Zhang, R. Tesch, P. M. Kowalski, M. Avdeev, E. Y. Kuo, D. J. Gregg, P. Kegler, E. V. Alekseev, and B. J. Kennedy. *Tilting and Distortion in Rutile-Related Mixed Metal Ternary Uranium Oxides: A Structural, Spectroscopic, and Theoretical Investigation*. Inorg. Chem., 60, 2246–2260, 2021. doi: 10.1021/acs.inorgchem.0c03077.

[282] T. Connor, O. Cheong, T. Bornhake, A. C. Shad, R. Tesch, M. Sun, Z. He, A. Bukayemsky, V. L. Vinograd, S. C. Finkeldei, and P. M. Kowalski. *Pyrochlore Compounds From Atomistic Simulations*. Front. Chem., 9, 2021. doi: 10.3389/fchem.2021.733321.

[283] P. Anithakumari, V. Grover, C. Nandi, K. Bhattacharyya, and A. K. Tyagi. *Utilizing non-stoichiometry in $Nd_2Zr_2O_7$ pyrochlore: exploring superior ionic conductors*. RSC Adv., 6 (100), 97566–97579, 2016. doi: 10.1039/c6ra08722a.

[284] R. C. Ewing, W. J. Weber, and J. Lian. *Nuclear waste disposal – pyrochlore ($A_2B_2O_7$): Nuclear waste form for the immobilization of plutonium and "minor" actinides*. J. Appl. Phys., 95(11), 5949–5971, 2004. doi: 10.1063/1.1707213.

[285] G. Beridze, A. Birnie, S. Koniski, Y. Ji, and P. M. Kowalski. *DFT+U as a reliable method for efficient ab initio calculations of nuclear materials*. Prog. Nucl. Energy, 92, 142–146, 2016. doi: 10.1016/j.pnucene.2016.07.012.

[286] Y. Li, P. M. Kowalski, G. Beridze, A. R. Birnie, S. Finkeldei, and D. Bosbach. *Defect formation energies in $A_2B_2O_7$ pyrochlores*. Scr. Mater., 107, 18–21, 2015. doi: 10.1016/j.scriptamat.2015.05.010.

[287] S. Hüfner and G. K. Wertheim. *Estimates of the Coulomb Correlation Energy from X-Ray Photoemission Data*. Phys. Rev. B, 7, 5086–5090, 1973. doi: 10.1103/PhysRevB.7.5086.

[288] A. Kotani and T. Yamazaki. *Systematic Analysis of Core Photoemission Spectra for Actinide Di-Oxides and Rare-Earth Sesqui-Oxides*. Prog. Theor. Phys., 108, 117–131, 1992. doi: 10.1143/ptps.108.117.

[289] B. Huang. *4f fine-structure levels as the dominant error in the electronic structures of binary lanthanide oxides*. J. Comput. Chem., 37(9), 825–835, 2015. doi: 10.1002/jcc.24272.

[290] Z.-D. He, R. Tesch, M. J. Eslamibidgoli, M. H. Eikerling, and P. M. Kowalski. *Low-spin state of Fe in Fe-doped NiOOH electrocatalysts*. Nat. Commun., 14(1), 2023. doi: 10.1038/s41467-023-38978-5.

[291] Y.-F. Li and A. Selloni. *Mechanism and Activity of Water Oxidation on Selected Surfaces of*

Pure and Fe-Doped NiO_x. ACS Catal., 4(4), 1148–1153, 2014. doi: 10.1021/cs401245q.

[292] L.-F. Li, Y.-F. Li, and Z.-P. Liu. *Oxygen Evolution Activity on NiOOH Catalysts: Four-Coordinated Ni Cation as the Active Site and the Hydroperoxide Mechanism*. ACS Catal., 10 (4), 2581–2590, 2020. doi: 10.1021/acscatal.9b04975.

[293] T. Eom, H.-K. Lim, W. A. Goddard, and H. Kim. *First-Principles Study of Iron Oxide Polytypes: Comparison of GGA+U and Hybrid Functional Method*. J. Phys. Chem. C, 119(1), 556–562, 2014. doi: 10.1021/jp508096b.

[294] D. Friebel, M. W. Louie, M. Bajdich, K. E. Sanwald, Y. Cai, A. M. Wise, M.-J. Cheng, D. Sokaras, T.-C. Weng, R. Alonso-Mori, R. C. Davis, J. R. Bargar, J. K. Nørskov, A. Nilsson, and A. T. Bell. *Identification of Highly Active Fe Sites in (Ni,Fe)OOH for Electrocatalytic Water Splitting*. J. Am. Chem. Soc., 137(3), 1305–1313, 2015. doi: 10.1021/ja511559d.

[295] Z. K. Goldsmith, A. K. Harshan, J. B. Gerken, M. Vörös, G. Galli, S. S. Stahl, and S. Hammes-Schiffer. *Characterization of NiFe oxyhydroxide electrocatalysts by integrated electronic structure calculations and spectroelectrochemistry*. Proc. Natl. Acad. Sci., 114(12), 3050–3055, 2017. doi: 10.1073/pnas.1702081114.

[296] M. T. Bender, Y. C. Lam, S. Hammes-Schiffer, and K.-S. Choi. *Unraveling Two Pathways for Electrochemical Alcohol and Aldehyde Oxidation on NiOOH*. J. Am. Chem. Soc., 142(51), 21538–21547, 2020. doi: 10.1021/jacs.0c10924.

[297] S. L. Dudarev, G. A. Botton, S. Y. Savrasov, C. J. Humphreys, and A. P. Sutton. *Electron-energy-loss spectra and the structural stability of nickel oxide: An LSDA+U study*. Phys. Rev. B, 57, 1505–1509, 1998. doi: 10.1103/PhysRevB.57.1505.

[298] O. Bengone, M. Alouani, P. Blöchl, and J. Hugel. *Implementation of the projector augmented-wave LDA+U method: Application to the electronic structure of NiO*. Phys. Rev. B, 62, 16392–16401, 2000. doi: 10.1103/PhysRevB.62.16392.

[299] W.-B. Zhang and B.-Y. Tang. *Stability of the polar NiO(111) surface*. J. Chem. Phys., 128 (12), 124703, 2008. doi: 10.1063/1.2835544.

[300] C. J. Flynn, S. M. McCullough, L. Li, C. L. Donley, Y. Kanai, and J. F. Cahoon. *Passivation of Nickel Vacancy Defects in Nickel Oxide Solar Cells by Targeted Atomic Deposition of Boron*. J. Phys. Chem. C, 120(30), 16568–16576, 2016. doi: 10.1021/acs.jpcc.6b06593.

[301] A. Rohrbach, J. Hafner, and G. Kresse. *Molecular adsorption on the surface of strongly correlated transition-metal oxides: A case study for CO/NiO(100)*. Phys. Rev. B, 69, 075413, 2004. doi: 10.1103/PhysRevB.69.075413.

[302] M. K. Carpenter and D. A. Corrigan. *Photoelectrochemistry of Nickel Hydroxide Thin Films*. J. Electrochem. Soc., 136(4), 1022–1026, 1989. doi: 10.1149/1.2096777.

[303] A. Varkey and A. Fort. *Solution growth technique for deposition of nickel oxide thin films*. Thin Solid Films, 235(1-2), 47–50, 1993. doi: 10.1016/0040-6090(93)90241-g.

[304] E. L. Ratcliff, J. Meyer, K. X. Steirer, A. Garcia, J. J. Berry, D. S. Ginley, D. C. Olson, A. Kahn, and N. R. Armstrong. *Evidence for near-Surface NiOOH Species in Solution-Processed NiO_x Selective Interlayer Materials: Impact on Energetics and the Performance of Polymer Bulk Heterojunction Photovoltaics*. Chem. Mater., 23(22), 4988–5000, 2011. doi: 10.1021/cm202296p.

[305] E. Şaşıoğlu, C. Friedrich, and S. Blügel. *Strength of the Effective Coulomb Interaction at Metal and Insulator Surfaces*. Phys. Rev. Lett., 109, 146401, 2012. doi: 10.1103/PhysRevLett.109.146401.

[306] A. J. Tkalych, K. Yu, and E. A. Carter. *Structural and Electronic Features of β-$Ni(OH)_2$ and β-NiOOH from First Principles*. J. Phys. Chem. C, 119(43), 24315–24322, 2015. doi: 10.1021/acs.jpcc.5b08481.

[307] J. Zaffran and M. C. Toroker. *Benchmarking Density Functional Theory Based Methods To Model NiOOH Material Properties: Hubbard and van der Waals Corrections vs Hybrid Functionals*. J. Chem. Theory Comput., 12(8), 3807–3812, 2016. doi: 10.1021/acs.jctc.6b00657.

[308] J. C. Conesa. *Electronic Structure of the (Undoped and Fe-Doped) NiOOH O_2*

Evolution Electrocatalyst. J. Phys. Chem. C, 120(34), 18999–19010, 2016. doi: 10.1021/acs.jpcc.6b06100.

[309] L. Demourgues-Guerlou, L. Fournès, and C. Delmas. *On the Iron Oxidation State in the Iron-Substituted γ Nickel Oxyhydroxides*. J. Solid State Chem., 114(1), 6–14, 1995. doi: 10.1006/jssc.1995.1002.

[310] T. Hofmann, T. H. Yu, M. Folse, L. Weinhardt, M. Bär, Y. Zhang, B. V. Merinov, D. J. Myers, W. A. Goddard, and C. Heske. *Using Photoelectron Spectroscopy and Quantum Mechanics to Determine d-Band Energies of Metals for Catalytic Applications*. J. Phys. Chem. C, 116 (45), 24016–24026, 2012. doi: 10.1021/jp303276z.

[311] S. Ryee and M. J. Han. *The effect of double counting, spin density, and Hund interaction in the different DFT plus U functionals*. Sci. Rep., 8, 2018. doi: 10.1038/s41598-018-27731-4.

[312] D. K. G. de Boer, C. Haas, and G. A. Sawatzky. *Auger spectra of compounds of Sc, Ti and Cr*. J. Phys. F: Metal Phys., 14(11), 2769–2780, 1984. doi: 10.1088/0305-4608/14/11/029.

[313] G. A. Sawatzky and D. Post. *X-ray photoelectron and Auger spectroscopy study of some vanadium oxides*. Phys. Rev. B, 20, 1546–1555, 1979. doi: 10.1103/PhysRevB.20.1546.

[314] E. Antonides, E. C. Janse, and G. A. Sawatzky. LMM *Auger spectra of Cu, Zn, Ga, and Ge. I. Transition probabilities, term splittings, and effective Coulomb interaction*. Phys. Rev. B, 15, 1669–1679, 1977. doi: 10.1103/PhysRevB.15.1669.

[315] T. Kaurila, J. Väyrynen, and M. Isokallio. *Experimental study of resonant photoemission in the metals V, Cr, Mn and Co*. J. Phys. Condens. Matter, 9(31), 6533–6542, 1997. doi: 10.1088/0953-8984/9/31/007.

[316] J. W. Bennett, B. G. Hudson, I. K. Metz, D. Liang, S. Spurgeon, Q. Cui, and S. E. Mason. *A systematic determination of Hubbard U using the GBRV ultrasoft pseudopotential set*. Comput. Mater. Sci., 170, 109137, 2019. doi: 10.1016/j.commatsci.2019.109137.

[317] I. V. Solovyev and P. H. Dederichs. *Ab initio calculations of Coulomb U parameters for transition-metal impurities*. Phys. Rev. B, 49, 6736–6740, 1994. doi: 10.1103/PhysRevB.49.6736.

[318] F. J. Galvez, E. Buendia, P. Maldonado, and A. J. Sarsa. *Optimized effective potential energies and ionization potentials for the atoms Li to Ra*. Eur. Phys. J. D, 50(3), 229–235, 2008. doi: 10.1140/epjd/e2008-00222-0.

[319] G. Shamov, G. Schreckenbach, and T. Vo. *A comparative relativistic DFT and ab initio study on the structure and thermodynamics of the oxofluorides of uranium(IV), (V) and (VI).* Chemistry, 13(17), 4932, 2007. doi: 10.1002/chem.200601244.

[320] J. P. Perdew, M. Ernzerhof, and K. Burke. *Rationale for mixing exact exchange with density functional approximations*. J. Chem. Phys., 105(22), 9982–9985, 1996. doi: 10.1063/1.472933.

[321] G. Kotliar, S. Y. Savrasov, K. Haule, V. S. Oudovenko, O. Parcollet, and C. A. Marianetti. *Electronic structure calculations with dynamical mean-field theory*. Rev. Mod. Phys., 78, 865–951, 2006. doi: 10.1103/RevModPhys.78.865.

[322] C. N. Berglund and W. E. Spicer. *Photoemission Studies of Copper and Silver: Experiment*. Phys. Rev., 136, A1044–A1064, 1964. doi: 10.1103/PhysRev.136.A1044.

[323] S. Hüfner, G. Wertheim, N. Smith, and M. Traum. *XPS density of states of copper, silver, and nickel*. Solid State Commun., 11(2), 323 – 326, 1972. doi: 10.1016/0038-1098(72)90242-6.

[324] C. S. Lawson, B. J. Tielsch, and J. E. Fulghum. *Study of the First Row Transition Metals by X-ray Photoelectron Spectroscopy*. Surf. Sci. Spectra, 4(4), 316–344, 1996. doi: 10.1116/1.1247829.

[325] I. Schnell, G. Czycholl, and R. C. Albers. *Unscreened Hartree-Fock calculations for metallic Fe, Co, Ni, and Cu from ab initio Hamiltonians*. Phys. Rev. B, 68, 245102, 2003. doi: 10.1103/PhysRevB.68.245102.

[326] W. E. Pickett, S. C. Erwin, and E. C. Ethridge. *Reformulation of the LDA+U method for a local-orbital basis*. Phys. Rev. B, 58, 1201–1209, 1998.

[327] G. Bergerhoff and I. D. Brown. *ICSD database*. In F. Allen, editor, *Crystallographic Databases*. International Union of Crystallography, Chester, 1987.

[328] D. R. L. (ed.). *Properties of Solids; Thermal and Physical Properties of Pure Metals*. In *CRC Handbook of Chemistry and Physics*, pages 12–219. CRC Press, Boca Raton, Florida, 84 edition, 2003.

[329] G.-X. Zhang, A. M. Reilly, A. Tkatchenko, and M. Scheffler. *Performance of various density-functional approximations for cohesive properties of 64 bulk solids*. New J. Phys., 20(6), 063020, 2018. doi: 10.1088/1367-2630/aac7f0.

[330] E. R. Ylvisaker, W. E. Pickett, and K. Koepernik. *Anisotropy and magnetism in the LSDA + U method*. Phys. Rev. B, 79, 035103, 2009. doi: 10.1103/PhysRevB.79.035103.

[331] Y. Shoaib Mohammed, Y. Yan, H. Wang, K. Li, and X. Du. *Stability of Ferromagnetism in Fe, Co, and Ni Metals under High Pressure with GGA and GGA+U*. J. Magn. Magn. Mater., 322 (6), 653 – 657, 2010. doi: 10.1016/j.jmmm.2009.10.033.

[332] Y. Fu and D. J. Singh. *Density functional methods for the magnetism of transition metals: SCAN in relation to other functionals*. Phys. Rev. B, 100, 045126, 2019. doi: 10.1103/PhysRevB.100.045126.

[333] J. Kübler. *Spin-density functional calculations for chromium*. J. Magn. Magn. Mater., 20(3), 277 – 284, 1980. doi: 10.1016/0304-8853(80)90446-1.

[334] J. Trygg, B. Johansson, O. Eriksson, and J. M. Wills. *Total Energy Calculation of the Magnetocrystalline Anisotropy Energy in the Ferromagnetic* $3d$ *Metals*. Phys. Rev. Lett., 75, 2871–2874, 1995. doi: 10.1103/PhysRevLett.75.2871.

[335] H. B. Michaelson. *The work function of the elements and its periodicity*. J. Appl. Phys., 48 (11), 4729–4733, 1977. doi: 10.1063/1.323539.

[336] B. Nieuwenhuys and W. Sachtler. *Crystal face specificity of nitrogen adsorption on a platium field emission tip*. Surf. Sci., 34(2), 317–336, 1973. doi: https://doi.org/10.1016/0039-6028(73)90121-0.

[337] M. Gajdos, A. Eichler, and J. Hafner. *CO adsorption on close-packed transition and noble metal surfaces: trends from ab initio calculations*. J. Phys. Condens. Matter, 16(8), 1141–1164, 2004. doi: 10.1088/0953-8984/16/8/001.

[338] A. Patra, J. E. Bates, J. Sun, and J. P. Perdew. *Properties of real metallic surfaces: Effects of density functional semilocality and van der Waals nonlocality*. Proc. Natl. Acad. Sci., 114 (44), E9188–E9196, 2017. doi: 10.1073/pnas.1713320114.

[339] N. V. Smith, G. K. Wertheim, S. Hüfner, and M. M. Traum. *Photoemission spectra and band structures of* d*-band metals. IV. X-ray photoemission spectra and densities of states in Rh, Pd, Ag, Ir, Pt, and Au*. Phys. Rev. B, 10, 3197–3206, 1974. doi: 10.1103/PhysRevB.10.3197.

[340] M. Cococcioni. *A LDA+U study of selected iron compounds*. PhD thesis, International School for Advanced Studies-SISSA, Trieste, 2002. iris.sissa.it/handle/20.500.11767/3939.YPBQ2zqxWc0.

[341] L. H. Bennett, editor. *Electronic Density of States*, Washington, 1971. Institute for Materials Research, National Bureau of Standards.

[342] S. Hüfner and G. Wertheim. *X-ray photoemission studies of the 3d metals from Mn to Cu*. Phys. Lett. A, 47(5), 349 – 350, 1974. doi: 10.1016/0375-9601(74)90122-4.

[343] W. Speier, J. C. Fuggle, R. Zeller, B. Ackermann, K. Szot, F. U. Hillebrecht, and M. Campagna. *Bremsstrahlung isochromat spectra and density-of-states calculations for the* $3d$ *and* $4d$ *transition metals*. Phys. Rev. B, 30, 6921–6930, 1984. doi: 10.1103/PhysRevB.30.6921.

[344] A. Vojvodic, J. K. Nørskov, and F. Abild-Pedersen. *Electronic Structure Effects in Transition Metal Surface Chemistry*. Top. Catal., 57(1-4), 25–32, 2013. doi: 10.1007/s11244-013-0159-2.

[345] G. A. Burdick. *Energy Band Structure of Copper*. Phys. Rev., 129(1), 138–150, 1963. doi: 10.1103/physrev.129.138.

[346] O. Jepsen, D. Glötzel, and A. R. Mackintosh. *Potentials, band structures, and Fermi surfaces*

in the noble metals. Phys. Rev. B, 23(6), 2684–2696, 1981. doi: 10.1103/physrevb.23.2684.

[347] J. Minár. *Correlation effects in transition metals and their alloys studied using the fully self-consistent KKR-based LSDA DMFT scheme*. J. Phys. Condens. Matter, 23(25), 253201, 2011. doi: 10.1088/0953-8984/23/25/253201.

[348] J. Heyd and G. E. Scuseria. *Efficient hybrid density functional calculations in solids: Assessment of the Heyd–Scuseria–Ernzerhof screened Coulomb hybrid functional*. J. Chem. Phys., 121(3), 1187–1192, 2004. doi: 10.1063/1.1760074.

[349] J. Paier, M. Marsman, and G. Kresse. *Why does the B3LYP hybrid functional fail for metals?* J. Chem. Phys., 127(2), 024103, 2007. doi: 10.1063/1.2747249.

[350] A. Stroppa and G. Kresse. *The shortcomings of semi-local and hybrid functionals: what we can learn from surface science studies*. New J. Phys., 10(6), 063020, 2008. doi: 10.1088/1367-2630/10/6/063020.

[351] W. Gao, T. A. Abtew, T. Cai, Y.-Y. Sun, S. Zhang, and P. Zhang. *On the applicability of hybrid functionals for predicting fundamental properties of metals*. Solid State Commun., 234-235, 10–13, 2016. doi: 10.1016/j.ssc.2016.02.014.

[352] N. J. Shevchik. *X-ray photoionization cross sections of d-band metals*. Phys. Rev. B, 13, 4217–4220, 1976. doi: 10.1103/PhysRevB.13.4217.

[353] V. Nemoshkalenko, V. Aleshin, Y. Kucherenko, and L. Sheludchenko. *Transition probability effect on the shape of electron energy distribution in X-ray electron spectra of copper, silver and palladium*. J. Electron Spectrosc. Relat. Phenom., 6(2), 145 – 150, 1975. doi: 10.1016/0368-2048(75)80006-5.

[354] H. Höchst, S. Hüfner, and A. Goldmann. *XPS-valence bands of iron, cobalt, palladium and platinum*. Phys. Lett. A, 57(3), 265 – 266, 1976. doi: 10.1016/0375-9601(76)90059-1.

[355] I. Yang, S. Y. Savrasov, and G. Kotliar. *Importance of Correlation Effects on Magnetic Anisotropy in Fe and Ni*. Phys. Rev. Lett., 87, 216405, 2001. doi: 10.1103/PhysRevLett.87.216405.

[356] A. Jain, G. Hautier, S. P. Ong, C. J. Moore, C. C. Fischer, K. A. Persson, and G. Ceder. *Formation enthalpies by mixing GGA and GGA+U calculations*. Phys. Rev. B, 84, 045115, 2011. doi: 10.1103/PhysRevB.84.045115.

[357] A. G. Petukhov, I. I. Mazin, L. Chioncel, and A. I. Lichtenstein. *Correlated metals and the LDA+U method*. Phys. Rev. B, 67, 153106, 2003. doi: 10.1103/PhysRevB.67.153106.

[358] M. T. Czyżyk and G. A. Sawatzky. *Local-density functional and on-site correlations: The electronic structure of La_2CuO_4 and $LaCuO_3$*. Phys. Rev. B, 49, 14211–14228, 1994. doi: 10.1103/PhysRevB.49.14211.

[359] X. Gonze, J.-M. Beuken, R. Caracas, F. Detraux, M. Fuchs, G.-M. Rignanese, L. Sindic, M. Verstraete, G. Zerah, F. Jollet, M. Torrent, A. Roy, M. Mikami, P. Ghosez, J.-Y. Raty, and D. Allan. *First-principles computation of material properties: The ABINIT software project*. Comput. Mater. Sci., 25(3), 478–492, 2002. doi: 10.1016/s0927-0256(02)00325-7.

[360] X. Gonze, B. Amadon, G. Antonius, F. Arnardi, L. Baguet, J.-M. Beuken, J. Bieder, F. Bottin, J. Bouchet, E. Bousquet, N. Brouwer, F. Bruneval, G. Brunin, T. Cavignac, J.-B. Charraud, W. Chen, M. Côté, S. Cottenier, J. Denier, G. Geneste, P. Ghosez, M. Giantomassi, Y. Gillet, O. Gingras, D. R. Hamann, G. Hautier, X. He, N. Helbig, N. Holzwarth, Y. Jia, F. Jollet, W. Lafargue-Dit-Hauret, K. Lejaeghere, M. A. L. Marques, A. Martin, C. Martins, H. P. C. Miranda, F. Naccarato, K. Persson, G. Petretto, V. Planes, Y. Pouillon, S. Prokhorenko, F. Ricci, G.-M. Rignanese, A. H. Romero, M. M. Schmitt, M. Torrent, M. J. van Setten, B. V. Troeye, M. J. Verstraete, G. Zérah, and J. W. Zwanziger. *The Abinit project: Impact, environment and recent developments*. Comput. Phys. Commun., 248, 107042, 2020. doi: 10.1016/j.cpc.2019.107042.

[361] M. Torrent, F. Jollet, F. Bottin, G. Zérah, and X. Gonze. *Implementation of the projector augmented-wave method in the ABINIT code: Application to the study of iron under pressure*. Comput. Mater. Sci., 42(2), 337–351, 2008. doi: 10.1016/j.commatsci.2007.07.020.

[362] A. A. Mostofi, J. R. Yates, Y.-S. Lee, I. Souza, D. Vanderbilt, and N. Marzari. *wannier90: A tool for obtaining maximally-localised Wannier functions*. Comput. Phys. Commun., 178(9), 685 – 699, 2008. doi: 10.1016/j.cpc.2007.11.016.

[363] J. Huang. *Surface charging behaviors of electrocatalytic interfaces with partially charged chemisorbates*. Curr. Opin. Electrochem., 33, 100938, 2022. doi: 10.1016/j.coelec.2022.100938.

[364] A. Hamelin. *Cyclic voltammetry at gold single-crystal surfaces. Part 1. Behaviour at low-index faces*. J. Electroanal. Chem., 407(1), 1–11, 1996. doi: 10.1016/0022-0728(95)04499-X.

[365] A. Huzayyin, J. H. Chang, K. Lian, and F. Dawson. *Interaction of Water Molecule with Au(111) and Au(110) Surfaces under the Influence of an External Electric Field*. J. Phys. Chem. C, 118(7), 3459–3470, 2014. doi: 10.1021/jp408001t.

[366] Z. K. Goldsmith, M. F. Calegari Andrade, and A. Selloni. *Effects of applied voltage on water at a gold electrode interface from ab initio molecular dynamics*. Chem. Sci., 12, 5865–5873, 2021. doi: 10.1039/D1SC00354B.

[367] H. Heinz, R. A. Vaia, B. L. Farmer, and R. R. Naik. *Accurate Simulation of Surfaces and Interfaces of Face-Centered Cubic Metals Using 12-6 and 9-6 Lennard-Jones Potentials*. J. Phys. Chem. C, 112(44), 17281–17290, 2008. doi: 10.1021/jp801931d.

[368] J. Le, M. Iannuzzi, A. Cuesta, and J. Cheng. *Determining Potentials of Zero Charge of Metal Electrodes versus the Standard Hydrogen Electrode from Density-Functional-Theory-Based Molecular Dynamics*. Phys. Rev. Lett., 119, 016801, 2017. doi: 10.1103/PhysRevLett.119.016801.

[369] P. M. Kowalski, T. Bornhake, O. Cheong, N. Dohrmann, A. L. K. Liston, S. K. Potts, A. Shad, R. Tesch, and Y.-Y. Ting. *Fundamentals of energy storage from first principles simulations: Challenges and opportunities*. Front. Energy Res., 10, 2023. doi: 10.3389/fenrg.2022.1096190.

[370] P. Saha and I. V. Zenyuk. *Electrokinetic Streaming Current Method to Probe Polycrystalline Gold Electrode-Electrolyte Interface Under Applied Potentials*. J. Electrochem. Soc., 168(4), 046511, 2021. doi: 10.1149/1945-7111/abf4aa.

[371] N. Vasiljevic, T. Trimble, N. Dimitrov, and K. Sieradzki. *Electrocapillarity Behavior of Au(111) in SO_4^{2-} and F^-*. Langmuir, 20(16), 6639–6643, 2004. doi: 10.1021/la049632f.

[372] B. Garlyyev, S. Xue, S. Watzele, D. Scieszka, and A. S. Bandarenka. *Influence of the Nature of the Alkali Metal Cations on the Electrical Double-Layer Capacitance of Model Pt(111) and Au(111) Electrodes*. J. Phys. Chem. Lett., 9(8), 1927–1930, 2018. doi: 10.1021/acs.jpclett.8b00610.

[373] V. Stamenkovic, B. S. Mun, K. J. Mayrhofer, P. N. Ross, N. M. Markovic, J. Rossmeisl, J. Greeley, and J. K. Nørskov. *Changing the Activity of Electrocatalysts for Oxygen Reduction by Tuning the Surface Electronic Structure*. Angew. Chem., 118(18), 2963–2967, 2006. doi: 10.1002/ange.200504386.

[374] M. J. Eslamibidgoli, J. Huang, T. Kadyk, A. Malek, and M. Eikerling. *How theory and simulation can drive fuel cell electrocatalysis*. Nano Energy, 29, 334–361, 2016. doi: 10.1016/j.nanoen.2016.06.004.

[375] Z. A. C. Ramli and S. K. Kamarudin. *Platinum-Based Catalysts on Various Carbon Supports and Conducting Polymers for Direct Methanol Fuel Cell Applications: a Review*. Nanoscale Res. Lett., 13(1), 2018. doi: 10.1186/s11671-018-2799-4.

[376] R. Khatib, A. Kumar, S. Sanvito, M. Sulpizi, and C. S. Cucinotta. *The nanoscale structure of the Pt-water double layer under bias revealed*. Electrochim. Acta, 391, 138875, 2021. doi: 10.1016/j.electacta.2021.138875.

[377] J. Huang, J. Zhang, and M. Eikerling. *Unifying theoretical framework for deciphering the oxygen reduction reaction on platinum*. Phys. Chem. Chem. Phys., 20, 11776–11786, 2018. doi: 10.1039/C8CP01315B.

[378] M. J. Eslamibidgoli and M. H. Eikerling. *Atomistic Mechanism of Pt Extraction at Oxidized*

Surfaces: Insights from DFT. Electrocatalysis, 7(4), 345–354, 2016. doi: 10.1007/s12678-016-0313-2.

[379] A. Frumkin and O. Petrii. *Potentials of zero total and zero free charge of platinum group metals*. Electrochim. Acta, 20(5), 347–359, 1975. doi: 10.1016/0013-4686(75)90017-1.

[380] Y. Zhang and W. Yang. *Comment on "Generalized Gradient Approximation Made Simple"*. Phys. Rev. Lett., 80, 890–890, 1998. doi: 10.1103/PhysRevLett.80.890.

[381] B. Hammer, L. B. Hansen, and J. K. Nørskov. *Improved adsorption energetics within density-functional theory using revised Perdew-Burke-Ernzerhof functionals*. Phys. Rev. B, 59, 7413–7421, 1999. doi: 10.1103/PhysRevB.59.7413.

[382] K. Yang, J. Zheng, Y. Zhao, and D. G. Truhlar. *Tests of the RPBE, revPBE, τ-HCTHhyb, ωB97X-D, and MOHLYP density functional approximations and 29 others against representative databases for diverse bond energies and barrier heights in catalysis*. J. Chem. Phys., 132(16), 164117, 2010. doi: 10.1063/1.3382342.

[383] K. Tonigold and A. Groß. *Dispersive interactions in water bilayers at metallic surfaces: A comparison of the PBE and RPBE functional including semiempirical dispersion corrections*. J. Comput. Chem., 33(6), 695–701, 2012. doi: 10.1002/jcc.22900.

[384] A. Kovalenko and F. Hirata. *Three-dimensional density profiles of water in contact with a solute of arbitrary shape: a RISM approach*. Chem. Phys. Lett., 290(1), 237–244, 1998. doi: 10.1016/S0009-2614(98)00471-0.

[385] M. W. Mahoney and W. L. Jorgensen. *A five-site model for liquid water and the reproduction of the density anomaly by rigid, nonpolarizable potential functions*. J. Chem. Phys., 112(20), 8910–8922, 2000. doi: 10.1063/1.481505.

[386] W. F. v. G. H. J. C. Berendsen, J. P. M. Postma and J. Hermans. *Intermolecular Forces*. Reidel, Dordrecht, 1981.

[387] M. Matsugami, N. Yoshida, and F. Hirata. *Theoretical characterization of the "ridge" in the supercritical region in the fluid phase diagram of water*. J. Chem. Phys., 140(10), 104511, 2014. doi: 10.1063/1.4867974.

[388] A. Kovalenko and F. Hirata. *First-principles realization of a van der Waals–Maxwell theory for water*. Chem. Phys. Lett., 349(5), 496–502, 2001. doi: 10.1016/S0009-2614(01)01241-6.

[389] F. Hirata and R. M. Levy. *Ionic association in methanol and related solvents: an extended RISM analysis*. J. Phys. Chem., 91(18), 4788–4795, 1987. doi: 10.1021/j100302a028.

[390] R. T. Cygan, J.-J. Liang, and A. G. Kalinichev. *Molecular Models of Hydroxide, Oxyhydroxide, and Clay Phases and the Development of a General Force Field*. J. Phys. Chem. B, 108(4), 1255–1266, 2004. doi: 10.1021/jp0363287.

[391] R. Tesch, P. M. Kowalski, and M. H. Eikerling. *Properties of the Pt(111)/electrolyte electrochemical interface studied with a hybrid DFT–solvation approach*. J. Phys. Condens. Matter, 33(44), 444004, 2021. doi: 10.1088/1361-648x/ac1aa2.

[392] D. E. Smith and L. X. Dang. *Computer simulations of NaCl association in polarizable water*. J. Chem. Phys., 100(5), 3757–3766, 1994. doi: 10.1063/1.466363.

[393] G. Chuev, S. Chiodo, S. Erofeeva, M. Fedorov, N. Russo, and E. Sicilia. *A quasilinear RISM approach for the computation of solvation free energy of ionic species*. Chem. Phys. Lett., 418(4), 485–489, 2006. doi: 10.1016/j.cplett.2005.10.117.

[394] W. L. Jorgensen, J. Chandrasekhar, J. D. Madura, R. W. Impey, and M. L. Klein. *Comparison of simple potential functions for simulating liquid water*. J. Chem. Phys., 79(2), 926–935, 1983. doi: 10.1063/1.445869.

[395] M. Sprik, J. Hutter, and M. Parrinello. *Ab initio molecular dynamics simulation of liquid water: Comparison of three gradient-corrected density functionals*. J. Chem. Phys., 105(3), 1142–1152, 1996. doi: 10.1063/1.471957.

[396] A. D. Boese. *Density Functional Theory and Hydrogen Bonds: Are We There Yet?* ChemPhysChem, 16(5), 978–985, 2015. doi: 10.1002/cphc.201402786.

[397] A. K. Soper. *The Radial Distribution Functions of Water as Derived from Radiation Total*

Scattering Experiments: Is There Anything We Can Say for Sure? ISRN Phys. Chem., 2013, 1–67, 2013. doi: 10.1155/2013/279463.

[398] S. Zhao, Y. Liu, H. Liu, and J. Wu. *Site-site direct correlation functions for three popular molecular models of liquid water*. J. Chem. Phys., 139(6), 064509, 2013. doi: 10.1063/1.4817784.

[399] A. Ben-Naim and Y. Marcus. *Solvation thermodynamics of nonionic solutes*. J. Chem. Phys., 81(4), 2016–2027, 1984. doi: 10.1063/1.447824.

[400] V. Feldman, A. Kornyshev, and M. Partenskiĭ. *Density functional simulation of interfacial relaxation and capacity of a model metal/electrolyte interface*. Solid State Commun., 53(2), 157–164, 1985. doi: 10.1016/0038-1098(85)90117-6.

[401] J. Huang, P. Li, and S. Chen. *Potential of zero charge and surface charging relation of metal-solution interphases from a constant-potential jellium-Poisson-Boltzmann model*. Phys. Rev. B, 101, 125422, 2020. doi: 10.1103/PhysRevB.101.125422.

[402] H. Heinz, T.-J. Lin, R. Kishore Mishra, and F. S. Emami. *Thermodynamically Consistent Force Fields for the Assembly of Inorganic, Organic, and Biological Nanostructures: The INTERFACE Force Field*. Langmuir, 29(6), 1754–1765, 2013. doi: 10.1021/la3038846.

[403] S. Sakong and A. Groß. *The electric double layer at metal-water interfaces revisited based on a charge polarization scheme*. J. Chem. Phys., 149(8), 084705, 2018. doi: 10.1063/1.5040056.

[404] A. K. Rappe, C. J. Casewit, K. S. Colwell, W. A. Goddard, and W. M. Skiff. *UFF, a full periodic table force field for molecular mechanics and molecular dynamics simulations*. J. Am. Chem. Soc., 114(25), 10024–10035, 1992. doi: 10.1021/ja00051a040.

[405] P. Li, J. Huang, Y. Hu, and S. Chen. *Establishment of the Potential of Zero Charge of Metals in Aqueous Solutions: Different Faces of Water Revealed by Ab Initio Molecular Dynamics Simulations*. J. Phys. Chem. C, 125(7), 3972–3979, 2021. doi: 10.1021/acs.jpcc.0c11089.

[406] S. Schnur and A. Groß. *Properties of metal–water interfaces studied from first principles*. New J. Phys., 11(12), 125003, 2009. doi: 10.1088/1367-2630/11/12/125003.

[407] A. M. Maldonado, S. Hagiwara, T. H. Choi, F. Eckert, K. Schwarz, R. Sundararaman, M. Otani, and J. A. Keith. *Quantifying Uncertainties in Solvation Procedures for Modeling Aqueous Phase Reaction Mechanisms*. J. Phys. Chem. A, 125(1), 154–164, 2021. doi: 10.1021/acs.jpca.0c08961.

[408] S. Lange, P. M. Kowalski, M. Pšenička, M. Klinkenberg, S. Rohmen, D. Bosbach, and G. Deissmann. *Uptake of 226Ra in cementitious systems: A complementary solution chemistry and atomistic simulation study*. Appl. Geochem., 96, 204–216, 2018. doi: 10.1016/j.apgeochem.2018.06.015.

[409] S. Sakong, M. Naderian, K. Mathew, R. G. Hennig, and A. Groß. *Density functional theory study of the electrochemical interface between a Pt electrode and an aqueous electrolyte using an implicit solvent method*. J. Chem. Phys., 142(23), 234107, 2015. doi: 10.1063/1.4922615.

[410] A. Malek and M. H. Eikerling. *Chemisorbed Oxygen at Pt(111): a DFT Study of Structural and Electronic Surface Properties*. Electrocatalysis, 9(3), 370–379, 2017. doi: 10.1007/s12678-017-0436-0.

[411] H. Ogasawara, B. Brena, D. Nordlund, M. Nyberg, A. Pelmenschikov, L. G. M. Pettersson, and A. Nilsson. *Structure and Bonding of Water on Pt(111)*. Phys. Rev. Lett., 89, 276102, 2002. doi: 10.1103/PhysRevLett.89.276102.

[412] S. Meng, E. G. Wang, and S. Gao. *Water adsorption on metal surfaces: A general picture from density functional theory studies*. Phys. Rev. B, 69, 195404, 2004. doi: 10.1103/PhysRevB.69.195404.

[413] T. Jacob and W. A. Goddard. *Agostic Interactions and Dissociation in the First Layer of Water on Pt(111)*. J. Am. Chem. Soc., 126(30), 9360–9368, 2004. doi: 10.1021/ja049920y.

[414] J. Heras and L. Viscido. *Work function changes upon water contamination of metal surfaces*.

Applications of Surf. Sci., 4(2), 238–241, 1980. doi: 10.1016/0378-5963(80)90133-6.

[415] E. Langenbach, A. Spitzer, and H. Lüth. *The adsorption of water on Pt(111) studied by irreflection and UV-photoemission spectroscopy*. Surf. Sci., 147(1), 179–190, 1984. doi: 10.1016/0039-6028(84)90174-2.

[416] V. Tripkovic, M. E. Björketun, E. Skúlason, and J. Rossmeisl. *Standard hydrogen electrode and potential of zero charge in density functional calculations*. Phys. Rev. B, 84, 115452, 2011. doi: 10.1103/PhysRevB.84.115452.

[417] J. Huang, T. Zhou, J. Zhang, and M. Eikerling. *Double layer of platinum electrodes: Non-monotonic surface charging phenomena and negative double layer capacitance*. J. Chem. Phys., 148(4), 044704, 2018. doi: 10.1063/1.5010999.

[418] N. Li and J. Lipkowski. *Chronocoulometric studies of chloride adsorption at the Pt(111) electrode surface*. J. Electroanal. Chem., 491(1-2), 95–102, 2000. doi: 10.1016/s0022-0728(00)00199-6.

[419] F. Zeng, C. Mebrahtu, L. Liao, A. K. Beine, and R. Palkovits. *Stability and deactivation of OER electrocatalysts: A review*. J. Energy Chem., 69, 301–329, 2022. doi: 10.1016/j.jechem.2022.01.025.

[420] M. Yu, E. Budiyanto, and H. Tüysüz. *Principles of Water Electrolysis and Recent Progress in Cobalt-, Nickel-, and Iron-Based Oxides for the Oxygen Evolution Reaction*. Angew. Chem. Int. Ed., 61(1), 2021. doi: 10.1002/anie.202103824.

[421] Y.-F. Li, J.-L. Li, and Z.-P. Liu. *Structure and Catalysis of NiOOH: Recent Advances on Atomic Simulation*. J. Phys. Chem. C, 125(49), 27033–27045, 2021. doi: 10.1021/acs.jpcc.1c06170.

[422] H. Bode, K. Dehmelt, and J. Witte. *Zur Kenntnis der Nickelhydroxidelektrode—I.Über das Nickel (II)-hydroxidhydrat*. Electrochim. Acta, 11(8), 1079–1087, 1966. doi: 10.1016/0013-4686(66)80045-2.

[423] M. J. Eslamibidgoli, A. Groß, and M. Eikerling. *Surface configuration and wettability of nickel(oxy)hydroxides: a first-principles investigation*. Phys. Chem. Chem. Phys., 19(34), 22659–22669, 2017. doi: 10.1039/c7cp03396f.

[424] J. D. Michael, E. L. Demeter, S. M. Illes, Q. Fan, J. R. Boes, and J. R. Kitchin. *Alkaline Electrolyte and Fe Impurity Effects on the Performance and Active-Phase Structure of NiOOH Thin Films for OER Catalysis Applications*. J. Phys. Chem. C, 119(21), 11475–11481, 2015. doi: 10.1021/acs.jpcc.5b02458.

[425] A. C. Garcia, T. Touzalin, C. Nieuwland, N. Perini, and M. T. M. Koper. *Enhancement of Oxygen Evolution Activity of Nickel Oxyhydroxide by Electrolyte Alkali Cations*. Angew. Chem. Int. Ed., 58(37), 12999–13003, 2019. doi: 10.1002/anie.201905501.

[426] N. Sac-Epée, M. R. Palacìn, A. Delahaye-Vidal, Y. Chabre, and J.-M. Tarascon. *Evidence for Direct γ-NiOOH <-> β-Ni(OH)$_2$ Transitions during Electrochemical Cycling of the Nickel Hydroxide Electrode*. J. Electrochem. Soc., 145(5), 1434–1441, 1998. doi: 10.1149/1.1838501.

[427] S. Klaus, Y. Cai, M. W. Louie, L. Trotochaud, and A. T. Bell. *Effects of Fe Electrolyte Impurities on Ni(OH)$_2$/NiOOH Structure and Oxygen Evolution Activity*. J. Phys. Chem. C, 119(13), 7243–7254, 2015. doi: 10.1021/acs.jpcc.5b00105.

[428] I. C. Man, H.-Y. Su, F. Calle-Vallejo, H. A. Hansen, J. I. Martínez, N. G. Inoglu, J. Kitchin, T. F. Jaramillo, J. K. Nørskov, and J. Rossmeisl. *Universality in Oxygen Evolution Electrocatalysis on Oxide Surfaces*. ChemCatChem, 3(7), 1159–1165, 2011. doi: 10.1002/cctc.201000397.

[429] F. Calle-Vallejo, A. Krabbe, and J. M. García-Lastra. *How covalence breaks adsorption-energy scaling relations and solvation restores them*. Chem. Sci., 8(1), 124–130, 2017. doi: 10.1039/c6sc02123a.

[430] Z.-D. He, S. Hanselman, Y.-X. Chen, M. T. M. Koper, and F. Calle-Vallejo. *Importance of Solvation for the Accurate Prediction of Oxygen Reduction Activities of Pt-Based Electrocatalysts*. J. Phys. Chem. Lett., 8(10), 2243–2246, 2017. doi: 10.1021/acs.jpclett.7b01018.

[431] M. Vandichel, K. Laasonen, and I. Kondov. *Oxygen Evolution and Reduction on Fe-doped NiOOH: Influence of Solvent, Dopant Position and Reaction Mechanism*. Top. Catal., 63

(9-10), 833–845, 2020. doi: 10.1007/s11244-020-01334-8.

[432] M. Vandichel, M. Busch, and K. Laasonen. *Oxygen Evolution on Metal-oxy-hydroxides: Beneficial Role of Mixing Fe, Co, Ni Explained via Bifunctional Edge/acceptor Route*. ChemCatChem, 12(5), 1436–1442, 2020. doi: 10.1002/cctc.201901951.

[433] J. M. P. Martirez and E. A. Carter. *Effects of the Aqueous Environment on the Stability and Chemistry of β-NiOOH Surfaces*. Chem. Mater., 30(15), 5205–5219, 2018. doi: 10.1021/acs.chemmater.8b01866.

[434] G. S. Karlberg, J. Rossmeisl, and J. K. Nørskov. *Estimations of electric field effects on the oxygen reduction reaction based on the density functional theory*. Phys. Chem. Chem. Phys., 9(37), 5158, 2007. doi: 10.1039/b705938h.

[435] J. Huang, M. Li, M. J. Eslamibidgoli, M. Eikerling, and A. Groß. *Cation Overcrowding Effect on the Oxygen Evolution Reaction*. JACS Au, 1(10), 1752–1765, 2021. doi: 10.1021/jacsau.1c00315.

[436] C. K. Jung, L. Braunwarth, and T. Jacob. *Grand Canonical ReaxFF Molecular Dynamics Simulations for Catalytic Reactions*. J. Chem. Theory Comput., 15(11), 5810–5816, 2019. doi: 10.1021/acs.jctc.9b00687.

[437] Y. Khalak, B. Baumeier, and M. Karttunen. *Improved general-purpose five-point model for water: TIP5P/2018*. J. Chem. Phys., 149(22), 224507, 2018. doi: 10.1063/1.5070137.

[438] S. Plimpton. *Fast Parallel Algorithms for Short-Range Molecular Dynamics*. Journal of Computational Physics, 117(1), 1–19, 1995. ISSN 0021-9991. doi: https://doi.org/10.1006/jcph.1995.1039.

List of publications

Journal articles

- Z.-D. He, **R. Tesch**, M. J. Eslamibidgoli, M. Eikerling, P. M. Kowalski, *Low-spin state of Fe in Fe-doped NiOOH electrocatalyst materials*, Nat. Commun. 14, 3498, 2023, doi: 10.1038/s41467-023-38978-5.
- P. M. Kowalski, T. Bornhake, O. Cheong, N. Dohrmann, A. L. Koch Liston, A. Shad, S. K. Potts, **R. Tesch**, Y.-Y. Ting, *Fundamentals of Energy Storage from First Principles Simulations: Challenges and Opportunities*, Front. Energy Res. 10, 1096190, 2023, doi: 10.3389/fenrg.2022.1096190.
- **R. Tesch** and P. M. Kowalski, *Hubbard U parameters for transition metals from first principles*, Phys. Rev. B 105, 195153, 2022, doi: 10.1103/PhysRevB.105.195153.
- T. Connor, O. Cheong, T. Bornhake, A. Shad, **R. Tesch**, M. Sun, Z. He, A. Bukayemsky, V. L. Vinograd, S. C. Finkeldei, P. M. Kowalski, *Pyrochlore Compounds from Atomistic Simulations*, Front. Chem. 9, 733321, 2021, doi: 10.3389/fchem.2021.733321.
- **R. Tesch**, P. M. Kowalski, M. H. Eikerling, *Properties of the Pt(111)/Electrolyte Electrochemical Interface Studied with a Hybrid DFT–Solvation Approach*, J. Phys.: Condens. Matter, 33, 444004, 2021, doi: 10.1088/1361-648X/ac1aa2.
- G. L. Murphy, Z. Zhang, **R. Tesch**, P. M. Kowalski, M. Avdeev, E. Y. Kuo, D. J. Gregg, P. Kegler, E. V. Alekseev, B. J. Kennedy, *Tilting and Distortion in Rutile-Related Mixed Metal Ternary Uranium Oxides: A Structural, Spectroscopic, and Theoretical Investigation*, Inorg. Chem., 60, 4, 2246, 2021, doi: 10.1021/acs.inorgchem.0c03077.
- M. Schalenbach, **R. Tesch**, P. M. Kowalski, R.-A. Eichel, *Volcano Plots for Alloy-Electrocatalysts Rethought: Site-specific and Interacting Descriptors for Kinetics and Bonding Strengths*, in preparation.

Conference talks

- **R. Tesch**, M. Eikerling, P. M. Kowalski, *Towards accurate computation of charged electrochemical interfaces at realistic reaction conditions*, European Materials Research Society (E-MRS) Spring meeting, May 2023 (Strasbourg).
- **R. Tesch**, M. H. Eikerling, P. M. Kowalski, *Simulating the Pt(111)/Electrolyte Interface with DFT-ESM-RISM*, 31^{st} Topical Meeting of the International Society of Electrochemistry (ISE),

May 2022 (Aachen).

- **R. Tesch**, M. H. Eikerling, P. M. Kowalski, *The Pt(111)/Electrolyte Electrochemical Interface Described by DFT Coupled to Classical Solvation Theory*, European Materials Research Society (E-MRS) Fall meeting, September 2021 (online).

Conference posters

- **R. Tesch**, Z. He, M. J. Eslamibidgoli, M. H. Eikerling, P. M. Kowalski, *Understanding electrocatalytic behavior of Fe:NiOOH catalysts for the oxygen evolution reaction*, Workshop Materials and Technologies for the Energy Transition, Subtopic 3.2: "Power-Based Fuels and Chemicals", June 2023 (Jülich).
- **R. Tesch**, M. Eikerling, P. Kowalski, *Properties of the Pt(111)/electrolyte interface from a hybrid DFT/classical simulation approach*, NIC Symposium, September 2022 (Jülich).
- P. M. Kowalski, **R. Tesch**, M. H. Eikerling, Performance of hybrid DFT/ESM-RISM scheme for the computation of Pt(111) electrochemical interface, Psi-k conference, August 2022 (Lausanne).
- Z.-D. He, **R. Tesch**, M. J. Eslamibigoli, M. Eikerling, P. Kowalski, *Computational investigation of Fe-doped NiOOH electrocatalysts*, 31^{st} Topical Meeting of the International Society of Electrochemistry (ISE), May 2022 (Aachen).
- **R. Tesch**, G. Murphy, P. M. Kowalski, *Structures of mixed d and f elements oxides (MUO_4) from combination of experiment and first principles simulations*, European Materials Research Society (E-MRS) Fall meeting, September 2021 (online).
- O. Cheong, **R. Tesch**, T. Bornhake, A. Shad, M. H. Eikerling, P. M. Kowalski, A *DFT study of the impact of explicit and implicit solvation on the HCOOH/CO selectivity of CO_2 reduction reaction on Pb(100) surface*, European Materials Research Society (E-MRS) Fall meeting, September 2021 (online).
- **R. Tesch**, B. Verlinden, O. Cheong, M. H. Eikerling, P. M. Kowalski, *Computation of Solvent Effects in Electrochemical and Organic Systems*, 748. Heraeus seminar "Nanoscale Physics of Electrochemical and Biological Media", May 2021 (online).
- **R. Tesch**, M. Eikerling, P. Kowalski, *Parameterization of ESM-RISM for the Pt(111)–Electrolyte Interface*, Deutsche Physikalische Gesellschaft (DPG) Spring Meeting, March 2021 (online).
- **R. Gocht**, M. Eikerling, P. Kowalski, *Deriving Hubbard U Parameters for d-Metals from First Principles*, NIC Symposium, February 2020 (Jülich).

Awards

- Young Researcher Award of the European Materials Research Society (E-MRS), awarded at the E-MRS Spring meeting 2023, May 2023 (Strasbourg).

- 2nd price of the HITEC Communicator Award for the talk *Revealing the Unseen: Atomic-Scale Simulations of Energy Materials* at the HITEC Graduate School Symposium, June 2021 (Jülich).

Band / Volume 618
$Na_5YSi_4O_{12}$-type Na^+ superionic conductors for solid-state batteries
A. Yang (2023), X, 150 pp
ISBN: 978-3-95806-731-8

Band / Volume 619
Development of industry-scalable processes for nanocrystalline silicon oxide in silicon heterojunction solar cells
D. Qiu (2023), 202 pp
ISBN: 978-3-95806-734-9

Band / Volume 620
Photonic Sintering of Garnet-Based Solid-State Batteries
W. S. Scheld (2024), XII, 153 pp
ISBN: 978-3-95806-737-0

Band / Volume 621
Ceria-based composites for application in Oxygen transport membranes
L. Fischer (2024), xiii, 216 pp
ISBN: 978-3-95806-739-4

Band / Volume 622
Investigations of Air Quality Aspects with the Urban Climate Model PALM4U
R. Wegener, U. Javed, R. Dubus, and D. Klemp (2024), 93 pp
ISBN: 978-3-95806-741-7

Band / Volume 623
The Chemical Budget of Radicals and Reaction Mechanisms of the Atmospheric Oxidation of Monoterpenes Investigated in the Atmospheric Simulation Chamber SAPHIR
Y. S. Pang (2024), VI, 158 pp
ISBN: 978-3-95806-742-4

Band / Volume 624
Optimizing spectral electrical impedance tomography technology for improved subsurface characterization
H. Wang (2024), xxix, 113 pp
ISBN: 978-3-95806-744-8

Band / Volume 625
On a multi-spectral method for measuring aerosol properties, suitable for operation on iagos passenger aircraft
P. Weber (2024), ca 123 pp
ISBN: 978-3-95806-746-2

Schriften des Forschungszentrums Jülich
Reihe Energie & Umwelt / Energy & Environment

Band / Volume 626
Modellierung der flächendifferenzierten Grundwasserneubildung für Schleswig-Holstein
Endbericht
I. McNamara, B. Tetzlaff, T. Wolters, F. Wendland (2024), 96 pp
ISBN: 978-3-95806-748-6

Band / Volume 627
Modeling orographic gravity waves from source to termination to improve parameterization schemes in climate models
S. Rhode (2024), xii, ii, 138 pp
ISBN: 978-3-95806-750-9

Band / Volume 628
Abscheidung kolumnarer Wärmedämmschichten mittels Suspensionsplasmaspritzen (SPS) und Plasma Spray – Physical Vapor Deposition (PS-PVD) Prozess
J. Joeris (2024), vii, 133 pp
ISBN: 978-3-95806-752-3

Band / Volume 629
Structure and properties of electrochemical interfaces from first principles simulations
R. Tesch (2024), xvi, 161 pp
ISBN: 978-3-95806-753-0

Energie & Umwelt / Energy & Environment
Band / Volume 629
ISBN 978-3-95806-753-0

Mitglied der Helmholtz-Gemeinschaft

JÜLICH
Forschungszentrum